



HAL
open science

Adequacy of new electrolyte compositions and nanostructured protective layers for the cathode of molten carbonate fuel cells

Arturo Melendez-Ceballos

► **To cite this version:**

Arturo Melendez-Ceballos. Adequacy of new electrolyte compositions and nanostructured protective layers for the cathode of molten carbonate fuel cells. Chemical Physics [physics.chem-ph]. Université Pierre et Marie Curie - Paris VI; Instituto Nacional de Investigaciones Nucleares (ININ), 2017. English. NNT : 2017PA066103 . tel-01622125

HAL Id: tel-01622125

<https://theses.hal.science/tel-01622125>

Submitted on 24 Oct 2017

HAL is a multi-disciplinary open access archive for the deposit and dissemination of scientific research documents, whether they are published or not. The documents may come from teaching and research institutions in France or abroad, or from public or private research centers.

L'archive ouverte pluridisciplinaire **HAL**, est destinée au dépôt et à la diffusion de documents scientifiques de niveau recherche, publiés ou non, émanant des établissements d'enseignement et de recherche français ou étrangers, des laboratoires publics ou privés.

Université Pierre et Marie Curie

THESE

Pour obtenir le grade de

Docteur de l'Université Pierre et Marie Curie – Paris VI

Ecole Doctorale de Chimie Physique et Chimie Analytique (ED 388)

Institut de Recherche de Chimie Paris (IRCP) / Equipe Interfaces, Electrochimie, Energie (I2E)

Adéquation de nouvelles compositions d'électrolytes et de revêtements protecteurs nanostructurés de la cathode pour les piles à combustible à carbonates fondus

Adequacy of new electrolyte compositions and nanostructured protective layers for the cathode of molten carbonate fuel cells

Présentée par :

Arturo Meléndez-Ceballos

Thèse de doctorat de Chimie Physique et Chimie Analytique

Dirigée par Prof. Michel Cassir

Présentée et soutenue publiquement le 28/04/2017

Devant un jury composé de :

LAGERGREN Carina	Professeur à KTH, Stockholm	Rapporteur
CHAMELOT Pierre	Professeur à l'Université de Toulouse	Rapporteur
CAVADIAS Siméon	Professeur à Chimie ParisTech	Examineur
ROLLET Anne-Laure	Chargée de Recherche CNRS à Paris VI	Examinatrice
LAIR Virginie	Maître de conférences à Chimie ParisTech	Examinatrice
FERNANDEZ Suilma M.	Chercheur à l'ININ Mexique	Invitée
BOUALLOU Chakib	Professeur à Mines ParisTech	Invité
CASSIR Michel	Professeur à Chimie ParisTech	Directeur de Thèse



Dedication

To my beloved wife and family,

In memory of my grandmothers
Ana María and María Luisa.

Acknowledgements

The work of this thesis has been carried out at “Institute de Recherche de Chimie Paris” (IRCP) UMR 8247 at the laboratory “Interfaces, Électrochimie, Énergie” (I2E) under the wise direction of Prof. Michel Cassir. This work was possible thanks to “Consejo Nacional de Ciencia y Tecnología” (CONACyT) with the scholarship 314518 SICOB 218619 and the project PLANEX ANR-11-EQPX-0-01.

I have no means to express my infinite gratitude to Michel Cassir for his constant support, scientific insight, and friendship.

I would like to thank the reviewers, Carina Lagergren and Pierre Chamelot of having taken the time for reviewing and commenting this thesis and taking part of the jury.

I am thankful also to the excellent jury members Siméon Cavadias, Anne-Laure Rollet, Virginie Lair, Suilma M. Fernandez and Chakib Bouallou.

Through this almost four years of Ph.D. studies materialized in this thesis, I learned and applied the basics of high temperature electrochemistry in molten carbonates for fuel cell applications and CO₂ electrolysis. It has been a hard task not only for the technical difficulties encountered in working with such harsh media, but also because of the steep learning curve involved in switching between electromechanical engineering and analytical chemistry. This has been one of the most beautiful challenges in my life, which has opened my mind and spirit to a whole vast new world called science. For that, I am grateful to all those who believed I could make such a big change in my career without turning out to be a “Kafkaian metamorphosis”. Among them, Suilma M. Fernandez V. who kicked off this adventure and became a very close friend and collaborator, Michel Cassir that has supported every step during this Ph.D. and has become my greatest mentor and friend, and all the I2E team at the IRCP, who has been there to encourage and support this journey each on their own way.

I would like to thank my beloved wife Ana Paola DíazGómez Treviño who constantly helped me and encouraged me to continue in the difficult task of learning

analytical chemistry, her help with all the chemical problems I had to solve at the beginning of this adventure in my early years as master student and Ph.D. were crucial to my success. I have been lucky finding such a good partner, friend, lover, critic, ally, confident and future scientist. Thanks for all the patience, sacrifices and effort made to be with me in this adventure.

I would like to acknowledge also:

- The useful advice of Armelle Ringuedé and Virginie Lair on impedance spectroscopy, general electrochemistry and thermodynamics.

- All the help I got from Valérie Albin on all the experimental work in this thesis and her patience while teaching me in franglish all the secrets on experimenting with molten salts.

- To Marine Tassé to have taught me all the procedure and details to operate the ALD and to Marie-Hélène Chavanne for her efficient help in our continuous fight *vs* the ALD machine.

- The excellent work carried out by Camille Crapart during her master degree internship and Angeliki Brouzgou during her post-doc internship at I2E.

- To the chemistry department of the ININ, especially to Dr. Eduardo Ordóñez Regil, Ing. Rafael Basurto Sanchez and Dr. Jaime Jimenez Becerril.

- To Stephan Borensztajn for his excellent work at SEM UPMC, he is the responsible of the most beautiful SEM images in this thesis.

- To Philippe Vermaux for his constant help and availability at the SEM platform at IRCP.

- The availability and fast response of Elisabeth Brochet and Marjorie Sadaoui-Eudier at the administration.

- The helpful hand of Jean Francois Engrand and Lionel Lechoix at the machine workshop.

- To all the Post-Docs, Ph.D. students, interns and all the people that have helped me by sharing their knowledge, friendship and support. Especially, Jose de Jesus Cazares Marinero, Aziz Nechache, Elise Nanimaury, Anna Evans, Francois Lebreau, Amandine Calmet, Geoffrey Bonneau, Efrain Palma Anaya (el ahijao), Karima Lassoued, Nour ElHouda Ghanmi, Diego A. Mendoza Muñiz, Marya Dronova, Oumaima Gharbi, Manel Ben-Osman, Dorra Dallel, Junsoo Han, Stéphanie Delannoy, Fethi Bedioui, Andrey Grishin and all the people that I have found at the ENSCP.

Contents

I. Introduction	7
I.1. The molten carbonate fuel cell	11
I.2. Molten Carbonate Fuel Cell Optimization	18
I.2.1. Cathode optimization	19
I.2.2. Electrolyte optimization	21
I.3. The aim of this thesis.....	23
II. Materials and Methods	25
II.1. Atomic Layer Deposition (ALD)	27
II.2. As-deposited and after-test material characterization.....	28
II.3. Electrochemical methods.....	29
II.3.1. Electrochemical Impedance Spectroscopy (EIS)	29
II.3.2. Chronopotentiometry and Chronoamperometry	34
II.3.3. Modified cathodes and electrolyte	35
II.3.4. CO ₂ reduction in carbonate media	37
II.4. Ni solubility measurements	38
II.5. Single-cell set-up	38
III. ALD processed coatings for MCFC cathode protection.....	43
III.1. Metal oxides deposited by ALD	45
III.1.1. Deposition parameters	45
III.1.2. Characterization of as-deposited materials	46
III.1.3. After tests characterization	48
III.1.4. Electrochemical performance of protective coatings	51
III.1.5. Ni solubility	54
III.2. Conclusions.....	54
III.3. Scientific papers.....	55
IV. Electrolyte modification with Cs and Rb additives.....	57
IV.1. Theoretical approach.....	60
IV.1.1. Reaction-rate equations for oxygen reduction.....	60
IV.1.2. Nishina's reaction order analysis.....	63
IV.2. Oxygen and CO ₂ kinetics in Cs modified electrolyte	66
IV.2.1. Data analysis by Nishina's diffusion cases.....	68
IV.2.2. The charge transfer resistance dependency on P_{O_2} and P_{CO_2}	71

IV.3.	Porous NiO behavior in Cs and Rb modified electrolytes	73
IV.4.	Conclusions	78
IV.5.	Scientific papers	79
V.	CO₂ Reduction: study by chronopotentiometry	81
V.1.	The importance of CO ₂ reduction in molten carbonates	83
V.2.	Synthesis of previous works by cyclic voltammetry	84
V.3.	Chronopotentiometry on Gold and Graphite electrodes	85
V.3.1.	Chronopotentiometric measurements	85
V.3.2.	Current reversal chronopotentiometry (CRC)	90
V.3.3.	Transition time analysis	91
V.4.	Chronoamperometry	93
V.5.	Conclusions	94
V.6.	Scientific papers	96
VI.	Single-cell tests in fuel cell mode	97
VI.1.	General concepts	99
VI.1.1.	MCFC operated with hydrogen and CO	99
VI.1.2.	MCEC for CO ₂ reduction	102
VI.2.	Cell assembly and operation	102
VI.2.1.	The gas recovery flange concept and design modification	103
VI.2.2.	Tape-cast of carbonate eutectic	104
VI.2.3.	Calculating the carbonate/matrix ratio	106
VI.3.	Electrochemical measurements on reference cell	107
VI.3.1.	OCP	108
VI.3.2.	I-E curves and fuel cell output power	108
VI.3.3.	EIS	109
VI.4.	Conclusions	111
	General conclusions and prospects	113
	Bibliography	117
	Index of figures	127
	Index of tables	130
	Publications	131

List of Symbols and Acronyms

A	Geometric electrode area, cm ²
ac / AC	Alternating current
ALD	Atomic Layer Deposition
Atm.	Atmosphere
BET	Brunauer–Emmett–Teller porosimetry analysis
BOP	Balance of Plant
CA	Chronoamperometry
C _d	Double layer capacitance, Farads
CP	Chronopotentiometry
CRC	Current reversal chronopotentiometry
CV	Cyclic Voltammetry
DBP	Dibutyl Phthalate
DC	Direct Current
DRT	Distribution of Relaxation Times
<i>E</i>	Potential, V
EDS	Energy Dispersion Spectroscopy
E _i	Starting potential in cyclic voltammetry, V
E-I	Current-Potential or Polarization curves
EIS	Electrochemical Impedance Spectroscopy
<i>emf</i>	Electromotive force
E _{τ/4}	Potential at ¼ of the transition time, V
<i>F</i>	Faraday constant
FC	Fuel Cell
FE	Fast Equilibrium between adsorbed and diffused species
<i>Fd(X)</i>	Feeding flow rate of reactant X, sccm

GC	Gas Chromatography
GC-MS	Gas Chromatography coupled to Mass Spectroscopy
i	Current, A
ICP-AES	Inductively Coupled Plasma to Auger Electron Spectroscopy
K	Equilibrium constant
K	Kelvin Degrees
KKR	Kramers-Kronig dispersion relations
M	Mass, g
MCFC	Molten Carbonate Fuel Cell
MFCs	Mass Flow Controllers
MtCO ₂	Mega ton of CO ₂
MWh	Mega Watt hour
n	Number of electrons transferred
OCP	Open Circuit Potential
PAFC	Phosphoric Acid Fuel Cell
PEMFC	Polymer Electrolyte Membrane Fuel Cell
POCP	Peroxy carbonate path
POP	Peroxide path
Pr(X)	Production rate of reactant X, moles·s ⁻¹ or sccm or Kg·min ⁻¹
PVB	Polyvinyl Butyral
R	Ideal gas constant, J·mole ⁻¹ ·K ⁻¹
RA-RD	Reduction of Adsorbed and then Reduction of Diffusing species
R_{ct}	Charge Transfer Resistance, Ω
RD-RA	Reduction of Diffusing and then Reduction of Adsorbed species
RDS	Rate Determining Step
R_e	Electrolyte Resistance, Ω
R_{mt}	Mass Transfer Resistance, Ω

R_{tot}	Total resistance, Ω
sccm	Standard cubic centimeter per minute
SEM	Scanning Electron Microscopy
SOFC	Solid Oxide Fuel Cell
SOP	Superoxide path
SR	Simultaneous Reduction of adsorbed and diffusing species
T	Temperature, K
TGA-DSC	Thermogravimetric analysis with differential scanning calorimetry
TWh	Tera Watt hour
$U(X)$	Utilization factor of reactant X, moles·s ⁻¹ or sccm
V	Volume, cm ³
$X(an)$	Reactant X at anode
$X(cat)$	Reactant X at cathode
XPS	X-ray Photoelectron Spectroscopy
Z'	Real Impedance, Ω
Z''	Imaginary impedance, Ω
Z_F	Faradaic Impedance
$Z(j\omega)$	Impedance function
Z_w	Warburg impedance
B_1, B_2	Reaction Orders
C_{Ox}	Concentration of the electroactive oxide species, mole·cm ³
C_x	Concentration of species x, mole·cm ⁻³
C_x^0	Bulk concentration of reactant x, mole·cm ⁻³
σ_{app}	Apparent Warburg coefficient, $\Omega \cdot s^{-1/2}$
D_x	Diffusion Coefficient of species x, cm ² ·s ⁻¹
H_{CO_2}	Henry constant for CO ₂
K_d	Dissociation constant

P_{or}	Porosity, %
P_x	Partial pressure of gas x, atm.
$V_{carb(x)}$	Volume of carbonates of component x, cm ³
V_{void}	Void Volume, cm ³
X_{ads}	Species X adsorbed
f	Frequency, Hz
f_c	Characteristic relaxation frequency, Hz
$f(x)$	Function of x
$f_r(x)$	Flooding ration of component x, %
i_0^0	Standard exchange current density, A·cm ⁻²
i_n	Transfer current density, A·cm ⁻²
j	Applied current density, A·cm ⁻²
η	Overpotential, V
σ	Warburg coefficient, $\Omega \cdot s^{1/2}$
τ	Relaxation time in EIS, transition time in CP, both in s
ω	Angular frequency, rad·s ⁻¹
p_1, q_1	Stoichiometry coefficients from reactants
p_2, q_2	Stoichiometry coefficients from products
α_a, α_c	Apparent transfer coefficients
β_1, β_2	Reaction orders related to charge transfer resistance
ρ_{app}	Apparent density, g·cm ⁻³
ΔG_f	Free Gibbs enthalpy, kJ· moles ⁻¹
°C	Celsius Degrees

I. Introduction

*“There is a single light of science, and to
brighten it anywhere is to brighten it
everywhere.”*

Isaac Asimov

Energy production and greenhouse gas emissions, especially CO₂, are among the main concerns of the present world. Annually 23,322 TWh of electricity are generated, from which 41.3 % proceed from coal, 21.7 % from natural gas and 4.4 % from oil. The rest is provided by nuclear plants, hydraulic sources or other renewable sources. The amount of annual greenhouse emissions that come from non-sustainable energy sources is more than 4,678.53 MtCO₂, which represents 14.5 % of the total CO₂ emitted by energy-related combustion processes. Reducing these gas emissions without sacrificing the energy generation capacity is one of the main interest of energy research around the globe [1].

Each year we note an important progress in terms of renewable and clean energy technologies; wind, solar, nuclear and hydraulic energy are the more used and investigated. Nevertheless, other technologies are available to change the energy generation balance towards a cleaner and more sustainable energy supply system, among which are the fuel cells (FC). A fuel cell is an electrochemical device that can transform the energy contained in gas fuels as hydrogen, natural gas or biogas directly into electricity by means of an electrochemical reaction. The advantages of fuel cells over the conventional generation systems are higher conversion efficiency and a very low or in some cases even a zero CO₂ emission.

A fuel cell, as any electrochemical device, is composed of three main components: the anode, electrolyte and cathode; these components are assembled together in what is called a single cell. To gather as much energy as possible, the single cells are piled up in a "stack", each single cell is separated from another by a current collector and a gas compartment that feeds the anode or cathode gases to the corresponding electrode. A fuel cell generation system can be composed of several stacks and the balance of plant (BOP) that is the equipment necessary to control the temperature, as well as to clean, supply and control the infeed and exhaust gases from the system and also collect and transform the electricity generated to be sent to the grid.

There are several types of fuel cells, which are classified in low temperature (50-220 °C) and high temperature (600-850 °C) as shown in Figure I.1. Each type of fuel cell has different particularities and specific development problems to overcome for a full commercialization. At low temperatures, the most developed are the phosphoric acid

fuel cells (PAFC) and, in particular, the polymer electrolyte membrane fuel cell (PEMFC), which has already proven its feasibility from small portable applications up to public transport applications. Nevertheless, progress has to be made to reduce the cost and increase the life time of PEMFC, since the use of precious metal catalysts and the eventual electrode degradation and membrane poisoning are still problems that must be strongly addressed [2].

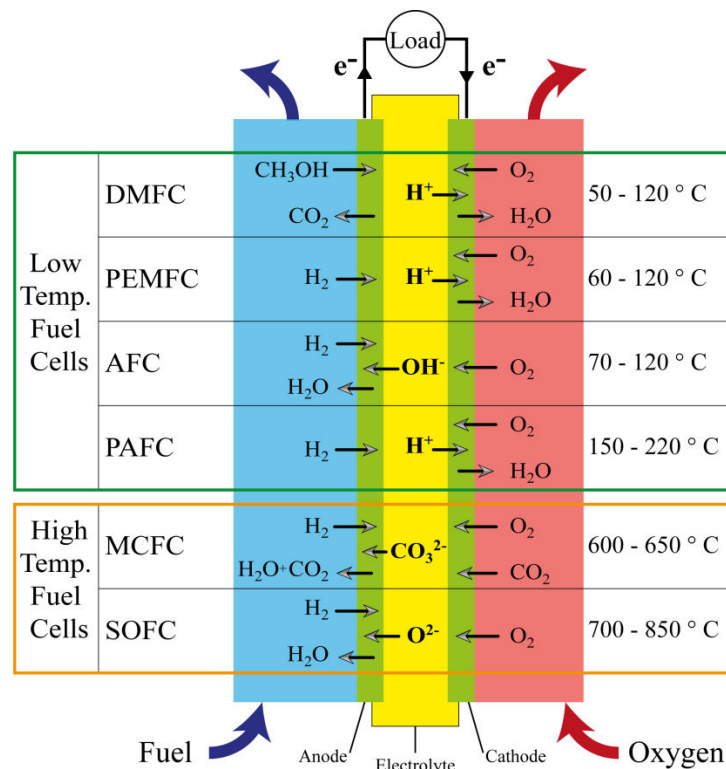


Figure I.1- Fuel cell classification by temperature, working principle and main components.

In the side of high temperature, solid oxide fuel cells (SOFC) are promising technologies for stationary energy generation, but one of their main drawbacks is the difficulty to build a high temperature gastight seal between the fragile ceramic materials of the cells and the anode and cathode compartments. Contrarily, molten carbonate fuel cells (MCFC) have been studied for long time and are now the most widely used fuel cell technology for stationary energy generation around the world, representing 63 % of all the stationary power generation as shown in Figure I.2 [3].

It is always a concern for any emerging technology to reduce material costs and manufacturing complexity as to improve the performance and lifetime of their components if one wishes to make it prevail. In the case of the MCFC, several years of industrial testing and commercial installations have proven the feasibility of this technology. Commercialization has already begun around the world with a maximum stack lifetime of about 4 years, after which the stacks have to be replaced in a complex and onerous manner, since the stack is the most expensive part of the fuel cell system [4]. However, important breakthroughs are necessary to increase the lifetime and performance of the fuel cell to achieve an even more profitable and reliable system. In the next sections, we will overview the basics of the MCFC technology, state-of-the-art materials and the most important problems that should be addressed to ensure a longer stack lifetime.

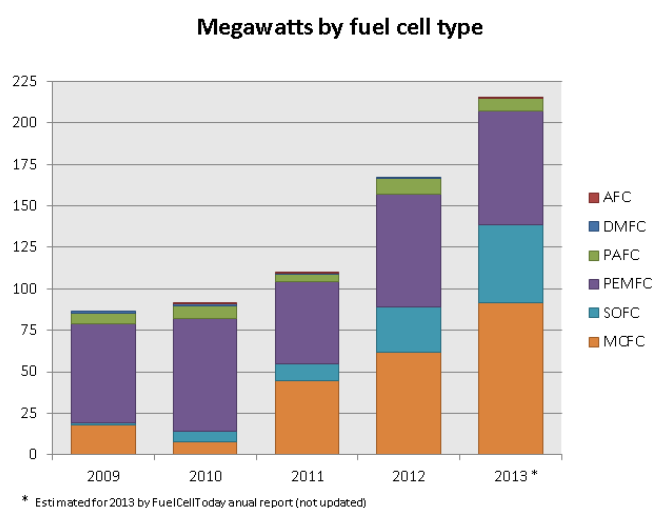


Figure I.2- Total MW of power generated by fuel cell type.

I.1. The molten carbonate fuel cell.

The concept of a molten carbonate fuel cell was already known in the early XX century, but it was not developed as a working system until the 1950s [5]. What makes attractive the idea of using molten salts at a temperature ranging between 650 to 750 °C ? High temperature allows to get rid of expensive catalysts and permits fuel flexibility, (hydrogen, methane, natural gas, biogas, syngas, CO, coal gas, gasoil, ethanol,

propane or biomass). Moreover, impurity of feeding gases is less dramatic in MCFCs than for low temperature technologies; nevertheless, sulfur contents in feed gases could be lethal [6]. Even though the most usual fuel for MCFC devices is natural gas, the fact that CO could be used as fuel offers the possibility of converting fuel from organic origins, *e.g.* biomass, and organic wastes. Biogas proceeding from anaerobic digestion of wastewater, organic waste, agricultural waste, industrial waste, animal by-products or wood, are beginning to be in use. However, most of the time, depending on its origin, its composition is varying and some species such as HCl or H₂S must be removed to avoid electrode poisoning and corrosion of peripheral components [7]. In Figure I.3, a basic schema of a MCFC installation is depicted and the main external components are presented; as it is shown, there is an output stream between 340 to 400 °C available to be used as heat source for a building or another process that requires heat. The use of the residual heat in that manner is called cogeneration, also if the anode residual stream is used in an expansion turbine to generate more electricity.

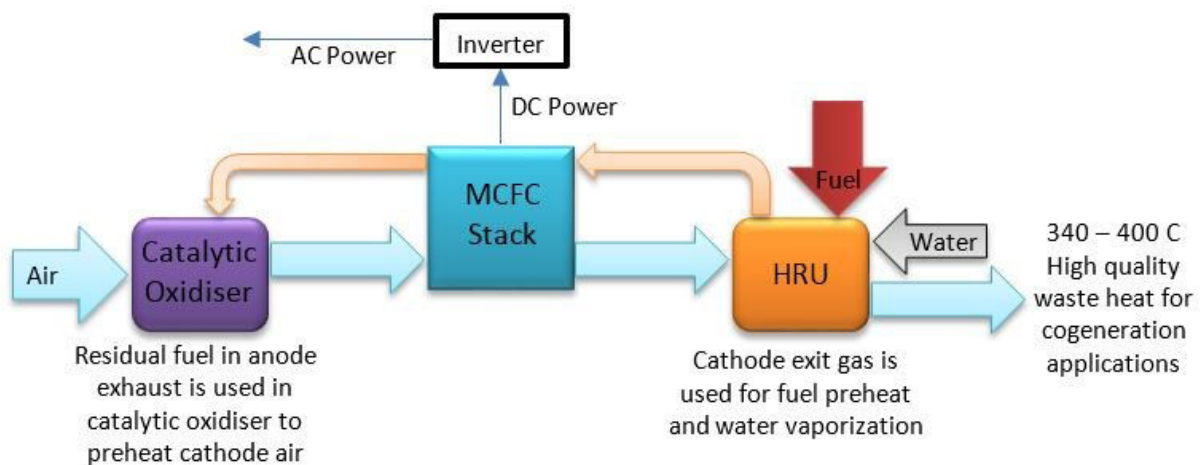


Figure I.3- General scheme of a MCFC installation.

The electrical efficiency for this type of fuel cell varies from 47 to 48 % with the potential to reach up to 57 % and an overall efficiency above 80 % when combining heat and power [8]. Regarding the fuel reforming capabilities of the MCFC, by using the waste heat, three main concepts can be used: external reforming, where the reforming unit is an independent component of the system and is feed with heat from the MCFC by means

of heat exchangers; internal reforming, that incorporates small reforming units within the stacks of the MCFC; and direct reforming system that consist in the incorporation of a catalyst in the gas path inside the stack. These three systems are depicted in Figure I.4 shown herein.

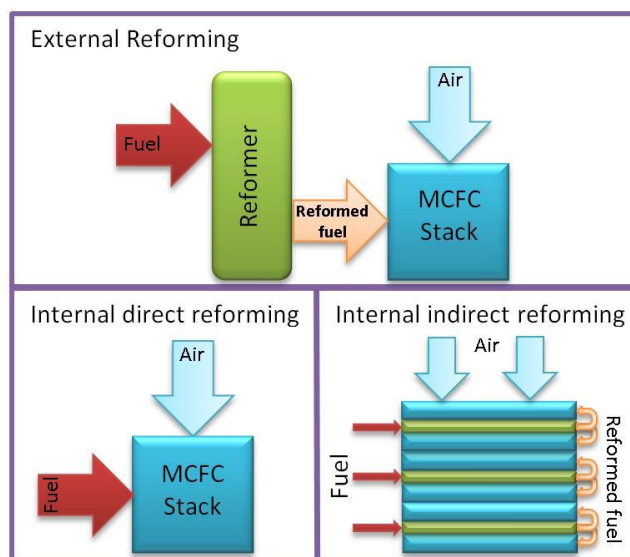


Figure I.4- Scheme of three different concepts of fuel cell reforming of infeed stream.

Focusing on the MCFC stack itself, as any electrochemical system, it is composed of at least three main components, the anode, electrolyte and cathode. The anode consists of a porous nickel plate, containing aluminum or chromium small particles, separated from the cathode by the electrolyte, which is constituted by a porous lithium aluminate membrane holding carbonates, when molten, by means of capillary action. The cathode is constituted by porous nickel oxidized and lithiated *in-situ*; The assembly of these three components is known as a single cell, the coupling of several single cells forms what is known as AS fuel cell stack. A scheme of a single cell is shown in

Figure I.5, where the main components are shown: the frame, which ensures the arrival of the anode and cathode gases, the corrugated plates and collector plates that provide the electrical contact that will drain the available electrons at each electrode.

Molten carbonates are non-toxic and highly conductive salts (1 S cm^{-1} @ $650 \text{ }^\circ\text{C}$) and they can be mixed in eutectics with low melting points (*e.g.* $488 \text{ }^\circ\text{C}$ for $(\text{Li}_{0.62}$ -

$K_{0.38})_2CO_3$) [9]. Even though there are many different carbonate mixtures that could serve as electrolyte, *e.g.* $(Li_{0.62}-K_{0.38})_2CO_3$, $(Li_{0.52}-Na_{0.48})_2CO_3$, $(Li_{0.43}-K_{0.57})_2CO_3$, and $(Li_{0.435}-Na_{0.315}-K_{0.25})_2CO_3$, which have physical properties like density, surface tension, electrical conductivity and oxoacidity that are suitable for MCFC application [10], the two first mentioned are the most studied among and will be used as the standard reference electrolytes along this thesis.

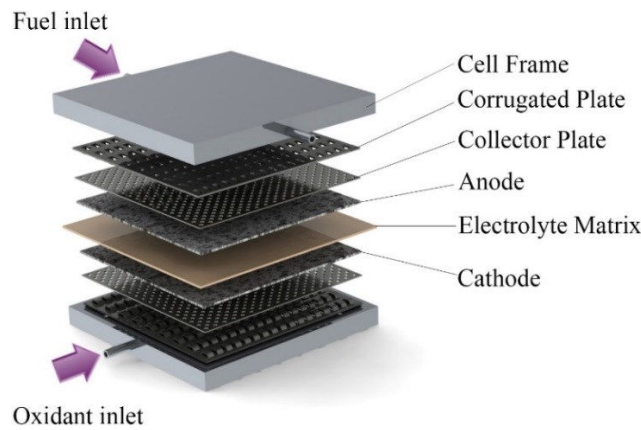


Figure I.5- Scheme of a MCFC single cell components.

As water, molten carbonates present an acidity domain. In the case of water, this acidity domain is governed by the ionization of water. Similarly, molten carbonates dissociate, according to the following equilibrium:



Where M is the alkaline ion (Li, Na, K, Cs, Rb or other) and (l), (s) and (g) are the liquid, solid and gas phase, respectively. Since the molten carbonates are strong electrolytes, the equilibrium can be also defined in its ionic form:



In the oxoacidity concept, O^{2-} is an electron pair donor associated an oxo-acid CO_2 forming an oxo-base CO_3^{2-} [11]. The self-dissociation equilibrium constant, K , has the following expression:

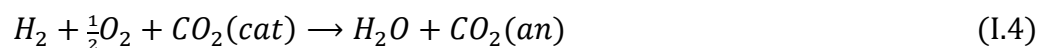
$$K = \frac{a(M_2O) \cdot P_{CO_2}}{a(M_2CO_3)} \quad (I.3)$$

Where $a(M_2O)$ and $a(M_2CO_3)$ are the activities of the corresponding reactants and P_{CO_2} is the partial pressure of carbon dioxide. Thus, the oxoacidity level of the electrolyte lays on the capability to gain or release an oxide ion. So, the oxoacidity can be fixed by imposing a carbon dioxide partial pressure or by adding oxides in the melt. High partial pressures of CO_2 represent, for instance, highly oxoacidic media.

Potential-oxoacidity diagrams also known as Pourbaix-type diagrams are useful to determine the electrochemical stability domain of the species in the molten salts at a given activity [12,13]. In the case of molten carbonates, the diagram vertical limits are established by the dissociation constant while the positive limits are defined by the oxidation of O^{2-} into peroxide, superoxide or oxygen ions. The main redox couples considered in the oxidation side of the diagram are LiO_2/O_2 , M_2O/MO_2 and Li_2O/Li_2O_2 . All the standard potentials of the different couples are referred to the LiO_2/O_2 system being its standard potential equal to zero. Then it is possible to express the Nernst potential of each couple as a function of P_{CO_2} as has been stated by Cassir *et al.* [14]. In molten carbonate mixtures, the limiting reduction reactions are the reduction of alkali ions to metals, CO_2 to CO in oxoacidic media or CO_2 to $C_{graphite}$ in oxobasic media and H_2O to H_2 . However, only the reduction of gases leads to a variation of the potential with P_{CO_2} . An example of the potential-oxoacidity diagram for the Li-K (62-38 mol %) that has been used in the majority of the experiments of this thesis is presented in Figure I.6.

Oxoacidity is a key concept in the chemistry of molten carbonates with a direct influence on the electrochemical reactions at the electrodes and the degradation/dissolution of the cathode, as well as at the stainless steel separator plates. Thus, by controlling the oxoacidity, it is possible to reduce the solubility of Ni in the molten carbonates or favor the presence of a given redox specie.

The global cell reaction involves the consumption of CO_2 at cathode and its recycling at anode:



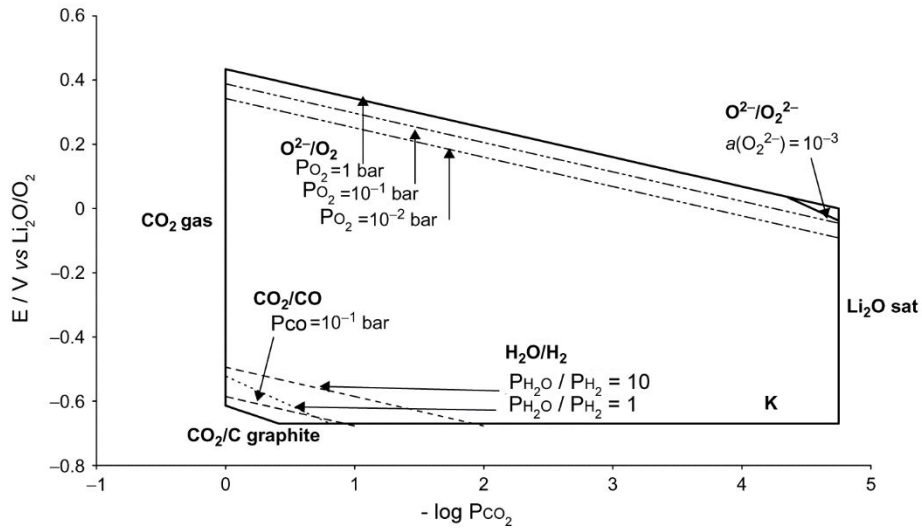


Figure I.6- Potential-oxoacidity diagram for Li-K (62-38 mol%) at 650 °C that allows the study of each redox system as function of P_{CO_2} .

At the cathode side, the oxidant is always air containing CO_2 , which has the particularity of being part of the reduction reaction:



This reaction could follow different oxygen reduction mechanisms because molecular oxygen is not stable in such media and produces reduced oxygen species, O_2^{2-} and O_2^- . Appleby and Nicholson [15–18] described two possible paths for these species, the superoxide path (SOP) and the peroxide path (POP), expressed as follows:

Superoxide Path (SOP):



Peroxide Path (POP):



$$[O_2^{2-}] = K_2 P_{O_2}^{0.5} P_{CO_2}^{-1.0} \quad (I.12)$$



The presence of both O_2^{2-} and O_2^- has been confirmed by electron spin resonance (ESR) and *in situ* Raman spectroscopy in Na_2CO_3 , K_2CO_3 , Li_2CO_3 and $(Li_{0.62}-K_{0.38})_2CO_3$ eutectic [19–21]. A third path for oxygen reduction was proposed by Dunks and Selman [22] involving the species peroxy carbonate CO_4^{2-} which appears as a possible pathway deduced from electrochemical measurements, but it has never being detected by other characterization techniques. This mechanism is described as follows:

Peroxy carbonate path (POCP):



$$[CO_4^{2-}] = K_3 P_{O_2}^{0.5} \quad (I.14)$$



Equilibria I.6, I.11 and I.13 represent the concentration of the species with respect to gas partial pressures. Nevertheless, in reality, there is no one single species present in the electrode vicinity when the oxygen reduction reaction is taking place, the species proposed above could be all present at the same time at different concentrations; depending on the oxoacidity of the carbonate melt (or CO_2 partial pressure) and O_2 partial pressure, the predominant species will change. Thus, the whole electrochemical interaction of species at the electrode can become very complex to be analyzed by simple methods. Nevertheless, Nishina *et al.* have proposed a reaction order analysis based on electrochemical impedance spectroscopy (EIS) to elucidate the dominant species and even deduce interesting values such as the diffusion coefficients of the involved species [23]. This approach will be explained in detail in section IV.1.2. since it will be taken as a reference to evaluate the influence of additives in this thesis.

At the anode, the overall hydrogen oxidation, that is more rapid than oxygen reduction is given by:



Of course, this representation is subdivided into different steps involving adsorbed hydrogen. Among the controversial mechanisms proposed in the literature, we will only show that given by Sammels *et al.* [24] that is the most widely accepted and the simplest, it is expressed as:



It should be pointed out that the anode of MCFC has reached a good state of development, allowing it to work efficiently as electrocatalyst with a very good endurance. The main concern around MCFC technology are the cathode properties, such as corrosion resistance, electroactivity and catalytic properties, and the electrolyte conductivity. Hence, we will detail in the next sections the issues, recent developments and the proposal of this thesis to modify the cathode and electrolyte for improving the MCFC performance and stack lifetime.

I.2. Molten Carbonate Fuel Cell Optimization

Since the first concepts of MCFC were tested, several important breakthroughs along decades of research have allowed the MCFC to become a feasible technology of clean energy generation. In the very first MCFC tests, developed by Broers *et al.* [25] in the middle 1950's, the matrix was composed of porous MgO impregnated with a mixture of carbonates forming a paste, the electrodes were thin layers of metal powders painted on the electrolyte, the collectors were made of silver wire mesh pressed by stainless steel perforated plates, the whole stack was compressed between two thick stainless steel plates by mechanical force. This first fuel cell had a current output around 50 mA cm⁻¹ and a lifetime of 6 months before electrolyte loss decreased its performance significantly. After decades of research, the stack materials were improved and fine

tuned to the point of reaching a maximum current density of 150 mA cm^{-1} , with a power output of 120 mW cm^{-1} and a lifetime of 5 years in continuous operation. LiAlO_2 reinforced by aluminum or alumina micro-rods substituted MgO . The cathode and anode evolved into a nickel plate of micro and macro porosity homogenously distributed and, in the case of the anode, nickel is mixed with 5 % Al or Cr to increase its corrosion resistance. The bipolar plates are made of stainless steel covered by a nickel layer or in some cases made of special austenitic alloys [4]. Nevertheless, there are still important breakthroughs to be achieved; as shown in Table I.1, research is focused on two main objectives: increasing power output and increasing the stack lifetime. The corresponding strategies for reaching such goals are also shown in Table I.1.

Table I.1- MCFC improvement objectives and proposed strategies

Power Density Increase		Stack Lifetime Increase	
Actual	Target	Actual	Target
120 mW cm^{-2}	200 mW cm^{-2}	5 years	10 years
<ul style="list-style-type: none"> ↑ Working temperature ↑ Electrolyte conductivity ↓ Polarization losses at electrodes ↓ Interfacial contact resistance between bipolar plates and electrodes 		<ul style="list-style-type: none"> ↓ Electrolyte losses ↓ Cathode dissolution ↓ Working temperature ↑ Lifetime of electrolyte matrix 	

We will focus on the MCFCs' cathode and electrolyte, since their improvement will affect positively both goals by reducing the cathode dissolution and/or increasing its electroactivity and by rendering the electrolyte whether more conductive and/or more active.

I.2.1. Cathode optimization

At present, lithiated NiO is the material of choice for MCFC cathode application. Pure NiO is an n-type semiconductor and the doping with Li^+ ion enhances the conductivity by creating extra electron holes for conduction by replacing Ni^{2+} with Ni^{3+} , thus enhancing the electrical conductivity of the cathode. Lithiated NiO also offers better

catalytic properties for oxygen reduction reaction as compared to bare NiO. The lithiation process takes place *in situ* at the start-up of the cell, the formed phase being $\text{Li}_x\text{Ni}_{1-x}\text{O}$, the equilibrium Li content was determined to be less than 0.2 by means of nuclear microprobe [26]. Although NiO fulfils the performance requirements such as catalytic activity and electrical conductivity, its dissolution in carbonate electrolyte is one of the issues that limits MCFC lifetime [27]. NiO dissolution occurs according to the following scheme:



Since NiO dissolution occurs by the formation of Ni^{2+} and O^{2-} , its solubility and dissolution rate in molten carbonates depends directly on the oxobasic character of the melt, on the temperature and on CO_2 partial pressure at the cathode gas feed. In general, an increment in temperature or CO_2 partial pressure will lead to a faster NiO dissolution. Such dissolution provokes an increase in the cathode polarization due to structural changes and Ni shortening, occurring when the Ni^{2+} ions migrates to the anode where they are then reduced by the fuel, forming solid nickel particles that precipitates later along the electrolyte matrix providing pathways for electron conduction. For reducing the solubility of the state-of-the-art nickel cathode, two research approaches are commonly followed: the first consist in finding a different cathode material that could or not contain Ni in its composition, the second approach consist in protecting the cathode material with a coating of one or more oxides.

Several studies have been dedicated to both approaches. In the case of alternative cathode materials, LiFeO_2 , Li_2MnO_3 and LiCoO_2 have been investigated; LiFeO_2 and Li_2MnO_3 showed a low electrical conductivity (0.0014 Scm^{-1} @ $650 \text{ }^\circ\text{C}$) that can be increased by doping with Co and Nb (increase up to 60 times of the conductivity); nevertheless, their conductivity is well below that of NiO [28–32]. Contrarily, LiCoO_2 showed a promising performance due to its low resistivity ($1 \text{ } \Omega \text{ cm}^{-1}$ @ $650 \text{ }^\circ\text{C}$) and the solubility of nickel ($0.5 \text{ } \mu\text{g cm}^{-2} \text{ h}^{-1}$), 10 times less than NiO [33–40]. However, the drawback of LiCoO_2 cathodes lays down in the voltage drop between cathode and current collector due to the higher resistance at this interphase that is 2.5 times bigger than with NiO and also on the lower mechanical strength compared to NiO. Thus, this

provokes a major difficulty for commercial fabrication of large area cathodes. The ternary system $\text{LiFeO}_2\text{-LiCoO}_2\text{-NiO}$ has also been tested by Bloom *et al.* [29,41] with very interesting results approaching the behavior of NiO. Similar results were also obtained by Wijaysinghe *et al.* [42,43]. Even though these kinds of materials perform well in comparison with NiO, their long term performance has not been yet studied.

The second approach for protecting nickel cathode from dissolution is by coating it with selected oxides or mixture of oxides. This has the advantage of maintaining the cheap and efficient NiO-based cathode, but improving its corrosion resistance by the thin protective layer. Hence, most of the research efforts have developed this approach to reach effective cathode protection. Some of the deposition techniques used are sol-gel [44–49], electroless deposition [50], electrochemical deposition [51–58] and sputtering [59]. Among the materials deposited on the nickel cathode are TiO_2 , CeO_2 , CoOOH , Co_3O_4 , $\text{La}_{0.8}\text{Sr}_{0.2}\text{CoO}_3$, La_2O_3 , Y_2O_3 , $\text{LiMg}_{0.05}\text{Co}_{0.95}\text{O}_2$ and $\text{Mg}_{0.05}\text{Fe}_{0.01}\text{Ni}_{0.94}\text{O}$. From all of them, La, Ce, Ti and Co based coatings seem to be the most promising. However, it is important to be fully aware of the problems related to the deposition techniques, as homogeneity, thickness, adherence to the substrate, porosity reduction, coating conformity or deposition complexity, which makes them relatively difficult to take to the production line in commercial fuel cell application. Nevertheless, protecting the cathode in this way seems to be more effective than changing the whole cathode material. Hence, we decided to use a novel ultra-thin layer deposition technique, Atomic Layer Deposition (ALD), more detail about this technique will be given in section II.1.

I.2.2. Electrolyte optimization

The nature of the molten carbonate electrolyte does not only affect the electrochemical parameters, such as electrolyte resistance, ion conductivity, diffusion coefficients, mass transport and polarization phenomena, but also cathode wettability, volatility, wet seal properties, matrix retention and electrolyte distribution. Hence, optimizing the MCFC electrolyte is a challenging topic that could increase the lifetime and performance of the fuel cell. As was already mentioned, the nature of the eutectic and its oxobasic properties also may influence favorably the electrode kinetics and, in particular, at the cathode side where the reduction reaction is known to be slow. Even if $(\text{Li}_{0.52}\text{-Na}_{0.48})_2\text{CO}_3$, electrolyte has interesting properties, such as higher ionic conductivity, better cell performances in certain conditions [60–64], lower effective

volatility [62,65] and a lower solubility of the nickel cathode with respect to $(\text{Li}_{0.62}\text{-K}_{0.38})_2\text{CO}_3$ [64,66], but this eutectic presents some drawbacks. Below 600°C , $(\text{Li}_{0.52}\text{-Na}_{0.48})_2\text{CO}_3$ cells have lower performances than $(\text{Li}_{0.62}\text{-K}_{0.38})_2\text{CO}_3$ cells probably due to a lower oxygen solubility and a higher surface tension; the first mentioned parameter seems to be the major cause of low performances at low temperatures [67]. Furthermore, $(\text{Li}_{0.62}\text{-K}_{0.38})_2\text{CO}_3$ eutectic oxoacidity is higher than that of $(\text{Li}_{0.52}\text{-Na}_{0.48})_2\text{CO}_3$ and thus, it causes a faster NiO dissolution [68]. It is therefore necessary to modify the nature of these electrolytes for optimizing their behaviour in MCFC. This can be achieved by the addition of relatively small quantities of other salts like carbonates of Rb, Cs, La, Sr, Ba and Mg or by adding other types such as halogens (F^- , Cl^- , Br^- and I^-), NO_3^- , SO_4^{2-} , CrO_4^{2-} , MoO_4^{2-} or WO_4^{2-} [69]. However, the addition of the last mentioned cations is difficult to study since their interaction in the molten carbonates is not yet fully understood. Henceforward, addition of carbonate additives is more interesting, especially those of Rb and Cs, which, have a favorable influence on MCFC performance. Experiments have been reported in single cells with $\text{Li}_{0.75}\text{Cs}_{0.25}$ carbonate electrolytes showing higher cell potentials, lower cathode and anode overpotentials than $\text{Li}_{0.68}\text{K}_{0.32}$ or $\text{Li}_{0.52}\text{Na}_{0.48}$, usual carbonate eutectics [70]. Cs_2CO_3 is thermally stable up to 700°C and some $\text{Li}_2\text{CO}_3\text{-Cs}_2\text{CO}_3$ mixtures have melting points below 550°C [71]. These mixtures have also lower surface tension [72] and greater oxygen solubility as well as increased electrode kinetics, especially at low temperature. But they also have a disadvantage because of their relative acidity which promotes NiO dissolution. However, this drawback may be compensated by using Li-rich $\text{Li}_2\text{CO}_3\text{-K}_2\text{CO}_3\text{-Cs}_2\text{CO}_3$ mixtures since NiO solubility is inversely proportional to Li content in the melt and operating at reduced temperatures. Interesting patents report the improvement of a MCFC with a Li-K or Li-Na electrolyte modified by the addition of different proportions of Cs or Rb (from 0.05 % to 25 %) [73,74]. This solution is extremely attractive because the favorable role of Cs or Rb can be combined to the usual properties of Li-Na or Li-K classical melts.

I.3. The aim of this thesis

In the present research project, the main objective is to improve the MCFC cathode dissolution resistance and performance by means of two main guidelines: one is cathode modification *via* ultra-thin layer deposits of oxides, especially TiO_2 , CeO_2 , Co_3O_4 and Nb_2O_5 onto commercial cathode material by means of a powerful deposition technique: Atomic Layer Deposition (ALD). The second is electrolyte modification by additives to improve the oxygen reduction reaction, specifically by addition of Cs_2CO_3 and Rb_2CO_3 to standard carbonate mixtures such as $(\text{Li}_{0.62}\text{-K}_{0.38})_2\text{CO}_3$ and $(\text{Li}_{0.52}\text{-Na}_{0.48})_2\text{CO}_3$. The influence of such cations on the cathode reaction kinetics at a gold flag electrode and on the performance of a commercial cathode material will be thoroughly analyzed. At this initial stage, electrochemical tests are carried out in a half-cell configuration. As a final stage, the materials with the best characteristics will be tested in a single cell set-up and their performance in real MCFC conditions evaluated.

As part of the novel applications of MCFC technology, we will also study CO_2 reduction in molten carbonates of $(\text{Li}_{0.62}\text{-K}_{0.38})_2\text{CO}_3$, $(\text{Li}_{0.52}\text{-Na}_{0.48})_2\text{CO}_3$ and $(\text{Na}_{0.56}\text{-K}_{0.44})_2\text{CO}_3$ by chronopotentiometry and chronoamperometry at gold flag and graphite electrodes for better understanding the mechanisms behind the reduction process. As a result, new electrode materials are proposed and evaluated for CO_2 reduction in molten carbonate media. This part of the study will pursue previous research already carried out by our team by means of cyclic voltammetry.

In summary, this work will evaluate a novel deposition method for protecting the MCFC cathode from dissolution without detrimental effect on the electrochemical properties. Coatings of TiO_2 , CeO_2 , Co_3O_4 and Nb_2O_5 will be tested. In parallel, we will also evaluate the modification of the $(\text{Li}_{0.62}\text{-K}_{0.38})_2\text{CO}_3$ electrolyte with additives such as Cs or Rb carbonates and their effect on oxygen reduction kinetics and eventual benefit in the case of CO_2 reduction in molten carbonate media.

Finally, after operating directly in the molten carbonate bulk in most of this work, we will test our findings in a new single cell set-up.

II. Materials and Methods

“An experiment is a question which science poses to Nature, and a measurement is the recording of Nature’s answer.”

Max Planck

II.1. Atomic Layer Deposition (ALD)

Atomic layer deposition is a chemical gas phase deposition technique developed in Finland in the 1970's by T. Suntola [75]. In ALD, reactant gas pulses are separately introduced into a chamber, where the substrates to be coated are placed. Growth is achieved through self-terminating surface reactions. Self-terminating means that only one monolayer of reactant gas species can be adsorbed to the surface during a pulse. The pulses containing reactant gases are separated by purging pulses where the ALD reactor is flushed with an inert gas. The purging pulses ensure that the reactant gas pulses do not mix. Mixing of the reactant gas pulses would lead to continuous growth and the accurate thickness control of the deposition process would be lost. By-products like detached ligands and excess reactants are also flushed away by the purging pulses. A complete set of reactant gas pulses and purging pulses needed to deposit a certain compound are referred to as a cycle. If deposition parameters have been chosen properly, the number of cycles rather than the concentration of the reactant species determines the film thickness [76]. An illustration of a deposition cycle is shown in Figure II.1.

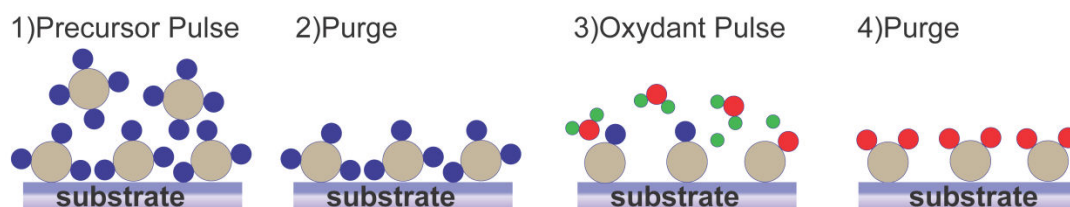


Figure II.1- Schema of the purge and pulse sequence in ALD.

An ALD machine from Picosun[®] model SUNALE[™] R-series was used to deposit all the protective layers studied herein. The deposition parameters are detailed in section III.1. for every deposited material. In our case, the reactor is a vertical flow type reactor, the precursor, oxidant and carrier flows from the top to the bottom of the deposition chamber. The substrate is placed at the middle onto a grill as shown in the scheme of Figure II.2. A homogenous deposition of a thin layer is assured by controlling the gas

flow of inert gas to the chamber, the working pressure of the system should be kept between 7 and 12 hPa in this specific reactor model.

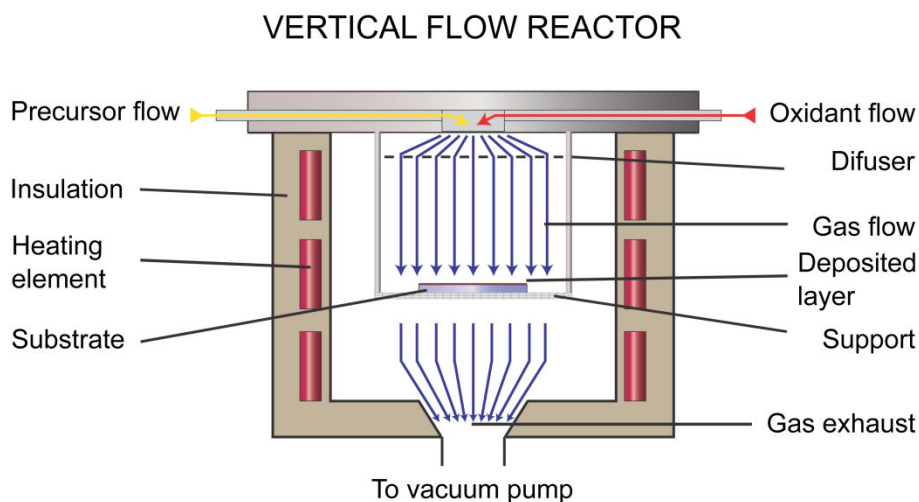


Figure II.2- Vertical gas flow reactor scheme.

After each deposition process, materials should be characterized to assure the quality and homogeneity of the thin layers, this is done by using typical material characterization techniques on the as-deposited materials. Also, material characterization after-testing is performed to evaluate the modifications of the as-deposited materials by the molten carbonate media.

II.2. As-deposited and after-test material characterization

Unless otherwise noted on the scientific papers of section III.3. , for most samples, X-ray diffraction was performed with a PANalyticalX'pert Pro from Anton Paar with Cu-K α 1 radiation ($\lambda=1.54056\text{\AA}$). The diffraction pattern was obtained by scanning between 20 and 80° by steps of 0.02 (2 θ °) with a fixed counting time of 2.3 s and sample rotation of 3 rpm. Once the data were obtained, Scherrer analysis calculation was used to obtain the average crystal size of the deposited layer by determining the angular position and FWHM of the peaks between 28 and 60 2theta degrees. Scanning Electron Microscopy (SEM) and Energy Dispersion Spectroscopy (EDS) analyses were performed with a ZEISS® Ultra 55 microscope to evaluate the surface morphology and to measure layer thicknesses. In some cases, Raman spectra were obtained in a Lab Raman HR-800 from

Horiba Jobin Yvon® spectrometer with a spectral resolution of 2 cm⁻¹ and Olympus® microscope using a 10X or 100X objective lenses. Spectra were recorded from 100 to 1800 cm⁻¹ with a He-Ne laser of wavelength 632.81 nm and grid of 600 or 1800. Spectrometer calibration was performed with Si (1 1 1). Some samples were also analyzed by X-ray photoelectron spectroscopy (XPS), the X-ray photoelectron spectra were recorded using a Thermo Scientific K-Alpha X-ray photoelectron spectrometer with a monochromator Al K α X-ray ($h\nu = 1486.61$ eV) for sample excitation. An argon ion beam was used to prevent samples surface charging. The spectrometer energy calibration was obtained using Au 4f 7/2 and Cu 2p 3/2 photoelectron lines. The position of the adventitious carbon C 1s peak at 284.6 eV was used as an internal reference in each sample to determine the binding energies with an accuracy of ± 0.1 eV. The residual pressure in the analysis chamber was maintained below 1×10^{-8} Torr, during data acquisition. The survey spectra of each concerned sample were obtained between 0 and 1000 eV. The spectra was collected and analyzed with Advantage 4.0 software.

II.3. Electrochemical methods

II.3.1. Electrochemical Impedance Spectroscopy (EIS)

Electrochemical impedance spectroscopy (EIS) studies the response of an electrochemical system to the application of a periodic small amplitude alternating current (ac) signal. The measurements are based in acquiring data of the system response for various ac frequencies. That is why it is called impedance spectroscopy. From electrical circuit theory, any electrical circuit could be expressed as a complex impedance by following Ohm's and Kirchhoff laws and by taking the $Z(j\omega)$ expressions of a resistance (R), a capacitance ($1/j\omega C$) or an inductance ($j\omega L$). Thus, for example, the impedance of a resistance connected in parallel with a capacitance will be expressed by:

$$Z(j\omega) = R - j \frac{1}{\omega C} \quad (\text{II.1})$$

To extrapolate the circuit response to the phenomena taking place in an electrochemical cell, equivalent electrical circuits can be modeled to approximate the real

impedance response of a given electrochemical system. Thus, interpreting the electrochemical behavior through distributed elements in an equivalent circuit is complex, but essential for interpreting impedance spectra. Ideally, a faradaic process will be composed of an electrolyte resistance R_e , a double layer capacitance C_d , and a faradaic impedance Z_F , the circuit that will represent those contributions is shown in Figure II.3-a). Impedance Z_F can be decomposed in two components, a resistance accounting for the charge transfer resistance R_{ct} and in the case of a semi-infinite diffusion process a Warburg element Z_w defined as:

$$Z_F = R_{ct} + [\sigma\omega^{-1/2} - j(\sigma\omega^{-1/2})] \quad (\text{II.2})$$

Where:

$$\sigma = \frac{RT}{F^2 A \sqrt{2}} \left(\frac{1}{D_O^{1/2} C_O} + \frac{1}{D_R^{1/2} C_R} \right) \quad (\text{II.3})$$

Where A is the area of the electrode, D_O and D_R are the diffusion coefficients and C_O and C_R the concentration of the oxidized and reduced species respectively. This equivalent circuit is shown in Figure II.3-b).

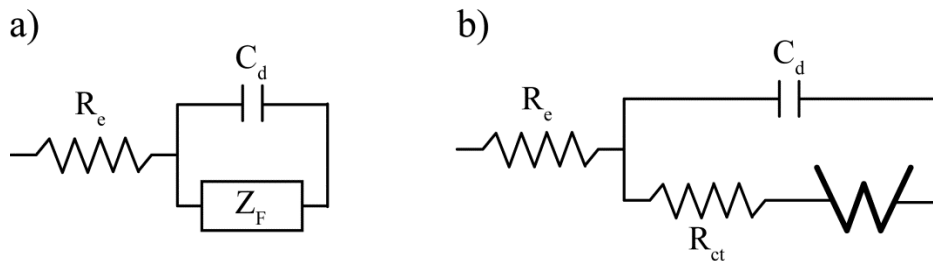


Figure II.3- Equivalent circuit for a simple faradaic electron transfer with semi-infinite diffusion a) with Z_F component, b) with decomposition of Z_F .

The response of such circuit can be represented by a Nyquist plot relating the imaginary (y axis) and real (x axis) impedance, as the one presented in Figure II.4 where the values of R_e and R_{ct} can be easily determined, the first one is the distance from the origin to the first intersection of the semicircle with the x axis, the second is the diameter of the semicircle. The double layer capacitance can also be deduced from the maximum of the semicircle known as relaxation frequency where $\omega = 1/R_{ct}C_d$. The

behavior is controlled at high frequencies by the charge transfer and at low frequencies by mass transfer. The semi-infinite diffusion described by the Warburg impedance will form a straight line with a 45 ° angle.

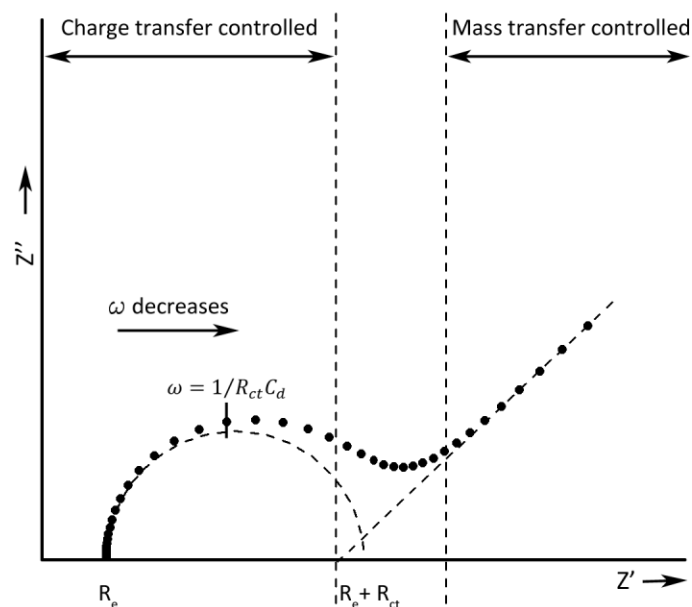


Figure II.4- Nyquist plot of the impedance data for an electrochemical reaction with semi-infinite diffusion and the parameters that can be found in it.

More complex systems responses contain information about the interphase, its structure, the reactions taking place at the inner and outer Helmholtz plane and even information of chemical reactions preceding or succeeding the reaction at the electrode. It has become a useful tool to analyze electrode processes and complex interphases. However, EIS is a very sensitive technique and should be used with care since the analysis of the data is performed most of the time by fitting an equivalent circuit that must represent the physical and chemical phenomena taking place in the system. This equivalent circuit approach is tricky since the data can be well fitted by several different circuits that might not represent the phenomena at the electrode. For this reason, seeking for a more objective analysis tool has been the objective for some researchers leading to the development of Kramers-Kronig dispersion relations (KKR) for the validation of the experimental data. This method first developed by Kramers and Kronig [77] was further developed by Bode [78,79], where a series of equations can calculate the real part from the imaginary part, or the phase from the modulus or *vice versa* from

a given impedance data set. However, the equations are valid only if the EIS data complies with the four indispensable conditions for good data acquisition that are: linearity, causality, stability and finiteness. The method most widely used to evaluate the KKR consists on the approximation of the experimentally acquired impedance data by the Voigt model followed by a transformation of the modeled data. This method developed by Orazem was further modified by Boukamp [80] allowing isolation of data that does not comply with KKR conditions by the inspection of the relative residual plots. In Figure II.5 an example of data validation using Boukamp's Kramers-Kronig test (K-K test V1.01) is shown. In this work, the acceptable quality of data was determined to be $\pm 2\%$ error, upper and lower limits are depicted with a red line in Figure II.5, some points at low frequencies are out of the limit, but in general the quality of the data is considered good since the rest of the points fall into the established limits.

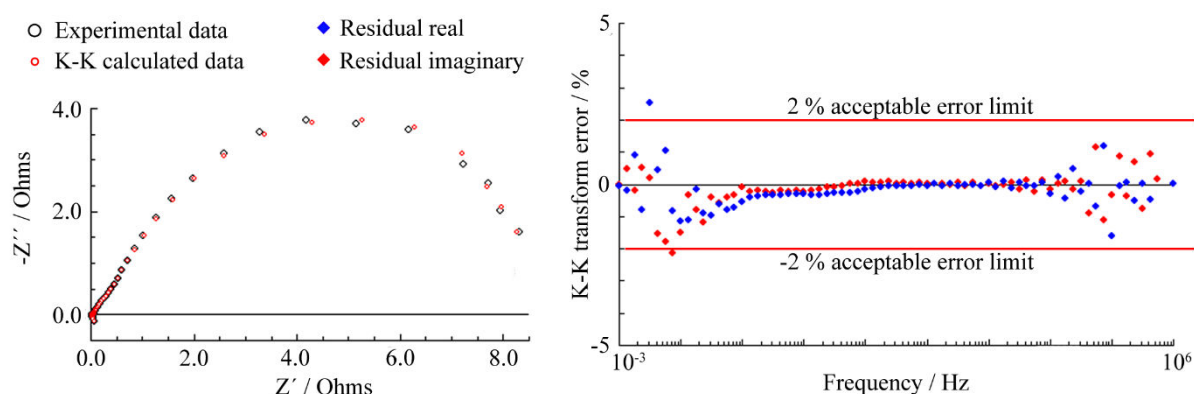


Figure II.5- Example of data validation by Kramers-Kronig transforms by using the program developed by Boukamp K-K test V1.01.

It should be pointed out that it is very difficult to work with molten carbonates, results better than the one shown below are difficult to obtain. However, all EIS data were taken at least 3 times and in some cases even up to 8 times to be completely sure the system was stable, in some cases electrode re-polishing was necessary and in others, waiting for a long period of time (between 24 and 48 h) for the atmosphere to stabilize; in any case, only the data with less than $\pm 2\%$ error were taken to make all the analyses presented in this thesis.

Another important tool in EIS that has become popular is the distribution of relaxation times (DRT) [81,82], its main objective is to avoid the use of circuit modeling to subtract valuable information from EIS. The DRT, also known as a transformation to the τ -domain was first introduced by Maxwell and later expanded by Debye who used it in dielectric spectroscopy to describe the time required for dipolar molecules to reversibly orient themselves with the external ac electric field; in other words, is the time that takes for a system to which an excitation signal was applied to return or “relax” to equilibrium after the excitation was removed. In impedance spectroscopy the relaxation time is related to the characteristic relaxation frequency f_c which corresponds to the frequency where the switching between two conduction mechanisms occurs [83]. Every phenomena in an electrochemical system has a relaxation time τ related to the inverse of f_c by $\tau = 1/\omega_c$; however, transformation to the τ -domain emphasizes the larger contributions to the frequency dispersion that are visible as more or less sharp peaks where their positions define the major time constants of the electrochemical cell. Thus, following the peak position and height as function of a variable like temperature, partial pressure or polarization provides information on the electrochemical processes [81]. The DRT denoted as the function $Y(\tau)$ can be obtained by solving the following expression:

$$Z(\omega) = R_0 + R_{pol} \int_0^{\infty} \frac{Y(\tau)}{1+j\omega\tau} d\tau \quad \text{with} \quad \int_0^{\infty} Y(\tau) d\tau = 1 \quad (\text{II.4})$$

Where $Z(\omega)$ is the impedance data, R_0 is the ohmic (frequency independent) part of the impedance and R_{pol} is the polarization resistance. The term $\left[\frac{Y(\tau)}{1+j\omega\tau} \right] d\tau$ specifies the fraction of the overall polarization with relaxation times between τ and $\tau + d\tau$. Unfortunately, the entire impedance spectra $Z(\omega)$ cannot be measured, only a fraction of it is sampled over a finite frequency range, therefore the convolution equation II.4 cannot be solved analytically. Additionally, even if we could have the entire impedance spectra, there are many possible solutions for $Y(\tau)$, even if we apply a major restriction such that $Y(\tau)$ should be positive for all τ values that will reduce considerably the solutions. Several routes to obtain the DRT have been proposed: Fourier transform (FT) and fast Fourier transform (FFT) [81,84,85], maximum entropy [86,87] and Tikhonov regularization (TR) [82,88,89]. Boukamp *et Rolle* [90] have compared those approaches and have find them not completely satisfactory in the sense that all of them require manipulation of some factors or variables to deliver a fair DRT representation. However, for practical purposes, any of the previously mentioned approaches

can be successfully used to elucidate the phenomena taking place at the electrochemical system independently of an equivalent circuit model if care is taken when evaluating the DRT and parameters are properly selected. For this thesis, the route to the DRT presented by Wan *et al.* [82] by means of the MatLab® package DRTTOOLS [91] will be used to identify the contributions for the single cell tests in Chapter VI.

II.3.2. Chronopotentiometry and Chronoamperometry

Chronopotentiometry is based on the measurement of the potential variation with respect to time when a constant current is applied to an electrochemical system. When applying the current, the potential will first present a fast variation as double layer capacitance is charged, until a potential where a species can be oxidized or reduced. The length of the potential plateau formed will last until the species being oxidized or reduced is depleted and a drastic potential variation will occur until another electrode process appears at a given potential forming a second plateau. The length of a plateau related to any electrode process is known as transition time (τ) and will depend under certain conditions on the concentration of the electroactive species. For diffusion-controlled reactions on a plane electrode, transition time will be given by (Sand's equation):

$$\tau^{1/2} = \frac{\pi^{1/2} n F A C_0 D_0^{1/2}}{2 i} \quad (\text{II.5})$$

Where C_0 is the concentration of the electroactive species in the bulk of the solution in $\text{mol}\cdot\text{cm}^{-3}$, i is the applied current (amp.), D is the diffusion coefficient of the diffusing species in $\text{cm}^2\cdot\text{s}^{-1}$, F is the Faraday constant, A is the electrode area in cm^2 and n is the number of electrons involved in the reaction. An example of a chronopotentiogram and the transition time measurement from the curve is shown in Figure II.6. From a series of similar chronopotentiometric measurements in a range of applied currents, further analysis of τ by Sand's equation is possible. If the values of concentration and diffusion coefficients are known, then, finding the number of electrons transferred is possible, or *vice versa*.

Sand's equation is valid in a simple reaction of an electroactive species that is reduced in one or more steps where each produce a well-defined potential plateau, for more complicated scenarios like more than one electroactive species reacting

simultaneously and involving adsorption phenomena at the electrode, other relations deriving from Sand's equation can be considered. The τ relations for these cases are presented in Table V.1 in chapter V, where a more complex analysis of τ is employed.

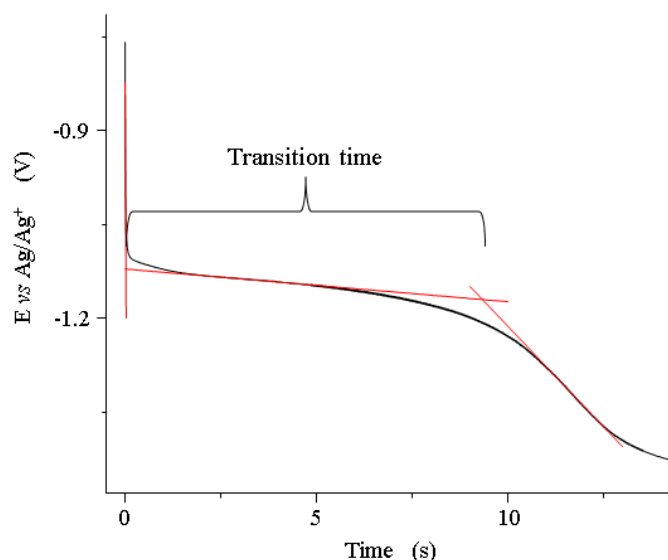


Figure II.6. Chronopotentiogram at a graphite electrode in Li-Na, 650 °C, $P_{CO_2}=0.5$ atm, with a current of -1.5 mA

II.3.3. Modified cathodes and electrolyte

A half-cell set up was used for testing the modified cathodes and electrolytes. The high-temperature electrochemical cell was a single-compartment crucible of dimensions 70 x 50 mm² contained in an alumina Al₂O₃ reactor of dimensions 250 x 60 mm², hermetically sealed by a stainless steel cover with a Viton™ O-ring. The whole electrochemical set-up shown in Figure II.7 consists on a cylindrical furnace k) that is used to heat up the carbonate mixture i) contained into an alumina crucible h). An alumina spacer j) is used to center the crucible in the hot zone of the furnace. A water cooled stainless steel cover g) closes the reactor hermetically. The cover has six leak free inlet/outlet ports to introduce alumina tubes of different diameters, through these ports the electrodes, thermocouples and gases are introduced. In this way, a controlled atmosphere is maintained into the reactor [92,93]. Temperature was controlled at a constant temperature of 650°C by means of a calibrated chromel/alumel thermocouple, the electrolyte was a mixture of lithium and potassium carbonates of high grade purity

>98% (Sigma-Aldrich®), in a proportion of 62:38 mol%. The standard cathode atmosphere was a mixture of Air/CO₂ (70:30 mol%) of high grades purity (Air Liquide®) at 650°C and a pressure of 1 atm. A carbonate melt was prepared and stabilized 24 h at 650°C for each coated sample. After stabilizing the molten carbonate eutectic under the selected cathode atmosphere, samples were immersed in the melt and electrochemical measurements were performed. In order to determine the electrochemical performance of the coated samples, a three-electrode system was used. The working electrode being the as-deposited sample on porous nickel substrate of dimensions 10 x 10 x 0.5 mm, the counter electrode was a gold wire of 1mm diameter and the reference electrode a silver wire dipped into an Ag₂SO₄ (10⁻¹mol kg⁻¹) saturated (Li_{0.62}-K_{0.38})₂CO₃ eutectic in an alumina tube sealed by a porous alumina membrane. Electrochemical experimental data were collected using a potentiostat/galvanostat (AutoLab® PGSTAT-302N).

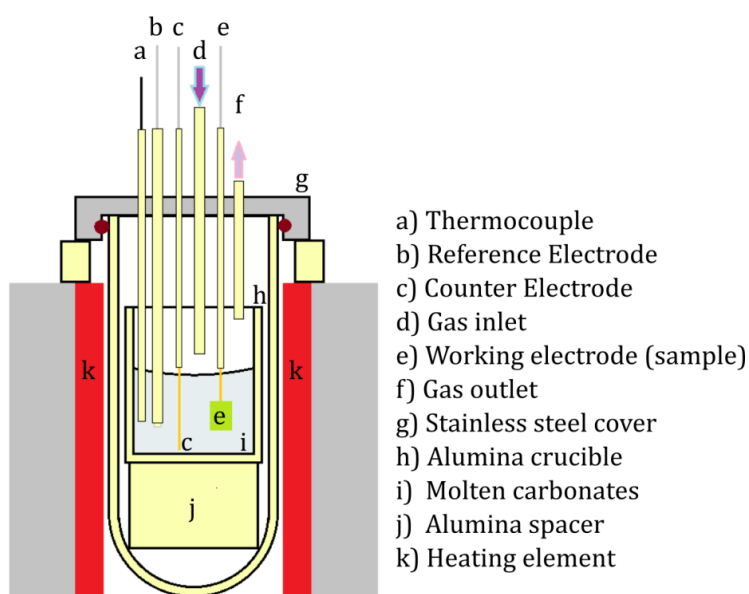


Figure II.7- Half-cell set up for cathode material and modified electrolyte testing.

Open Circuit Potential (OCP) was collected for ALD deposited samples from 0 to 230 h of immersion. OCP measurements were interrupted periodically to perform electrochemical impedance spectroscopy (EIS). EIS parameters were: scanning frequencies set from 10⁻³ to 10⁶ Hz, with 11 points per decade and signal amplitude of 5 mV respecting the system linearity. After each EIS test, OCP measurements were

restarted. This procedure was performed for 230 h with EIS performed at regular intervals.

For determining the electrode kinetics in modified and bare molten carbonate eutectics, the same half-cell set up was used, in this case instead of a modified cathode a gold plate was used, both faces were polished with sand paper up to grain 4000. The partial pressure of oxygen and CO₂ was varied keeping a constant flow rate of 50 Nml min⁻¹ using Ar as dissolution gas at 1 atm. pressure, according to Table II.1. Each time the atmosphere composition was changed, a stabilization time of at least 12 h was attained, the electrode was re-polished and stabilized in the carbonate mixture for 30 minutes before performing EIS measurements.

Table II.1- Gas compositions tested.

Gas Composition O ₂ /CO ₂ /Ar atm. %	Gas Composition O ₂ /CO ₂ /Ar atm. %
7/30/63	14/20/66
14/30/56	14/30/56
21/30/49	14/40/46
28/30/42	14/50/36

The gases used were of high purity grade (Air Liquide®), flow rates of each individual gas was varied accordingly to get the desired partial pressure by means of a BROOKS® mass flow controller 4800 series™ specifically calibrated for each gas.

II.3.4. CO₂ reduction in carbonate media

The same type of half-cell set up was used to investigate CO₂ reduction by means of chronopotentiometry, the electrode was a gold flag of dimensions 10 x 10 x 0.5 mm and a graphite plate of dimensions 10 x 10 x 1 mm that were used alternately for each condition tested. The molten carbonates used as electrolytes were (Li_{0.62}-K_{0.38})₂CO₃, (Li_{0.52}-Na_{0.48})₂CO₃ and (Na_{0.56}-K_{0.44})₂CO₃. For each carbonate eutectic three atmosphere compositions were studied each with both gold and graphite electrodes, the compositions were 5, 10, 20, 30, 50 and 100 % CO₂, the dilution gas was Ar. Gas control, potentiostat and gas quality used were the same as in previous section. Gold and

graphite electrodes were polished to grain 2400 and then on 4000 followed by immersion in an ultrasonic bath (50:50 vol%, ethanol:water) for ten minutes.

For the chronopotentiometric study, the imposed current was varied between 0.5 and 30 mA in steps of 0.5 or 1 mA per cycle, each current was imposed for a 30 s period. After each imposed current, a re-equilibration time of 20 min was set before the next measurement.

II.4. Ni solubility measurements

The solubility of bare porous nickel and coated porous nickel samples were measured individually from the different $(\text{Li}_{62}\text{-K}_{38})_2\text{CO}_3$ melts used in the experiments. Small amounts of carbonates (about 1.4 g) were withdrawn randomly three times from the molten carbonate bulk at the end of each electrochemical characterization, which corresponds to 230 h immersion. After solidification, each carbonate sample was hand-milled to obtain a fine powder from which 2 g were dissolved in 10ml of HNO_3 at 3 vol. %. Afterwards, nickel content was determined by ICP-AES (ICAP 6000 Series from Thermo Fisher Scientific). The calibration was performed using Aldrich atomic absorption standard solution of Ni, dissolved in HNO_3 at 3 vol. % at different concentrations to obtain a calibration curve within we expected to find the nickel concentration value. From the obtained concentration, the weight parts per million ($\text{mg}\cdot\text{kg}^{-1}$ or wt ppm) of dissolved Ni along 230 h immersion in molten carbonates were found for each sample.

II.5. Single-cell set-up

A complete cell set-up was developed with the help of Fiaxell® testing systems. Two concepts were developed for MCFC: the open flange and the gastight mounting systems. In one hand, the open flange concept does not aim to separate the anode and cathode gases at the exit of the fuel cell. Instead it evacuates those gases through alumina foam placed at the cell periphery where they burn in a controlled way into the furnace this allows a very fast mounting and testing of the cell and gives us the possibility of testing button cells of several dimensions.

On the other hand, a gas tight testing system evacuates the gases out of the furnace through exhaust pipes, with this system mounting the cell takes more time and is a more delicate operation but allows us to analyze the inlet and exhaust gases with a gas chromatograph (GC) for more complex characterization.

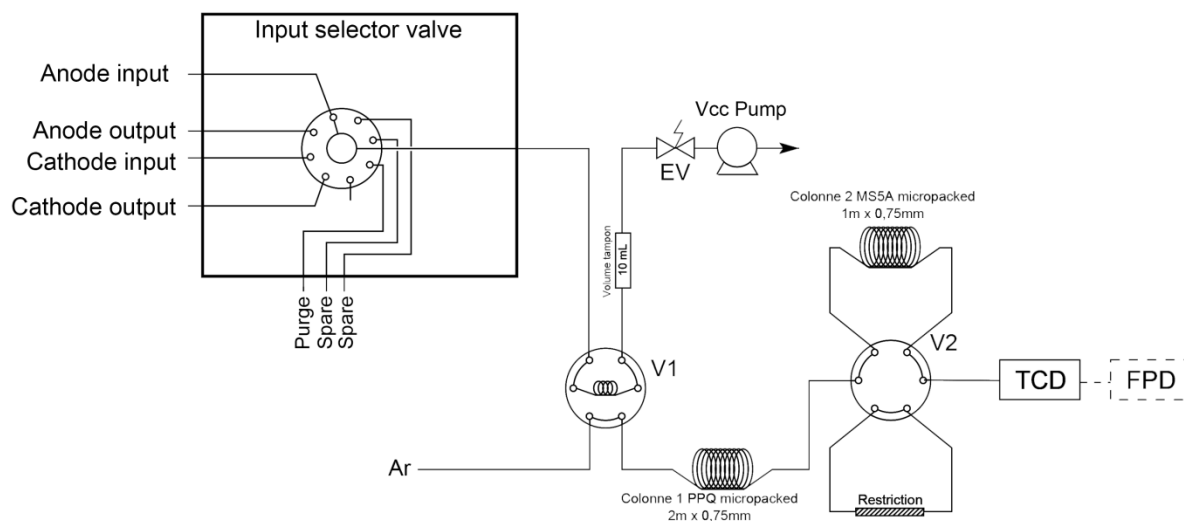


Figure II.8- Schema of GC configuration for fuel cell gas stream composition measurements.

A GC from Thermo Fisher Scientific® model Trace 1300™ specially adapted for our application according to diagram shown in Figure II.8 was used to analyze the input and output gases of the complete cell set up. The electrochemical tests on the complete cell set up were carried out with a potentiostat/galvanostat from Princeton applied research® model Parstat 4000+™ and a laboratory power supply HCS-3200™ from Manson Engineering Industrial Ltd. The wiring diagram of the system is shown in Figure II.9. Where V = Voltmeter and AM = Ammeter.

A gas supply system specially designed for our application was used, consisting of six mass flow controllers (MFCs) from BROOKS® instruments model 5800Series™ controlled via RS485 protocol by a PC. The accuracy of the MFCs was assured to be <1 % FS by specific gas calibration of the gasses used. A diagram of the gas supply system and control is shown in Figure II.10. The hydrogen was supplied by a hydrogen generator model HK-250-EU from LNI-Swissgas®.

Water was supplied to the system by means of a peristaltic pump ISMATEC® model Reglo-ICC™ with two independent channels (Ch1 and Ch2), each one with 8 rollers to assure a smooth supply of water to the fuel cell. The startup procedure and conditioning of the single cell is performed according to the Table II.2 shown below.

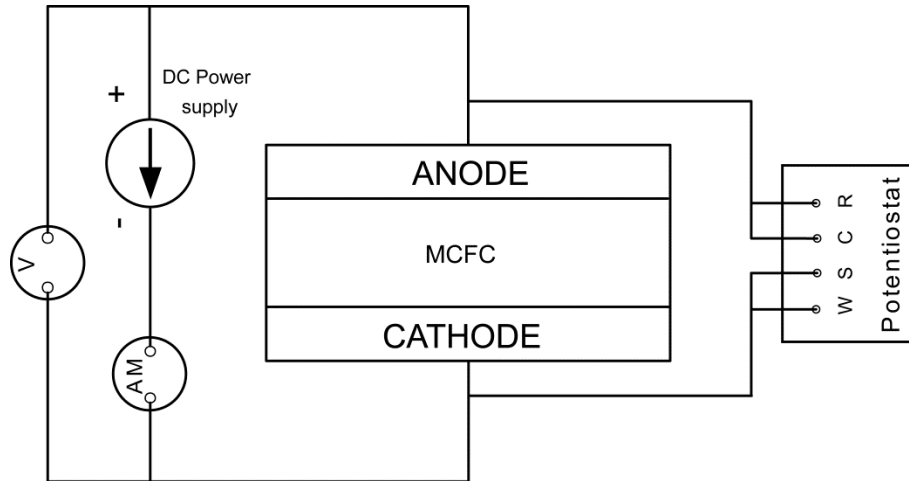


Figure II.9- Electrical wiring of complete fuel cell electronic components.

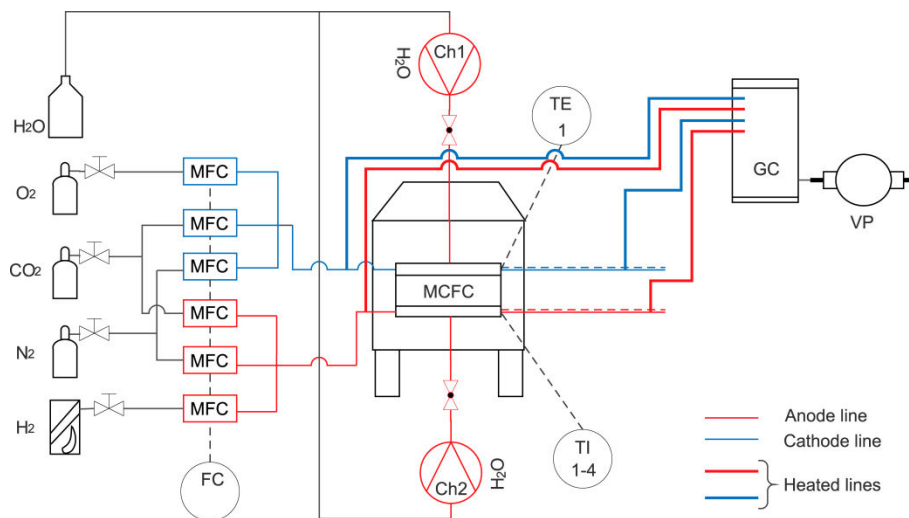


Figure II.10- Gas and water supply schema of complete cell testing system.

After the preconditioning step, the single cell is operated with the standard cathode and anode atmospheres being $H_2/CO_2/H_2O$ (64/16/20 %) on the anode side and $O_2/CO_2/N_2$ (15/30/55 %) at the cathode side.

Table II.2- Preconditioning sequence for MCFC operation.

Step	Temp. (° C)	Time (h)	Gas	Flow rate (sccm)	Total time (hr)
1	26	0	Air	50	0
2	140	8			8
3	160	20			28
4	380	60			88
5	450	28	CO ₂	50	116
6	450	10			126
7	480	8			134
8	510	18			152
9	650	9	Normal	150	161

III. ALD processed coatings for MCFC cathode protection

“Most people say that it is the intellect which makes a great scientist. They are wrong: it is character.”

Albert Einstein

III.1. Metal oxides deposited by ALD

Following the approach for protecting the MCFC cathode by means of an ultra-thin layer of metal oxide, we have decided to evaluate the protecting capabilities and electrochemical performance of five metal oxides deposited onto the porous nickel cathode material by ALD in various thicknesses. The chosen materials and their thicknesses are shown in Table III.1.

Table III.1- ALD deposited materials for cathode protection.

Material	Thicknesses (nm)		
Co ₃ O ₄	50		
TiO ₂	50	300	
CeO ₂	27	127	
Nb ₂ O ₅	5	50	300

These protective layers are later characterized before and after testing in molten Li-K carbonate eutectic mixture. From these tests, we have obtained very interesting results that have been already published in the articles of section III.3. In this chapter, we will first summarize the principal results and compare them thoroughly.

III.1.1. Deposition parameters

As already explained in section II.1. ALD is very interesting for depositing ultra-thin layers since the thickness control is very accurate and the resulting layers are conformal, homogenous, dense and, in most cases, crystalline as deposited. Thickness is controlled through number of cycles if the deposition parameters lay in the ALD window of the precursor used. To choose the right parameters, an ALD literature specific for each metal oxide was taken as starting point, then the parameters found were tested and tuned to get the best deposition quality and thickness control possible with our ALD reactor. For the materials tested herein, deposition parameters used are shown in Table III.2. Precursor and oxidant pulses are relatively long to ensure homogenous coverage of the samples that hanged vertically by a small metal frame.

Table III.2- ALD deposition parameters for all the deposited materials.

Material	Precursor	Temperature (°C)	Pulse (s)	Purge (s)	Oxidant	Pulse (s)	Purge (s)	Substrate temperature (°C)
TiO ₂	Ti(OCH(CH ₃) ₂) ₄	60	0.5	2.0	H ₂ O	0.5	2.0	250
CeO ₂	Ce(TMHD) ₄	180	3.0	2.5	O ₃	4.0	2.5	300
Co ₃ O ₄	Co(TMHD) ₃	160	1.5	3.0	O ₃	1.5	6.0	240
Nb ₂ O ₅	Nb(OCH ₂ CH ₃) ₅	80	0.5	3.0	H ₂ O	0.1	3.0	300

For characterization purposes, several samples were ALD-processed at the same time. For each material, at least four porous nickel plates and two pieces of silicon wafer cuts were placed in the deposition chamber. As-deposited samples were characterized before and after immersion in molten carbonates, as described further on.

III.1.2. Characterization of as-deposited materials

In our scientific papers attached at the end of this chapter, a more detailed characterization is available for some of the samples including X-ray photoemission spectroscopy (XPS), energy dispersive X-ray spectroscopy (EDS) and Raman spectroscopy. These characterizations are not shown herein since our objective is to compare the differences between the protective layers and underline their advantages. For that purpose in this section we will only compare the data available for all the protective materials used.

A compilation of all the SEM micrographs of the as-deposited layers is shown in Figure III.1, where we observe that the deposited layers are conformal, dense and homogenous as expected. Their thickness was measured from the images shown and from layers deposited over silicon wafers that were placed in the deposition chamber close to the nickel substrates at the same time. Both measurements were congruent with an error of ± 3 nm. As can be appreciated in the micrographs, substrates were cut to analyze the cross section of the layers, which detached from the substrate around the cut area. This indicates that substrate and deposit were separate entities with no intermediate or mixed phase formed between them. This fact makes clear that material diffusion process did not take place during the deposition of the metal oxide layer, something that could happen if high deposition temperatures are used or if as-deposited material is annealed after deposition to increase layer crystallization.

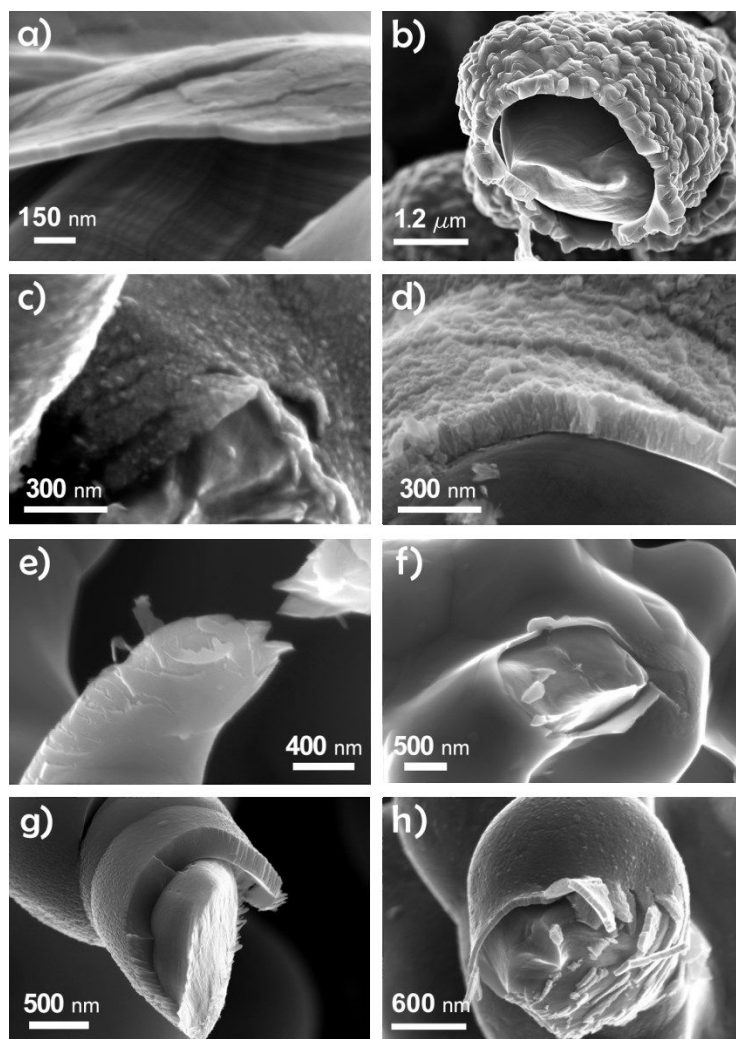


Figure III.1- SEM micrographs of the as-deposited layers onto porous nickel substrates: TiO_2 50 and 300 nm (a, b), CeO_2 27 and 127 nm (c, d), Nb_2O_5 5, 50 and 300 (e, f, g) and Co_3O_4 50 nm (h).

The X-ray diffractograms of the as-deposited samples shown the formation of crystalline deposits of CeO_2 , TiO_2 and Co_3O_4 , however, Nb_2O_5 was amorphous as deposited. It was only after heat treatment 1h at 650 °C in air that the layers deposited onto Si (1 1 1) became crystalline; this was confirmed by performing grazing incidence X-ray diffraction (XRD). Thus, crystallization of Nb_2O_5 immersed in molten carbonate was assumed to occur in the same way.

III.1.3. After tests characterization

After electrochemical tests, materials had shown structure transformations as could be expected since the working temperature is 650 °C and the molten carbonates constitute a rough environment. Most of the materials formed interfacial mixed compounds as shown in Table III.3, except for CeO₂ that did not show evidence of a mixed Ni or Li compound by the characterization techniques used. Full determination of the composition of the interfacial compounds was not possible since the layers are thin and the compounds have a natural gradient in composition with high Ni content at the interphase with nickel substrate and considerable lithium content at the interphase with the carbonates. In consequence, just an estimation of the possible compositions was obtained.

Table III.3- Different phases found in the tested samples after immersion in molten carbonates for 230 h by various techniques and their reference articles.

Material	Molten carbonate composition	Possible phases	Analysis techniques used	References
TiO ₂	Li ₂ CO ₃ -K ₂ CO ₃ (62:38 mol %) or Li ₂ CO ₃ -Na ₂ CO ₃ (52:48 mol %)	Li ₂ TiO ₃ Li _x Ti _y NiO _{1.6} : x ≤ 0.5, y ≤ 0.14 Li _x Ti _y NiO ₂ : x ≤ 0.5, y ≤ 0.11 Li _x Ti _y NiO _{3.6} : x ≤ 0.5, y ≤ 0.4 NiO Li _x Ni _{1-x} O	XRD, EDS, XPS	[59,94-96]
CeO ₂		CeO ₂ NiO Ni Li _x Ni _{1-x} O	XRD, EDS, XPS, RAMAN	[97-100]
Co ₃ O ₄		NiO-CoO solid solution Li-Ni-Co-O LiCoO ₂ CoO Co ₃ O ₄	XRD, EDS, XPS, RAMAN	[54,56,57,101,102]
Nb ₂ O ₅		Nb ₂ O ₅ LiNbO ₃ Li-Ni-Nb-O	XRD, XPS	[103]

Only in the case of TiO₂, determination of the predominant compound Li₂TiO₃ was possible since the XRD data shown clearly the formation of this phase; for the Ni containing phase, a range of Li and Ti content in the NiO mesh was determined by EDS and XPS more precisely. Also in case of Nb₂O₅ and Co₃O₄, determination of the

predominant phases LiNbO_3 and LiCoO_3 was possible but not that of the Ni containing compounds. In the SEM images shown in Figure III.2, we observe the modification of the deposited metal oxide layers. In the case of TiO_2 (Figure III.2 a and b), the deposits are transformed into octahedral crystals mainly formed by Li_2TiO_3 ; underneath, NiO and Ni rich phases were found. For CeO_2 (Figure III.2 c and d), round particles of CeO_2 were formed on the surface where the layer is present, but they do not have a homogeneous size or distribution on the substrate. Regarding the Co_3O_4 layers (Figure III.2 e), agglomerates of LiCoO_2 dominate at the surface impeding further oxidation of Ni, since LiCoO_2 is very stable in carbonates. For Nb_2O_5 covered samples, big crystals seem to be formed with no contrast difference in SEM, but different phases were identified by XPS.

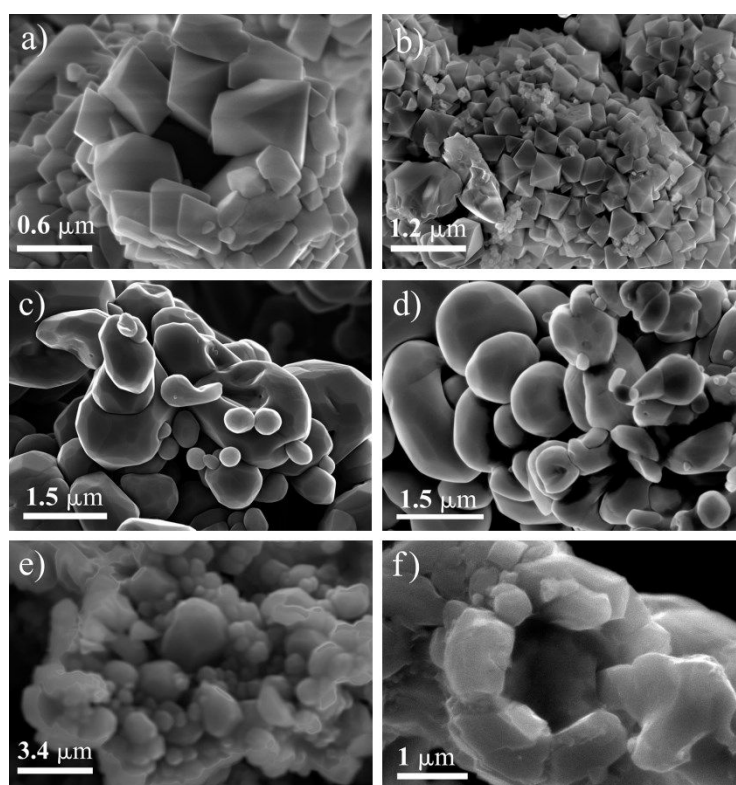


Figure III.2- SEM images of some samples after immersion in molten Li-K carbonate eutectic for 230 h at 650 °C: TiO_2 50 and 300 nm (a, b), CeO_2 27 and 127 nm (c, d), Co_3O_4 50 nm (e) and Nb_2O_5 50 nm (f).

XRD data, shown in Figure III.3, present the most intense peaks found in the samples after 230 h immersion time in Li-K carbonate eutectic at 650 °C, which corresponds mainly to cubic NiO; contrarily, on the Co_3O_4 sample, the presence of metallic Ni is as high as NiO confirming that the low activity of this sample is due mainly

to the formation of LiCoO_2 compound that prevents oxidation and lithiation of Ni. Contrarily to electrodeposited layers of Co_3O_4 from Mendoza *et al.* [54] that were mechanically stable for only 12 h of immersion, ALD-processed layers are mechanically stable after 230 h immersion. This is due to the reduced thickness and the highly dense layer produced by ALD that is transformed into LiCoO_2 and mixed Li-Ni-Co-O phases, preventing mechanical detachment.

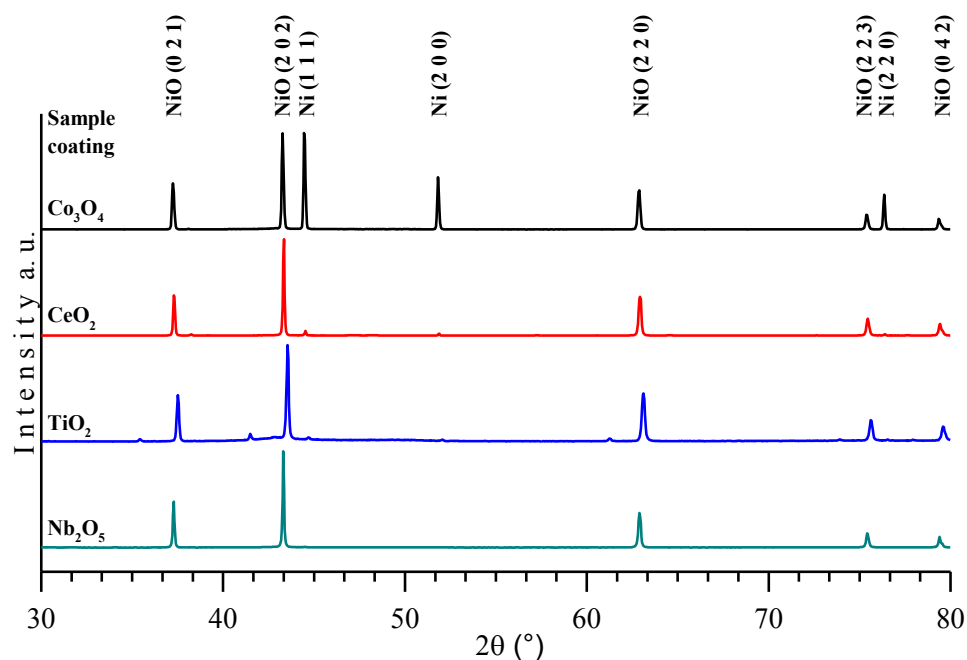


Figure III.3- XRD diffractograms for all samples after 230 h immersion in molten Li-K carbonates at 650 °C.

In the case of Nb_2O_5 samples, analyzed by regular and grazing XRD, they did not show any feature related to Nb_2O_5 and other techniques were used to find other present phases. According to the characterization after electrochemical test, mixed phases were present in most of the samples; a fact that could be beneficial in reducing the solubility of Ni in the molten carbonate eutectics. In the next section, electrochemical tests performed to the samples while immersed in the molten carbonates will be presented to determine whether the presence of the protective layers could affect or beneficiate the electrochemical performance of the cathode material.

III.1.4. Electrochemical performance of protective coatings

The as-deposited samples were immersed into molten Li-K eutectic carbonate mixture; for each sample, the crucible, reference and counter electrodes, and Li-K eutectic were new to avoid crossed contamination. Figure III.4 shows the OCP evolution over 230 h immersion times for all the samples covered by a thin coating of around 50 nm. Thicker samples did not present a good OCP behavior and are not presented herein. Bare porous Ni cathode was used as reference; the black line shows the typical behavior of Ni immersed in eutectic Li-K molten carbonates. Before Ni reaches its balance potential, around 0 V *vs.* Ag/Ag⁺, where it is considered ready to work as MCFC cathode, it goes through a complex oxidation/lithiation process.

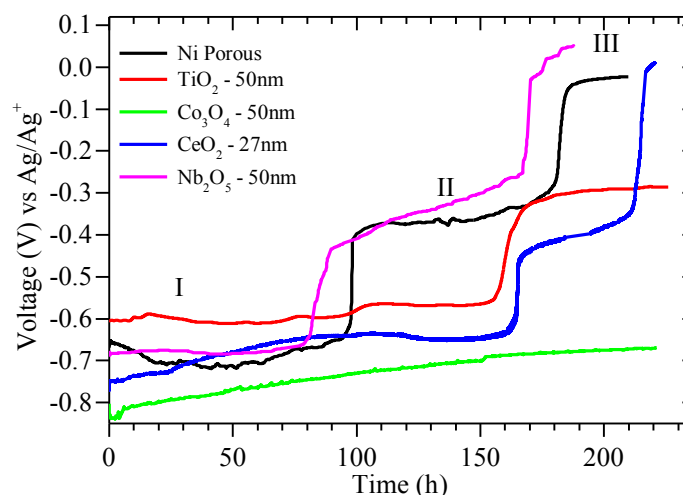


Figure III.4- OCP evolution over 230h immersion time for the most relevant samples :TiO₂ 50 nm, Co₃O₄ 50 nm, CeO₂ 27 nm and Nb₂O₅ 50 nm.

This process can be observed through three plateaus. The first one at -0.7 V *vs.* Ag/Ag⁺ (I) is characteristic of the Ni oxidation process. A second plateau at around -0.4 V *vs.* Ag/Ag⁺ (II) is associated to the NiO lithiation process. Finally, the third plateau at around 0 V *vs.* Ag/Ag⁺ (III) corresponds to the stabilization of the Ni cathode [104]. The whole process of *in-situ* oxidation-lithiation lasts about 230 h in our experimental conditions. Once the cathode is protected with an oxide layer, the OCP evolves in a different manner indicating that the oxidation/lithiation process has been influenced by the deposited material. The presence of a thin Nb₂O₅ layer seems to accelerate the

oxidation and lithiation process, allowing to reach the equilibrium potential before standard porous Ni. Contrarily, Co_3O_4 thin layer seems to seriously slow down the oxidation and lithiation process which is confirmed by XRD where a big amount of metallic Ni is present in the sample after 230 h immersion, in contrast with the rest of the samples [105]. This can be due to the formation of LiCoO_2 that stops further oxygen and lithium penetration in the material. CeO_2 -coated sample behaves similarly to standard porous Ni, reaching the balance potential about 30 h after porous Ni cathode. TiO_2 has a first and second plateau; the third plateau did not appear during the 230 h of immersion. Nevertheless, TiO_2 could reach the equilibrium potential when the experiment is extended to 250 h since the second plateau shows up at the same potential and probably the time at which it should appear is also displaced as the first plateau around 60 h from standard Ni cathode. Regarding OCP behavior, CeO_2 and Nb_2O_5 show the best performance, TiO_2 could also be considered a good candidate assuming that it reaches the equilibrium potential around 250 h. The Co_3O_4 -coated sample did not perform as expected and is not considered a good candidate for cathode modification by itself.

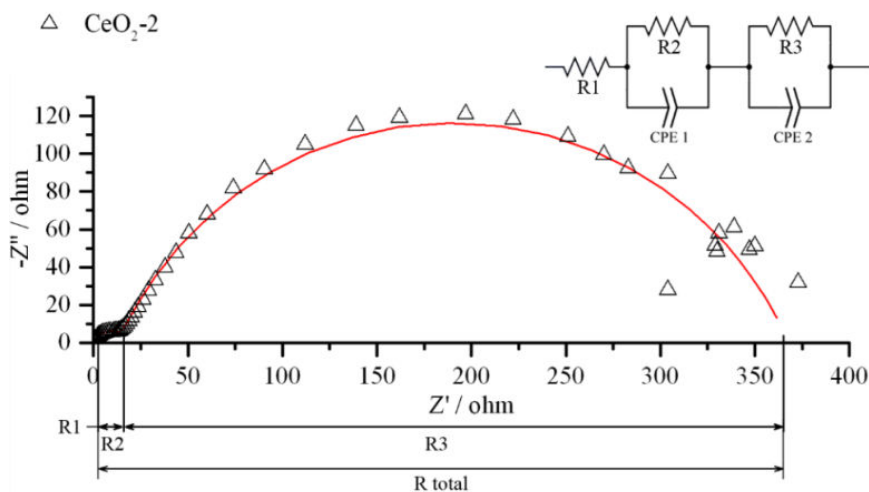


Figure III.5- EIS Nyquist representation of CeO_2 coated sample and the equivalent circuit used to fit the data. The fitting is shown in red.

Together with the OCP data, electrochemical impedance spectroscopy (EIS) data were collected and information such as electrolyte resistance (R_1), charge transfer resistance (R_2) and mass transfer resistance (R_3) can be deduced. In Figure III.5, a

Nyquist diagram together with the corresponding equivalent circuit used to deduce that information are shown. From the fitting, total resistance R_{tot} ($R_{\text{tot}} = R_1 + R_2 + R_3$) was deduced for all the samples, total resistance evolution with time is shown in Figure III.6. As it can be observed, after 230 h immersion in molten carbonates and once the OCP equilibrium potential is reached, NiO pristine cathode has a resistance of 348 ohms while Co_3O_4 presents a resistance of 5 ohms, the lowest from all the samples; this is in agreement with the formation of LiCoO_2 which is much more conductive than NiO [29,35]. CeO_2 presents a lower resistance than NiO around 320 ohms, while TiO_2 shows a total resistance of 540 ohms that is 60 % higher than standard porous Ni. Unfortunately, Nb_2O_5 showed such a high resistance (over 2500 ohms) that it is not shown in the graph for comparison. This high resistance is not surprising since Nb_2O_5 is highly resistive, but what is impressive is that even though total resistance is very high, the OCP shows a fast evolution to balance potential. This could be due to the presence of catalytic or electrocatalytic activity that has not been completely understood.

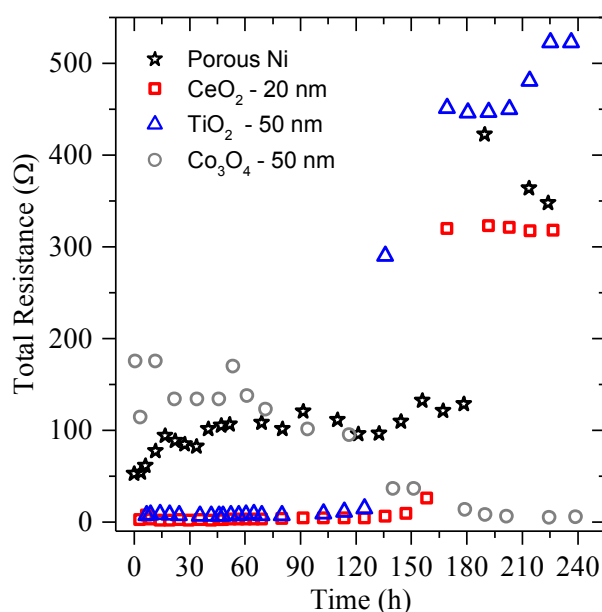


Figure III.6- Total resistance evolution over immersion time.

Coatings of CeO_2 seems to be the most promising electrochemically, since they do not affect the OCP and present a similar resistance as Ni cathode. Nevertheless, the most important parameter to determine the effectiveness of a coating together with the

electrochemical behavior is the actual solubility of Ni. This important test is presented in the next section where the influence of the layer on Ni solubility was determined.

III.1.5. Ni solubility

The main objective of this chapter is to demonstrate that Ni dissolution could be reduced by applying a very thin layer of metal oxide without affecting the properties of the MCFC cathode. To accomplish such objective, Ni content was determined by ICP-AES as explained in section II.4. ; then, the solubility of Ni in weight part per millions (wt. ppm) was obtained for all the samples after 230 h immersion in the molten Li-K carbonates at 650 °C. The solubility values of Ni are shown in Table III.4. According to the previous sections, CeO₂ and TiO₂ present a favorable electrochemical behavior, but solubility data show that TiO₂ decreases considerably the solubility of Ni, while CeO₂ does it in a lesser extent. Nevertheless, the best compromise between cathode protection and electrochemical performance seems to be found in CeO₂ thin layer. This protective coating could enhance the lifetime of the fuel cell without compromising its performance; a better material could be a mixture of TiO₂ and Co₃O₄ that could allow keeping the outstanding protection and reducing the cathode resistance under that of NiO, without impeding the oxidation/lithiation process.

Table III.4- Solubility values of Ni for the cathodes coated by different metal oxides after 230 h immersion in molten Li-K carbonates at 650 °C.

Sample coating	Bare Ni	TiO ₂	CeO ₂	Nb ₂ O ₅	Co ₃ O ₄
Ni content in (wt. ppm)	15	8.6	10	10	12

III.2. Conclusions

From the findings in this section, we established the utility and convenience of ALD-processed metal oxide ultra-thin layers as a novel method to protect the MCFC cathode. Results showed that CeO₂ is the most stable and electrochemically similar to bare Ni cathode, the reduction of Ni solubility is not negligible, from 15 wt. ppm for bare Ni to 10 wt. ppm. Nevertheless, TiO₂ performed very well regarding Ni solubility

reduction up to 8.6 wt. ppm; this is almost half from that of bare Ni. Furthermore, Co_3O_4 presents the best performance regarding total cathode resistance, 50 times smaller than bare Ni cathode; unfortunately, its OCP behavior is very poor. Since the conductivity of LiCoO_2 is high and its stability is very good in molten Li-K carbonates, it could be used to protect the current collectors and bipolar plates of the MCFC in direct contact with the carbonates which requires a good conductivity. In addition, a very interesting material could be developed by properly by mixing TiO_2 and Co_3O_4 in a thin layer.

Nb_2O_5 demonstrated a great stability in molten Li-K carbonates, but even though its OCP behavior is promising its very high resistance due to its semi-conductive nature makes it unsuitable for cathode protection. Nevertheless, it could serve as a very good protective coating for MCFC gaskets, and auxiliary equipment that should be in close contact with the molten carbonates but that does not require electronic conductivity.

III.3. Scientific papers

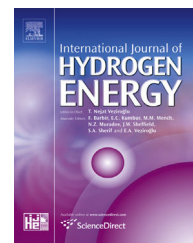
As mentioned previously, a series of four articles have been published reporting the results obtained concerning MCFC cathode protection by ultra-thin layers deposited by ALD. These scientific papers are attached in this section to facilitate the reader access to more detailed data and comparison.



ELSEVIER

Available online at www.sciencedirect.com

SciVerse ScienceDirect

journal homepage: www.elsevier.com/locate/ijhydene

TiO₂ protective coating processed by Atomic Layer Deposition for the improvement of MCFC cathode

A. Meléndez-Ceballos^{a,b,d}, S.M. Fernández-Valverde^b, C. Barrera-Díaz^c,
V. Albin^d, V. Lair^d, A. Ringuedé^d, M. Cassir^{d,*}

^a Universidad Autónoma del Estado de México, Facultad de Química, Paseo Colón Intersección Paseo Tollocan S/N, C.P. 50120 Toluca, Estado de México, Mexico

^b Depto. De Química, Instituto Nacional de Investigaciones Nucleares, A.P.18-1027, México D.F. C.P. 11801, Mexico

^c Centro Conjunto de Investigación en Química Sustentable, UAEM – UNAM, Carretera Toluca-Atlaconulco, Km 14.5, Unidad El Rosedal, C.P. 50200, Toluca, Estado de México, Mexico

^d Laboratoire d'Electrochimie, Chimie des Interfaces et Modélisation pour l'Énergie, UMR 7575 CNRS, ENSCP Chimie-Paristech, 11 rue Pierre et Marie Curie, F-75231 Paris Cedex 05, France

ARTICLE INFO

Article history:

Received 23 May 2013

Received in revised form

18 July 2013

Accepted 21 July 2013

Available online 28 August 2013

Keywords:

MCFC

Cathode

Titanium oxide

Coating

ALD

Electrochemistry

ABSTRACT

One of the main issues for optimizing the molten carbonate fuel cell (MCFC) is the control of the corrosion and dissolution of the state-of-the-art porous nickel oxide cathode. A protective coating constituted by more stable oxides seems to be the best solution. In this paper, very thin layers of TiO₂ (50 and 300 nm) are processed by a sequential CVD technique, Atomic Layer Deposition (ALD), which produces high quality, homogeneous and conformal layers. Structural, morphological and electrochemical behaviors of TiO₂-coated samples are tested in a Li₂CO₃–K₂CO₃ (62:38 mol%) eutectic melt under a standard cathode atmosphere: CO₂/air (70:30 bar%). Ni solubility is determined by ICP-AES. The protective role of TiO₂ layers and the consequent decrease in Ni solubility have been clearly evidenced.

Copyright © 2013, Hydrogen Energy Publications, LLC. Published by Elsevier Ltd. All rights reserved.

1. Introduction

One of the main issues of the Molten Carbonate Fuel Cells (MCFC) operating at temperatures around 650 °C, is the short lifetime of the cell components due to material degradation. Furthermore, the components of the fuel cell such as the anode, cathode, electrolyte matrix, current

collectors and interconnectors which are exposed to corrosive environments are required to last up to 40,000 h of operation for being feasible for commercial purposes [1]. The state-of-the-art MCFC cathode is constituted by porous Ni which is oxidized and lithiated in situ to form Li_xNi_{1-x}O. This oxide tends to dissolve partially into the carbonate melt. Ni²⁺ diffuses to the anode where it can be reduced by

* Corresponding author. Tel.: +33 155426387; fax: +33 144276750.

E-mail address: michel-cassir@ens.chimie-paristech.fr (M. Cassir).

hydrogen yielding metallic nickel, which causes a short circuit between the anode and cathode resulting in an MCFC stack failure [2,3]. In the last decade several approaches have been proposed to protect the MCFC cathode [4–6]; however, it is still delicate to fully overcome the feasibility for commercial production. Titanium is resistant to corrosion due to the formation of a TiO_2 passive layer on its surface at high temperature. Ti species have been studied under MCFC operation conditions and reported in previous papers [7–12]. Thermodynamic predictions of Ti species have been established for both cathode and anode conditions [11]. The electrochemical behavior of Ni–Ti alloys has been investigated also in molten Li/Na carbonate eutectic at 650 °C under the usual MCFC cathode conditions [8]. In view of these studies, titanium, titanium oxide and Ni–Ti alloys are promising candidate materials for MCFC cathode protection. In an earlier research, TiO_2 has been tested as protective layer deposited by sputtering on porous nickel [6]. The layers obtained by this technique were homogeneous, and three different layers of titanium dioxide with thickness of 200, 600 and 800 nm were evaluated. Layers with thicknesses of 600 and 800 nm tend to inhibit the cathode performance. However, layer adhesion of titanium oxide onto porous nickel by this technique was poor producing a fast degradation of the oxide layer. Hong et al. have also analyzed the effect of TiO_2 coatings realized by sol–gel on Ni powder [12]. These authors have found that the coated material had an appropriate pore-size distribution and porosity and also allowed a significant decrease in nickel oxide solubility in Li/K carbonate eutectic by about 48–77%, according to the titania content; however, long term behavior and electrochemical properties have not been developed in this study. Thus, in order to increase long-term protection and layer adhesion of titania coatings, Atomic Layer Chemical Vapor Deposition (ALCVD), known as Atomic Layer Deposition (ALD), was selected. It is a chemical gas phase deposition technique developed in Finland in the 1970's by T. Suntola [13]. In ALD, reactant gas pulses are separately introduced to reach the substrates to be coated. Growth is achieved through self-terminating surface reactions. Self-terminating means that only one monolayer of reactant gas species can be adsorbed to the surface during a pulse. The pulses containing reactant gases are separated by purging pulses where the ALD reactor is flushed with an inert gas. The purging pulses ensure that the reactant gas pulses do not mix. Mixing of the reactant gas pulses would lead to continuous growth and the accurate thickness control of the deposition process would be lost. By-products like detached ligands and excess reactants are also flushed away by the purging pulses. A complete set of reactant gas pulses and purging pulses needed to deposit a certain compound are referred to as a cycle. If deposition parameters have been chosen properly, the number of cycles rather than the concentration of the reactant species determines the film thickness [14]. An illustration of the deposition cycle is shown in Fig. 1. The aim of this investigation was to test the performance of ALD-processed TiO_2 on porous nickel substrate as protective layer for MCFC cathode application by determining the electrochemical behavior, surface

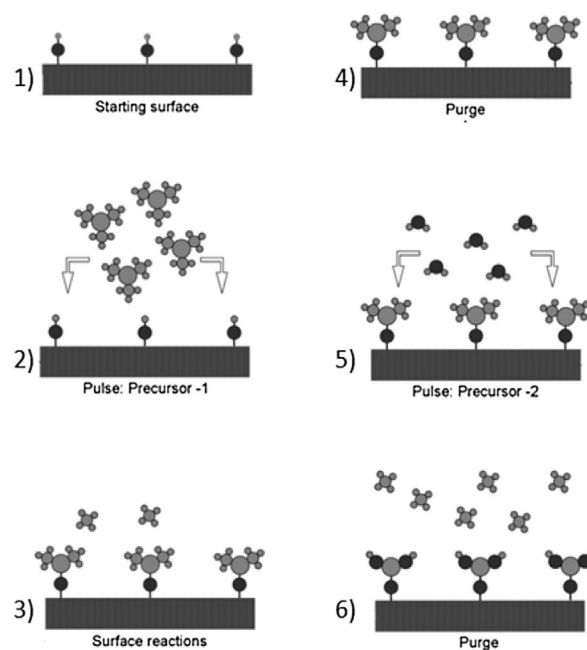


Fig. 1 – ALD cycle for 1 precursor and water as oxidizing agent.

changes and nickel solubility in an electrolyte eutectic mixture of Li_2CO_3 – K_2CO_3 (62:38 mol%) under standard cathode atmosphere.

2. Experimental

2.1. TiO_2 layer deposition using ALD

A known deposition route was followed using halide-free and non-corrosive titanium alkoxides as precursors for TiO_2 [15,16]. A thin layer of TiO_2 was deposited on a commercial porous nickel substrate (produced by Doosan, South-Korea) by means of ALD technique using a vertical flow type reactor (Picosun SUNALE™ R-series). Titanium isopropoxide, $\text{Ti}(\text{OCH}(\text{CH}_3)_2)_4$ (Sigma–Aldrich®) was used as precursor and distilled water as oxidizing agent. In order to prepare the TiO_2 layer, $\text{Ti}(\text{OCH}(\text{CH}_3)_2)_4$ was introduced into the precursor chamber using the following conditions: pulse time 0.5 s, purge time 2 s, N_2 line flow of $150 \text{ cm}^3 \text{ min}^{-1}$. From the precursor chamber the reactant was introduced into the reactor by a N_2 flow. The precursor was sublimated (at 60 °C) and the water was supplied at 25 °C. The reactor temperature was kept at 250 °C with a N_2 flow of $300 \text{ cm}^3 \text{ min}^{-1}$, the precursor pulse and purge were followed by water pulse and purge, this cycle was repeated until the desired thickness was reached. The growth rate of TiO_2 layer over the porous nickel substrate was 0.3 \AA/cycle . Two different samples were processed with this technique: 167 cycles and 1000 cycles were used for layers of 50 and 300 nm, respectively. The samples were named TiO_2 -1 and TiO_2 -2 for the 50 and 300 nm TiO_2 coated Ni porous cathodes, respectively.

2.2. Electrolyte and cell

Lithium and potassium carbonates, of high grade purity >98% (Sigma–Aldrich®), were mixed in a proportion of 62:38 mol%. The high-temperature electrochemical cell was a single-compartment crucible of dimensions 70 × 50 mm² contained in an alumina Al₂O₃ reactor of dimensions 250 × 60 mm² hermetically sealed by a stainless steel cover with a Viton O-ring. The whole electrochemical set-up was fully described in previous papers [17]. Temperature was controlled at a constant temperature of 650 °C by means of a calibrated chromel/alumel thermocouple. The standard cathode atmosphere was a mixture of Air/CO₂ (70:30 bar%) of high grade purity (Air Liquide®) at 650 °C and a pressure of 1 atm. For each TiO₂-coated sample, a carbonate melt was prepared and stabilized 24 h at 650 °C. After stabilizing the molten carbonate eutectic under the selected cathode atmosphere, samples were immersed in the melt and electrochemical measurements were performed for 230 h. After electrochemical tests, the samples were rinsed with deionized water to remove the carbonates, dried at 100 °C in an oven and kept in small plastic boxes to prevent contamination before further analysis. The samples were then renamed as TiO₂-1A and TiO₂-2A.

2.3. Electrochemical measurements

The electrochemical experimental data was collected using a potentiostat/galvanostat (AutoLab® PGSTAT-302N with FRA module). Two electrochemical techniques were used: Chronopotentiometry at $I = 0$, following the Open Circuit Potential (OCP) and Electrochemical Impedance Spectroscopy (EIS). A three-electrode system was used, the working electrode being a porous Ni foil (10 × 10 × 0.5 mm) covered by a protective layer of TiO₂, the counter electrode was a gold wire and the reference electrode a silver wire dipped into an Ag₂SO₄ (10⁻¹ mol kg⁻¹) saturated eutectic melt in an alumina tube sealed by a porous alumina membrane. The parameters used for impedance measurements are the following: scanning frequencies set from 0.001 to 10⁶ Hz, with 11 points per decade, and signal amplitude of 5 mV respecting the system linearity. OCP data were collected continuously in regular intervals of time except when EIS measurements were performed. This procedure was followed from 0 to 230 h.

2.4. Characterization

2.4.1. Characterization of deposited TiO₂ layer on porous Ni
The TiO₂ layer was characterized by X-ray diffraction and SEM-EDS. XRD was performed in a PANalyticalX'pert pro from Anton Paar with Cu–K α 1 radiation ($\lambda = 1.54056$ Å). The diffraction pattern was obtained by scanning between 20 and 80° by steps of 0.02 (2 θ) with a fixed counting time of 2.3 s and sample rotation of 3 rpm. Once the data were obtained, Scherrer analysis calculation was used to obtain the average crystal size of the deposited layer. Scanning Electron Microscopy (SEM) and Energy Dispersion Spectroscopy (EDS) were performed with a ZEISS® Ultra 55 microscope on TiO₂-coated substrates to evaluate the surface, the morphology and to measure the layer thickness. The conditions used were 7 kV and magnifications of 5000, 500,000 and 250,000 \times .

The X-ray photoelectron spectra were recorded using a Thermo Scientific K-Alpha X-ray photoelectron spectrometer with a monochromatized Al K α X-ray ($h\nu = 1486.61$ eV) for sample excitation. An argon ion beam was used to prevent samples surface charging. The spectrometer energy calibration was obtained using Au 4f 7/2 and Cu 2p 3/2 photoelectron lines. The position of the adventitious carbon C 1s peak at 284.6 eV was used as an internal reference in each sample to determine the binding energies with an accuracy of ± 0.1 eV. The residual pressure in the analysis chamber was maintained below 1×10^{-8} Torr during data acquisition. The survey spectrum of TiO₂-1A and TiO₂-2A was obtained between 0 and 1000 eV. The spectra were collected and analyzed with Advantage 4.0 software.

2.4.2. Cathode characterization after the electrochemical experiments

After the electrochemical experiments the coated cathodes were characterized using the same diffractometer and SEM with the same experimental parameters as described above. Only the chemical analysis by EDS mapping was performed for both samples in a Phillips XL-30 microscope coupled to an EDAX microprobe.

2.5. Cathode solubility

The solubility of bare porous nickel and TiO₂-coated nickel (thickness of 50 and 300 nm, respectively) was measured individually using three different (Li₆₂–K₃₈)₂CO₃ melts. Small amounts of carbonates were withdrawn randomly three times from the molten carbonate bulk at the end of the electrochemical characterizations, which corresponds to 230 h. After solidification, each sample was hand-milled and 2 g of carbonate powder were dissolved in 10 ml of HNO₃ 3 vol%. Both nickel and titanium contents were determined by ICP-AES (ICAP 6000 Series from Thermo Fisher Scientific). The calibration was performed for each separate element using Aldrich atomic absorption standard solutions, dissolved in HNO₃ 3 vol%.

3. Results and discussions

3.1. Material characterization before tests

The diffraction patterns of porous Ni covered by TiO₂-1 and TiO₂-2 layers before immersion in molten Li₂CO₃–K₂CO₃ are shown in Fig. 2. Apart from nickel substrate, the other peaks can, in both cases, be indexed using the ICDD pattern file 01-078-2486 and correspond to titanium dioxide in the anatase structure. The values of the average crystallite size, determined by the Scherrer equation, are 46 and 60 nm for TiO₂-1 and TiO₂-2, respectively. It is relevant to note a remarkable feature concerning these ALD-processed thin layers which are crystalline as-deposited at 250 °C without the need of high-temperature annealing treatments. SEM micrographs of TiO₂-1 and TiO₂-2 coated samples are shown in Figs. 3 and 4, respectively. In both cases, a dense and homogeneous layer covers all the substrate uniformly. Layer thicknesses, as measured from Figs. 3(e) and 4(e), are 50 ± 10 and 300 ± 12 nm,

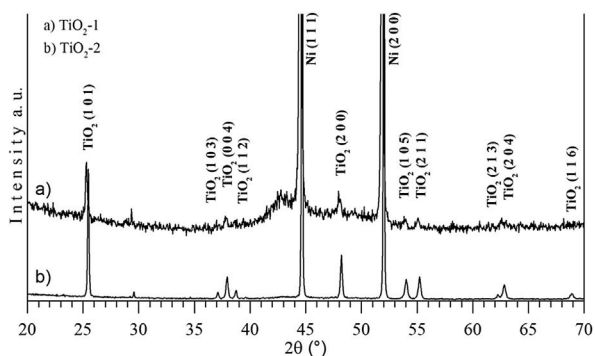


Fig. 2 – XRD pattern of TiO₂-1 and TiO₂-2 before immersion in molten Li₂CO₃–K₂CO₃ (62:38 mol%) at 650 °C during 230 h.

respectively, and confirmed the expected deposition thickness according to ALD conditions. EDS analyses only showed the dispersive X-ray energies of titanium ($K\alpha$ 4.508 eV, $L\alpha$ 0.452 eV), nickel ($K\alpha$ 7.471 eV, $L\alpha$ 0.851 eV) and oxygen ($K\alpha$ 0.525 eV). For example, in the case of TiO₂-1, atomic ratios of Ti, Ni and O are 4, 85 and 11%, respectively, which can be considered in conformity with the presence of TiO₂, Ni (results obtained by XRD) and small amounts of NiO.

3.2. Material characterization after immersion and electrochemical tests

Both coated cathodes were tested in molten Li₂CO₃–K₂CO₃ (62:38 mol%) eutectic mixture for 230 h. Fig. 5 shows the diffractogram of TiO₂-2A. The peaks at 2θ : 35.9, 43.58, 43.71 and 63.39 correspond to the ICDD pattern file 00-033-0831 of Li₂TiO₃, which is in agreement with the thermodynamic stability of this lithiated oxide and to previous experimental studies [10,11]. In the case of TiO₂-1A diffractogram shown in Fig. 6, there is no evidence of a Li₂TiO₃ phase, which is most probably due to the small amount of TiO₂ available at the surface. Instead, the peaks relative to NiO are shifted from the ICDD pattern file 00-004-0835 with an average of 0.24 ± 0.03 in 2θ , which matches better with ICDD file 01-081-0095 of Li_{0.4}Ni_{1.6}O₂. This shift may indicate the incorporation of Li into NiO lattice. Other peaks marked (□) can be observed at 2θ : 35.43, 42.87 and 62.83, detail 2 in Fig. 6. These peaks belong to a cubic phase Li–Ti–O close to the ICDD pattern file 01-072-0427 of Li_{1.2}Ti_{1.8}O₄ and ICDD file 01-072-0426 of Li_{0.33}Ti_{1.66}O₄, which could indicate the existence of a Li–Ti–O phase with different stoichiometry in which Ni could be integrated into the Li–Ti–O phase lattice. Some of the peaks marked with (?) have not been clearly identified; however, they seem to have a cubic crystal structure similar to the referenced NiO but with a phase shift in 2θ of -1.90 ± 0.18 , which is interesting because

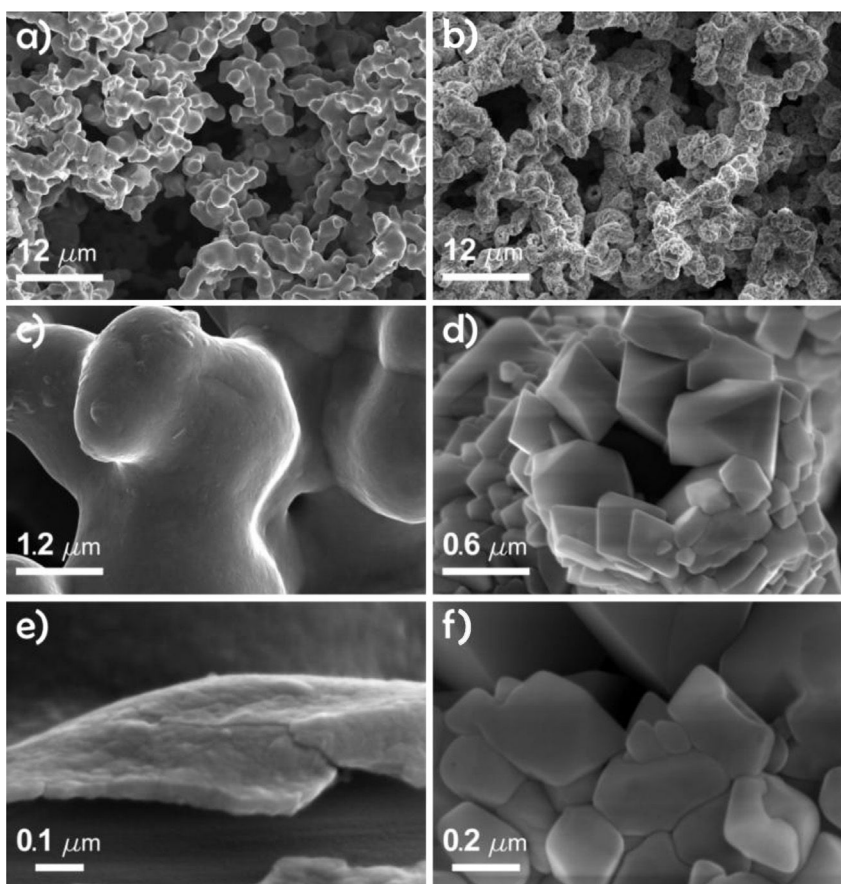


Fig. 3 – SEM micrographs of porous Ni cathode covered by an ALD processed TiO₂ layer of 50 nm before (a,c,e) and after 230 h of immersion in molten Li₂CO₃–K₂CO₃ (62:38 mol%) at 650 °C (b,d,f).

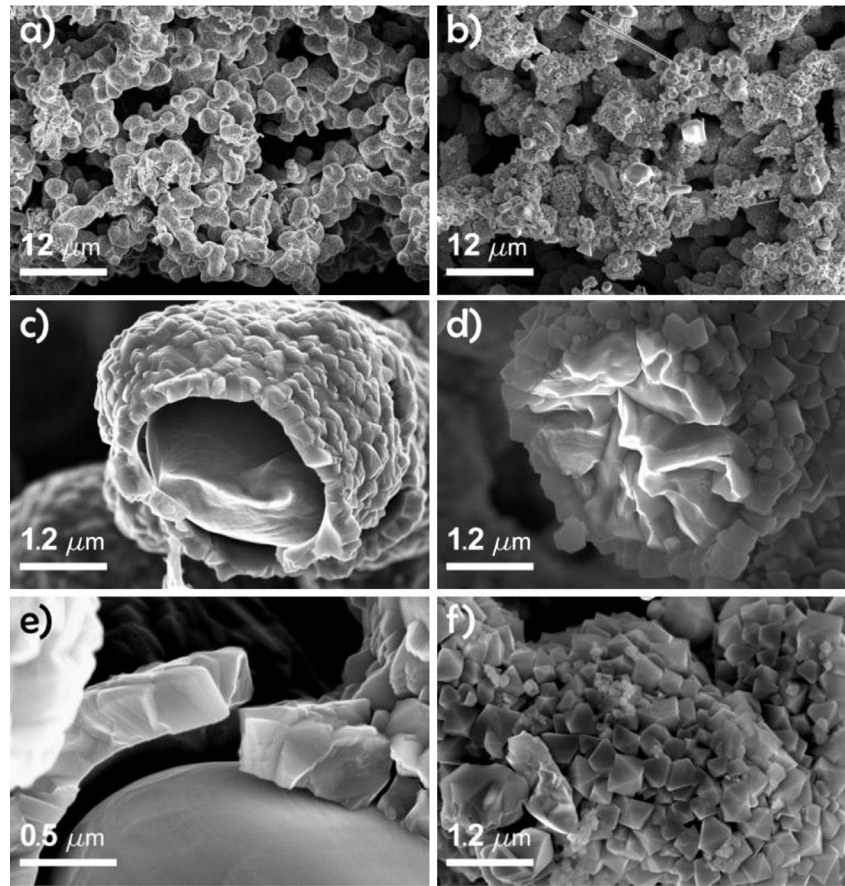


Fig. 4 – SEM micrographs of porous Ni electrode covered by an ALD processed TiO_2 layer of 300 nm before (a,c,e) and after 230 h of immersion in molten $\text{Li}_2\text{CO}_3\text{--K}_2\text{CO}_3$ (62:38 mol%) at 650 °C (b,d,f).

this shift can be produced by Li and Ti integration into the NiO matrix forming a Li–Ti–Ni–O phase.

After, immersion and electrochemical tests, SEM micrographs of $\text{TiO}_2\text{-1A}$ (Fig. 3(b,d,f)) and $\text{TiO}_2\text{-2A}$ (Fig. 4(b,d,f)) show a surface transformation where mainly rhombohedral crystals are present, and where cubic and orthorhombic crystals are also visible but in less proportion on the surface. $\text{TiO}_2\text{-1A}$ does not show the presence of the initial TiO_2 layer, instead

nickel seems fully oxidized. EDS analysis of $\text{TiO}_2\text{-1A}$ shows a composition of NiO, with Li and Ti integrated into the lattice, corresponding more likely to a $\text{Li}_x\text{Ti}_y\text{NiO}_{1.98\pm 0.02}$ phase with values $x \leq 0.5$ and $y \leq 0.11$. It is also probable to find a second phase, $\text{Li}_x\text{Ti}_y\text{NiO}_{1.65\pm 0.02}$ with values $x \leq 0.5$ and $y \leq 0.14$. Even though the precise lattice parameters are unknown cubic or

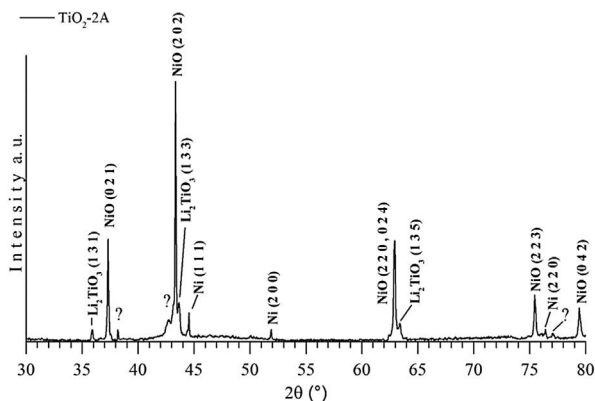


Fig. 5 – XRD pattern of $\text{TiO}_2\text{-2A}$ after immersion in molten $\text{Li}_2\text{CO}_3\text{--K}_2\text{CO}_3$ (62:38 mol%) at 650 °C during 230 h.

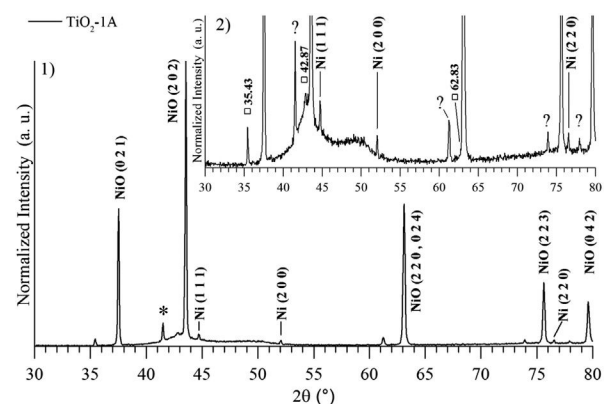


Fig. 6 – XRD pattern of $\text{TiO}_2\text{-1A}$ after immersion in molten $\text{Li}_2\text{CO}_3\text{--K}_2\text{CO}_3$ (62:38 mol %) at 650 °C during 230 h, (1) normalized to with respect to the highest peak, (2) normalized with respect to the unknown (?) peak.

rhombohedral crystal structures are possible since NiO can take those forms. Fig. 3(d) and (f) shows the surface morphology with cubic and rhombohedral crystals. Fig. 7 shows the EDS mapping of dispersed Ti on the surface of NiO for TiO₂-1A, this result confirms the incorporation of Ti into the NiO lattice.

The chemical composition of TiO₂-2A obtained by EDS (results not shown here) also indicates the formation of a mixed Li–Ti–Ni–O phase apart of the well identified Li₂TiO₃. The proposed stoichiometry for the mixed phase is Li_xTi_yNiO_{3.59±0.06} where $x \leq 0.5$ and $y \leq 0.36$ with a crystal structure also similar to NiO. In Fig. 4(d), corresponding to TiO₂-2A, a new layer is clearly visible with an average size of 520 nm instead of the TiO₂ initial layer of 300 nm. The effectiveness of TiO₂ layer as cathode protection seems to be confirmed by the thickness increase most probably due to the presence of nickel inside the new layer formed by rhombohedral and orthorhombic crystals. The distribution of the crystals on the modified surface is shown in Fig. 4(f). Fig. 8 shows the EDS mapping of Ti, Ni and O on the surface of TiO₂-2A. Also in this case a well-distributed mixed phase is likely. It was not our purpose to deepen this analysis, but obviously complementary analyses are required to determine exactly the mixed Li–Ni–Ti–O compound.

The normalized survey XPS spectra of TiO₂-1A and TiO₂-2A samples are shown in Fig. 9. Ti 2p, 3s, 3p and Ni 2p, Ni 3s binding energies were detected. The peak intensity of titanium is higher in the TiO₂-2A sample than in the TiO₂-1A sample. After argon sputtering about 5 Å, the survey spectrum reveals the same composition for titanium, nickel and oxygen for both samples.

An amplification of titanium peaks for both spectra is reported in Fig. 10 showing the differences between Binding Energies (BE). Ti 2p 3/2 BE is lower for titanium in the TiO₂-1A sample than in the TiO₂ sample, suggesting the presence of titanium in a lower oxidation state than the initial Ti (IV) deposited by ALD. In the case of oxygen, the TiO₂-1A peak has a lower intensity and a smaller FWHM (Full-Width at Half Maximum) than that of TiO₂-2A, showing the difference in oxidation states present in this latter. Finally the Ni has almost the same XPS spectrum for both samples.

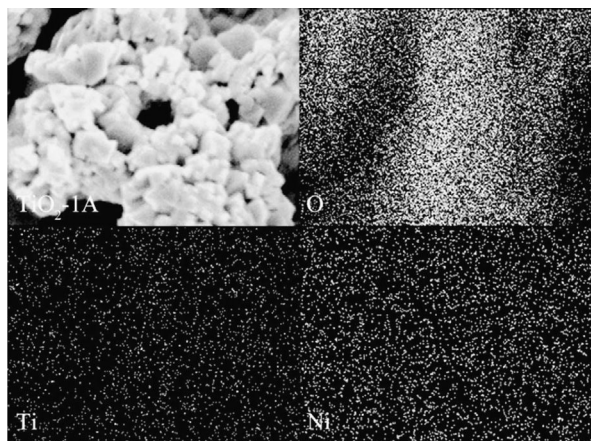


Fig. 7 – EDS mapping of TiO₂-1A, after immersion in molten Li₂CO₃–K₂CO₃ (62:38 mol%) at 650 °C during 230 h.

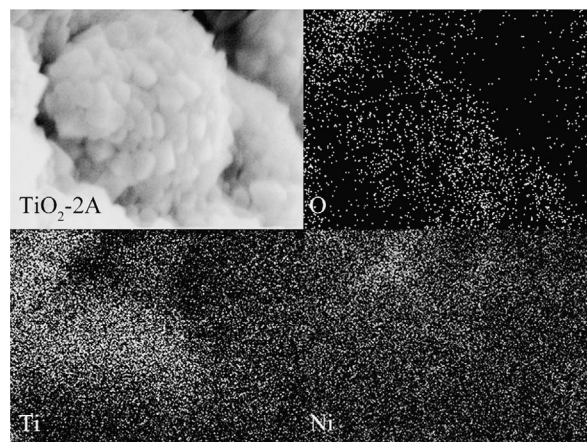


Fig. 8 – EDS mapping of TiO₂-2A, after immersion in molten Li₂CO₃–K₂CO₃ (62:38 mol%) at 650 °C during 230 h.

3.3. Electrochemical behavior

3.3.1. Chronopotentiometric data

Fig. 11 shows the OCP evolution all over 230 h of immersion of the bare porous nickel cathode in molten Li₂CO₃–K₂CO₃ (62:38 mol%) at 650 °C. Porous nickel OCP behavior, investigated previously by different authors, among which Yazici et al. and Antolini [2,18], can be attributed to *in situ* Ni oxidation followed by NiO lithiation process on the nickel porous surface. The three plateaux observed in Fig. 11 are related to the modification of the porous Ni electrode into Li_xNi_{1-x}O, in a progressive way. The first plateau-like tendency from 0 to 98 h is ascribed to *in situ* oxidation of metallic nickel:



After the first potential jump, at 98 h, a second plateau is reached at a potential around $-0.4 \text{ V}/(\text{Ag}/\text{Ag}^+)$. This plateau corresponds to the *in situ* lithiation of NiO, which is associated to an increase in the nickel valence from Ni(II) to Ni(III), as reported by Nishina et al. from XPS measurements [19]. The

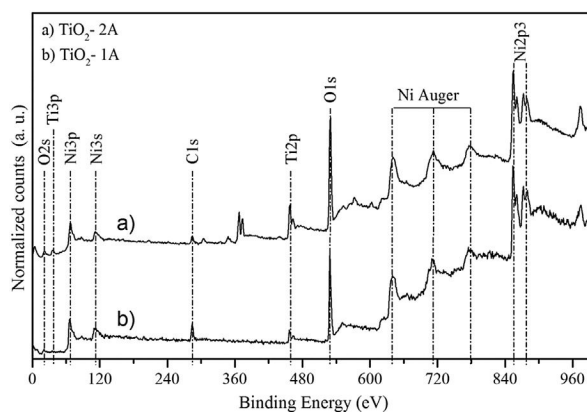


Fig. 9 – XPS Survey of TiO₂-2A and TiO₂-1A after immersion in molten Li₂CO₃–K₂CO₃ (62:38 mol%) at 650 °C during 230 h.

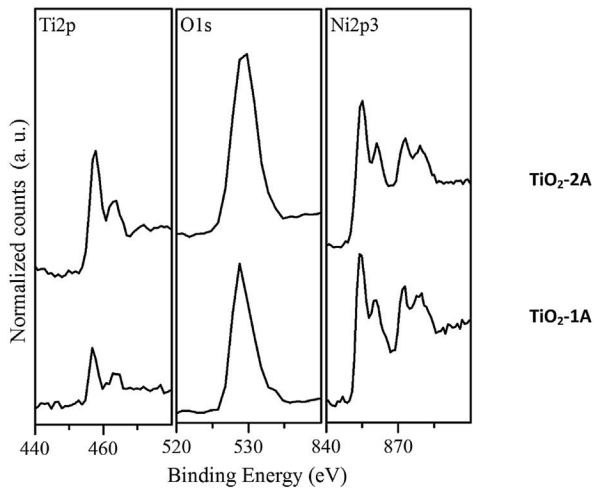


Fig. 10 – Amplification of Ti, O and Ni peaks of survey in Fig. 9 for TiO₂-2A and TiO₂-1A.

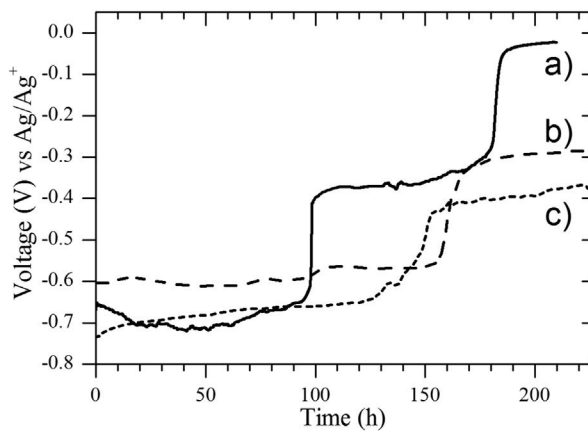


Fig. 11 – OCP evolution over time of immersion in molten Li₂CO₃–K₂CO₃ (62:38 mol%) at 650 °C during 230 h (a) porous Ni, (b) TiO₂-1A (50 nm), (c) TiO₂-2A (300 nm).

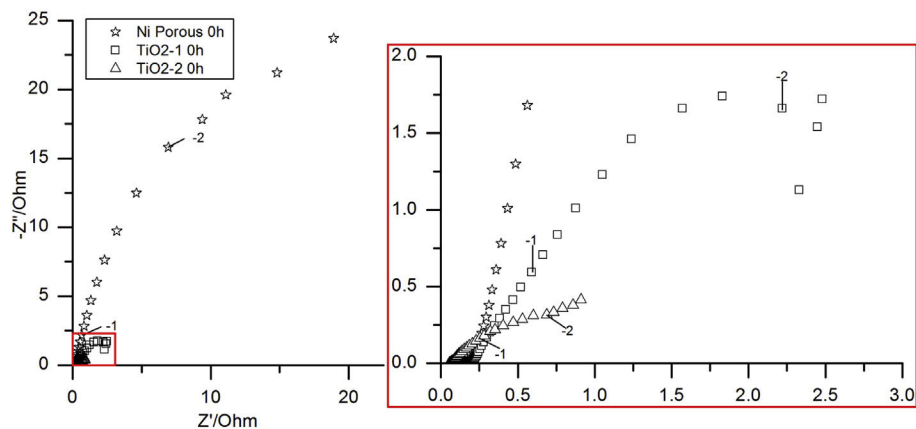
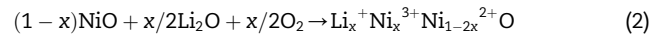


Fig. 12 – Nyquist impedance diagrams of: (☆) porous Ni, (□) TiO₂-1A (50 nm), (△) TiO₂-2A 300 nm, at 0 h immersion in molten Li₂CO₃–K₂CO₃ (62:38 mol%) at 650 °C.

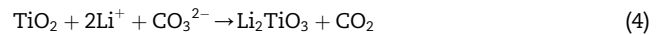
incorporation of lithium into the NiO lattice seems to follow this reaction [20–22]:



The general formula commonly used for lithiated nickel oxide is Li_xNi_{1-x}O. In the cathode environment, the equilibrium lithium content in NiO, estimated by nuclear microprobe, is roughly 0.2 atm% of lithium [23]. After 182 h, the lithiation process is completed and the third plateau at –0.03 V/(Ag/Ag⁺) corresponds to an equilibrium potential between O₂, CO₂ and carbonates. At this stage, the electrode works as a stable cathode for oxygen reduction:



With respect to the bare porous Ni cathode, the TiO₂-coated Ni can have different effects. First of all, TiO₂ can be oxidized spontaneously into lithium titanate:



Secondly, the coated oxide can inhibit or delay the oxidation and lithiation of Ni. Finally, as seen in the structural part of our study, an intimate interaction between the substrate and the coating is likely to occur. The first plateau corresponding roughly to Ni oxidation combined to that of TiO₂ is somehow similar to that of porous Ni before 98 h, even though there are differences probably attributed to the change in the cathode/electrolyte interface. After 98 h, the same plateau still remains for both TiO₂-1A and TiO₂-2A samples and the potential jump occurs at around 150 h. The second plateau is still observed up to 230 h, showing that the equilibrium between the Ni cathode and the melt is longer to establish. It can be noted that the plateau in the case of TiO₂-1A has a higher potential than in the case of TiO₂-2A, which shows that the thicker is the protective layer, the more difficult it is to reach the final potential relative to oxygen reduction. These observations are in agreement with a similar study realized with sputter-deposited TiO₂ in contact with Li₂CO₃–Na₂CO₃ [7].

3.3.2. Electrochemical impedance spectroscopy analysis

Impedance diagrams were registered each 10 h from 0 to 230 h. Fig. 12 shows a typical Nyquist plot of impedance

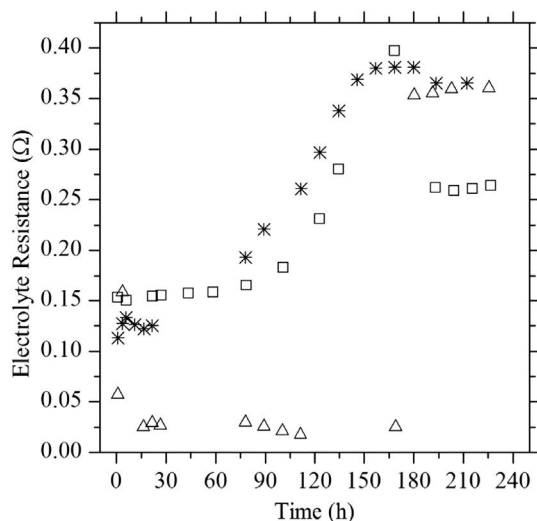


Fig. 13 – Electrolyte resistance vs time of immersion in molten $\text{Li}_2\text{CO}_3\text{--K}_2\text{CO}_3$ (62:38 mol%) at 650 °C: (*) porous Ni, (□) $\text{TiO}_2\text{-1A}$ (50 nm), (△) $\text{TiO}_2\text{-2A}$ (300 nm).

diagram taken for $\text{TiO}_2\text{-1}$, $\text{TiO}_2\text{-2}$ and porous nickel at time 0 h. EC-Lab 10 software was used to fit the data considering the simple equivalent electrical circuit composed of a resistance in series with two circuits associating a resistance and a constant phase element in parallel. In Fig. 13 the electrolyte resistance as a function of time is reported, while the electrode total contribution variations are depicted in Fig. 14. Analyzing the impedance diagrams, the TiO_2 -coated Ni largely decreases the total resistance of the system. Moreover, the thicker is the coating the lower is the resistance: at 10^{-2} Hz for instance, $R(\text{TiO}_2\ 1\text{A}) = 0.7\ \Omega$ and $R(\text{TiO}_2\ 2\text{A}) = 1.2\ \Omega$, which is almost 6 times lower than the system resistance based on uncovered porous Ni. A focus on the highest frequencies used in these diagrams allowed us measuring the electrolyte

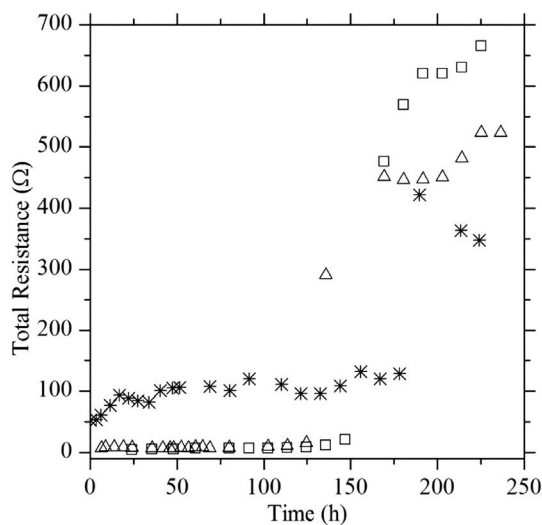


Fig. 14 – Total resistance vs time of immersion in molten $\text{Li}_2\text{CO}_3\text{--K}_2\text{CO}_3$ (62:38 mol%) at 650 °C during 230 h: (*) porous Ni, (□) $\text{TiO}_2\text{-1A}$ (50 nm), (△) $\text{TiO}_2\text{-2A}$ (300 nm).

resistance. Its variations are reported in Fig. 13 as a function of immersion time, for the three samples used as working electrodes. These electrolyte values evolve during the immersion duration. Three main zones can be distinguished for porous nickel as well as for $\text{TiO}_2\text{-1A}$, but only two for $\text{TiO}_2\text{-2A}$. These zones and the corresponding electrolyte resistance values are summarized in Table 1. The different values of electrolyte resistance, obtained in strictly the same conditions, are surely caused by the variation of the working electrode surface value. The initial geometrical surface is the same whatever the sample considered. Nevertheless, two of them are TiO_2 -coated. Thus, the specific surface area, and as a direct consequence the electrochemically active surface area are modified from one sample to another. Electrolyte resistance decrease is a result of an increase in the surface, which means that the 300 nm deposit presents a largely higher specific surface area than the others. After 180 h of immersion, the electrolyte resistance is lower when using $\text{TiO}_2\text{-1A}$, which could indicate a less effective modification of the phase and the film, and thus of the surface area.

Considering the total resistance, most of the differences are observed after 150–170 h of immersion, whatever the sample. Before this duration, the most resistive is the porous nickel electrode, while the titanium oxide coatings largely decrease the system losses. After 170 h, the porous Ni electrode has already reached an equilibrium state and the global resistance progressively decreases, whereas, the coated samples follow a different trend. For both TiO_2 -coated electrodes the resistance increases dramatically at around 140–150 h before reaching a kind of plateau. It is obvious that after 230 h, the coated samples are still far from equilibrium.

3.4. Solubility

Ni and titanium solubility measurements are gathered in Table 2 and compared when available with some literature data [12,24,25]. The solubility of porous nickel in our conditions is slightly lower than the values found in the literature, which is most probably due to the gaseous atmosphere used, with less CO_2 ratio in our case. The effect of the coating layer is clear: whatever the thickness of the coating, the solubility decreases of about 50%; however, the higher value for 300 nm thickness is likely to be due to the presence of nickel oxide grains detached mechanically in the molten carbonate melt. The value of 11.1 ppm is a medium value between two independent measurements (10.5 and 11.7 ppm) and at this stage it is difficult to analyze the reproducibility of solubility values. It is also worthy to note that the solubility of titanium is always

Table 1 – Electrolyte resistance and corresponding time zones according to Fig. 12.

	Zone I		Zone II		Zone III	
	Time limits	R (Ω)	Time limits	R (Ω)	Time limits	R (Ω)
Porous Ni	0–60 h	0.12	65–145 h	0.37	150–240 h	0.37
$\text{TiO}_2\text{-1A}$	0–90 h	0.15	95–155 h	0.25	160–240 h	0.25
$\text{TiO}_2\text{-2A}$	0–180 h	0.02	–	–	180–240 h	0.35

Table 2 – Solubility of nickel and titanium in pure nickel and TiO₂-coated nickel (wt ppm). Comparison with the literature.

Samples	Ni	TiO ₂ -coated Ni 2.5 ^a or 5 ^b mol%	TiO ₂ -coated Ni (50 nm)	TiO ₂ -coated Ni (150 nm)	TiO ₂ -coated Ni (300 nm)
Ni	15		8.2	6.5	11.1
	18.1* [12]	17.8 ^{a,*} [12] 6.8 ^{b,*} [12]			
	17.9* [24] 16.8* [25]				
Ti			1.3	1.2	<1

*P_{O₂}/P_{CO₂} = 0.33/0.67 (bar/bar).

extremely low which supports the idea of using TiO₂ as a protective coating, even though we proved that the final surface material is a mixed Li–Ni–Ti–O compound.

4. Conclusions

This paper not only confirms the promising features of titanium-based materials for optimizing the operation of MCFC devices, which has been previously developed in a few papers, but also gives a good scientific background for the integration of TiO₂ as an ultrathin coating for the protection of the state of the art cathode. The use of a high-quality technique such as ALD, which scalability is already proven in electronic or electroluminescence industries, allowed processing TiO₂-coatings, crystalline as deposited at 250 °C without any further annealing process. These coatings are spontaneously transformed when immersed during 230 h in molten Li₂CO₃–K₂CO₃ in lithium titanate, which is thermodynamically stable in this melt. A gradual evolution of the coating in a mixed Li–Ni–Ti–O structure is evidenced by a combination of XRD, EDS and XPS analyses, obtaining possibly structures, such as Li_xTi_yNiO_{1.98} and Li_xTi_yNiO_{1.65}. The *in situ* electrochemical behavior is affected by these coatings because of the complexity of the oxidation/lithiation processes, added to the interdiffusion of elements between the substrate and the protective layer. OCP time-evolution showed similar tendencies with or without coatings in the first 100 h. Afterward, it was found that reaching a stable TiO₂-coated cathode for oxygen reduction is a slower process than that with a bare porous nickel. However, this evolution combining a lithiation/interdiffusion process is likely to produce a stable mixed NiO-based cathode. Impedance spectroscopy allowed to follow the time-evolution of the electrolyte resistance and the global system resistance. It can be deduced that the TiO₂-coating is favorable to the whole reduction process but the tendency is reversed after 150 h of immersion. Longer immersion times would be necessary to analyze more precisely the evolution of the coated samples. In any case, all these results show the feasibility of such high-quality coatings enriched progressively by nickel diffusion to form a stable compound, which protects the porous nickel substrate and decreases significantly nickel solubility. Furthermore, titanium solubility is extremely low in molten carbonates and this is a key aspect to integrate it in MCFC devices.

REFERENCES

- [1] Bischoff M. Molten carbonate fuel cells: a high temperature fuel cell on the edge of commercialization. *J Power Sources* 2006;160:842–5.
- [2] Yazici M, Selman J. Dissolution of partially immersed nickel during *in situ* oxidation in molten carbonate: cyclic, stripping and square wave voltammetry measurements. *J Electroanal Chem* 1998;457:89–97.
- [3] Orfield ML, Shores DA. Solubility of NiO in molten Li₂CO₃, Na₂CO₃, K₂CO₃ and Rb₂CO₃ at 910 °C. *J Electrochem Soc* 1988;135:1662–8.
- [4] Antolini E. The stability of molten carbonate fuel cell electrodes: a review of recent improvements. *Appl Energy* 2011;88:4274–93.
- [5] Kulkarni A, Giddey S. Materials issues and recent developments in molten carbonate fuel cells. *J Solid State Electrochem* 2012;16:3123–46.
- [6] Mendoza L, Albin V, Cassir M, Galtayries A. Electrochemical deposition of Co₃O₄ thin layers in order to protect the nickel-based molten carbonate fuel cell cathode. *J Electroanal Chem* 2003;548:95–107.
- [7] Albin V, Mendoza L, Gourba A, Ringuedé A, Billard A, Brioso P, et al. Morphological, structural and electrochemical analysis of sputter-deposited ceria and titania coatings for MCFC application. *J Power Sources* 2006;160:821–6.
- [8] Belhomme C, Gourba E, Cassir M, Tess C. Chemical and electrochemical behaviour of Ni–Ti in the cathodic conditions used in molten carbonate fuel cells. *J Electroanal Chem* 2001;503:69–77.
- [9] Chauvaut V, Cassir M. Behaviour of titanium species in molten Li₂CO₃–Na₂CO₃ and Li₂CO₃–K₂CO₃ in the anodic conditions used in molten carbonate fuel cells. II. Electrochemical intercalation of Li⁺ in Li₂TiO₃ at 600 and 650 °C. *J Electroanal Chem* 1999;474:9–15.
- [10] Chauvaut V, Duval E, Malinowska B, Cassir M. XPS study of titanium species exposed to molten Li₂CO₃–Na₂CO₃ in the anodic conditions used in molten carbonate fuel cells. *J Mater Sci* 1999;34:2015–22.
- [11] Chauvaut V, Cassir M, Denos Y. Behavior of titanium species in molten Li₂CO₃–Na₂CO₃ and Li₂CO₃–K₂CO₃ under anodic and cathodic conditions. I – thermodynamic predictions at 550–750 °C. *Electrochim Acta* 1998;43:1991–2003.
- [12] Hong MZ, Lee HS, Kim MH, Park EJ, Ha HW, Kim K. TiO₂-coated Ni powder as a new cathode material for molten carbonate fuel cells. *J Power Sources* 2006;156:158–65.
- [13] Haukka S, Kytökiivi A, Lakomaa E-L, Lehtovirta U, Lindblad M, Lujala V, et al. The utilization of saturated gas–solid reactions in the preparation of heterogeneous catalysts. *Stud Surf Sci Catal* 1995;91:957–66.

- [14] Leskela M, Ritala M. Atomic layer deposition (ALD): from precursors to thin film structures. *Thin Solid Films* 2002;409:138–46.
- [15] Ritala M, Leskelä M, Niinistö L, Haussalo P. Titanium isopropoxide as a precursor in atomic layer epitaxy of titanium dioxide thin films. *Chem Mater* 1993;5:1174–81.
- [16] Aarik J, Aidla A, Uustare T, Ritala M, Leskelä M. Titanium isopropoxide as a precursor for atomic layer deposition: characterization of titanium dioxide growth process. *Appl Surf Sci* 2000;161:385–95.
- [17] Malinowska B, Cassir M, Delcorso F, Devynck J. Thermodynamic and electrochemical behavior of nickel in molten $\text{Li}_2\text{CO}_3\text{--Na}_2\text{CO}_3$ modified by addition of calcium carbonate. *J Electroanal Chem* 1995;389:21–9.
- [18] Antolini E. Behaviour of Ni, NiO and $\text{Li}_x\text{Ni}_{1-x}\text{O}$ in molten alkali carbonates. *J Mater Sci* 2000;35:1501–5.
- [19] Nishina T, Takizawa K, Uchida I. Electrochemical characterization of in situ NiO formation in a molten carbonate. *J Electroanal Chem* 1989;263:87–96.
- [20] Minh NQ. Technological status of nickel oxide cathodes in molten carbonate fuel cells – a review. *J Power Sources* 1988;24:1–19.
- [21] Oliver PM, Parker SC, Wackrodt WC. Computer Simulation of the crystal morphology of NiO. *Model Simul Mater Sci Eng* 1993;1:755–60.
- [22] Cassir M, Belhomme C. Technological applications of molten salts: the case of the molten carbonate fuel cell. *Plasma Ions* 1999;1:3–15.
- [23] Belhomme C, Cassir M, Tessier C, Berthoumieux E. Lithium depth profile in NiO molten carbonate fuel cell cathode by nuclear microprobe. *Electrochem Solid-State Lett* 2000;3:216–9.
- [24] Scaccia S. Investigation on NiO solubility in binary and ternary molten alkali metal carbonates containing additives. *J Mol Liq* 2005;116:67–71.
- [25] Brenscheidt T, Nitschké F, Söllner O, Wendt H. Molten carbonate fuel cell research II. Comparing the solubility and the in-cell mobility of the nickel oxide cathode material in lithium/potassium and lithium/sodium carbonate melts. *Electrochim Acta* 2001;46:783–97.



Electrochemical properties of Atomic layer deposition processed CeO₂ as a protective layer for the molten carbonate fuel cell cathode



A. Meléndez-Ceballos^{a,b}, V. Albin^b, S.M. Fernández-Valverde^{a,*}, A. Ringuedé^b,
M. Cassir^{b,*}

^a Depto. De Química, Gerencia de Ciencias Básicas, Instituto Nacional de Investigaciones Nucleares, A.P.18-1027, México D.F. C.P.11801, México

^b Laboratoire d'Electrochimie, Chimie des Interfaces et Modélisation pour l'Énergie UMR 7575 CNRS, ENSCP Chimie-Paristech 11 rue Pierre et Marie Curie, F-75231 Paris Cedex 05, France

ARTICLE INFO

Article history:

Received 15 December 2013

Received in revised form 5 May 2014

Accepted 5 May 2014

Available online 14 May 2014

Keywords:

MCFC
Cathode
Cerium oxide
Coating
ALD
Electrochemistry

ABSTRACT

In order to increase the lifetime and performance of the molten carbonate fuel cell, it is compulsory to control the corrosion and dissolution of the state of the art porous nickel oxide cathode. A protective coating constituted by more stable oxides appears to be the best approach. Previous research on CeO₂ coatings obtained by DC reactive magnetron sputtering to protect the Molten carbonate fuel cell cathode gave promising results but it was necessary to improve the coating adhesion. In this paper Atomic Layer Deposition, producing high quality, homogeneous and conformal layers, was used to obtain thin layers of CeO₂ (20 nm and 120 nm) deposited over porous nickel. CeO₂-Ni coated samples were tested as cathodes in Li₂CO₃-K₂CO₃ (62–38 mol %) eutectic mixture under standard cathode atmosphere (CO₂/air 30:70 vol. %). Structural and morphological characterizations of the nickel coated cathode before and after electrochemical tests in the molten carbonate melt are reported together with the Open Circuit Potential evolution all over 230 h for both the bare porous nickel and the CeO₂-coated samples.

© 2014 Elsevier Ltd. All rights reserved.

1. Introduction

Fuel cells (FC) are a promising technology for alternative energy generation. Different types exist and their working principles determine their suitability for different applications ranging from micro-scale portable low temperature fuel cells like Polymer Exchange Membrane (PEMFC) to stationary megawatt scale high temperature fuel cells like Solid Oxide (SOFC) and Molten Carbonate (MCFC). These cells are suitable for stationary energy generation due to their resistance to poisoning, internal reforming ability and the less expensive construction compared to other fuel cells that incorporate precious metals like platinum. Even though MCFC technology has been around for decades, there are still many challenges regarding material science and stack engineering breakthroughs. One of the main issues of the MCFC operating at temperatures around 650 °C, is the short lifetime of the cell components due to material degradation. Furthermore, MCFC components such as the anode, cathode, electrolyte matrix, current collectors and

interconnectors which are exposed to corrosive environments are required to last more than 40,000 hours of operation for being feasible at a commercial level [1].

The state of the art MCFC cathode is constituted by porous Ni which is oxidized and lithiated *in situ* to form Li_xNi_{1-x}O. This oxide tends to dissolve partially into the carbonate melt. Ni²⁺ diffuses to the anode where it can be reduced by hydrogen yielding metallic nickel, which causes a short-circuit between the anode and cathode resulting in a MCFC stack failure [2,3]. In the last decade several approaches have been proposed to protect the MCFC cathode [4–10]; however, it is still delicate to establish their feasibility for commercial production.

Ceria has been previously studied in the literature under MCFC conditions demonstrating that it is a promising oxide to reduce Ni dissolution due to its stability [7,9,10]. Thus, in order to increase long-term protection of the Ni cathode, ceria coatings were processed in the present work by Atomic Layer Chemical Vapor deposition (ALCVD), also known as atomic layer deposition (ALD) similar to a sequential CVD. ALD is a chemical gas phase deposition technique developed in Finland in the 1970s by T. Suntola [11]. Even though this technique is relatively expensive it offers several advantages: high-quality ultrathin films, homogenous, conformal, crystalline as-deposited and scalability, e.g. large-area flat

* Corresponding author.

E-mail addresses: suilma.fernandez@inin.gob.mx (S.M. Fernández-Valverde), michel.cassir@chimie-paristech.fr (M. Cassir).

panel displays based on thin film electroluminescence (TFEL) and semi-conductors industry [11,12]. ALD has already been successfully used to produce functional materials based on ceria or titania for solid oxide fuel cells (SOFC) and MCFC [13,14].

In ALD, pulses of the reactant gases are separately introduced into the reaction chamber where substrates are coated following several steps. Growth is achieved through self-terminating surface reactions. Self-terminating means that only one monolayer of reactant gas species can be adsorbed to the surface during a pulse. The pulses containing reactant gases are separated by purging pulses where the ALD reactor is flushed with an inert gas. The purging pulses ensure that the reactant gas pulses do not mix. Mixing of the reactant gas pulses would lead to continuous growth and the accurate thickness control of the deposition process would be lost. By-products like detached ligands and excess reactants are also flushed away by the purging pulses. A complete set of reactant gas pulses and purging pulses needed to deposit a certain compound are referred to as a cycle. If deposition parameters have been chosen properly, the number of cycles rather than the concentration of the reactant species determine the film thickness [15]. CeO₂ deposited as a thin film by ALD form compact and crack-free layers, in comparison with other techniques like electrochemical deposition [16–18]. Therefore, the aim of this investigation is to test nanocrystalline CeO₂ deposited by ALD onto a porous nickel substrate as cathode to evaluate its performance as a protective layer for MCFC application by determining its electrochemical behavior in Li₂CO₃-K₂CO₃ (62-38 mol %) under standard cathode atmosphere and its surface changes after 230 h of immersion.

2. Experimental

2.1. CeO₂ layer deposition on porous nickel using ALD

To determine the ALD deposition parameters, thin layers of CeO₂ were processed by ALD over a Si monocrystal oriented in the 111 plane. With the determined parameters, CeO₂ coatings were deposited over commercial porous nickel substrate (produced by Doosan, South-Korea) [19] with the vertical flow type reactor (Picosun SUNALE™ R-series). Four different samples were processed with this technique. A known deposition route was followed using halide-free and non-corrosive Ce(TMHD)₄ (tetrakis(2,2,6,6-tetramethyl 1-3,5-heptanedionate Ce(IV)) as precursor for CeO₂ [20,21]. For the Ce(TMHD)₄ (Strem Chemicals), ozone was used as oxidizing agent. In order to prepare the CeO₂ layer, Ce(TMHD)₄ was sublimated at 180 °C and introduced into the precursor chamber by a N₂ flow of 150 cm³ min⁻¹ using the following conditions: pulse time 3 s, and purge time 2.5 s. Ozone was supplied at room temperature by a N₂ flow of 100 cm³ min⁻¹ with pulses of 4 s and purge times of 2.5 s. The reactor temperature was kept at 300 °C in a N₂ flow of 300 cm³ min⁻¹, the precursor pulse and purge were followed by ozone pulse and purge, this cycle being repeated until the desired thickness was reached. Two different thicknesses were processed with this technique: two samples of 27 nm, and two samples of 127 nm. The samples were named CeO₂-1 and CeO₂-2 for the 27 and 127 nm CeO₂-coated Ni porous cathodes, respectively.

2.2. Electrolyte and cell

The high-temperature electrochemical cell was a single-compartment crucible of dimensions 70 × 50 mm² contained in an alumina Al₂O₃ reactor of dimensions 250 × 60 mm², hermetically sealed by a stainless steel cover with a Viton O-ring. The whole electrochemical set-up was fully described in a previous paper [22]. Temperature was controlled at a constant temperature of 650 °C

by means of a calibrated chromel/alumel thermocouple, the electrolyte was a mixture of lithium and potassium carbonates of high grade purity >98% (Sigma-Aldrich®), in a proportion of 62:38 mol%. The standard cathode atmosphere was a mixture of Air/CO₂ (70:30 mol%) of high grades purity (Air Liquide®) at 650 °C and a pressure of 1 atm. A carbonate melt was prepared and stabilized 24 h at 650 °C for each CeO₂-coated sample. After stabilizing the molten carbonate eutectic under the selected cathode atmosphere, samples were immersed in the carbonate melt and electrochemical measurements were performed for 230 h. After electrochemical tests, samples were rinsed with deionized water to remove the carbonates, dried at 100 °C in an oven and kept in small plastic boxes to prevent contamination before further analysis.

2.3. Electrochemical measurements

To determine the electrochemical performance of the coated samples, a three-electrode system was used, the working electrode being the as-deposited CeO₂-1 and CeO₂-2 on porous nickel substrate of dimensions 10 × 10 × 0.5 mm, the counter electrode was a brand new gold wire of 1 mm diameter (4 cm) and the reference electrode a silver wire dipped into an Ag₂SO₄ (10⁻¹ mol kg⁻¹) saturated Li-K carbonate eutectic in an alumina tube sealed by a porous alumina membrane. Electrochemical experimental data were collected using a potentiostat/galvanostat (AutoLab® PGSTAT-302 N). Open Circuit Potential (OCP) was collected for CeO₂-1 and CeO₂-2 samples from 0 to 230 h of immersion. OCP measurements were interrupted periodically to perform electrochemical impedance spectroscopy (EIS). EIS parameters were: scanning frequencies set from 0.001 to 10⁶ Hz, with 11 points per decade and signal amplitude of 5 mV respecting the system linearity. After each EIS test, OCP measurements were restarted. This procedure was performed for 230 h with EIS performed at regular intervals.

2.4. Characterization

2.4.1. Characterization of deposited CeO₂ layer on porous Ni by ALD

The CeO₂ layers were characterized by X-ray diffraction, XPS and SEM-EDS. XRD was performed in a PANalyticalX'pert Pro from Anton Paar with Cu-Kα1 radiation (λ=1.54056 Å). The diffraction pattern was obtained by scanning between 20 and 80° by steps of 0.02 (2θ°) with a fixed counting time of 2.3 s and sample rotation of 3 rpm. Once the data were obtained, Scherrer analysis calculation was used to obtain the average crystal size of the deposited layer by determining the angular position and FWHM of the peaks between 28 and 60 2θ degrees. Scanning Electron Microscopy (SEM) and Energy Dispersion Spectroscopy (EDS) analyses were performed with a ZEISS® Ultra 55 microscope to evaluate the surface morphology and to measure layer thicknesses. Raman spectra were obtained for samples of Ni porous coated with CeO₂ in a Lab Raman HR-800 from Horiba Jobin Yvon spectrometer with a spectral resolution of 2 cm⁻¹ and Olympus BX41 microscope using a 50X objective lens to focus the laser beam on the sample. Spectra were recorded from 100 to 1800 cm⁻¹ with a He-Ne laser of wavelength 532.07 nm and grid of 600, filter D 0.3, hole of 200 μm, slit of 100 μm. Spectrometer calibration was performed with Si (1 1 1). The X-ray photoelectron spectra were recorded using a Thermo Scientific K-Alpha X-ray photoelectron spectrometer with a monochromator Al Kα X-ray (hν = 1486.61 eV) for sample excitation. An argon ion beam was used to prevent samples surface charging. The spectrometer energy calibration was obtained using Au 4f 7/2 and Cu 2p 3/2 photoelectron lines. The position of the adventitious carbon C 1s peak at 284.6 eV was used as an internal reference in each sample to determine the binding energies with an accuracy of ± 0.1 eV. The residual pressure in the analysis chamber was maintained below 1 × 10⁻⁸

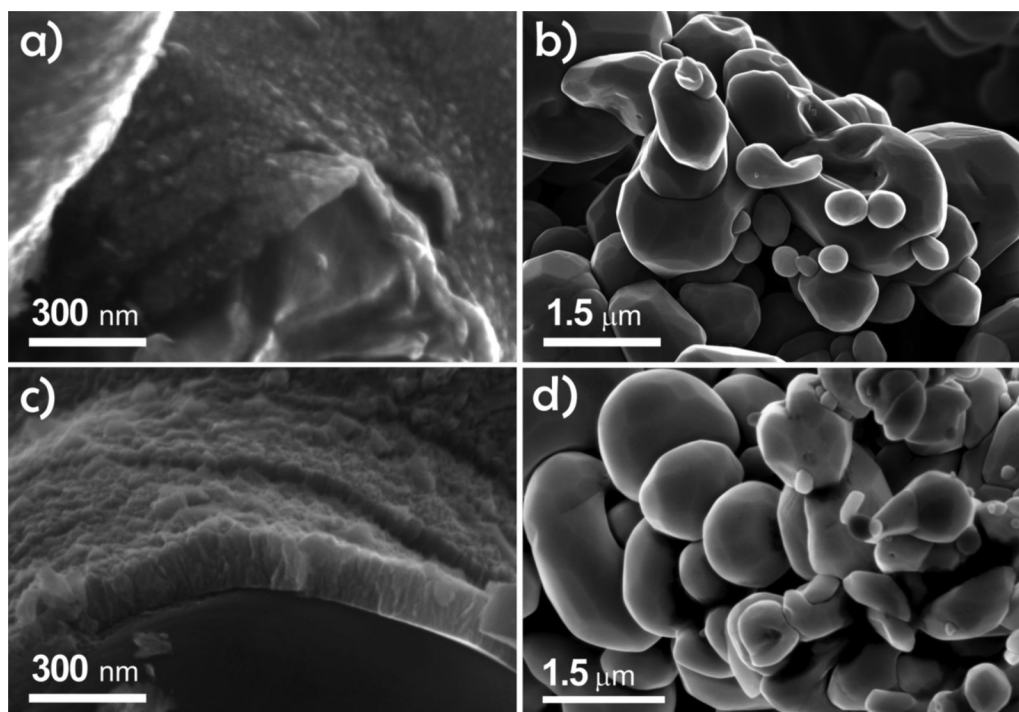


Fig. 1. SEM micrographs of ALD as-deposited CeO_2 coatings, before (a, c); and after immersion in 230 h of immersion in Li_2CO_3 - K_2CO_3 (62:38 mol %) at 650°C . (b, d). 27 nm thick sample (a, b); 127 nm sample (c, d).

Torr, during data acquisition. The survey spectrum of CeO_2 -1A was obtained between 0 and 1000 eV. The spectra was collected and analyzed with Advantage 4.0 software.

2.4.2. Cathode characterization after the electrochemical experiments

After the electrochemical experiments in the molten carbonate mixture, the cathodes were characterized in the same conditions with the same XRD-diffractometer, XPS, SEM-EDS and Raman Spectrometer.

2.5. Cathode solubility

The solubility of bare porous nickel and CeO_2 -coated nickel (thickness of 20 and 120 nm, respectively) was measured individually using three independent $(\text{Li}_{62}\text{-K}_{38})_2\text{CO}_3$ melts. Small amounts of carbonates (about 6 g) were withdrawn randomly three times from the molten carbonate bulk at the end of the electrochemical characterizations, which corresponds to 230 h. After solidification, each sample was hand-milled and 2 g of carbonate powder were dissolved in 10 ml of HNO_3 3 vol %. Nickel content was determined by ICP-AES (ICAP 6000 Series from Thermo Fisher Scientific). The calibration was performed for each separate element using Aldrich atomic absorption standard solutions, dissolved in HNO_3 3 vol %.

3. Results and Discussions

3.1. Material Characterization before electrochemical tests

SEM micrographs of as-deposited CeO_2 -1 and CeO_2 -2 coated samples are presented in Figs. 1a) and 1c). Layer thicknesses, as measured from Figs. 2a) and 2c), were of 27 ± 3 nm for CeO_2 -1, and 127 ± 3 nm for CeO_2 -2 samples, respectively. Thicknesses are not completely uniform due to flow variations through cavities in the porous samples. Chemical analysis performed by EDS only showed the dispersive X-ray energies of ceria ($L\alpha$ 4.839 eV, $L\beta$ 5.613 eV),

nickel ($K\alpha$ 7.471 eV, $L\alpha$ 0.851 eV) and oxygen ($K\alpha$ 0.525 eV). For example, in the case of CeO_2 -1, atomic ratios of Ni, O and Ce were 92, 7 and 1%, respectively. In order to form CeO_2 2 at. % of oxygen are needed and, therefore, probably 5 at. % of NiO were formed on the surface, the remaining material is only porous Ni.

Fig. 2 shows the diffraction pattern of porous nickel covered with cerium oxide, sample CeO_2 -1, before immersion in molten Li_2CO_3 - K_2CO_3 . The highest diffraction peaks correspond to the ICDD pattern file 00-004-0850 of Ni porous substrate with a cubic structure. The small diffraction peaks correspond to planes (1 1 1), (2 0 0), (2 2 0), (3 1 1) and (2 2 2) of CeO_2 , also in a cubic structure (ICDD pattern file 03-065-5923) and the three remaining peaks are related to nickel oxide in a cubic structure (ICDD pattern file 01-089-3080). These results confirm the presence of Ni, CeO_2 and small amounts of NiO in this sample, as suggested before from the EDS chemical analysis.

The average crystal size determined by the Scherrer equation for CeO_2 -1 and CeO_2 -2 samples (average value obtained from CeO_2 main planes) give values of 19 and 44 nm, respectively. It is relevant to note that the as-deposited coatings at 300°C are crystalline. Annealing was not required to crystallize the thin film of cerium oxide, which is a remarkable feature of the ALD-process.

3.2. Material characterization after immersion and electrochemical tests

CeO_2 -coated cathodes were tested in molten Li_2CO_3 - K_2CO_3 (62:38 mol. %) eutectic mixture for 230 h. SEM micrographs of CeO_2 -1 and CeO_2 -2 samples after immersion, shown in Figs. 2b) and 2d), disclose the coating transformation from a well-defined layer of cubic crystals of CeO_2 into thicker particles likely to be crystals of $\text{Li}_x\text{Ni}_{1-x}\text{O}$ mixed with cerium oxide. In effect, CeO_2 particles are separated from the lithiated nickel oxide particles, e.g. as can be seen in the case of the particle close to the cavity in the center of the micrograph. Round particles seem to be regularly trunked octahedra of CeO_2 , as reported recently by Ying Tan *et al.* during the

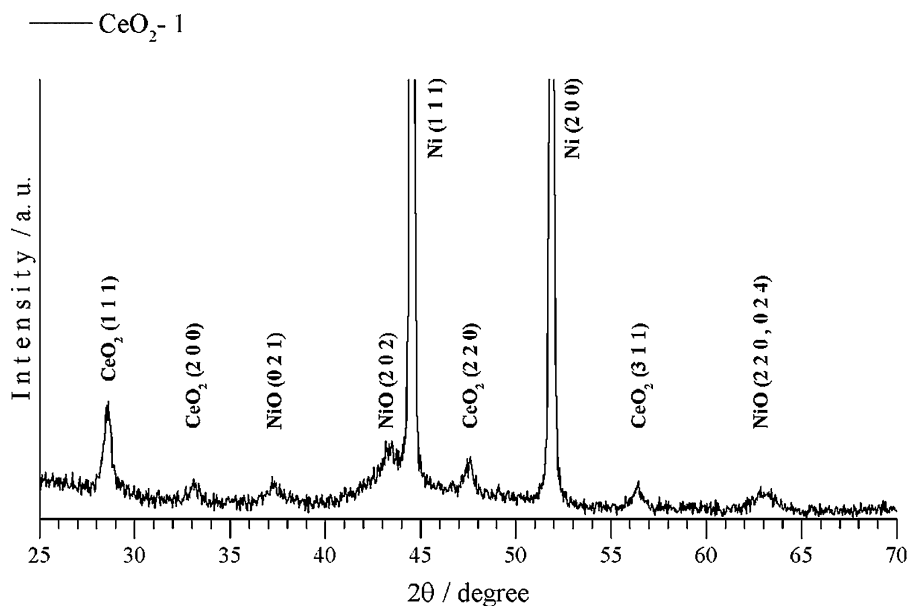


Fig. 2. XRD of as-deposited CeO_2 thin film of 27 nm onto nickel.

hydrothermal synthesis of CeO_2 ; the other cerium particles have the morphology of hexagonal particles also reported by the same authors [23].

Fig. 3 shows the diffraction pattern of sample CeO_2 -1 after immersion in the melt, where peaks marked as (○) correspond to planes of CeO_2 (ICDD pattern 00-034-0394) that remain present in the sample, peaks marked (●) correspond to a lithiated CeO_2 compound. In a previous study by Chauvaut *et al.*, where CeO_2 was exposed for 504 h to Li_2CO_3 - Na_2CO_3 (52:48 mol %), the lithiation limit for CeO_2 was found to be of 25 at. % [9]. In its gradual evolution, the CeO_2 coating seems to be transformed into $\text{Li}_{0.25}\text{Ce(III)}_{0.25}\text{Ce(IV)}_{0.75}\text{O}_2$, which is in agreement with an XPS analysis of CeO_2 after electrochemical tests [9]. Peaks marked with (□) correspond to $\text{Li}_{0.51}\text{Ni}_{1.16}\text{O}_2$ rhombohedral phase (ICDD diffraction pattern 01-088-1607). However, the peak intensities are slightly different from those of the pattern, which is probably due

to a lower Li content, since Belhomme *et al.* determined a medium Li content of 0.2 at. % in a $\text{Li}_x\text{Ni}_{1-x}\text{O}$ compound [24]. 2θ peaks not marked in Fig. 5 correspond to a mixed $\text{Li}_x\text{Ni}_y\text{O}_2$ phase, where $0.06 < x < 0.51$ and $0.49 < y < 0.94$ (ICDD patterns, 00-049-0035 and 01-081-2411). From the previous results, we can assume that there are at least three phases: lithiated CeO_2 , $\text{Li}_x\text{Ni}_{1-x}\text{O}$ and, probably in a minor ratio, $\text{Li}_x\text{Ni}_y\text{O}_2$.

The Raman spectrum of Fig. 4 shows vibrations at 183.3 cm^{-1} . In the range from 127 to 190 cm^{-1} , R. Kirste *et al.* found vibrations which were attributed to acoustical and phonon modes induced by Li insertion into ZnO which is comparable to NiO. Modes appearing at 393, 584, 898.8 and 1435.6 cm^{-1} are attributed by Lopez-Iturbe *et al.* and Mironova-Ulmane *et al.* [25,26] to Ni-O vibrations. The vibration mode at 551.6 cm^{-1} is characteristic of Li-O vibrations and is reported together with the vibration mode at 463.6 cm^{-1} as characteristic for LiNiO_2 [25,27]. According to R. Kirste *et al.*, a

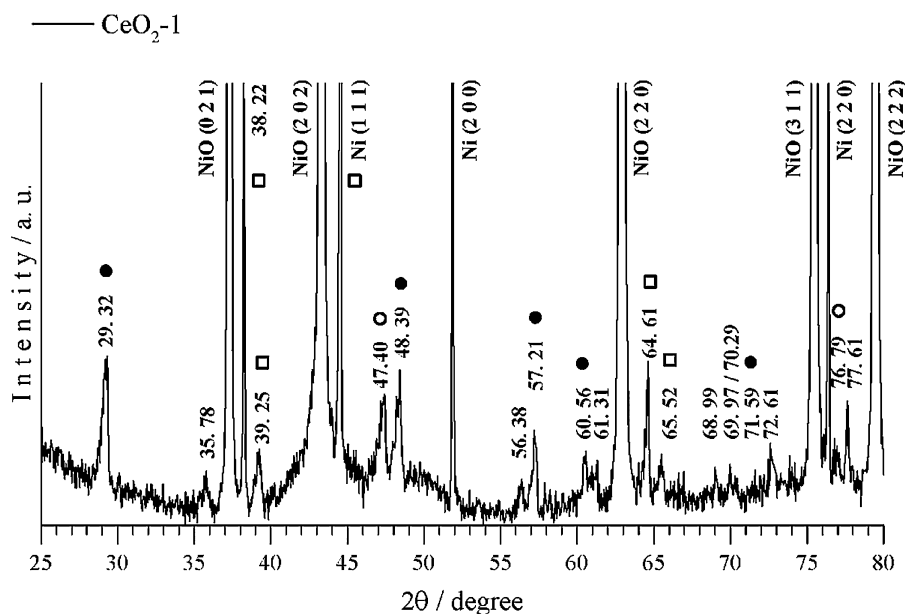


Fig. 3. XRD of CeO_2 thin film of 27 nm deposited onto nickel after the 230 h of immersion in Li_2CO_3 - K_2CO_3 (62-38 mol %) at 650°C .

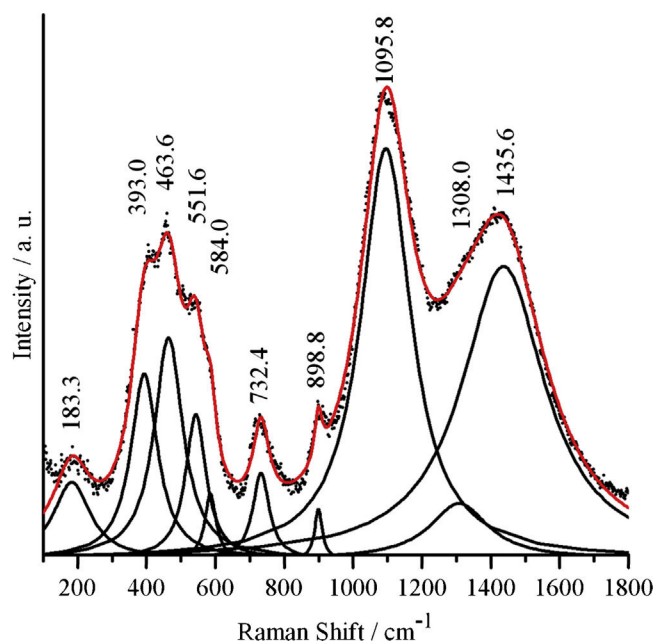


Fig. 4. Raman spectra of CeO₂ thin film of 27 nm deposited on nickel after 230 h of immersion in Li₂CO₃-K₂CO₃ (62-38 mol %) at 650 °C.

Li-O vibration is found at 732.4 cm⁻¹ and the peak at 1095.8 cm⁻¹ corresponds to O-O vibration, the last one being common to NiO and LiO compounds, the peak at 1308 cm⁻¹ is also common to those compounds [28]. CeO₂ has its characteristic mode at 464 cm⁻¹ [18]; Raman spectrometry performed on CeO₂-1 sample showed only a vibration mode at 462.4 cm⁻¹. The presence of a CeO₂ structure has been already confirmed by XRD as a lithiated phase in sample CeO₂-1A; hence the CeO₂ characteristic vibration mode certainly contributes to the 463.6 cm⁻¹ peak.

The normalized survey XPS spectra of CeO₂-1, as-deposited (dotted line) and after immersion in the carbonate melt with electrochemical tests (continuous line), are shown in Fig. 5. The peaks corresponding to the binding energies of cerium are well defined in the as-deposited sample where the most notorious binding energies correspond to Ce 3d, O 1s and C 1s [29,30]. After 230 h of immersion in molten carbonates, well-defined nickel oxide peaks, Ni 2p, Ni 3s and the corresponding Auger peaks, appear in the

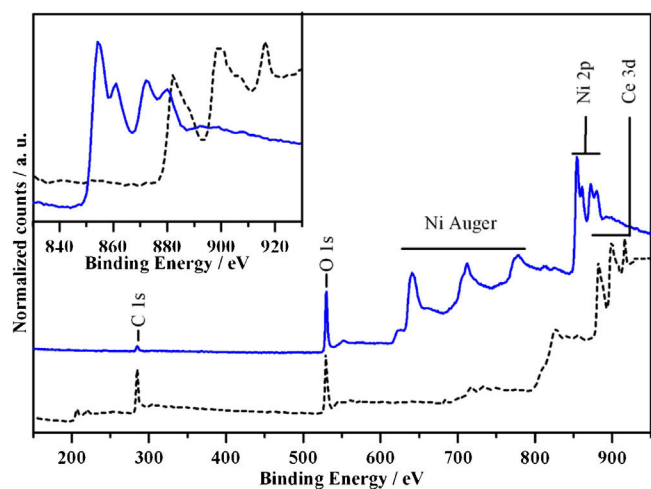


Fig. 5. XPS survey of as-deposited CeO₂-1 sample (dotted line) and after immersion in molten Li₂CO₃-K₂CO₃ (62:38 mol %) with electrochemical tests at 650 °C during 230 h (continuous line).

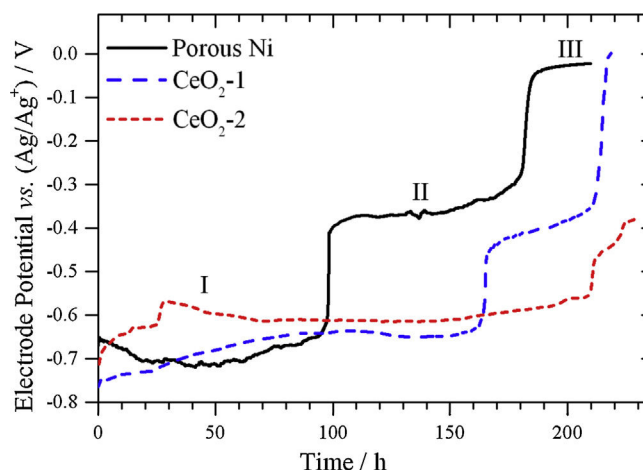


Fig. 6. OCP evolution over 230 h of immersion in Li₂CO₃-K₂CO₃ (62-38 mol %) at 650 °C: Ni cathode, CeO₂-1 and CeO₂-2.

survey spectrum and cerium peaks are no longer visible, as can be noted in the upper-left detail of Fig. 5 [31]. Apparently, in the analyzed sample ceria outer layer cannot be clearly detected, which can be due to the depth analysis of XPS and the fact that ceria might have diffused into the NiO substrate, resulting in a very low ceria to nickel oxide ratio. Moreover, previous XPS analyses of a ceria pellet, after immersion in Li₂CO₃-Na₂CO₃, showed that the behavior of the ceria surface is quite complex and includes apart of Ce(IV) species, Ce(III) originated from the exposure to X-rays in the spectrometer inducing a surface reduction of Ce(IV) or from the formation of Ce₂O₃ [9]. At this stage, XPS analysis indicates that the presence of ceria is not significant at the outer surface of the electrode.

Even though XPS results were not fully conclusive, XRD and Raman spectroscopy tend to prove the hypothesis of three different compounds on the surface of the coated samples: lithiated CeO₂, Li_xNi_{1-x}O and Li_xNi_yO₂.

3.3. Electrochemical behavior

3.3.1. Chronopotentiometric data

Fig. 6 shows the OCP evolution all over 230 h of immersion of the bare porous nickel cathode in molten Li₂CO₃-K₂CO₃ (62:38 mol %) at 650 °C. Porous nickel OCP behavior, investigated previously by different authors, among which Yazici *et al.* and Antolini [2,32], can be attributed to the *in situ* Ni oxidation followed by the NiO lithiation process on the nickel porous surface. The three plateaus I, II and III observed in Fig. 6 are related to the modification of the porous Ni electrode into Li_xNi_{1-x}O, in a progressive way. The first plateau-like tendency from 0 to 98 h is ascribed to the *in situ* oxidation of metallic nickel:



After the first potential jump at 98 h, a second plateau is reached at a potential around -0.4 V/(Ag/Ag⁺). This plateau corresponds to the *in situ* lithiation of NiO, which is probably associated to an increase in the nickel valence from Ni(II) towards Ni(III), as reported by Nishina *et al.* from XPS measurements [33]. The incorporation of lithium into the NiO lattice seems to follow this reaction [34,35]:



The general formula commonly used for lithiated nickel oxide is Li_xNi_{1-x}O. In the cathode environment, the equilibrium lithium content in NiO, estimated by nuclear microprobe, is roughly 0.2 at % of lithium [24]. After 182 h, the lithiation process is completed and the third plateau at -0.03 V/(Ag/Ag⁺) corresponds to an

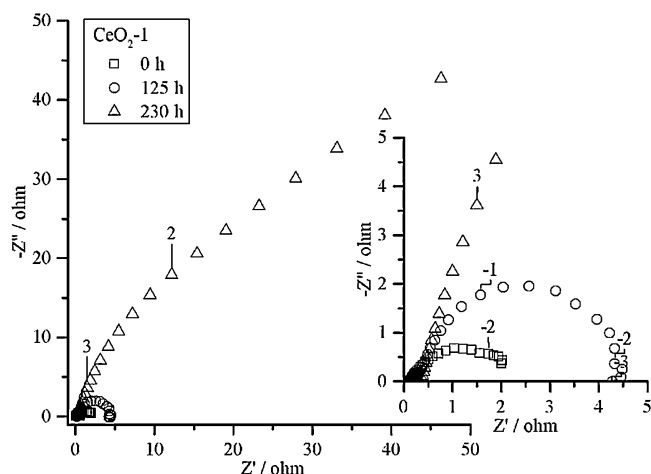


Fig. 7. Nyquist diagram of CeO₂-1 impedance recorded at 0, 125 and 230 h of immersion in Li₂CO₃-K₂CO₃ (62–38 mol %) at 650 °C.

equilibrium potential between O₂, CO₂ and carbonates. At this stage, the electrode works as a stable cathode for oxygen reduction:



CeO₂-coated Ni behaves in a similar way to bare Ni. The first plateau for CeO₂-1 in Fig. 6 starts at about -0.76 V, 100 mV less than bare Ni, due to the presence of the CeO₂ layer, while the substrate is being oxidized from Ni to NiO, the potential starts rising to reach a potential closer to that of the first plateau of bare Ni (-0.65 V). The presence of CeO₂ provokes a time delay for the second plateau appearing after 165 h, which is about 65 h later than for the bare Ni cathode. Afterwards, an abrupt potential increase can be observed at 212 h before reaching the third plateau corresponding to the oxygen reduction potential, just 30 h after bare Ni sample. This behavior indicates that CeO₂ causes a small delay in the whole Ni oxidation and lithiation process. However, it must be noted that the final potential reached with the CeO₂-coated sample is higher than that with the bare nickel cathode, which seems to show the good electrocatalytic properties of ceria towards the oxygen reduction.

For CeO₂-2 sample, OCP evolution depicted in Fig. 6 shows the behavior of a thicker layer of CeO₂. As expected, the presence of a 127 nm CeO₂ layer delays even more the oxidation of Ni; in this case, the potential jump of the second plateau occurs after 210 h, confirming that CeO₂ slows down Ni oxidation. The total time of 230 h was not enough to register the third plateau with the CeO₂-2 sample; however, the potential in the last minutes reached the value of the second plateau for bare Ni, indicating that the increase in thickness of the CeO₂ layer does not affect the plateau potential reached. In this study, CeO₂-coated samples prove to be comparable to the bare porous Ni cathode, as far as the OCP evolution is concerned.

3.3.2. Electrochemical Impedance Spectroscopy data

Electrochemical Impedance Spectroscopy (EIS) was performed every 10 h from 0 to 230 h of electrode immersion in Li-K carbonate eutectic melt. Figs. 7 and 8 shows the Nyquist diagrams of CeO₂-1 and CeO₂-2 respectively, recorded at 0, 125 and 230 h. Both CeO₂ samples seem to behave in quite a similar way up to the 125 h; however, as expected the total resistance is higher for the thicker sample, which is more pronounced before immersion in the molten electrolyte. An evident difference appears in the plot at 230 h, which is likely to be related to the layer thickness but also to a different evolution of the sample and of the diffusion behavior. Fig. 9 shows a comparison of bare Ni porous, CeO₂-1 and CeO₂-2 Nyquist

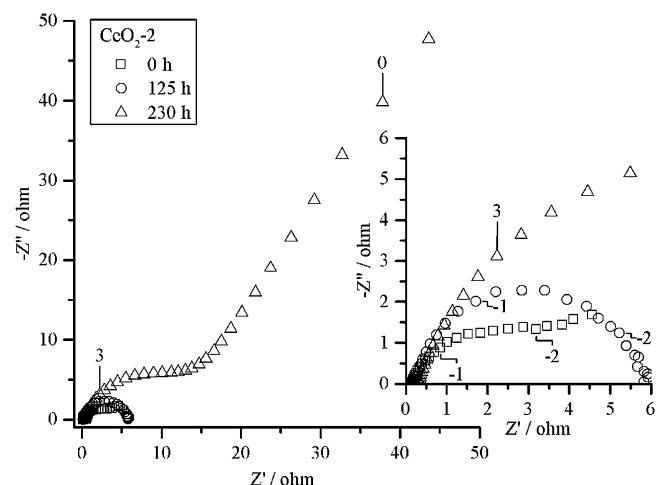


Fig. 8. Nyquist diagram of CeO₂-2 impedance recorded at 0, 125 and 230 h of immersion in Li₂CO₃-K₂CO₃ (62–38 mol %) at 650 °C.

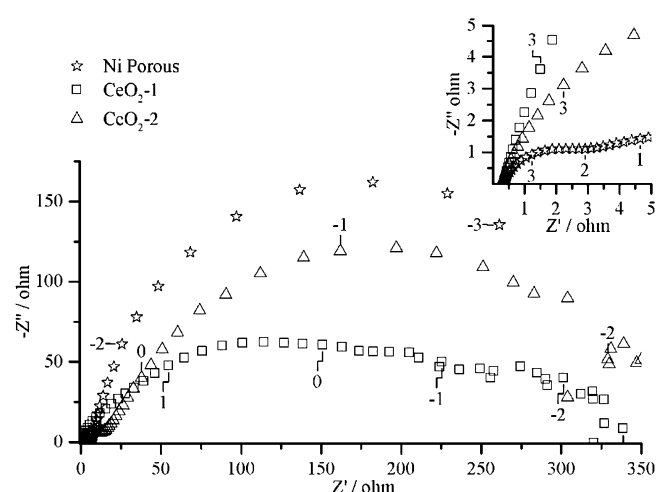


Fig. 9. Nyquist diagram comparing bare Ni, CeO₂-1 and CeO₂-2 impedance recorded 230 h of immersion in Li₂CO₃-K₂CO₃ (62–38 mol %) at 650 °C.

diagrams at 230 h of immersion in the carbonate melt. It appears that the coated samples have a lower resistance than bare porous Ni and, in particular, for CeO₂-1 sample. Resistance data over time were calculated by fitting the electrical circuit shown in Fig. 10 to the Nyquist plots (an example is given on CeO₂-2 sample), where R1 represents the electrolyte resistance, R2 the charge transfer resistance and R3 the mass transfer resistance. The sum of R1, R2 and R3

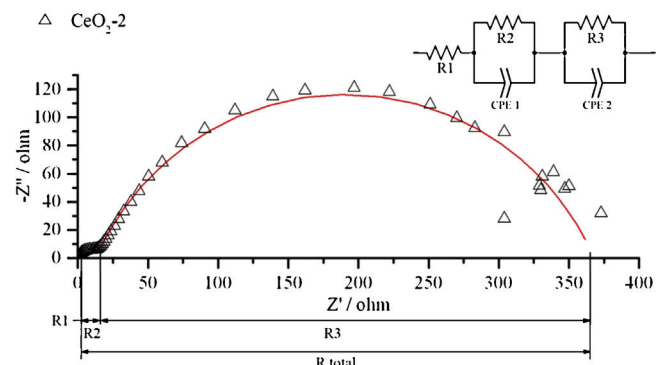


Fig. 10. Equivalent circuit used to fit EIS data obtained and fitting example, experimental data (Δ), fitted data (line).

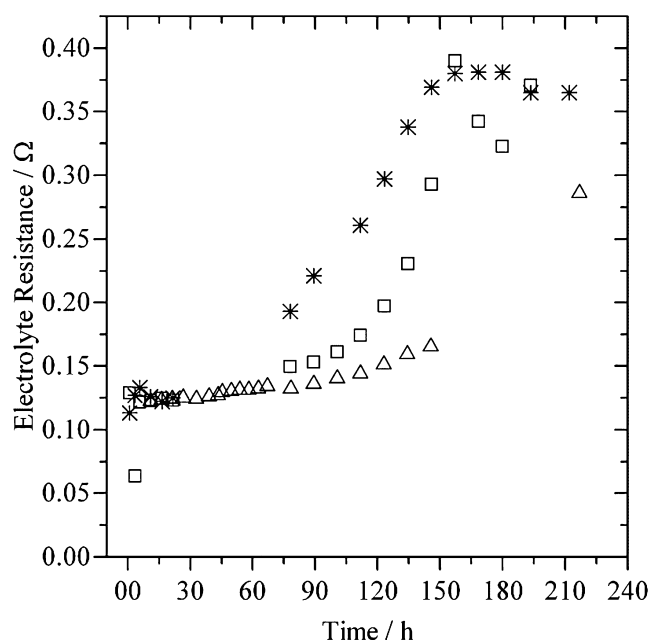


Fig. 11. Electrolyte resistance evolution over 230 h of immersion in $\text{Li}_2\text{CO}_3\text{-K}_2\text{CO}_3$ (62-38 mol %) at 650 °C, (*) Ni, (□) $\text{CeO}_2\text{-1}$, (Δ) $\text{CeO}_2\text{-2}$.

represents the total resistance of the system, which is roughly close to the value of R_2 , the major component. The electrolyte resistance evolution over the immersion time is shown in Fig. 11; considering that the electrolyte resistance should roughly remain constant, its evolution estimated through EIS measurements corresponds to the electroactive area of the electrode dependent on the oxidation/lithiation process. As it can be observed, the $\text{CeO}_2\text{-1}$ (□) sample exhibits almost the same behavior as porous Ni (*) over 230 h of immersion time. Even though there is a delay of about 50 h for the $\text{CeO}_2\text{-1}$ resistance to start rising, the final electrolyte resistance is practically the same, showing that the 27 nm covered sample suffers a surface modification process very close to that of Ni, which indicates that CeO_2 thin coating of 27 nm does not affect the Ni oxidation and lithiation processes. For the $\text{CeO}_2\text{-2}$ (Δ) sample of 127 nm the behavior shows a delay in the resistance rising of 80 h with respect to porous Ni and a final electrolyte resistance lower than porous Ni and $\text{CeO}_2\text{-1}$, showing that after 230 h immersion a thicker layer of ceria delays the Ni oxidation, lithiation and surface modification.

The total resistance evolution over the time is shown in Fig. 12. For the CeO_2 coated cathodes, the resistance over the first 150 h is about two orders of magnitude lower than that of porous Ni. After 150 h, $\text{CeO}_2\text{-coated}$ samples resistance starts increasing rapidly. $\text{CeO}_2\text{-1}$ (□) reaches stability after 180 h at $320 \pm 3 \Omega$, a lower resistance than porous Ni (*) 350 Ω. For $\text{CeO}_2\text{-2}$ (Δ), total resistance at 217 h is 375 Ω, as high as porous Ni which suggests that CeO_2 coatings either decrease total cathode resistance or at least do not affect it negatively, which makes them suitable for MCFC applications.

3.4. Solubility of Ni on molten carbonates after 230 h immersion.

Ni solubility measurements are gathered in Table 1, in our conditions the solubility of bare porous nickel is slightly lower than the values found in the literature [36,37], which is most probably due to the gaseous atmosphere used, with less CO_2/O_2 ratio in our case. The effect of the coating layer is clear: whatever the thickness of the coating, the solubility decreases. However, the thicker coating of 127 nm is more effective, reaching 50% less with respect to the

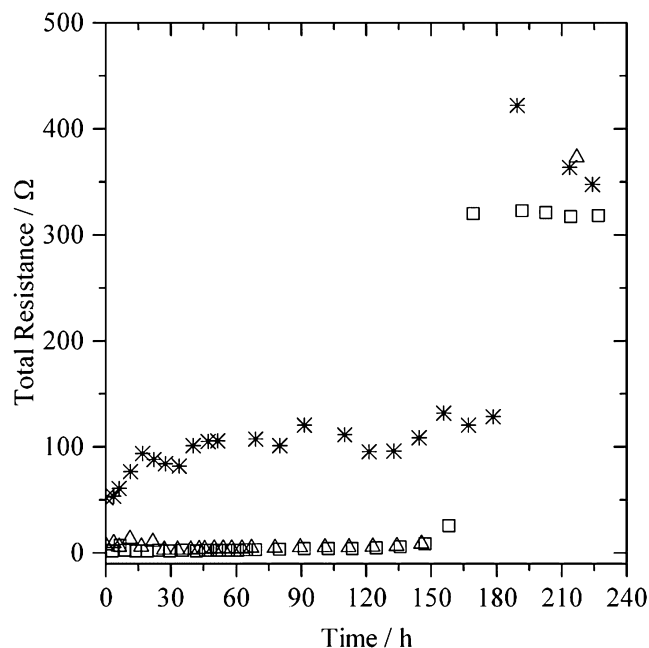


Fig. 12. Total resistance evolution over 230 h of immersion in $\text{Li}_2\text{CO}_3\text{-K}_2\text{CO}_3$ (62-38 mol %) at 650 °C, (*) Ni, (□) $\text{CeO}_2\text{-1}$, (Δ) $\text{CeO}_2\text{-2}$.

Table 1

Solubility of Ni of CeO_2 covered cathodes compared to bare Ni.

Sample	Solubility (wt ppm)
Porous Ni	15
$\text{CeO}_2\text{-1A}$	10
$\text{CeO}_2\text{-2A}$	8

bare nickel. The higher solubility value for the 27 nm-thick sample is likely to be due to a partial protection of the Ni substrate with NiO more exposed to the carbonate melt. The value of cerium solubility is extremely low (< 1 wt. ppm), which is in accordance with the literature [9] and supports the idea of using CeO_2 as a protective coating.

4. Conclusions

This paper confirms the promising features of cerium-based materials by the use of a high-quality deposition technique such as ALD, which scalability is already proven in electronic or electroluminescence industries. We succeeded in processing CeO_2 by ALD in form of coatings of different thicknesses for the effective protection of the MCFC cathode. These coatings are spontaneously transformed when immersed during 230 h in molten $\text{Li}_2\text{CO}_3\text{-K}_2\text{CO}_3$ into a complex but stable interface, containing lithiated CeO_2 , $\text{Li}_x\text{Ni}_{1-x}\text{O}$ and, probably in a minor ratio, $\text{Li}_x\text{Ni}_y\text{O}_2$. The *in situ* electrochemical behavior is affected by these coatings because of the complexity of the oxidation/lithiation processes added to the interdiffusion of elements between the substrate and the protective layer. OCP time-evolution showed similar tendencies with or without coatings in the first 100 h. However, it was found that reaching a stable $\text{CeO}_2\text{-coated}$ cathode for oxygen reduction is a slower process than that with a bare porous nickel. This evolution combining a lithiation/interdiffusion process is likely to produce a stable mixed NiO-based cathode with good electrochemical performance comparable to the state-of-the-art cathode which indicates clearly that the presence of CeO_2 does not affect significantly the OCP evolution. The electrolyte and total resistance evolution vs. time showed

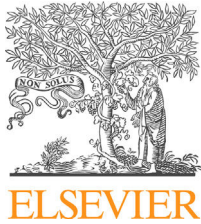
clearly that CeO₂-coated materials are comparable to the state of the art cathode, showing a good conductivity after the 230 h immersion. An important aspect is the protective effectiveness of CeO₂ coatings that reduced the solubility in about 50% with respect to that of bare NiO without affecting electrochemical performance. All these results show the feasibility of such high-quality coatings enriched progressively by nickel diffusion to form a stable compound to be integrated in MCFC devices.

Acknowledgments

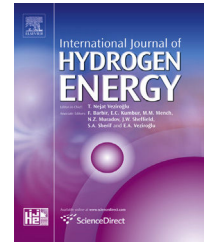
This work was supported by the French program PLANEX ANR-11-EQPX-0-01 and benefited of a Mexican CONACYT Ph.D. scholarship 314518.

References

- [1] M. Bischoff, Molten carbonate fuel cells: A high temperature fuel cell on the edge of commercialization, *J. Power Sources* 160 (2006) 842–845.
- [2] M. Yazici, J. Selman, Dissolution of partially immersed nickel during in situ oxidation in molten carbonate: cyclic, stripping and square wave voltammetry measurements, *J. Electroanal. Chem.* 457 (1998) 89–97.
- [3] M.L. Orfield, D.A. Shores, Solubility of NiO in Molten Li₂CO₃, Na₂CO₃, K₂CO₃ and Rb₂CO₃ at 910, (C.J. Electrochem. Soc. 135 (1988) 1662–1668.
- [4] E. Antolini, The stability of molten carbonate fuel cell electrodes: A review of recent improvements, *Appl. Energy* 88 (2011) 4274–4293.
- [5] A. Kulkarni, S. Giddey, Materials issues and recent developments in molten carbonate fuel cells, *J. Solid State Electrochem.* 16 (2012) 3123–3146.
- [6] L. Mendoza, V. Albin, M. Cassir, A. Galtayries, Electrochemical deposition of Co₃O₄ thin layers in order to protect the nickel-based molten carbonate fuel cell cathode, *J. Electroanal. Chem.* 548 (2003) 95–107.
- [7] V. Albin, L. Mendoza, A. Gourba, A. Ringuedé, A. Billard, P. Briois, M. Cassir, Morphological, structural and electrochemical analysis of sputter-deposited ceria and titania coatings for MCFC application, *J. Power Sources* 160 (2006) 821–826.
- [8] C. Belhomme, E. Gourba, M. Cassir, C. Tessier, Chemical and electrochemical behaviour of Ni–Ti in the cathodic conditions used in molten carbonate fuel cells, *J. Electroanal. Chem.* 503 (2001) 69–77.
- [9] V. Chauvaut, V. Albin, H. Shneider, M. Cassir, H. Ardelean, A. Galtayries, Study of cerium species in molten Li₂CO₃–Na₂CO₃ in the conditions used in molten carbonate fuel cells- I- Thermodynamic, chemical and surface properties, *J. Appl. Electrochem* 30 (2000) 1405–1413.
- [10] M. Cassir, V. Chauvaut, A. Alfarra, V. Albin, Study of cerium species in molten Li₂CO₃–Na₂CO₃ in the conditions used in molten carbonate fuel cells- II- Potentiometric and voltammetric behaviour, *J. Appl. Electrochem* 30 (2000) 1415–1420.
- [11] T. Suntola, J. Antson, Method for producing compound thin films, US Patent 4,058,430, 1977.
- [12] M. Cassir, A. Ringuedé, L. Niinistö, Input of atomic layer deposition for solid oxide fuel cell applications, *J. Mater. Chem.* 20 (2010) 8987–8993.
- [13] E. Ballée, A. Ringuedé, M. Cassir, M. Putkonen, L. Niinistö, Synthesis of a thin-layered ionic conductor, CeO₂–Y₂O₃, by atomic layer deposition in view of solid oxide fuel cell applications, *Chem. Mater.* 21 (2009) 4614–4619.
- [14] A. Meléndez-Ceballos, S.M. Fernández-Valverde, C. Barrera-Díaz, V. Albin, V. Lair, A. Ringuedé, M. Cassir, TiO₂ protective coating processed by Atomic Layer Deposition for the improvement of MCFC cathode, *Int. J. Hydrogen Energy* 38 (2013) 13443–13452.
- [15] J. Päiväsääri, J. Niinistö, P. Myllymäki, C. Dezelah IV, C.H. Winter, M. Matti Putkonen, L. Nieminen, Niinistö, Atomic Layer Deposition of Rare Earth Oxides, *Topics Appl. Physics.* 106 (2007) 15–32.
- [16] K. Kamada, N. Enomoto, J. Hojo, Optimization of electrochemical synthesis conditions for dense and doped ceria thin films, *Electrochim. Acta* 54 (2009) 6996–7000.
- [17] V. Lair, L.S. Živković, O. Lupan, A. Ringuedé, Synthesis and characterization of electrodeposited samaria and samaria-doped ceria thin films, *Electrochim. Acta* 56 (2011) 4638–4644.
- [18] L.S. Živković, V. Lair, O. Lupan, M. Cassir, A. Ringuedé, Electrochemical synthesis and characterization of nanorods, nanocolumnar ceria-based thin films on different glass substrates, *Chemical Physics Letters* 494 (2010) 237–242.
- [19] J. Y. Youn, B. H. Ryu, J. Y. Yoo, M. Y. Shin, H., Moon, Woon Y. Choi, T. W. Lee, I. G. Chang, K. H. Moon, Manufacturing method of porous metal electrode for molten carbonate fuel cells using dry process, Patent WO2009084893A3.
- [20] E. Gourba, A. Ringuedé, M. Cassir, A. Billard, J. Päiväsääri, J. Niinistö, M. Putkonen, L. Niinistö, Characterisation of Thin Films of Ceria-Based Electrolytes for Intermediate Temperature – Solid Oxide Fuel Cells (IT-SOFC), *Ionics* 9 (2002) 15–20.
- [21] Z. Fan, J. An, A. Iancu, F.B. Prinz, Thickness effects of yttria-doped ceria interlayers on solid oxide fuel cells, *J. Power Sources* 218 (2012) 187–191.
- [22] B. Malinowska, M. Cassir, F. Delcorso, J. Devynck, Thermodynamic and electrochemical behavior of nickel in molten Li₂CO₃–Na₂CO₃ modified by addition of calcium carbonate, *J. Electroanal. Chem.* 389 (1995) 21–29.
- [23] J.P. Ying Tan, H. Ru Tan, C. Boothroyd, Y. Lim Foo, C. Bin He, M. Lin, Three-Dimensional Structure of CeO₂ Nanocrystals, *J. Phys. Chem. C* 115 (9) (2011) 3544–4355.
- [24] C. Belhomme, M. Cassir, C. Tessier, E. Berthoumieux, Lithium depth profile in NiO molten carbonate fuel cell cathode by nuclear microprobe, *Electrochem. & Solid-State Lett.* 3 (2000) 216–219.
- [25] J. López-Iturbe, M.A. Camacho-López, L. Escobar-Alarcón, E. Camps, Synthesis and characterization of LiNiO₂ targets for thin film deposition by pulsed laser ablation, *Superficies y Vacío* 18 (4) (2005) 27–30.
- [26] N. Mironova-Ulmane, A. Kuzmin, J. Grabis, I. Sildos, V.I. Voronin, I.F. Berger, V.A. Kazantsev, Structural and Magnetic Properties of Nickel Oxide Nanopowders, *Solid State Phenomena* 168–169 (2011) 341–344.
- [27] C.M. Julien, M. Massot, Vibrational spectroscopy of electrode materials for rechargeable lithium batteries, III. Oxide frameworks, *Proc. Int. workshop on advanced techniques for energy sources, investigation and testing*, 1. 3 (2004) 1–17.
- [28] R. Kirste, Y. Aksu, M.R. Wagner, S. Khachadorian, S. Jana, M. Driess, C. Thomssen, A. Hoffmann, Raman and photoluminescence spectroscopic detection of surface-bound Li + O²⁻ defect sites in Li-doped ZnO nanocrystals derived from molecular precursors, *Chem. Phys. Chem.* 12 (2011) 1189–1195.
- [29] A.E. Huges, R.J. Taylor, B.R.W. Braun, L. Wilson, XPS and SEM characterization of hydrated cerium oxides conversion coatings, *Surf. And Interface Analysis.* 23 (1995) 540–550.
- [30] R. Radutoiu, C.M. Teodorescu, Satellites in Ce 3d X-Ray Photoelectron spectroscopy of ceria, *Digest J. of Nanomaterials and Biostructures.* 8 (2013) 1535–1549.
- [31] K.S. Kim, R.E. Davis, Electron Spectroscopy of the nickel-Oxygen System *J. Electron Spectrosc. Relat. Phenom.* 1(1972/73)251–278.
- [32] E. Antolini, Behaviour of Ni, NiO and Li_xNi_{1-x}O in molten alkali carbonates, *J. Mat. Sci.* 35 (2000) 1501–1505.
- [33] T. Nishina, K. Takizawa, I. Uchida, Electrochemical characterization of in situ NiO formation in a molten carbonate, *J. Electroanal. Chem.* 263 (1989) 87–96.
- [34] N.Q. Minh, Technological status of nickel oxide cathodes in molten carbonate fuel cells – A review, *J. Power Sources* 24 (1988) 1–19.
- [35] P.M. Oliver, S.C. Parker, W.C. Wackrodt, Modelling Computer simulation of the crystal morphology of NiO, *Modell. Simul. Mater. Sci. Eng.* 1 (1993) 755–760.
- [36] M. Cassir, C. Belhomme, Technological applications of molten salts: the case of the molten carbonate fuel cell, *Plasma & Ions* 1 (1999) 3–15.
- [37] S. Scaccia, Investigation on NiO solubility in binary and ternary molten alkali metal carbonates containing additives, *J. Mol. Liquids* 116 (2005) 67–71.

Available online at www.sciencedirect.com

ScienceDirect

journal homepage: www.elsevier.com/locate/he

Electrochemical behavior of $M_{x-1}O_x$ ($M = \text{Ti, Ce and Co}$) ultra-thin protective layers for MCFC cathode

A. Meléndez-Ceballos^{a,b}, V. Albin^a, A. Ringuedé^a,
S.M. Fernández-Valverde^{b,*}, M. Cassir^a

^a Institut de Recherche de Chimie Paris, CNRS – Chimie ParisTech, 11 rue Pierre et Marie Curie, F-75005 Paris, France

^b Depto. de Química, Instituto Nacional de Investigaciones Nucleares, A.P. 18-1027, México D.F. C.P.11801, Mexico

ARTICLE INFO

Article history:

Received 10 February 2014

Received in revised form

26 March 2014

Accepted 27 March 2014

Available online 24 April 2014

Keywords:

MCFC

Titanium oxide

Cerium oxide

Cobalt oxide

ALD

Electrochemistry

ABSTRACT

In the world of alternative energy sources, the Molten Carbonate Fuel Cell (MCFC) is one of the promising technologies for the efficient conversion of hydrogen or hydrocarbons to power and heat. One of the main issues for optimizing this device is the control of the dissolution of the state-of-the-art porous nickel oxide cathode. A protective coating by more stable metal oxides seems to be one of the best solutions. In this paper, ultra-thin layers of TiO_2 (50 nm), Co_3O_4 (50 nm) and CeO_2 (20 nm) were deposited on porous nickel substrates, by a sequential CVD technique, known as Atomic Layer Deposition (ALD), producing high quality, homogeneous and conformal layers. The electrochemical behavior and morphological features of the three coated samples were compared in a Li_2CO_3 – K_2CO_3 (62–38 mol%) eutectic melt under a standard cathode atmosphere (CO_2/air 30:70 vol%) for 230 h. Finally, the respective advantages and drawbacks of Co_3O_4 , TiO_2 and CeO_2 coatings are pointed out.

Copyright © 2014, Hydrogen Energy Publications, LLC. Published by Elsevier Ltd. All rights reserved.

Introduction

The Molten Carbonate Fuel Cell (MCFC) is a promising technology for high efficiency and sustainable energy generation when powered by environmentally friendly fuels such as biogas obtained from organic waste or hydrogen obtained from renewable energy sources. One of the main problems concerning this fuel cell is its cathode dissolution in the carbonate melt. The most common material used as cathode is nickel, which undergoes *in situ* oxidation and lithiation into the carbonate melt. Afterwards, nickel oxide starts dissolving and then may precipitate as metallic nickel at the anode side in presence of H_2 causing short-circuit between both

electrodes and inducing MCFC stack failure. To solve this problem, several approaches have been undertaken and can be divided in two groups: (i) modification of the cathode material; (ii) modification of the electrolyte composition. The current research effort takes into account the first approach and, more specifically, the modification of the standard porous nickel cathode by depositing an ultra-thin layer of a metal oxide that would at the same time protect the cathode and maintain or even improve its electrochemical performance.

Several deposition techniques have been used to process thin metal oxide layers onto porous nickel substrate for MCFC application, Pechini method [1], sol–gel [2,3], tape casting [2,4], electroless deposition [5], electrochemical deposition [6–13]

* Corresponding author.

E-mail addresses: suilma.fernandez@inin.gob.mx, suilma.fernandez@gmail.com (S.M. Fernández-Valverde).
<http://dx.doi.org/10.1016/j.ijhydene.2014.03.213>

0360-3199/Copyright © 2014, Hydrogen Energy Publications, LLC. Published by Elsevier Ltd. All rights reserved.

and sputtering [14]. Among the deposited species, titanium, cerium and cobalt oxides have shown good performance, reducing the solubility of nickel and maintaining acceptable electrochemical characteristics. Nevertheless, all the deposition techniques previously mentioned have some drawbacks concerning homogeneity, thickness, adherence to the substrate or deposition complexity. Atomic layer deposition (ALD) is a chemical gas phase deposition technique developed in Finland in the 1970s by T. Suntola [15]. In ALD, reactant gas pulses are separately introduced to reach the substrates to be coated. Growth is achieved through self-terminating surface reactions. Self-terminating means that only one monolayer of reactant gas species can be adsorbed to the surface during a pulse. The pulses containing reactant gases are separated by purging pulses where the ALD reactor is flushed with an inert gas. The purging pulses ensure that the reactant gas pulses do not mix. Mixing of the reactant gas pulses would lead to continuous growth and the accurate thickness control of the deposition process would be lost. By-products like detached ligands and excess reactants are also flushed away by the purging pulses. A complete set of reactant gas pulses and purging pulses needed to deposit a certain compound are referred to as a cycle. If the deposition parameters have been chosen properly, the number of cycles rather than the concentration of the reactant species determines the film thickness [16]. ALD has been previously employed to deposit TiO₂ onto porous Ni substrate used as cathode in MCFC [17], the study revealed a good protective effect of TiO₂ layer in terms of Ni solubility that has been reduced to half with respect to pure Ni cathode. CeO₂ and CeO₂-based compounds have also been processed by ALD and studied as MCFC cathode protection or Solid Oxide Fuel Cell (SOFC) electrolyte [18,19], showing also promising results. In this paper, a thorough comparison of ALD-deposited TiO₂, CeO₂ and Co₃O₄ protective layers and their electrochemical performance as MCFC cathodes are presented.

Experimental

Layer deposition using ALD

A known deposition route was followed using halide-free and non-corrosive precursors. Thin layers of TiO₂, CeO₂ or Co₃O₄ were deposited on a commercial porous nickel substrate (produced by Doosan, South-Korea) by means of ALD technique using a vertical flow type reactor (Picosun SUNALE™ R-series). Titanium isopropoxide [Ti(OCH(CH₃)₂)₄], Ce(TMHD)₄ [tetrakis(2,2,6,6-tetramethyl-3,5 heptanedionato)cerium(IV)] or Co(TMHD)₃ [tris(2,2,6,6-tetramethyl-3,5-heptanedionato)cobalt(III)] were used as precursors while distilled water or O₃

were used as oxidizing agents. In order to prepare the thin layers [17–22], precursor and oxidant on each case were introduced into the reactor chamber using the parameters given in Table 1.

Electrolyte and cell

The high-temperature electrochemical cell was a single-compartment crucible of dimensions 70 × 50 mm² contained in an alumina Al₂O₃ reactor of dimensions 250 × 60 mm², hermetically sealed by a stainless steel cover with a Viton O-ring. The whole electrochemical set-up was fully described in a previous paper [23]. Temperature controlled by means of a calibrated chromel/alumel thermocouple was maintained constant at 650 °C. The electrolyte was a mixture of lithium and potassium carbonates of high grade purity >98% (Sigma–Aldrich®), in a proportion of 62:38 mol%. The standard cathode atmosphere was a mixture of Air/CO₂ (70:30 mol%) of high grades purity (Air Liquide®) at 650 °C and a pressure of 1 atm. A carbonate melt was prepared and stabilized 24 h at 650 °C for each TiO₂, CeO₂ and Co₃O₄ coated samples. After stabilizing the molten carbonate eutectic under the selected cathode atmosphere, samples were immersed in the melt and electrochemical measurements were performed for 230 h. After electrochemical tests, samples were rinsed with deionized water to remove the carbonates, dried at 100 °C in an oven and kept in small plastic boxes to prevent contamination before further analysis.

Characterization

Characterization of oxide layers deposited on porous Ni by ALD
The as-deposited TiO₂, CeO₂ and Co₃O₄ layers were characterized after the deposition of the oxide layer and after 230 h immersion in carbonate eutectic melt by Scanning Electron Microscopy (SEM) and Energy Dispersion Spectroscopy (EDS). The analyses were performed with a ZEISS® Ultra 55 microscope to evaluate the surface, morphology and to measure layer thicknesses. X-ray diffraction (XRD) was performed in a PANalytical X'pert pro from Anton Paar with Cu–Kα1 radiation (λ = 1.54056 Å). The diffraction pattern was obtained by scanning between 20 and 80° by steps of 0.02 (2 θ°) with a fixed counting time of 2.3 s and sample rotation of 3 rpm.

Electrochemical characterization

To determine the electrochemical performance of the coated samples, a three-electrode system was used, the working electrode being the as-deposited TiO₂, CeO₂ and Co₃O₄ on porous nickel substrates of dimensions 10 × 10 × 0.5 mm, the counter electrode was a gold wire and the reference electrode a silver wire dipped into an Ag₂SO₄ (10⁻¹ mol kg⁻¹) saturated

Table 1 – Deposition parameters of ALD-processed coatings.

Deposited Material	Precursor	Temperature (°C)	Pulse time (s)	Purge time (s)	Oxidant	Pulse time (s)	Purge time (s)	Chamber T (°C)
TiO ₂	Ti(OCH(CH ₃) ₂) ₄	60	0.5	2	H ₂ O	0.5	2	250
CeO ₂	Ce(TMHD) ₄	180	3	2.5	O ₃	4	2.5	300
Co ₃ O ₄	Co(TMHD) ₃	160	1.5	3	O ₃	1.5	6	240

Li–K carbonate eutectic in an alumina tube sealed by a porous alumina membrane. Electrochemical experimental data were collected using a potentiostat/galvanostat (AutoLab® PGSTAT-302N). Open Circuit Potential (OCP) was collected (at $I = 0$ for TiO_2 , Co_3O_4 and CeO_2 coated samples) continuously from 0 to 230 h of immersion. OCP measurements were interrupted periodically to perform Electrochemical Impedance Spectroscopy (EIS). EIS parameters were: scanning frequencies set from 0.001 to 10^6 Hz, with 11 points per decade and signal amplitude of 5 mV respecting the system linearity. After each EIS test, OCP measurements were restarted. This procedure was performed for 230 h with EIS performed at regular intervals.

Solubility measurements

Nickel solubility was measured individually using three independent Li_2CO_3 – K_2CO_3 melts. Small amounts of carbonates (about 6 g) were withdrawn randomly three times from the molten carbonate bulk at the end of the electrochemical characterizations, which corresponds to 230 h. After solidification, each sample was hand-milled and 2 g of carbonate powder were dissolved in 10 ml of HNO_3 3 vol%. Nickel content was determined by ICP-AES (ICAP 6000 Series from Thermo Fisher Scientific). The calibration was performed for each separate element using Aldrich atomic absorption standard solutions, dissolved in HNO_3 3 vol%.

Results and discussion

This part includes new data on Co_3O_4 -coated Ni cathode compared to new results and a compilation of our own

published data on TiO_2 - and CeO_2 -coated Ni and the general literature.

Morphological, structural and solubility data

Figs. 1 and 2 show, respectively, the morphology of the as-deposited oxide coatings onto the porous Ni substrate before and after their immersion in molten Li_2CO_3 – K_2CO_3 (62–38 mol %) eutectic at 650 °C during 230 h. As shown in Fig. 1(a, d, g) and (b, e, h), the as-deposited layers are homogenous and conformal. The thickness of each layer was determined by SEM cross-section measurements, as shown in Fig. 1(c, f, i), resulting in 50 ± 3 nm, 27 ± 3 nm and 50 ± 3 nm for TiO_2 , CeO_2 and Co_3O_4 , respectively. Thicknesses are not completely uniform due to flow variations through cavities on the porous samples. The presence of TiO_2 (anathase), CeO_2 and Co_3O_4 phases have already been detected by XRD [11,17,18].

After testing the samples in the carbonate melt, as can be seen in Fig. 2(a, c, e), there is an evident change in porosity after 230 h of immersion in the carbonate eutectic for all the samples. CeO_2 and Co_3O_4 -coated samples, depicted in Fig. 2(c, d) and (e, f), respectively, present the most notable change in grain size, morphology and distribution. In contrast, TiO_2 sample Fig. 2(a, b) does not change dramatically in terms of porosity and morphology with respect to the as-deposited sample. EDS analysis (not shown in this paper) of the TiO_2 sample showed a surface mainly composed by Ni, Ti and O likely to form a Li–Ti–Ni–O phase as determined by XRD in previous studies [25,26]. These results were confirmed by XPS [17]. Table 2 summarizes the phases found after interaction at high temperature of the

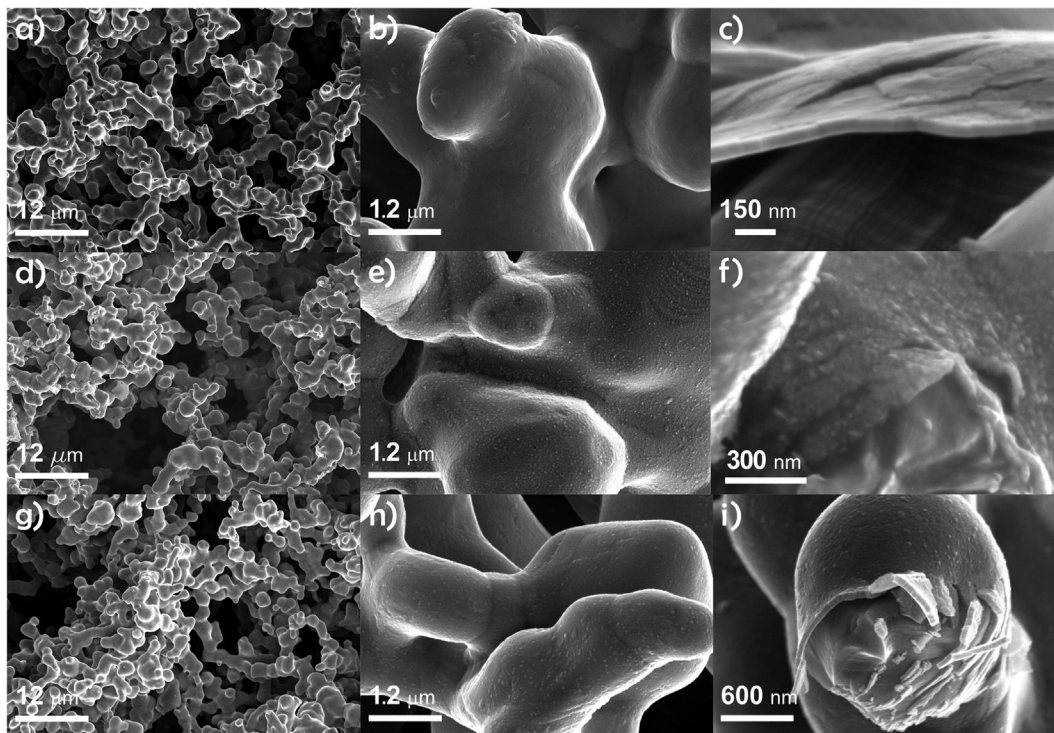


Fig. 1 – Porous Ni cathode covered by ALD, as deposited (a, d, g), zoom (b, e, h) and cross sections (c, f, i), samples before immersion in molten Li_2CO_3 – K_2CO_3 (62–38 mol%) at 650 °C during 230 h. Metal oxides ALD-processed: TiO_2 (a, b, c), CeO_2 (d, e, f) and Co_3O_4 (g, h, i).

coated-Ni substrate with the melt. In the case of the TiO_2 coating, the cathode surface is mainly composed by Li_2TiO_3 and mixed Li-Ni-Ti-O solid solutions; thus the presence of titanium species reduces the availability of Ni at the cathode surface, slowing down oxidation and lithiation processes. This interaction between the coating and its substrate is probably limiting the particles growth.

Contrarily, CeO_2 -coated cathode shows a more notorious particle growth than the TiO_2 sample due to the lack of interaction between CeO_2 and $\text{Li}_x\text{Ni}_{1-x}\text{O}$ that does not form a mixed NiO-CeO_2 phase [18]. After immersion in the carbonate melt, the coating evolves from cubic crystals of CeO_2 into much thicker particles, as seen in Fig. 2d. As summarized in Table 2, CeO_2 and $\text{Li}_x\text{Ni}_{1-x}\text{O}$ can be found at the surface of the coated sample. Thus, CeO_2 particles are separated from the lithiated nickel oxide particles, as has been reported before by Cassir et al. [26,27]. Round particles seem to be regularly truncated octahedral of CeO_2 , as reported recently by Ying Tan et al. [28] during hydrothermal synthesis of this compound; the other cerium particles have a hexagonal structure.

A radical decrease in Ni oxidation and lithiation rates can be observed in the case of Co_3O_4 coatings, even more radically than in the case of CeO_2 layers. This can be evidenced in Fig. 3

where a comparison of XRD patterns of the three coatings after immersion in the carbonate melt, focused on the detection of Ni species, shows a notable presence of Ni only in the case of the cobalt oxide coating. This means that the protective layer partially prevents Ni from oxidation. Shifts in NiO diffraction peaks correspond to the formation of $\text{Li}_x\text{Ni}_{1-x}\text{O}$ and, in the case of titanium, to a mixed Li-Ti-Ni-O compounds resulting in a larger shift. A compilation of the formed compounds is reported in Table 2.

Solubility measurements of Ni for each oxide-coated sample are presented in Table 3. A significant reduction in Ni solubility is achieved with the TiO_2 -coated sample with respect to the CeO_2 and Co_3O_4 samples, which is in good agreement with the literature. Nevertheless, Co_3O_4 coating showed a higher Ni solubility than expected, which is probably due to the thin layer used here to protect the Ni substrate compared to Co_3O_4 -coated Ni powder mentioned in the literature [1]. It should be reminded that, for all the described samples, our solubility data concern ultrathin protective layers and not fully coated Ni particles, hence the metal oxide content in mol% of coated powders is not directly comparable. Nevertheless, it serves as a good starting point for comparison in terms of the amount of dissolved Ni found in the carbonate melt after the tests.

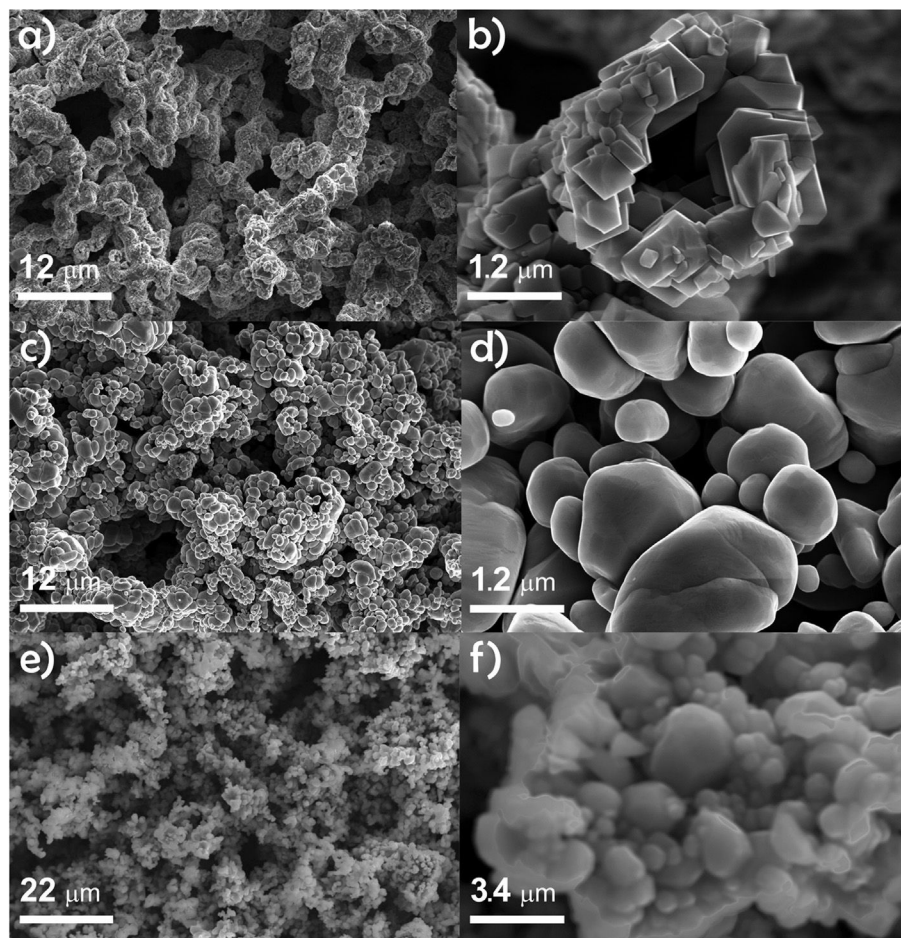


Fig. 2 – Porous Ni covered by ALD, as-deposited after 230 h immersion in molten $\text{Li}_2\text{CO}_3\text{-K}_2\text{CO}_3$ (62–38 mol%) at 650 °C, general view (a, c, e) and morphology detail (b, d, f). Metal oxides ALD-processed: TiO_2 (a, b), CeO_2 (c, d) and Co_3O_4 (e, f).

Table 2 – Possible titanium, cerium and cobalt phases, after immersion in $\text{Li}_2\text{CO}_3\text{--K}_2\text{CO}_3$ (62–38 mol%) during 230 h at 650 °C. Data extracted from the literature, including our own XRD and XPS tests.

Material	Molten carbonate composition	Possible phases	Analysis techniques used	References
TiO_2	$\text{Li}_2\text{CO}_3\text{--K}_2\text{CO}_3$ (62:38 mol%) $\text{Li}_2\text{CO}_3\text{--Na}_2\text{CO}_3$ (52:48 mol%)	Li_2TiO_3	XRD, EDS, XPS	[14,17,24,25]
		$\text{Li}_x\text{Ti}_y\text{NiO}_{1.6}$: $x \leq 0.5$, $y \leq 0.14$		
		$\text{Li}_x\text{Ti}_y\text{NiO}_2$: $x \leq 0.5$, $y \leq 0.11$		
		$\text{Li}_x\text{Ti}_y\text{NiO}_{3.6}$: $x \leq 0.5$, $y \leq 0.4$		
		NiO		
CeO_2		$\text{Li}_x\text{Ni}_{1-x}\text{O}$	XRD, EDS, XPS, RAMAN	[14,18,26,27]
		CeO_2		
		NiO		
		Ni		
Co_3O_4		$\text{Li}_x\text{Ni}_{1-x}\text{O}$	XRD, EDS, XPS, RAMAN	[9,11,12,29,30]
		NiO–CoO solid solution		
		Li–Ni–Co–O		
		LiCoO_2		
		CoO		
		Co_3O_4		

Electrochemical performance

Chronopotentiometry data

Fig. 4 shows the OCP evolution of the bare porous nickel cathode (solid line) all over 230 h of immersion in molten $\text{Li}_2\text{CO}_3\text{--K}_2\text{CO}_3$ (62:38 mol%) at 650 °C and the OCP evolution in the same conditions of TiO_2 (long dash line), CeO_2 (short dash line) and Co_3O_4 (dash-dot line) coated samples, respectively. Porous nickel OCP behavior, investigated previously by different authors, among which Yazici et al. and Antolini [31,32], attributed the plateaus to the *in situ* Ni oxidation followed by the NiO lithiation process on the nickel porous surface. The three plateaus of porous nickel observed in Fig. 4 are related to the modification of the porous Ni electrode into $\text{Li}_x\text{Ni}_{1-x}\text{O}$, in a progressive way. The first plateau (I) from 0 to 98 h is ascribed to the *in situ* oxidation of metallic nickel, after the first potential jump at 98 h, a second plateau (II) is reached at a potential around $-0.4 \text{ V}/(\text{Ag}/\text{Ag}^+)$. This plateau corresponds to the *in situ* lithiation of NiO, which is probably associated to an increase in the nickel valence from Ni(II) to Ni(III), as reported by Nishina et al. from XPS measurements

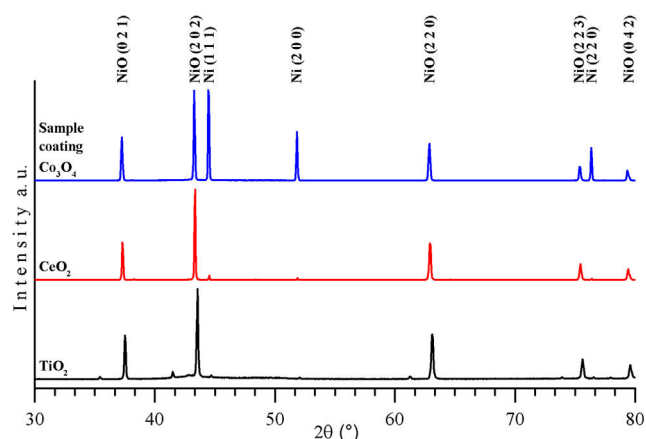


Fig. 3 – Diffractograms of ALD coated samples after 230 h immersion in molten $\text{Li}_2\text{CO}_3\text{--K}_2\text{CO}_3$ (62–38 mol%) at 650 °C.

[33]. At equilibrium, lithium content in NiO cathode was estimated by nuclear microprobe to be roughly 0.2 at% [34]. After 182 h, the lithiation process is completed and the third plateau (III) at $-0.03 \text{ V}/(\text{Ag}/\text{Ag}^+)$ corresponds to an equilibrium potential between O_2 , CO_2 and carbonates. At this stage, the electrode works as a stable cathode for oxygen reduction. In the case of the coated samples, as shown in Fig. 4, the first plateau for TiO_2 , CeO_2 and Co_3O_4 starts at about $-0.60 \text{ V}/(\text{Ag}/\text{Ag}^+)$, $-0.76 \text{ V}/(\text{Ag}/\text{Ag}^+)$ and $-0.83 \text{ V}/(\text{Ag}/\text{Ag}^+)$, respectively. With respect to the bare porous Ni cathode, TiO_2 and CeO_2 -coated Ni behave in a relatively similar way, which is not the case of Co_3O_4 -coated Ni that follows a very slow OCP evolution. The presence of TiO_2 and CeO_2 coatings provokes a time delay for the first potential jump appearing after 155 h and 165 h, respectively, which are about 55 h and 65 h later than for the bare Ni cathode. Afterwards, at the second plateau TiO_2 sample remains at the same OCP value $-0.28 \text{ V}/(\text{Ag}/\text{Ag}^+)$, whilst the second plateau of CeO_2 sample shows an abrupt potential increase from -0.35 to $0.01 \text{ V}/(\text{Ag}/\text{Ag}^+)$ at 212 h reaching the third plateau corresponding to the oxygen reduction potential, just 30 h after the bare porous Ni sample. This behavior indicates that CeO_2 causes a small delay in the whole Ni oxidation and lithiation process. However, it must be noted that the final potential reached with the CeO_2 -coated sample is higher than that with the bare nickel cathode, which

Table 3 – Solubility of Ni in molten $\text{Li}_2\text{CO}_3\text{--K}_2\text{CO}_3$ (62–38 mol%) eutectics for Co_3O_4 , TiO_2 and CeO_2 coated samples, own experimental data [18,19] compared to the literature.

Sample	Ni	TiO_2 -coated	CeO_2 -coated	Co_3O_4 -coated
Experimental data (wt. ppm)	15	8.2	10	12
Literature (wt. ppm)	18.1* [35]	17.8 ^a [35]	15.97 ^{a*} [1]	7.59 ^{a*} [1]
	18.1 [1]	6.8 ^b	9.3 ^{b*}	a: 10 mol%
	17.9* [36]	a: 2.5;	a: 2;	
	16.8* [37]	b: 5 mol%	b: 1 mol%	

* $P_{\text{O}_2}/P_{\text{CO}_2} = 0.33/0.67 \text{ bar/bar}$.

a and b: contents of TiO_2 , CeO_2 and Co_3O_4 in NiO-coated powders.

seems to evidence the good electrocatalytic properties of ceria towards oxygen reduction. OCP of Co_3O_4 reaches a value of $-0.72 \text{ V}/(\text{Ag}/\text{Ag}^+)$ after the 230 h of immersion time which indicates that Ni oxidation and lithiation are being partially impeded by Co_3O_4 . In fact, Co_3O_4 is rapidly transformed into LiCoO_2 and also in small amounts into a mixed Li–Ni–Co–O compound [9,11].

Electrochemical Impedance Spectroscopy data

Electrochemical Impedance Spectroscopy (EIS) was performed for porous Ni and all the coated samples after 230 h of electrode immersion in Li–K carbonate eutectic melt. As can be seen in Figs. 5 and 6, the Nyquist diagrams of porous Ni, TiO_2 , CeO_2 and Co_3O_4 show a different global behavior for each sample. From these impedance data the electrolyte resistance (R_1), charge transfer resistance (R_2) and mass transport resistance (R_3) were obtained by fitting the circuit shown in Fig. 7 to the Nyquist diagrams obtained along 230 h.

The total resistance evolution over the time is shown in Fig. 7. For the CeO_2 -coated cathodes, the resistance over the first 150 h is about two orders of magnitude lower than that of porous Ni. After 150 h, CeO_2 -coated sample resistance starts increasing rapidly and reaches stability after 165 h at 320Ω , a lower resistance than porous Ni (350Ω). The CeO_2 -coated sample final resistance is as high as porous Ni, which suggests that the CeO_2 coatings either decreases the total cathode resistance or at least do not affect it negatively. By contrast, TiO_2 -coated sample is stable until 120 h with a very low resistance, rapidly increases up at 165 h reaching a first plateau (at 450Ω), then increases again from 200 h to 225 h, reaching a second plateau (at 530Ω). The final resistance of TiO_2 -coated sample is the highest. Co_3O_4 sample behaves very differently than bare Ni, CeO_2 and TiO_2 -coated samples with respect to the total resistance behavior over time; while for these samples resistance starts at 50Ω for bare Ni, and 6Ω for CeO_2 and TiO_2 and increases after, Co_3O_4 sample resistance starts around 150Ω and decreases over time to 6Ω after 230 h. This indicates that Co_3O_4 in contact with the molten carbonates produces a very conductive lithiated Co phase: LiCoO_2 .

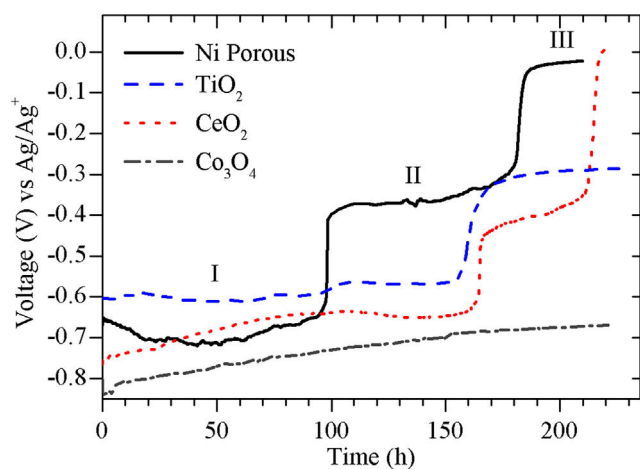


Fig. 4 – OCP evolution over immersion time in molten $\text{Li}_2\text{CO}_3\text{--K}_2\text{CO}_3$ (62–38 mol%) at $650 \text{ }^\circ\text{C}$ during 230 h. a) porous Ni, b) TiO_2 (50 nm), c) CeO_2 (27 nm), d) Co_3O_4 (50 nm).

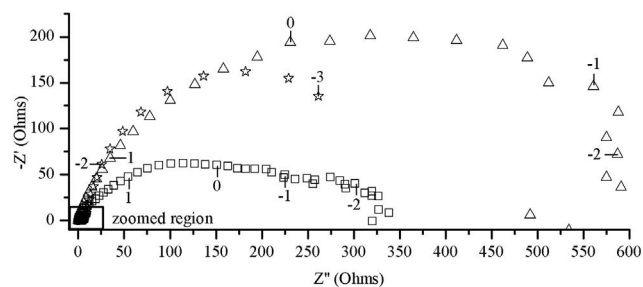


Fig. 5 – Nyquist impedance diagrams after 230 h immersion in Li–K carbonate eutectic melt of: (☆) porous Ni, (Δ) TiO_2 , (○) Co_3O_4 (□) CeO_2 . Frequency logarithms are given.

Co_3O_4 sample final resistance could increase if longer tests are performed due to Ni oxidation and lithiation.

If considering the electrolyte conductivity as constant, electrolyte resistance (R_1) evolution shown in Fig. 8 can be interpreted mainly as the change in electroactive area of the electrode (in contrast with the geometrical area). As can be observed in this figure, the electrolyte resistance for TiO_2 , CeO_2 and Ni samples increases with time, reaching the same stable value after 175 h. This evolution can be attributed to the *in situ* oxidation of Ni causing a structural and morphological change at the interface with the molten carbonates and increasing the electrode surface. It is remarkable that for Co_3O_4 -coated sample, this change does not occur during 230 h, meaning that Co_3O_4 coating decreases dramatically the oxidation rate of Ni as initially suggested by XRD data.

Fig. 9 shows a comparison of the charge transfer resistance (R_2) between bare Ni cathode and the three coated Ni cathodes with TiO_2 , CeO_2 and Co_3O_4 . Up to 120 h, all the samples have a

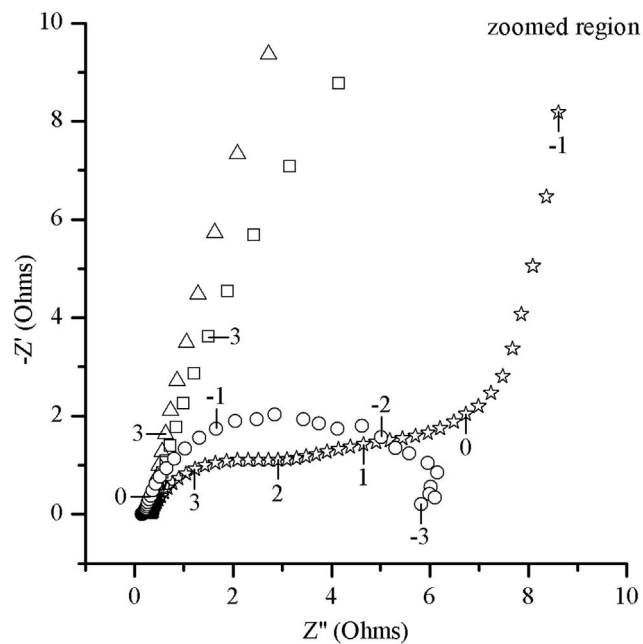


Fig. 6 – Zoomed region of diagram in Fig. 5: (☆) porous Ni, (Δ) TiO_2 , (○) Co_3O_4 , (□) CeO_2 . Frequency logarithms are given.

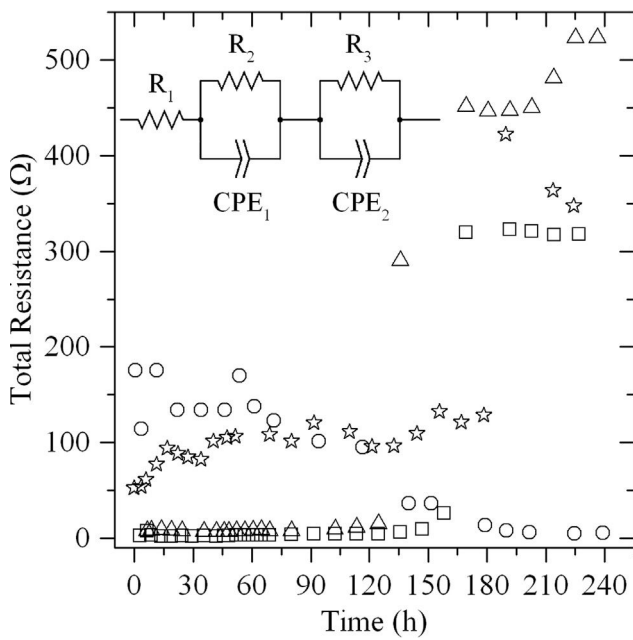


Fig. 7 – Total resistance vs. immersion time in molten $\text{Li}_2\text{CO}_3\text{-K}_2\text{CO}_3$ (62–38 mol%) at 650 °C during 230 h. (☆) porous Ni, (Δ) TiO_2 , (○) Co_3O_4 , (◻) CeO_2 .

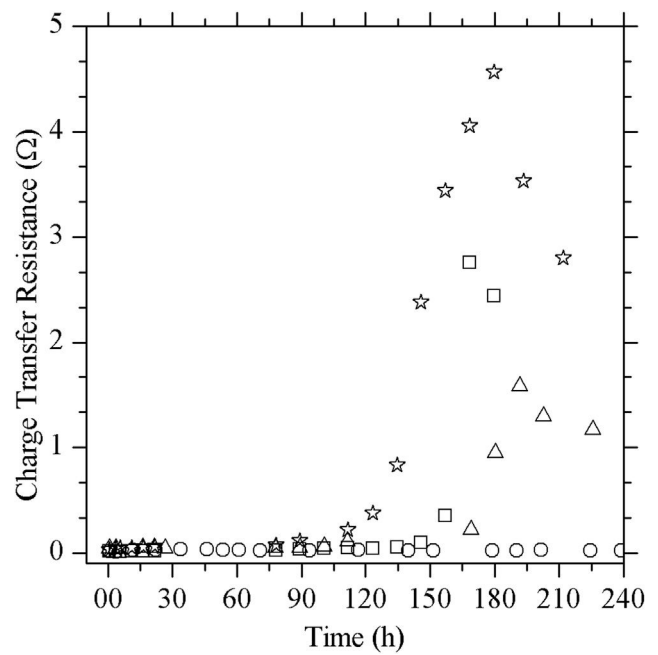


Fig. 9 – Charge transfer resistance vs. immersion time in molten $\text{Li}_2\text{CO}_3\text{-K}_2\text{CO}_3$ (62–38 mol%) at 650 °C during 230 h. (☆) porous Ni, (Δ) TiO_2 , (○) Co_3O_4 , (◻) CeO_2 .

similar behavior with a very low and constant value of R_2 . At 120 h, R_2 of bare Ni increases dramatically until reaching a maximum value of 4.7 Ω at 175 h before rapidly decreasing. The behavior of TiO_2 and CeO_2 -coated samples are relatively close to that of Ni, since R_2 rises at 150 h, reaches a maximum of 1.7 Ω and 2.7 Ω, respectively, and then decreases. It appears that R_2 evolution is strongly correlated to the transformation

process of the coating and the substrate (oxidation, lithiation and interdiffusion). At this level, one may note the beneficial effect of TiO_2 and CeO_2 coatings with a decrease in the charge transfer resistance. Here again, the behavior of Co_3O_4 is very different from the others, with R_2 almost constant at an average value of 0.024 Ω; this indicates clearly that lithiated Co compounds are remarkably conductive and stable in the carbonate melt.

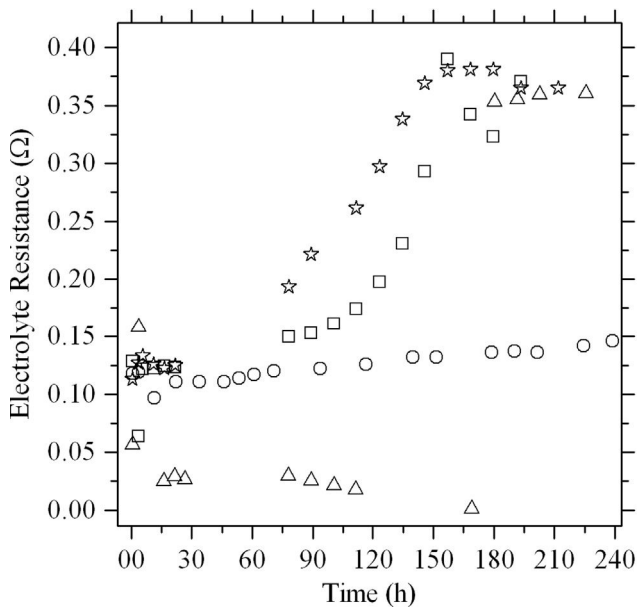


Fig. 8 – Electrolyte resistance vs. immersion time in molten $\text{Li}_2\text{CO}_3\text{-K}_2\text{CO}_3$ (62–38 mol%) at 650 °C during 230 h. (☆) porous Ni, (Δ) TiO_2 , (○) Co_3O_4 , (◻) CeO_2 .

Mass transfer resistance (R_3), has the highest values and its evolution is close to that of the total resistance, as shown in Fig. 10. TiO_2 and CeO_2 samples have a very low initial R_3 , which in the case of TiO_2 begins to increase at 120 h until reaching 600 Ω at 195 h and in the case of CeO_2 the increase begins at 150 h and is relatively moderate. Mass transfer is slower in the case of TiO_2 than for CeO_2 . Ni behavior is higher during the first 150 h, and increases until 190 h before slightly decrease. Co_3O_4 sample is always different, at the beginning it is nearly stable until 70 h before progressively decreasing. We may conclude that mass transfer is clearly favored with the Co coating, slightly favored with Ce coating, contrarily to the Ti coating which shows the highest R_3 .

Conclusions

This paper confirms the promising features of titanium ceria and cobalt-based materials processed by ALD for optimizing the operation of MCFC devices. TiO_2 , Co_3O_4 and CeO_2 coatings of different thicknesses have been processed for the effective protection of the MCFC cathode. When immersed during 230 h in molten $\text{Li}_2\text{CO}_3\text{-K}_2\text{CO}_3$, they are spontaneously transformed into a complex but stable interface. The *in situ* electrochemical

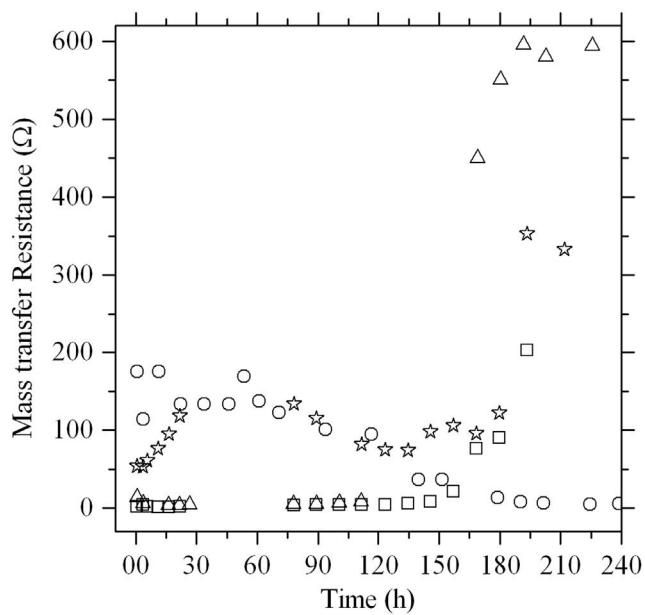


Fig. 10 – Mass transfer resistance vs. immersion time in molten $\text{Li}_2\text{CO}_3\text{--K}_2\text{CO}_3$ (62–38 mol%) at 650 °C during 230 h. (☆) porous Ni, (Δ) TiO_2 , (○) Co_3O_4 , (□) CeO_2 .

behavior is affected by these ultra-thin layers because of the complexity of the oxidation/lithiation processes added to the interdiffusion of elements between the substrate and the protective layer. The morphology of the crystals formed after immersion in molten carbonates was well evidenced by SEM, the porosity of the initial substrate being more or less respected according to the nature of the coating and the evolution of the interface. Similar tendencies have been found in OCP time-evolution for all the samples with or without coatings in the first 100 h. However, it was found that reaching a stable TiO_2 or CeO_2 -coated cathode for oxygen reduction is a slower process than that with a bare porous nickel. This evolution combining a lithiation/interdiffusion process is likely to produce a stable mixed NiO-based cathode with good electrochemical performance, comparable to the state-of-the-art cathode, which indicates that the presence of TiO_2 or CeO_2 does not affect significantly the OCP evolution. The evolution of resistances vs. time also showed that TiO_2 or CeO_2 -coated materials are comparable to the state-of-the-art cathode; however, the OCP evolution towards the oxygen reduction potential occurs with a delay, larger in the case of TiO_2 . Co_3O_4 sample showed the lowest resistances with respect to all the samples but never reached the oxygen reduction potential in 230 h of immersion. As for Ni solubility, TiO_2 coating is slightly better than the others. It is clear that the choice of the coating is a compromise between different properties: Ni solubility, OCP evolution and the different resistance values (electrolyte, charge transfer and mass transfer). In order to conclude which is the best coating, it will be necessary to analyze longer time operation, the stability of the complex interface and a thorough analysis of the kinetic parameters; however, all these coatings present an interest because of their known stability in molten carbonates and their electro-catalytic properties.

Acknowledgments

This work was supported by the French program PLANEX ANR-11-EQPX-0-01 and benefited of a Mexican CONACYT Ph.D. scholarship.

REFERENCES

- [1] Kim MH, Hong MZ, Kim Y-S, Park E, Lee H, Ha H-W, et al. Cobalt and cerium coated Ni powder as a new candidate cathode material for MCFC. *Electrochim Acta* 2006;51:6145–51.
- [2] Kim SG, Yoon SP, Han J, Nam SW, Lim TH, Oh I-H, et al. A study on the chemical stability and electrode performance of modified NiO cathodes for molten carbonate fuel cells. *Electrochim Acta* 2004;49:3081–9.
- [3] Simonetti E, Lo Presti R. Characterization of Ni porous electrode covered by a thin film of $\text{LiMg}_{0.05}\text{Co}_{0.95}\text{O}_2$. *J Power Sources* 2006;160:816–20.
- [4] Ganesan P, Colon H, Haran B, Popov BN. Performance of $\text{La}_{0.8}\text{Sr}_{0.2}\text{CoO}_3$ coated NiO as cathodes for molten carbonate fuel cells. *J Power Sources* 2003;115:12–8.
- [5] Durairajan A, Colon-Mercado H, Haran B, White R, Popov B. Electrochemical characterization of cobalt-encapsulated nickel as cathodes for MCFC. *J Power Sources* 2002;104:157–68.
- [6] Chen LJ, Zuo J, Lin C-J. A novel MCFC cathode material modified by the EPD technique. *Fuel Cells* 2003;3:220–3.
- [7] Kuk ST, Song YS, Suh S, Kima JY, Kim K. The formation of LiCoO_2 on a NiO cathode for a molten carbonate fuel cell using electroplating. *J Mater Chem* 2001;11:630–5.
- [8] Mendoza L, Albin V, Cassir M, Galtayries A. Electrochemical deposition of Co_3O_4 thin layers in order to protect the nickel-based molten carbonate fuel cell cathode. *J Electroanal Chem* 2003;548:95–107.
- [9] Mendoza L, Baddour-Hadjean B, Cassir M, Pereira-Ramos JP. Raman evidence of the formation of LT- LiCoO_2 thin layers on NiO in molten carbonate at 650 °C. *Appl Surf Sci* 2004;225:356–61.
- [10] Pauporté T, Mendoza L, Cassir M, Bernard MC, Chivot J. Direct low-temperature deposition of crystallized CoOOH films by potentiostatic electrolysis. *J Electrochem Soc* 2005;152:C49–53.
- [11] Mendoza L, Ringuedé A, Cassir M, Galtayries II A. Structural, morphological, chemical and electrochemical analysis of nickel covered by electrochemically deposited Co_3O_4 in molten $\text{Li}_2\text{CO}_3\text{--Na}_2\text{CO}_3$ at 650 °C. *J Electroanal Chem* 2005;576:147–60.
- [12] Escudero MJ, Rodrigo T, Mendoza L, Cassir M, Daza L. Porous nickel MCFC cathode coated by potentiostatically deposited cobalt oxide: I. A structural and morphological study. *J Power Sources* 2005;140:81–7.
- [13] Mansour C, Pauporté T, Ringuedé A, Albin V, Cassir M. Protective coating for MCFC cathode: low temperature potentiostatic deposition of CoOOH on nickel in aqueous media containing glycine. *J Power Sources* 2006;156:23–7.
- [14] Albin V, Mendoza L, Goux A, Ringuedé A, Billard A, Briois P, et al. Morphological, structural and electrochemical analysis of sputter-deposited ceria and titania coatings for MCFC application. *J Power Sources* 2006;160:821–6.
- [15] Haukka S, Kytökiivi A, Lakomaa E-L, Lehtovirta U, Lindblad M, Lujala V, et al. The utilization of saturated gas-solid reactions in the preparation of heterogeneous catalysts. *Stud Surf Sci Catal* 1995;91:957–66.

- [16] Leskela M, Ritala M. Atomic layer deposition (ALD): from precursors to thin film structures. *Thin Solid Films* 2002;409:138–46.
- [17] Meléndez-Ceballos A, Fernández-Valverde SM, Barrera-Díaz C, Albin V, Lair V, Ringuedé A, et al. TiO₂ protective coating processed by atomic layer deposition for the improvement of MCFC cathode. *Int J Hydrogen Energy* 2013;38:13443–52.
- [18] Meléndez-Ceballos A, Fernández-Valverde SM, Albin V, Lair V, Ringuedé A, Cassir M. ALD-processed CeO₂ protective layer and its electrochemical performance as MCFC cathode. *Electrochim Acta*; 2013 [under review].
- [19] Ballée E, Ringuedé A, Cassir M, Putkonen M, Niinistö L. Synthesis of a thin-layered ionic conductor, CeO₂-Y₂O₃, by atomic layer deposition in view of solid oxide fuel cell applications. *Chem Mater* 2009;21:4614–9.
- [20] Ritala M, Leskelä M, Niinistö L, Haussalo P. Titanium isopropoxide as a precursor in atomic layer epitaxy of titanium dioxide thin films. *Chem Mater* 1993;5:1174–81.
- [21] Aarik J, Aidla A, Uustare T, Ritala M, Leskelä M. Titanium isopropoxide as a precursor for atomic layer deposition: characterization of titanium dioxide growth process. *Appl Surf Sci* 2000;161:385–95.
- [22] Klepper KB, Nielsen O, Fjellvåg H. Epitaxial growth of cobalt oxide by atomic layer deposition. *J Cryst Growth* 2007;307:457–65.
- [23] Malinowska B, Cassir M, Delcorso F, Devynck J. Thermodynamic and electrochemical behavior of nickel in molten Li₂CO₃-Na₂CO₃ modified by addition of calcium carbonate. *J Electroanal Chem* 1995;389:21–9.
- [24] Chauvaut V, Cassir M, Denos Y. Behavior of titanium species in molten Li₂CO₃-Na₂CO₃ and Li₂CO₃-K₂CO₃ under anodic and cathodic conditions. I – thermodynamic predictions at 550–750 °C. *Electrochim Acta* 1998;43:1991–2003.
- [25] Belhomme C, Gourba E, Cassir M, Tessier C. Chemical and electrochemical behaviour of Ni-Ti in the cathodic conditions used in molten carbonate fuel cells. *J Electroanal Chem* 2001;503:69–77.
- [26] Cassir M, Chauvaut V, Alfara A, Albin V. Study of cerium species in molten Li₂CO₃-Na₂CO₃ in the conditions used in molten carbonate fuel cells – II – potentiometric and voltammetric behaviour. *J Appl Electrochem* 2000;30:1415–20.
- [27] Chauvaut V, Albin V, Shneider H, Cassir M, Ardelean H, Galtayries A. Study of cerium species in molten Li₂CO₃-Na₂CO₃ in the conditions used in molten carbonate fuel cells – I – thermodynamic, chemical and surface properties. *J Appl Electrochem* 2000;30:1405–13.
- [28] Ying Tan JP, Ru Tan H, Boothroyd C, Lim Foo Y, Bin He C, Lin M. Three-dimensional structure of CeO₂ nanocrystals. *J Phys Chem C* 2011;115:3544–50.
- [29] Escudero MJ, Ringuedé A, Cassir M, González-Ayuso T, Daza L. Porous nickel MCFC cathode coated by potentiostatically deposited cobalt oxide: III. Electrochemical behaviour in molten carbonate. *J Power Sources* 2007;171:261–7.
- [30] Escudero MJ, Mendoza L, Cassir M, Gonzalez T, Daza L. Porous nickel MCFC cathode coated by potentiostatically deposited cobalt oxide: II. Structural and morphological behavior in molten carbonate. *J Power Sources* 2006;160:775–81.
- [31] Yazici M, Selman J. Dissolution of partially immersed nickel during in situ oxidation in molten carbonate: cyclic, stripping and square wave voltammetry measurements. *J Electroanal Chem* 1998;457:89–97.
- [32] Antolini E. Behaviour of Ni, NiO and Li_xNi_{1-x}O in molten alkali carbonates. *J Mat Sci* 2000;35:1501–5.
- [33] Nishina T, Takizawa K, Uchida I. Electrochemical characterization of in situ NiO formation in a molten carbonate. *J Electroanal Chem* 1989;263:87–96.
- [34] Belhomme C, Cassir M, Tessier C, Berthoumieux E. Lithium depth profile in NiO molten carbonate fuel cell cathode by nuclear microprobe. *Electrochem Solid-State Lett* 2000;3:216–9.
- [35] Hong MZ, Lee HS, Kim MH, Park EJ, Ha HW, Kim K. TiO₂-coated Ni powder as a new cathode material for molten carbonate fuel cells. *J Power Sources* 2006;156:158–65.
- [36] Scaccia S. Investigation on NiO solubility in binary and ternary molten alkali metal carbonates containing additives. *J Mol Liq* 2005;116:67–71.
- [37] Brenschidt T, Nitschké F, Söllner O, Wendt H. Molten carbonate fuel cell research II. Comparing the solubility and the in-cell mobility of the nickel oxide cathode material in lithium/potassium and lithium/sodium carbonate melts. *Electrochim Acta* 2001;46:783–97.



ELSEVIER

Available online at www.sciencedirect.com

ScienceDirect

journal homepage: www.elsevier.com/locate/hydro

Investigation on niobium oxide coatings for protecting and enhancing the performance of Ni cathode in the MCFC

A. Meléndez-Ceballos ^{a,*}, S.M. Fernández-Valverde ^{b,**}, V. Albin ^a, V. Lair ^a,
J.Á. Chávez-Carvayar ^c, A. Ringuedé ^a, M. Cassir ^a

^a Chimie ParisTech, PSL Research University, CNRS, Institut de Recherche de Chimie Paris (IRCP), F-75005, Paris, France

^b Depto. de Química, Instituto Nacional de Investigaciones Nucleares, A.P.18-1027, México D.F., C.P.11801, México

^c Instituto de Investigaciones en Materiales, UNAM, Circuito Exterior s/n. Ciudad Universitaria, C. P. 04510, México, D. F., México

ARTICLE INFO

Article history:

Received 9 January 2016

Received in revised form

21 March 2016

Accepted 7 April 2016

Available online 10 May 2016

Keywords:

Molten carbonate

Cathode protection

Atomic layer deposition

Niobium oxide

ABSTRACT

This study addresses the problem of the nickel cathode dissolution, decreasing the lifetime of molten carbonate fuel cells, by a protective coating of Nb₂O₅ processed by atomic layer deposition ALD onto the porous cathode substrate. Samples of different thicknesses were tested electrochemically in molten Li₂CO₃-K₂CO₃ eutectic at 650 °C during 230 h by means of chronopotentiometry and electrochemical impedance spectroscopy. A significant decrease in the stabilization time with respect to the oxygen reduction potential is observed with niobium coatings, which could indicate an electrocatalytic process favoured by the presence of Nb. The structure and morphology of the coated samples are characterised by XRD, SEM and XPS before and after the electrochemical tests. Mixed lithiated Ni and Nb oxides are likely to be formed at the cathode surface. Interestingly, this Nb-containing mixed oxide not only can protect Ni cathode but also maintains its good performance.

© 2016 Hydrogen Energy Publications LLC. Published by Elsevier Ltd. All rights reserved.

Introduction

There are several types of fuel cells available commercially, each one aims at satisfying a specific niche of clean generated power, portable, mobile or stationary. Molten carbonate fuel cells (MCFC) are better suited for large-scale stationary generation of several MW, more than any type of fuel cell in the

market. MCFC device does not use any precious metal as catalyst making it cheaper to manufacture. Hence, MCFC is an interesting technology for producing clean energy from hydrocarbons, biogas or hydrogen-rich fuels.

The most common material used as MCFC cathode material is nickel, which undergoes *in situ* oxidation and lithiation in the carbonate melt, then nickel starts dissolving and, after reacting with hydrogen, might precipitate as

* Corresponding author.

** Corresponding author.

E-mail addresses: arturo.melendez@chimie-paristech.fr (A. Meléndez-Ceballos), suilma.fernandez@inin.gob.mx (S.M. Fernández-Valverde).

<http://dx.doi.org/10.1016/j.ijhydene.2016.04.045>

0360-3199/© 2016 Hydrogen Energy Publications LLC. Published by Elsevier Ltd. All rights reserved.

metallic nickel onto the anode, causing a short-circuit between both electrodes through the electrolyte [1,2]. One of the best solutions is to deposit a protective coating of a selected metal oxide onto the cathode. There are many studies dedicated to this approach in the literature, sol–gel, electrochemical deposition, chemical vapour deposition, plasma and laser sputtering of various metal oxides. For instance, CeO₂, TiO₂, Co₃O₄, Fe₂O₃, and mixtures of those have been studied with some significant results [3–10]. Nevertheless, even though addition of such layers decreases Ni solubility, they may also increase the cathode resistance and drop the cathode electrochemical performance. In recent studies, we have used atomic layer deposition (ALD), technique which allows processing ultra-thin and conformal layers, e.g. CeO₂, TiO₂, Co₃O₄, in order to maintain the electrocatalytic properties of the porous nickel substrate [11–13]. Interesting results were obtained, but there is still a need of more performing coatings, combining a protective role and electrocatalytic properties. Niobium compounds and, in particular oxides, are well known for their catalytic properties for oxidation processes; for instance, E. Heracleus et al. and A. Qiao et al. have used Ni–Nb–O and Ni–Nb–M–O compounds for catalysing the oxidative dehydrogenation of ethane reaction, explaining the increased activity of the Ni–O catalyst by the increased surface acidity conferred by Nb species at the surface [14–16]. Nevertheless, other authors have analysed the properties of niobium oxides for reduction processes. A. Takagaki et al. and R. Ohnishi et al. evaluated the performance of niobium oxides as catalysts for oxygen reduction reaction (ORR) in proton exchange membrane fuel cells (PEMFC) with good results [17,18]. As far as we know there are no specific mechanistic studies on niobium oxides grown on nickel oxide substrates [19,20]; however, pre-oxidised nickel–niobium alloy has already been suggested by Fang et al. as novel candidate material for replacing the classical nickel oxide cathode [21,22]. These authors obtained a significant drop in Ni solubility (8×10^{-6} instead of 17×10^{-6} mol fraction). They also mentioned that niobium oxide cannot be thermodynamically reduced by H₂ or CO in the anode MCFC atmosphere, which is favourable to the application because no metallic niobium would be deposited in the electrolyte.

In the present study, we investigated for the first time the structural, morphological and electrochemical behaviour of ALD-processed thin layers of different thicknesses of Nb₂O₅ onto the commercial porous Ni cathode. ALD is a chemical gas phase deposition technique first developed in Finland in the 1970s by T. Suntola et al. [23,24]. In ALD, reactant gas pulses are introduced separately in order to reach the substrates to be coated and growth is achieved through self-terminating surface reactions, which means that only one monolayer of reactant gas species can be adsorbed to the surface during a pulse. We worked in Li₂CO₃–K₂CO₃ bulk at 650 °C in conditions simulating MCFC cathode operation. Our aim here is to show whether ALD-processed niobium oxide coatings could play a protective role with respect to Ni cathode and maintain or improve the electrocatalytic properties of nickel. A deeper insight contemplating the mechanistic effect of niobium with respect to oxygen reduction kinetics is out of the scope.

Experimental

Atomic layer deposition of Nb₂O₅

A thin layer of Nb₂O₅ was deposited on a commercial porous nickel substrate (produced by Doosan Company, South-Korea) by means of ALD technique using a vertical flow type reactor (Picosun SUNALE™ R-series). Niobium ethoxide, Nb(OCH₂CH₃)₅ (Sigma–Aldrich®) was used as precursor and distilled water as oxidizing agent. In order to process the Nb₂O₅ layer, Nb(OCH₂CH₃)₅ was introduced into the precursor chamber using the following conditions: precursor pulse time 0.5 s, purge time 3 s, N₂ line flow of 100 cm³ min^{−1}, water pulse time 0.1 s, purge time 3 s [25]. The precursor was sublimated at 80 °C and the water vapour was supplied at 25 °C. The reactor temperature was kept at 300 °C with a N₂ flow of 300 cm³ min^{−1}, the precursor pulse and purge was followed by water pulse and purge, this cycle was repeated until the desired thickness was reached. The growth rate of Nb₂O₅ layers over the porous nickel substrate was ≈ 1 Å/cycle. Four different samples were processed by this technique to obtain 5, 20, 50 and 300 nm deposited layers.

Material characterization

Deposited layers were characterized by X-ray diffraction, SEM and XPS. XRD was performed in a PANalyticalX'pert Pro from Anton Paar with Cu–K_α1 radiation ($\lambda = 1.54056$ Å). The diffraction pattern was obtained by scanning between 20 and 120° by steps of 0.02 (2 θ) with a fixed counting time of 2.3 s in razing mode. Once the data were obtained, Scanning Electron Microscopy (SEM) analysis were performed with a ZEISS® Ultra 55 microscope to evaluate the surface, morphology and to measure the layer thickness. X-ray photoelectron spectra were recorded using a Thermo Scientific K-Alpha X-ray photoelectron spectrometer with a monochromator Al K_α X-ray ($h\nu = 1486.61$ eV) for sample excitation. An argon ion beam was used to prevent sample surface charging. The spectrometer energy calibration was obtained using Au 4f 7/2 and Cu 2p 3/2 photoelectron lines. The position of the adventitious carbon C 1 s peak at 284.6 eV was used as an internal reference in each sample to determine the binding energies with an accuracy of ± 0.1 eV. The residual pressure in the analysis chamber was maintained below 10^{-8} Torr, during data acquisition. Three samples of 50 nm niobium oxides deposited on porous nickel were analysed, one as-deposited and two others M1 and M2 after immersion in molten carbonate eutectic at 650 °C for 44 h and 144 h respectively. The survey spectrums were obtained between 0 and 1000 eV, for all samples. The spectra were collected and analysed with Advantage 4.0 software.

Electrochemical cell

Lithium and potassium carbonates, of high-grade purity >98% (Sigma–Aldrich®), were mixed in a proportion of 62:38 mol %. The high-temperature electrochemical cell was a single-compartment crucible of dimensions 70 × 50 mm² contained in an alumina Al₂O₃ reactor of dimensions 250 × 60 mm²

hermetically sealed by a stainless steel cover with a Viton O-ring. The whole electrochemical set-up was fully described in a previous papers [26]. Temperature was controlled at a constant value of 650 °C by means of a calibrated chromel/alumel thermocouple. The standard cathode atmosphere was a mixture of O₂/CO₂/Ar (14:30:56 atm. %) of high-grade purity (Air Liquide®) at 650 °C and a pressure of 1 atm. After stabilizing the molten carbonate eutectic under the selected cathode atmosphere, each sample was immersed in the molten carbonate eutectic and was used as working electrode to perform electrochemical measurements.

Electrochemical measurements

The electrochemical experimental data were collected using a potentiostat/galvanostat (AutoLab® PGSTAT-302N with FRA module). A three-electrode system was used, the working electrode being the modified porous Ni cathode (10 × 10 × 0.5 mm), the counter electrode was a gold wire and the reference electrode a silver wire dipped into an Ag₂SO₄ (10⁻¹ mol kg⁻¹) saturated electrolyte eutectic melt into an alumina tube sealed by a porous alumina membrane. Open circuit potential (OCP) was measured for a period of 230 h for the modified cathodes. The parameters used for impedance (EIS) measurements are the following: scanning frequencies set from 10⁻³–10⁶ Hz, with 11 points per decade, and signal amplitude of 5 mV respecting the system linearity. The fitting of the equivalent circuit was performed with Zview® V3.3e software.

Ni solubility

The solubility of bare porous nickel and 20 nm Nb₂O₅ coated porous nickel was measured individually from the different (Li₆₂-K₃₈)₂CO₃ melts used in the experiments. Small amounts of carbonates (about 1.4 g) were withdrawn randomly three times from the molten carbonate bulk at the end of the electrochemical characterizations, which corresponds to 230 h immersion. After solidification, each carbonate sample was hand-milled to obtain a fine powder. 2 g of carbonate powder were then dissolved in 10 ml of HNO₃ at 3 vol. %. Nickel content was determined by ICP-AES (ICAP 6000 Series from Thermo Fisher Scientific). The calibration was performed using Aldrich atomic absorption standard solutions, dissolved in HNO₃ at 3 vol. %.

Results and discussion

Material characterization

In Fig. 1, a comparison of SEM micrographs of the as-deposited Nb₂O₅ with thicknesses of 300 (a), 50 (b) and 5 (c) nm are shown. As can be observed, ALD deposits are dense, conformal and homogenous as expected. It should be noted, however, that the thinner is the layer the more it seems fragile, which is specifically the case in Fig. 1b) for a 5 nm coating. X-ray diffraction pattern shown in Fig. 2 was obtained from a sample coated with 300 nm of Nb₂O₅ over Si (0 0 1) and

heat treated at 650 °C for 4 h. Further analysis by software indicates the presence of 3 phases corresponding to ICDD pattern numbers 00-030-0873, 00-026-0885 and 01-071-0020 that belong to an orthorhombic Nb₂O₅, monoclinic Nb₂O₅ and tetragonal NbO₂ type crystals, respectively. Orthorhombic Nb₂O₅ constitutes the primary phase. The peak located at 2θ° value of 99.5211 was not identified as part of the previously mentioned phases. The average crystal size deduced from the peaks after applying the Sherrer equation is around 65 nm [27]. The different phases and consequent Ni and Nb valences, as well as lattice defects present in the material could facilitate the interaction of Nb with the undelaying Ni and possibly accelerate Li penetration which could play a favourable role in the cathode electrochemical behaviour.

XPS spectra of Nb (a), Ni (b) and O (c) peaks for the as-deposited 50 nm Nb₂O₅ coated nickel (1), samples after 44 h (2) and 144 h (3) immersion in the carbonate melt are shown in Fig. 3. The values of peak position and peak area in percentage as well as the related phases are summarized in Table 1. For each binding energy determination, the values obtained were corrected with respect to adventitious carbon taken as reference. In Fig. 3, changes in binding energies and percentages of different niobium, oxygen and nickel species are observed. In Fig. 3a₁, Nb 3d_{5/2} and Nb 3d_{3/2} are found at 207.5 eV and 210.2 eV, respectively, and correspond to Nb₂O₅ [28]. The Ni XPS spectrum in Fig. 3b₁ shows four peaks, the first peak at 852.5 corresponds to 2p_{3/2} Ni [29], probably present at the surface due to sample handling. Peaks at 855 and 860.3 eV belong to 2p_{3/2} and 2p_{3/2} satellites of NiO, respectively [30–32] the peak at 857 eV could be due to the presence of Ni-OH bonds as suggested by the literature [33,34]. The O spectra in Fig. 3c₁ shows the presence of two 1 s peaks, one at 530.5 eV which corresponds to the oxygen contained in Nb₂O₅ and NiO [31,35,36]. The peak present at 532.2 eV corresponds to O-H bonds found in molecular chemisorbed water or hydroxyl surface groups [31,33,37] maybe present due to sample handling. After 44 h in the carbonate melt, sample M1 (see Fig. 3a₂) shows clearly a change in shape and two new peaks appear on the spectra. Peaks at binding energies of 206.5 eV and 209.1 eV should correspond to a Li-Nb-O phase with defects or oxygen vacancies hence a lower binding energy than the values reported for LiNbO₃ [38,39]. Diffusion of Nb into Ni could have lower the binding energy of Nb₂O₅ peaks at 209.9 and 207.4 eV by replacing some Nb-O ligands by Ni-Nb this shift on Nb for Ni-Nb-O phases has been reported in literature [36,40]. In the case of Ni, the peak at 852.5 eV disappears. The 2p_{3/2} NiO peak, originally at 855 eV, is split in two peaks, one at 854.5 eV and another at 856.5 eV corresponding, most probably, to Ni^{II} and Ni-O defects, respectively [37,41]. The satellite 2p_{3/2} is displaced to a higher BE value of 861.2 eV. The observed shifts are proper to Li incorporation into the NiO matrix [41] and also could be due to Nb incorporation to form a more complex Li-Ni-Nb-O phase. A peak appearing at 865.5 eV could evidence the formation of a Nb₂O₅-rich NiO compound, such as NiNb₂O₆ similar to NiFe₂O₄ which presents also a peak at that BE [34]. Oxygen peak also shows a split in two contributions, one at 529.4 eV attributed to O 1 s of Li-Ni-O bonds [41] and another at 530.8 eV from the Nb-O bonds [39]. In sample M2, the binding energy of Nb 3d_{3/2} remain as in M1, while the

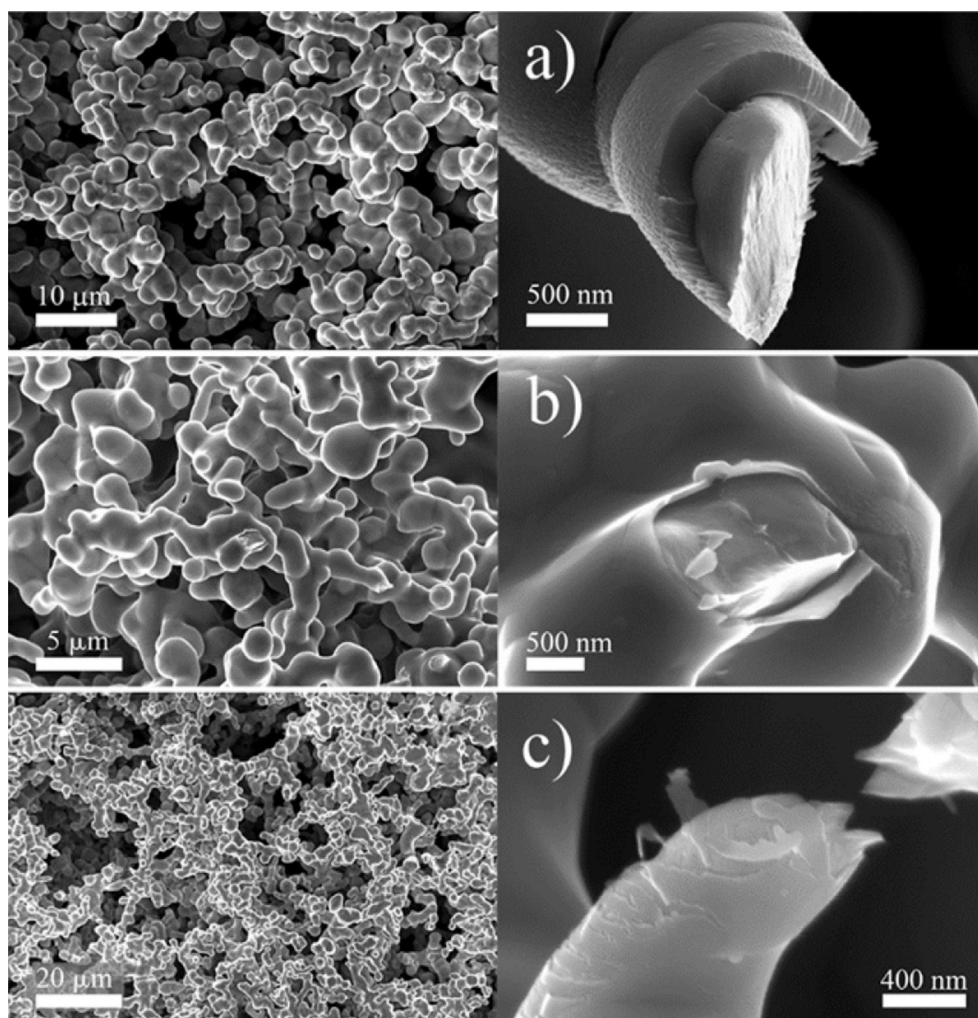


Fig. 1 – SEM images of the as-deposited Nb_2O_5 thin layers. Left side low magnification, right side high magnification close to a broken Ni grain. Thicknesses are: a) 300 nm, b) 50 nm, c) 5 nm layers.

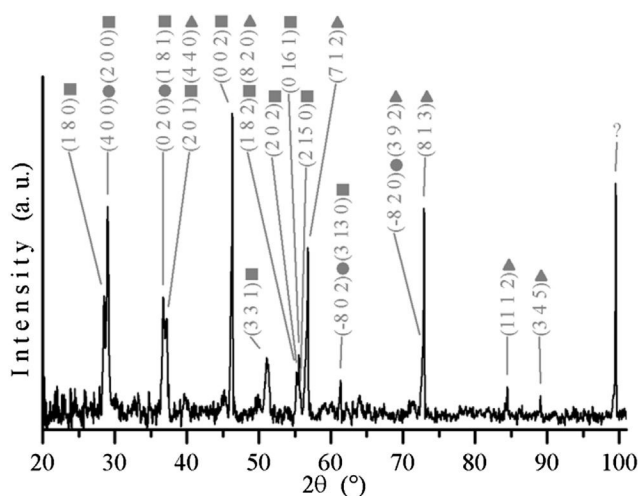


Fig. 2 – X-ray diffractogram of 300 nm Nb_2O_5 layer showing three identified phases: (■) Orthorhombic Nb_2O_5 ICDD (00-030-0873), (●) Monoclinic Nb_2O_5 ICDD (00-026-0885) and (▲) Tetragonal NbO_2 ICDD (01-071-0020). ? = unidentified peak at 99.5211 ($2\theta^\circ$). In parenthesis the (h k l) numbers of the corresponding phase.

$3d_{5/2}$ peak is shifted to a BE of 207.1 eV; this shift has been reported by Trifonov et al. in the oxidation of Ni-Nb alloys [40]. In our case, it might reflect further Nb and Li intercalation into the subjacent NiO, forming a Li-Ni-Nb-O phase. The Nb peaks at BE 209.4 and 206.5 eV correspond to the BE energies of LiNbO_3 , as shown by Aufray et al. [38]. Nb_2O_5 being available at the surface of the electrode, it is not surprising that lithiation of Nb_2O_5 takes place. In the case of Ni $2p_{3/2}$, peaks are shifted again to a lower BE of 854.3 and 856.1 eV, as previously mentioned they correspond to Ni^{II} and Ni-O defects, respectively. As can be noticed in Table 1, the area of the peaks has also changed and an increase from 25 to 33% in the peak area for the Ni-O defects might be caused by further Li and Nb incorporation in to the NiO lattice. Ni $2p_{3/2}$ satellite increased its BE to 861.3 eV and the peak at 865 remains. All Ni peaks indicate a strong Li and Nb interaction with NiO forming a Li-Ni-Nb-O phase [41,42]. Oxygen peaks show an increase in BE in respect to M1 sample and are now at 531.3 and 529.7 eV. According to Pawlak et al. [43] oxygen 1s spectra, is affected by the different metals present on the coordination shell of oxygen; thus, the shift in O1s peaks could be due to the presence

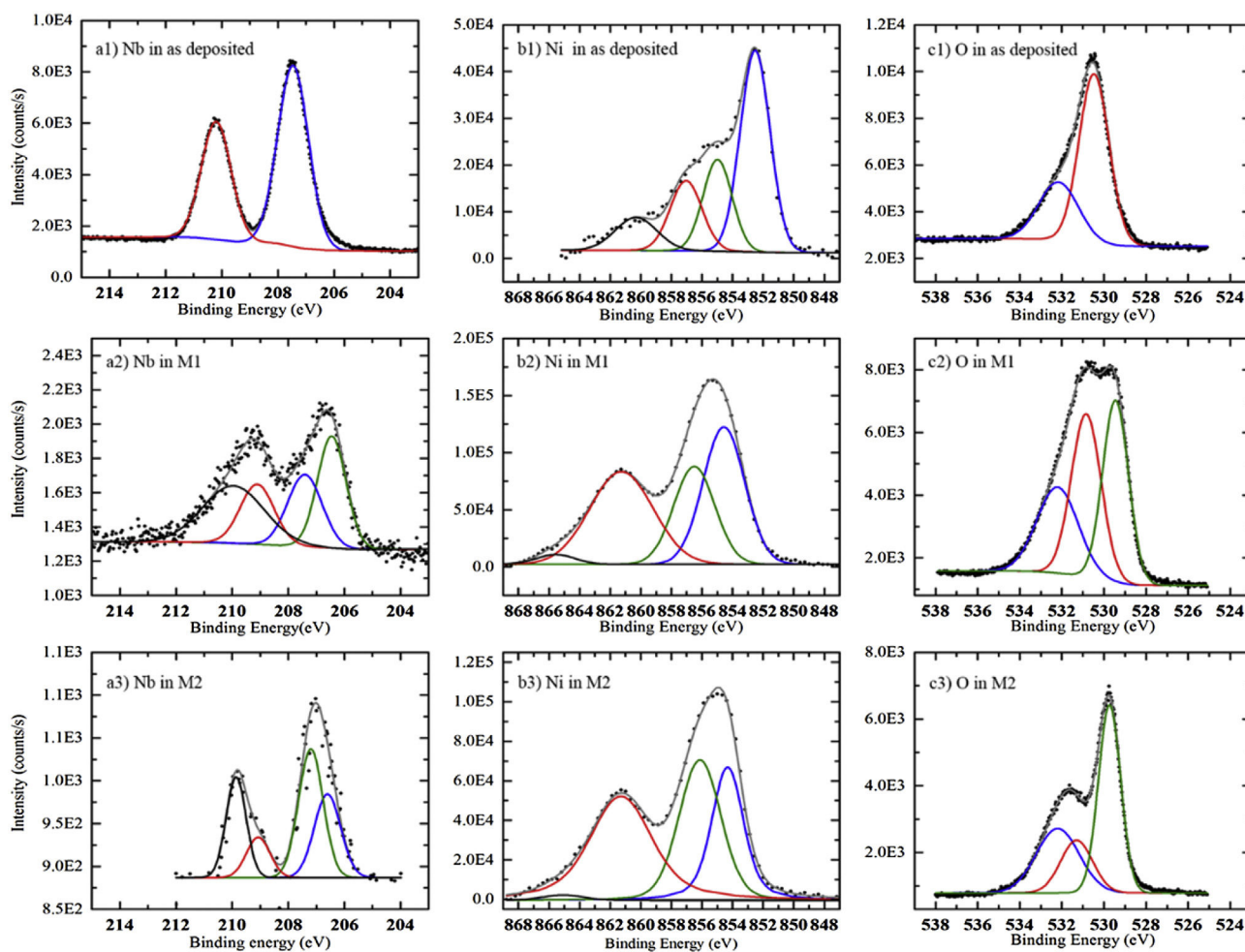


Fig. 3 – XPS spectra of all tested samples, a1), b1) and c1) corresponding to Nb_2O_5 as deposited on porous nickel by ALD, a2), b2) and c2) corresponding to sample M1 obtained after 44 h immersion time in a mixture of Li and K carbonates at 650°C and a3), b3) and c3) corresponding to sample M2 obtained after 144 h of immersion in the same conditions.

of Li-Ni-Nb-O phase. It is clear that the complex interaction between NiO, Nb_2O_5 and Li^+ in our media will require a more detailed XPS study to determine unambiguously the precise composition of the cathode surface after a long immersion in the molten $(\text{Li}_{62}\text{-K}_{38})_2\text{CO}_3$ eutectic.

Electrochemical characterization

Fig. 4 shows the evolution of the open circuit potential (OCP) for each tested sample over 230 h, corresponding to porous nickel and Nb_2O_5 coatings of 5 nm, 20 nm, 50 nm and 300 nm, respectively. As can be noted in Fig. 4, porous Ni follows a 2 step potential evolution where the plateaus are denoted as I (≈ -0.68 V), II (≈ -0.37 V) and III (≈ 0 V). The OCP behaviour of porous nickel has been investigated by different authors, among them Yazici et al. and Antolini [44,45], who attributed the steps to the *in situ* Ni oxidation followed by the NiO lithiation process on the porous nickel surface. The three plateaus corresponding to porous nickel, observed in Fig. 4, are related to the modification of the porous Ni electrode into $\text{Li}_x\text{Ni}_{1-x}\text{O}$, in a progressive way. The first plateau (I) from 0 to 98 h is ascribed to the *in situ* oxidation of metallic nickel, after

the first potential jump at 98 h, a second plateau (II) is reached at a potential around -0.4 V/(Ag/Ag⁺). This plateau corresponds to the *in situ* lithiation of NiO, which is probably associated to an increase in the nickel valence from Ni^{2+} to Ni^{3+} , as reported by Nishina et al. from XPS measurements [46]. At equilibrium, lithium content in NiO cathode was estimated by nuclear microprobe to be roughly 0.2 at% [47]. After 182 h, the lithiation process is completed and the third plateau (III) at -0.03 V/(Ag/Ag⁺) corresponds to an equilibrium potential between O_2 , CO_2 and carbonates. At this stage, the electrode works as a stable cathode for oxygen reduction.

Samples coated by a thin layer of Nb_2O_5 do not show the same behaviour as bare porous nickel. The 300 nm coated sample, shown in Fig. 4, reaches a potential around -0.4 V/(Ag/Ag⁺) very fast, in less than 25 h, and appears relatively stable until 63 h. Then, it increases slowly (in absolute value) with a mild slope until reaching -0.45 V/(Ag/Ag⁺) and remains relatively stable. Apparently, this Nb_2O_5 layer is too thick and blocks the nickel catalytic activity. When decreasing the thickness of the layer to 50 nm, as shown in Fig. 4, the OCP behaviour seems more favourable; even though it does not follow completely the Ni behaviour, it shows two potential

Table 1 – Peak data obtained from XPS spectra fitting shown in Fig. 3. Peak numbers are designed from high to low binding energies.

	Nb peaks			Ni peaks			O peaks											
	Peak number	Center (eV)	Area (%)	Peak number	Center (eV)	Area (%)	Peak number	Center (eV)	Area (%)									
As deposited	1	210.2	39	3d _{3/2}	1	860.3	11	2p _{3/2} , sat	1	532.2	31	1s						
	2	207.5	61	Nb ₂ O ₅	2	857	18	NiO	2	530.5	69	H ₂ O						
				3d _{5/2}				Ni-OH				1s						
				Nb ₂ O ₅								Nb ₂ O ₅ /NiO						
As in M1	1	209.9	31	3d _{3/2}	1	865.5	2	NiNb ₂ O ₆ ?	1	532.2	27	1s						
				Nb ₂ O ₅								H ₂ O						
				3d _{3/2}				2				861.2	37	2p _{3/2} , sat	2	530.8	37	1s
				LiNbO ₃										Li-Ni-Nb-O				Nb-O
3	207.4	22	3d _{5/2}	3	856.5	25	2p _{3/2}	3	529.4	36	1s							
			Li-Ni-Nb-O				Li-Ni-Nb-O				Li-Ni-O							
As in M2	1	209.9	15	3d _{3/2}	1	865	2	NiNb ₂ O ₆ ?	1	532.2	29	1s						
				Nb ₂ O ₅								H ₂ O						
				3d _{3/2}				2				861.3	39	2p _{3/2} , sat	2	531.3	23	1s
				LiNbO ₃										Li-Ni-Nb-O				Li-Nb-O
3	207.1	48	3d _{5/2}	3	856.1	33	2p _{3/2}	3	529.7	51	1s							
			Li-Ni-Nb-O				Li-Ni-Nb-O				Li-Ni-Nb-O							
4	206.5	18	3d _{5/2}	4	854.3	26												
			LiNbO ₃															

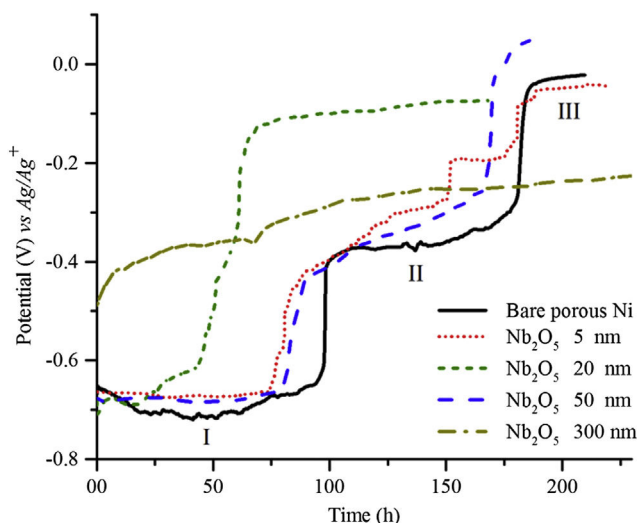


Fig. 4 – Open-circuit potential evolution vs. time over 230 h for porous Ni and Nb₂O₅ covered samples immersed in molten Li₂CO₃-K₂CO₃ eutectic at 650 °C.

steps. The first one occurs at 81 h, before that of nickel, up to a potential of -0.42 V/(Ag/Ag⁺) and continues increasing with a slight slope until 166 h where it jumps from -0.25 to -0.02 V/(Ag/Ag⁺) at 171 h, to finally reach its maximum potential 0.05 V/(Ag/Ag⁺) at 187 h. This behaviour indicates that nickel oxide is acting as a catalyst and the presence of Nb₂O₅ somehow accelerates the potential evolution reaching a favourable working potential in a shorter time. If we reduce the thickness of the protective Nb₂O₅ layer to 20 nm, as depicted in Fig. 4, the behaviour changes drastically from that of porous Ni and the 50 nm coated sample, showing a very small potential increment after 24 h immersion from -0.66 to -0.60 V/(Ag/Ag⁺) at 44 h. Then the potential increases rapidly from -0.60 to -0.1 V/(Ag/Ag⁺) at 79 h. Afterwards, the potential increases slowly during the next 89 h of the experiment, reaching a final value of -0.07 V/(Ag/Ag⁺) after 168 h of immersion in the molten carbonate melt at 650 °C. For the 20 nm coated sample, shown in Fig. 4, a good working potential is reached 112 h before the porous Ni electrode, which could indicate that the presence of Nb₂O₅ is increasing the catalytic properties of NiO or even that Nb₂O₅ is acting as a catalyst itself. It seems that the 20 nm is the most efficient coating with respect to the stabilisation of the Ni electrode.

The 5 nm Nb₂O₅-coated sample, described in Fig. 4 shows a behaviour close to that of the 50 nm coated sample and porous Ni. The initial potential remains stable at around -0.66 V/(Ag/Ag⁺) during 74 h when it starts to rise up to -0.42 V/(Ag/Ag⁺). Then it follows a slope similar to the 50 nm sample up to -0.27 V/(Ag/Ag⁺) at 150 h when it presents a fast increase in the form of a step up to -0.18 V/(Ag/Ag⁺) that remains stable until 175 h. After another potential step, it reaches a value of -0.05 V/(Ag/Ag⁺) remaining stable for the rest of the experiment. It seems that the first part of the OCP behaviour corresponds to the influence of Nb₂O₅, while the final two steps are a direct influence of the Ni oxidation/lithiation phenomenon already described. This hypothesis seems to be supported by the fact that the content of Nb₂O₅ is very small and even

though it influences the OCP behaviour, the final potential step occurs at the same time as the bare porous Ni reaching a potential around -0.04 V, which is a good value in terms of cathode equilibrium potential.

Even though the 20 nm and 50 nm coated samples could be considered close in terms of thickness, their OCP behaviour is not. The difference is due to the fact that the 20 nm sample could be more reactive towards NiO than the 50 nm sample, forming faster a mixed valence Li-Ni-Nb-O phase, as suggested by XPS analysis, that could stabilise the cathode faster than Li_xNi_{1-x}O phase and probably act as a good electrocatalyst. In the 50 nm sample, the presence of Nb₂O₅ at the extreme surface in contact with carbonates could block the effect of the mixed phase at the NiO-Nb₂O₅ interphase.

Electrochemical impedance spectroscopy data were recorded periodically and fitted to deduce resistance values, such as charge transfer resistance (R₁), mass transfer resistance (R₃) and total resistance (R_e + R₁ + R₂ + R₃) of the electrochemical system. Fig. 5 shows an example of data fitting and the corresponding equivalent circuit. It is necessary to consider a three-phenomenon circuit with a series of three sets of a resistor in parallel with a constant phase element (CPE) due to the presence of an arc at medium frequencies. The presence of this arc has been discussed by Escudero et al. [48], suggesting that this phenomenon, observed only during the first 8 h, is due to the formation of the Li_xNi_{1-x}O phase. In our case, this phenomenon is present along the 230 h for most of the samples except the 20 nm one. It is difficult to explain this phenomenon, probably not due to the oxidation/lithiation of Ni but maybe to the porosity of the material; anyhow, it is not our purpose to analyse deeply the origin of this middle frequency arc, which would require analysing the evolution of the distribution of relaxation times (DRT).

It is worth mentioning that for comparison, resistances and EIS data are presented at a similar OCP value instead of a given time; we have opted for this representation since the samples behave differently with respect to time. Fig. 6 shows different EIS data taken along 130 h of immersion time for the 20 nm-coated sample. We can note an increase in the total resistance vs. time up to 65 h, which is due to the growth of the

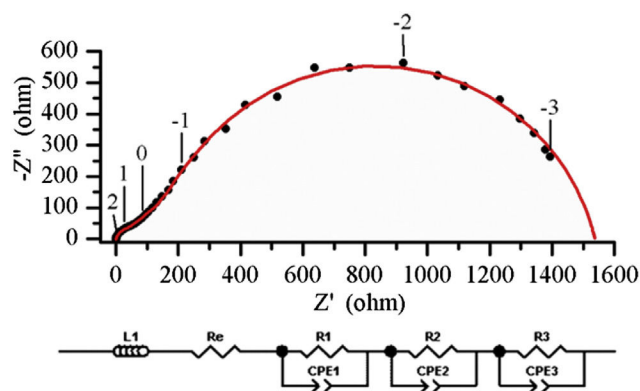


Fig. 5 – Nyquist representation of EIS data (●) of 50 nm Nb₂O₅ covered sample taken at 176 h immersion in molten Li₂CO₃-K₂CO₃ eutectic at 650 °C. Fitted with the equivalent circuit shown above (—). Numbers correspond to the logarithm of the frequency.

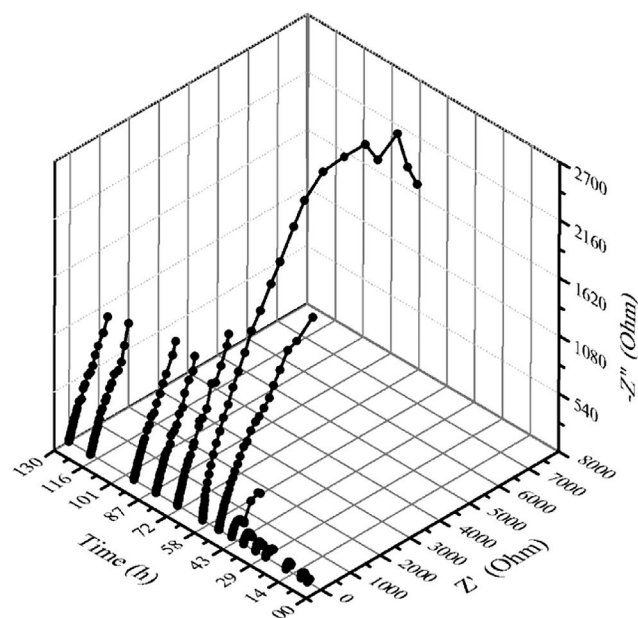


Fig. 6 – Nyquist representation of impedance data taken periodically over 130 h. Data corresponds to the 20 nm covered sample immersed in molten $\text{Li}_2\text{CO}_3\text{-K}_2\text{CO}_3$ eutectic at 650°C .

Table 2 – Charge transfer resistance (R_{ct}) and total resistance (R_{tot}) for each sample tested, taken from EIS data fitting at a comparable OCP value after the last potential step and close to 0 V.

	R_{ct}	R_{tot}
Porous Ni	2.3	350
5 nm	1.2	745
20 nm	12	1200
50 nm	29	1500
300 nm	101	1950

nickel oxide layer in interaction with the Nb_2O_5 ultrathin layer. After 65 h, the total resistance decreases, which is consistent with the lithiation of NiO and/or Nb_2O_5 increasing the conductivity. Nevertheless, the total resistance deduced from the impedance data at OCP potential around $-0.07\text{ V}/(\text{Ag}/\text{Ag}^+)$ is 4 times higher than that of bare porous Ni at similar potential. In Table 2, the influence of Nb_2O_5 layer thickness over the charge transfer resistance and total resistance is evidenced at their final steady state potential for all the samples. As could be expected due to the high resistivity of Nb_2O_5 , the charge transfer resistance increases when increasing the thickness as do the total resistance. Nevertheless, resistance values shown by the 5 nm and 20 nm samples could still be acceptable for MCFC cathode application. Fig. 7 shows a comparison of the Nyquist diagrams obtained for each sample at a similar potential close to 0 V/(Ag/Ag⁺). In this figure, we can observe that the 20 nm Nb_2O_5 coated sample seems to have a different diffusion regime than all the rest, probably due to a faster adsorption–desorption kinetics of dissolved oxygen and CO_2 at the surface of the electrode.

Fig. 8 shows the evolution of the total resistance (R_{tot}) for all the samples over immersion time. All the Nb_2O_5 coated samples present an increase in resistance up to a maximum that occurs before the final potential step: 169 h for 5 nm, 61 h for 20 nm and 163 h for 50 nm. This is not true for the porous Ni sample, which presents its maximum resistance at 189 h, just after the potential step. After reaching the maximum resistance value, all the samples show a significant resistance decrease due most likely to the formation of $\text{Li}_x\text{Ni}_{1-x}\text{O}$ or a mixed Li-Ni-Nb-O phase, more conductive than NiO. It is important to notice that the 20 nm sample shows a promising OCP behaviour knowing that the solubility of Ni decreases and that a catalytic effect of Nb is likely. It is important to point out two key points on the electrochemical study performed. The first is that the OCP of 20 nm coated Ni reaches rapidly a potential around 0 V/(Ag/Ag⁺) due to a rapid oxidation and lithiation of Ni; the second is that total resistance increases up to $8633\ \Omega$ and then decreases to a minimum value of $1200\ \Omega$. Even though the final resistance is high, this resistance drop cannot

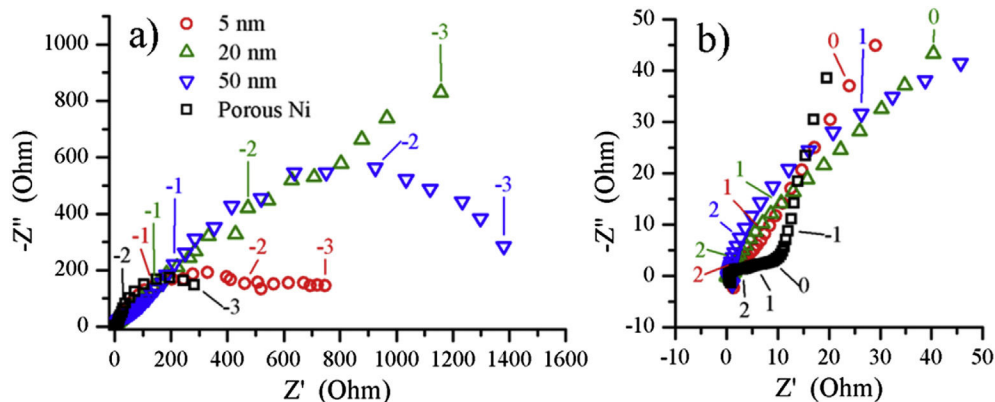


Fig. 7 – Superposed Nyquist diagrams of EIS data taken at plateau III (Fig. 5). a) General overview, b) Zoom into high frequency area. OCP voltage was around 0 V. All data taken with samples immersed in molten $\text{Li}_2\text{CO}_3\text{-K}_2\text{CO}_3$ eutectic at 650°C . Samples were: bare porous nickel (■), 5 nm (●), 20 nm (▲) and 50 nm (▼) covered samples. Numbers correspond to the logarithm of the frequency.

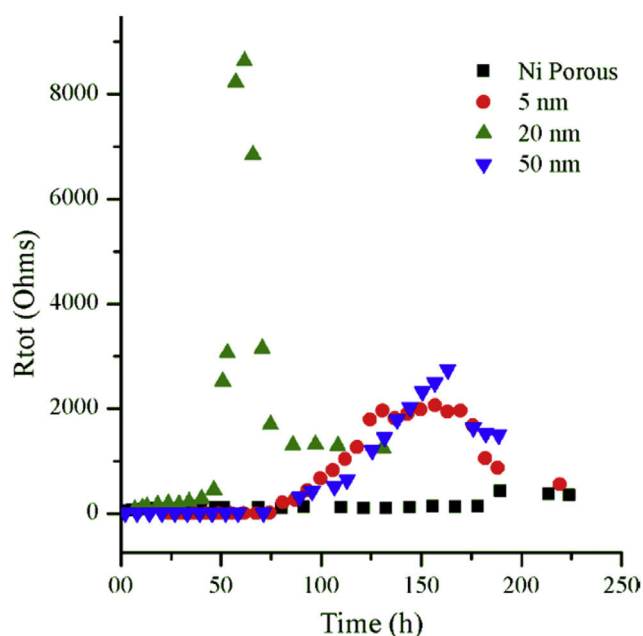


Fig. 8 – Total resistance evolution ($R_{tot} = R_e + R_1 + R_2 + R_3$) over time for: bare porous nickel (■), 5 nm (●), 20 m (▲) and 50 nm (▼) covered samples immersed in molten $\text{Li}_2\text{CO}_3\text{-K}_2\text{CO}_3$ eutectic at 650 °C.

be due only to lithiation, but to the presence of a mixed oxide phase. Further specific studies on the reduction kinetics of oxygen on the Nb-coated porous nickel cathode are necessary to determine whether Nb at surface is really facilitating the mass transport process of oxygen.

Solubility of Ni in molten Li-K eutectic carbonates was measured by means of ICP-AES to evaluate the protection conferred by the Nb_2O_5 coating. It can be seen that in comparison with bare porous Ni cathode with a solubility in molten $\text{Li}_2\text{CO}_3\text{-K}_2\text{CO}_3$ (62–38 mol %) eutectic carbonates at 650 °C of 15 wt. ppm, the 20 nm Nb_2O_5 protective layer reduced the Ni dissolution to 10 wt. ppm in strictly the same conditions. This demonstrates that coating the bare porous nickel cathode material with an ultra-thin layer of Nb_2O_5 is effective to protect the cathode of MCFC and, hence, for increasing its lifetime.

Conclusions

ALD-processed layers Nb_2O_5 were deposited onto porous nickel MCFC cathode in various thicknesses; as expected they were conformal and dense. Then, these samples were tested electrochemically in molten $\text{Li}_2\text{CO}_3\text{-K}_2\text{CO}_3$ (62–38 mol %) eutectic carbonates at 650 °C. Solubility of NiO was effectively decreased with a 20 nm Nb_2O_5 layer and the electrochemical performance shown by the OCP was satisfactory, especially for the 20 nm Nb_2O_5 covered sample, which allowed a very rapid potential increase. For the same sample, total resistance and mass transfer resistance showed an abrupt increment, followed by a rapid decrease, evidencing the presence of some kind of catalytic effect due to the presence of niobium. XPS

analysis showed that mixed phases of Ni-Nb-Li-O are present in the surface of the electrode; these phases could be responsible for the apparent catalytic behaviour. Even though the influence of Nb could modify oxygen reduction at the surface of the electrode, a more detailed kinetic study will be necessary to explain the role of Nb in the reduction mechanism. In brief, we have shown that Nb_2O_5 can be used as protective material for the MCFC cathode when deposited as a fine conformal and dense layer; this layer decreasing nickel solubility, accelerating the stabilisation of the electrode (OCP behaviour) and not affecting the catalytic performance of the state-of-the-art electrode, because of the formation of a mixed compound with interesting electrocatalytic properties that would require more insight.

Acknowledgements

The authors wish to thank the program ECOS-(M13P01) for financial support and also CONACYT for the Ph.D. scholarship 314518, as well as the mexican hydrogen network program 2015.

REFERENCES

- [1] Antolini E. The stability of molten carbonate fuel cell electrodes: a review of recent improvements. *Appl Energy* 2011;88:4274–93. <http://dx.doi.org/10.1016/j.apenergy.2011.07.009>.
- [2] Kulkarni A, Giddey S. Materials issues and recent developments in molten carbonate fuel cells. *J Solid State Electrochem* 2012;16:3123–46. <http://dx.doi.org/10.1007/s10008-012-1771-y>.
- [3] Baizeng F, Xinyu L, Xindong W, Shuzhen D. Surface modification of a MCFC anode by electrodeposition of niobium. *J Electroanal Chem* 1998;441:1–3. [http://dx.doi.org/10.1016/S0022-0728\(97\)00203-9](http://dx.doi.org/10.1016/S0022-0728(97)00203-9).
- [4] Chauvaut V, Cassir M, Denos Y. Behavior of titanium species in molten $\text{Li}_2\text{CO}_3\text{-Na}_2\text{CO}_3$ and $\text{Li}_2\text{CO}_3\text{-K}_2\text{CO}_3$ under anodic and cathodic conditions. I – thermodynamic predictions at 550–750 °C. *Electrochim Acta* 1998;43:1991–2003. [http://dx.doi.org/10.1016/S0013-4686\(97\)10139-6](http://dx.doi.org/10.1016/S0013-4686(97)10139-6).
- [5] Chauvaut V, Albin V, Schneider H, Cassir M, Ardéléan H, Galtayries A. Study of cerium species in molten $\text{Li}_2\text{CO}_3\text{-Na}_2\text{CO}_3$ in the conditions used in molten carbonate fuel cells. Part I: thermodynamic, chemical and surface properties. *J Appl Electrochem* 2000;30:1405–13. <http://dx.doi.org/10.1023/A:1026595117970>.
- [6] Belhomme C, Gourba E, Cassir M, Tessier C. Chemical and electrochemical behaviour of Ni–Ti in the cathodic conditions used in molten carbonate fuel cells. *J Electroanal Chem* 2001;503:69–77. [http://dx.doi.org/10.1016/S0022-0728\(01\)00375-8](http://dx.doi.org/10.1016/S0022-0728(01)00375-8).
- [7] Albin V, Mendoza L, Goux A, Ringuedé A, Billard A, Briois P, et al. Morphological, structural and electrochemical analysis of sputter-deposited ceria and titania coatings for MCFC application. *J Power Sources* 2006;160:821–6. <http://dx.doi.org/10.1016/j.jpowsour.2006.04.066>.
- [8] Mendoza L, Albin V, Cassir M, Galtayries A. Electrochemical deposition of Co_3O_4 thin layers in order to protect the nickel-based molten carbonate fuel cell cathode. *J Electroanal Chem* 2003;548:95–107. [http://dx.doi.org/10.1016/S0022-0728\(03\)00228-6](http://dx.doi.org/10.1016/S0022-0728(03)00228-6).

- [9] Wijayasinghe A, Bergman B, Lagergren C. LiFeO₂–LiCoO₂–NiO materials for molten carbonate fuel cell cathodes. Part II. Fabrication and characterization of porous gas diffusion cathodes. *Solid State Ion* 2006;177:175–84. <http://dx.doi.org/10.1016/j.ssi.2005.10.019>.
- [10] Wijayasinghe A, Bergman B, Lagergren C. LiFeO₂–LiCoO₂–NiO materials for molten carbonate fuel cell cathodes. Part I: powder synthesis and material characterization. *Solid State Ion* 2006;177:165–73. <http://dx.doi.org/10.1016/j.ssi.2005.10.018>.
- [11] Meléndez-Ceballos A, Fernández-Valverde SM, Barrera-Díaz C, Albin V, Lair V, Ringuedé A, et al. TiO₂ protective coating processed by atomic layer deposition for the improvement of MCFC cathode. *Int J Hydrog Energy* 2013;38:13443–52. <http://dx.doi.org/10.1016/j.ijhydene.2013.07.083>.
- [12] Meléndez-Ceballos A, Albin V, Fernández-Valverde SM, Ringuedé A, Cassir M. Electrochemical properties of atomic layer deposition processed CeO₂ as a protective layer for the molten carbonate fuel cell cathode. *Electrochim Acta* 2014;140:174–81. <http://dx.doi.org/10.1016/j.electacta.2014.05.025>.
- [13] Meléndez-Ceballos A, Albin V, Ringuedé A, Fernández-Valverde SM, Cassir M. Electrochemical behavior of M_x-1O_x (M = Ti, Ce and Co) ultra-thin protective layers for MCFC cathode. *Int J Hydrog Energy* 2014;39:12233–41. <http://dx.doi.org/10.1016/j.ijhydene.2014.03.213>.
- [14] Heracleous E, Lemonidou AA. Ni–Nb–O mixed oxides as highly active and selective catalysts for ethene production via ethane oxidative dehydrogenation. Part I: characterization and catalytic performance. *J Catal* 2006;237:162–74. <http://dx.doi.org/10.1016/j.jcat.2005.11.002>.
- [15] Heracleous E, Lemonidou AA. Ni–Nb–O mixed oxides as highly active and selective catalysts for ethene production via ethane oxidative dehydrogenation. Part II: mechanistic aspects and kinetic modeling. *J Catal* 2006;237:175–89. <http://dx.doi.org/10.1016/j.jcat.2005.11.003>.
- [16] Qiao A, Kalevaru VN, Radnik J, Martin A. Oxidative dehydrogenation of ethane to ethylene over Ni–Nb–M–O catalysts: effect of promoter metal and CO₂-admixture on the performance. *Catal Today* 2016;264:144–51. <http://dx.doi.org/10.1016/j.cattod.2015.08.043>.
- [17] Takagaki A, Takahashi Y, Yin F, Takanabe K, Kubota J, Domen K. Highly dispersed niobium catalyst on carbon black by polymerized complex method as PEFC cathode catalyst. *J Electrochem Soc* 2009;156:B811–5. <http://dx.doi.org/10.1149/1.3125801>.
- [18] Ohnishi R, Katayama M, Takanabe K, Kubota J, Domen K. Niobium-based catalysts prepared by reactive radio-frequency magnetron sputtering and arc plasma methods as non-noble metal cathode catalysts for polymer electrolyte fuel cells. *Electrochim Acta* 2010;55:5393–400. <http://dx.doi.org/10.1016/j.electacta.2010.04.090>.
- [19] Nowak I, Ziolk M. Niobium compounds: preparation, characterization, and application in heterogeneous catalysis. *Chem Rev* 1999;99:3603–24.
- [20] Wachs IE, Jehng J-M, Deo G, Hu H, Arora N. Redox properties of niobium oxide catalysts. *Catal Today* 1996;28:199–205. [http://dx.doi.org/10.1016/0920-5861\(95\)00229-4](http://dx.doi.org/10.1016/0920-5861(95)00229-4).
- [21] Fang B, Liu X, Wang X, Duan S. The mechanism of surface modification of a MCFC anode. *J Electroanal Chem* 1998;441:65–8. [http://dx.doi.org/10.1016/S0022-0728\(97\)00202-7](http://dx.doi.org/10.1016/S0022-0728(97)00202-7).
- [22] Fang B, Chen H. A new candidate material for molten carbonate fuel cell cathodes. *J Electroanal Chem* 2001;501:128–31. [http://dx.doi.org/10.1016/S0022-0728\(01\)00379-5](http://dx.doi.org/10.1016/S0022-0728(01)00379-5).
- [23] Ahonen M, Pessa M, Suntola T. A study of ZnTe films grown on glass substrates using an atomic layer evaporation method. *Thin Solid Films* 1980;65:301–7. [http://dx.doi.org/10.1016/0040-6090\(80\)90240-0](http://dx.doi.org/10.1016/0040-6090(80)90240-0).
- [24] Haukka S, Kytökivi A, Lakomaa E-L, Lehtovirta U, Lindblad M, Lujala V, et al. The utilization of saturated gas-solid reactions in the preparation of heterogeneous catalysts. In: Poncelet G, Martens J, Delmon B, Jacobs PA, Grange P, editors. *Stud. Surf. Sci. Catal.*, vol. 91. Elsevier; 1995. p. 957–66. ISSN 0167-2991, ISBN 9780444820785, [http://dx.doi.org/10.1016/S0167-2991\(06\)81839-2](http://dx.doi.org/10.1016/S0167-2991(06)81839-2). (<http://www.sciencedirect.com/science/article/pii/S0167299106818392>).
- [25] Kukli K, Ritala M, Leskelä M, Lappalainen R. Niobium oxide thin films grown by atomic layer epitaxy. *Chem Vap Depos* 1998;4:29–34.
- [26] Moutiers G, Cassir M, Piolet C, Devynck J. Thermodynamic and voltammetric study of oxygen systems in molten Na₂CO₃-K₂CO₃ (56-44 mol.%) eutectic at 750°C. *Electrochim Acta* 1991;36:1063–71. [http://dx.doi.org/10.1016/0013-4686\(91\)85316-Y](http://dx.doi.org/10.1016/0013-4686(91)85316-Y).
- [27] Pecharsky VK, Zavalij PY. *Fundamentals of powder diffraction and structural characterization of materials*. 2nd ed. Spring Street, New York, NY 10013, USA: Springer; 2009.
- [28] Gomes MAB, Bulhões LO de S, Castro SC de, Damião AJ. The electrochromic process at Nb₂O₅ electrodes prepared by thermal oxidation of niobium. *J Electrochem Soc* 1990;137:3067–70. <http://dx.doi.org/10.1149/1.2086161>.
- [29] McIntyre NS, Cook MG. X-ray photoelectron studies on some oxides and hydroxides of cobalt, nickel, and copper. *Anal Chem* 1975;47:2208–13. <http://dx.doi.org/10.1021/ac60363a034>.
- [30] Matienzo J, Yin LI, Grim SO, Swartz WE. X-ray photoelectron spectroscopy of nickel compounds. *Inorg Chem* 1973;12:2762–9. <http://dx.doi.org/10.1021/ic50130a005>.
- [31] Mansour AN, Melendres CA. Characterization of α-Ni(OH)₂ by XPS. *Surf Sci Spectra* 1994;3:255–62. <http://dx.doi.org/10.1116/1.1247754>.
- [32] Venezia AM, Bertinello R, Deganello G. X-ray photoelectron spectroscopy investigation of pumice-supported nickel catalysts. *Surf Interface Anal* 1995;23:239–47. <http://dx.doi.org/10.1002/sia.740230408>.
- [33] Payne BP, Biesinger MC, McIntyre NS. The study of polycrystalline nickel metal oxidation by water vapour. *J Electron Spectrosc Relat Phenom* 2009;175:55–65. <http://dx.doi.org/10.1016/j.elspec.2009.07.006>.
- [34] Biesinger MC, Payne BP, Grosvenor AP, Lau LWM, Gerson AR, Smart RSC. Resolving surface chemical states in XPS analysis of first row transition metals, oxides and hydroxides: Cr, Mn, Fe, Co and Ni. *Appl Surf Sci* 2011;257:2717–30. <http://dx.doi.org/10.1016/j.apsusc.2010.10.051>.
- [35] Özer N, Chen D-G, Lampert CM. Preparation and properties of spin-coated Nb₂O₅ films by the sol-gel process for electrochromic applications. *Thin Solid Films* 1996;277:162–8. [http://dx.doi.org/10.1016/0040-6090\(95\)08011-2](http://dx.doi.org/10.1016/0040-6090(95)08011-2).
- [36] Rojas E, Delgado JJ, Guerrero-Pérez MO, Bañares MA. Performance of NiO and Ni–Nb–O active phases during the ethane ammoxidation into acetonitrile. *Catal Sci Technol* 2013;3:3173–82. <http://dx.doi.org/10.1039/C3CY00415E>.
- [37] Malinowska B. *Etude électrochimique du nickel en milieu carbonate fondu en vue de son application à la réalisation de cathodes de piles à combustibles*. Paris: Paris 6; 1996.
- [38] Aufray M, Manuel S, Fort Y, Eschbach J, Rouxel D, Vincent B. New synthesis of nanosized niobium oxides and lithium niobate particles and their characterization by XPS analysis. *J Nanosci Nanotechnol* 2009;9:4780–5. <http://dx.doi.org/10.1166/jnn.2009.1087>.

- [39] Kaufherr N, Eichorst DJ, Payne DA. X-ray photoelectron spectroscopy studies of alkoxide-derived lithium niobate. *J Vac Sci Technol A* 1996;14:299–305. <http://dx.doi.org/10.1116/1.579892>.
- [40] Trifonov AS, Lubenchenko AV, Polkin VI, Pavolotsky AB, Ketov SV, Louzguine-Luzgin DV. Difference in charge transport properties of Ni-Nb thin films with native and artificial oxide. *J Appl Phys* 2015;117:125704. <http://dx.doi.org/10.1063/1.4915935>.
- [41] Oku M, Tokuda H, Hirokawa K. Final states after Ni2p photoemission in the nickel–oxygen system. *J Electron Spectrosc Relat Phenom* 1991;53:201–11. [http://dx.doi.org/10.1016/0368-2048\(91\)85039-V](http://dx.doi.org/10.1016/0368-2048(91)85039-V).
- [42] Moses AW, Flores HGG, Kim J-G, Langell MA. Surface properties of LiCoO₂, LiNiO₂ and LiNi_{1-x}Co_xO₂. *Appl Surf Sci* 2007;253:4782–91. <http://dx.doi.org/10.1016/j.apsusc.2006.10.044>.
- [43] Pawlak DA, Ito M, Oku M, Shimamura K, Fukuda T. Interpretation of XPS O (1s) in mixed oxides proved on mixed perovskite crystals. *J Phys Chem B* 2002;106:504–7. <http://dx.doi.org/10.1021/jp012040a>.
- [44] Yazici MS, Selman JR. Dissolution of partially immersed nickel during in situ oxidation in molten carbonate: cyclic, stripping and square wave voltammetry measurements. *J Electroanal Chem* 1998;457:89–97. [http://dx.doi.org/10.1016/S0022-0728\(98\)00126-0](http://dx.doi.org/10.1016/S0022-0728(98)00126-0).
- [45] Antolini E. Behaviour of Ni, NiO and Li_xNi_{1-x}O in molten alkali carbonates. *J Mater Sci* 2000;35:1501–5. <http://dx.doi.org/10.1023/A:1004745332382>.
- [46] Nishina T, Takizawa K, Uchida I. Electrochemical characterization of in situ NiO formation in a molten carbonate. *J Electroanal Chem Interfacial Electrochem* 1989;263:87–96. [http://dx.doi.org/10.1016/0022-0728\(89\)80126-3](http://dx.doi.org/10.1016/0022-0728(89)80126-3).
- [47] Belhomme C, Cassir M, Tessier C, Berthoumieux E. Lithium depth profile in NiO molten carbonate fuel cell cathode by nuclear microprobe. *Electrochem Solid-State Lett* 2000;3:216–9. <http://dx.doi.org/10.1149/1.1391006>.
- [48] Escudero MJ, Ringuedé A, Cassir M, González-Ayuso T, Daza L. Porous nickel MCFC cathode coated by potentiostatically deposited cobalt oxide: III. Electrochemical behaviour in molten carbonate. *J Power Sources* 2007;171:261–7. <http://dx.doi.org/10.1016/j.jpowsour.2007.06.013>.

IV. Electrolyte modification with Cs and Rb additives

“Anybody who has been seriously engaged in scientific work of any kind realizes that over the entrance to the gates of the temple of science are written the words: Ye must have faith. It is a quality, which the scientist cannot dispense with.”

Max Planck

As already pointed out, one of the possibilities to improve the overall performance of the MCFC is by acting over the properties of its electrolyte. Hence, increasing the electrolyte conductivity or enhancing the diffusion of oxygen and carbon dioxide species could increment the power density produced by MCFCs. However, improving these parameters is delicate since the oxoacidity of the melt changes influencing cathode solubility. In order to increase the lifetime of MCFCs, without affecting their performance, we developed and tested ultra-thin conformal layers deposited by ALD to protect the cathode, in Chapter 0. In the present chapter, we propose the modification of the electrolyte, by additions of Cs or Rb ions, in order to improve the overall MCFC performance without reducing the expected stack lifetime.

Evaluating the performance of an electrolyte based in DC potentiometric or galvanometric methods is a relatively easy task when working at room temperature as in water-based solutions or in ionic liquids, but this is not the case when working in molten carbonate media at high temperatures. Electrode materials are difficult to select in such media since most metals oxidize and some noble metals as platinum and silver does not withstand the aggressive environment. Only gold can support being immersed in molten carbonates without being rapidly affected. However, when performing electrochemistry DC techniques such as cyclic voltammetry or chronopotentiometry, the electrode passivates after few cycles and re-polishing is necessary. In addition, DC techniques tend to modify the chemical equilibrium of the electrolyte when applying very low or very high potentials, an equilibrium that takes long time to be recovered. For those reasons, when working in molten carbonate electrolyte, less aggressive AC techniques such as electrochemical impedance spectroscopy (EIS) are preferred. The disadvantage of EIS is that data analysis is not a straightforward process since fitting through equivalent circuits is necessary. Nevertheless, EIS could be effectively used to determine interesting electrochemical parameters if the system is well known.

In our case, the molten carbonate system is well known and has been studied by several authors by EIS using gold as working electrode [23,106–112]. Since our objective is to determine if the addition of Cs and Rb in the electrolyte could improve its performance, we have chosen Nishina's reaction order analysis as a tool to evaluate the influence of Cs addition in molten Li-K carbonates. However, an improvement in the accuracy of Nishina's proposal was proposed by taking into account a Gerischer-type

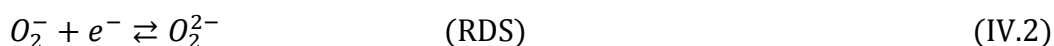
element leading to a better fit of the data obtained by EIS with our experimental setup. In the next sections, an extended discussion on the Gerischer element taken in account is presented.

IV.1. Theoretical approach

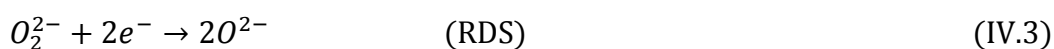
IV.1.1. Reaction-rate equations for oxygen reduction

As has been presented in the introduction chapter, the oxygen reduction mechanism is still not rigorously described in the literature since it can follow different reaction paths, according to literature, the most probable reduced oxygen species are O_2^{2-} , O_2^- and CO_4^{2-} being their mechanisms: the superoxide path (SOP), the peroxide path (POP) and the Peroxycarbonate (POCP) respectively; expressed as follows:

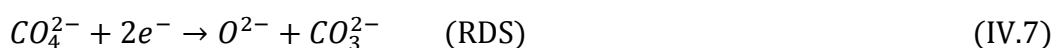
SOP:



POP:



POCP:



For analyzing the kinetic behavior of oxygen species, a rate-equation can be derived for each of the mechanisms previously mentioned following the “quasi-equilibrium method” described by Bockris and Srinivasan [113] that assumes one reaction of the mechanism as the rate limiting step (RDS); since the rest of the reactions are assumed to be much faster, they are considered in quasi-equilibrium. Thus, considering the rate equation of the RDS and the equilibrium conditions of the other reactions, the overall current-potential could be derived. This method was used by Prins-Jansen and Makkus [114,115] to determine the reaction-rate equations for the mechanisms described above and assuming the reaction marked RDS as the rate-limiting step leading to an equation of the form:

$$i_n = i_0^0 (C_{O_2}^0)^{B_1} (C_{CO_2}^0)^{B_2} \left(\left(\frac{C_{CO_2}}{C_{CO_2}^0} \right)^{p_1} \left(\frac{C_{O_2}}{C_{O_2}^0} \right)^{q_1} e^{\frac{\alpha_a F \eta}{RT}} - \left(\frac{C_{CO_2}}{C_{CO_2}^0} \right)^{p_2} \left(\frac{C_{O_2}}{C_{O_2}^0} \right)^{q_2} e^{\frac{-\alpha_c F \eta}{RT}} \right) \quad (IV.8)$$

Where i_0^0 is the standard exchange current density, B_1 and B_2 are the reaction orders with which the dependencies of the reaction rates on gas compositions are established, powers p_1 and q_1 follow the stoichiometry of the reactions relating oxygen and carbon dioxide concentrations to the concentration of the chemical reactant. Powers p_2 and q_2 are determined by the stoichiometry of the products of the RDS and their relation with the concentration of oxygen and carbon dioxide. The apparent transfer coefficients α_a and α_c are determined by the preceding or succeeding reactions from the RDS, meaning that α_c is given by the transfer coefficient α plus the number of electron-transfer steps preceding the RDS, similarly, α_a is given by the number of electrochemical steps following the RDS minus the transfer coefficient α . For all the mechanisms, we can assume the first electrochemical step as rate-determining, so $\alpha_c = 0.5$. In Table IV.1, the values for all the coefficients of the three mechanisms are shown.

Table IV.1- Coefficients for reaction IV.12 for the three mechanisms described (eq. IV.1 to IV.7) [114].

Mechanism	p_1	q_1	p_2	q_2	B_1	B_2	α_a	α_c
Superoxide	0	-2	$\frac{3}{4}$	$-\frac{1}{2}$	0.625	-0.75	2.5	0.5
Peroxide	0	-2	$\frac{1}{2}$	-1	0.375	-1.25	1.5	0.5
Peroximonocarbonate	0	-1	$\frac{1}{2}$	0	0.375	-0.25	1.5	0.5

Coefficients can vary if a different RDS is taken or if partial coverage of the electrode is considered for adsorbed species, Makkus [115] has proposed several

different coefficients and has taken into account several RDS to analyze; nevertheless, the ones shown in Table IV.1 are considered the more likely [114]. Now, considering that the previously described reaction rate equation takes in consideration that all the reaction steps are carried out on the electrode surface, we should assume that the dissolved oxygen and carbon dioxide do not react until they reach the electrode surface. Since this assumption is not valid due to the low stability of molecular oxygen in the molten carbonate media, the chemical reactions preceding the electrochemical steps are assumed to be completed in the bulk or at the electrolyte-gas interphase. So with these new assumptions, the reaction rate equation can be rewritten as:

$$i_n = i_0^0 (C_{O_2}^0)^{B_1} (C_{CO_2}^0)^{B_2} \left(\left(\frac{C_{CO_2}}{C_{CO_2}^0} \right)^q e^{\alpha_a F \eta} - \left(\frac{C_{Ox}}{C_{Ox}^0} \right)^p e^{-\frac{\alpha_c F \eta}{RT}} \right) \quad (IV.9)$$

Where C_{Ox} refers now to the electroactive oxide species O_2^- , O_2^{2-} or CO_4^{2-} depending of the mechanism SOP, POP or POCP, respectively. The coefficients of the equation remain the same as per Table IV.1 except for p and q which new values are noted in Table IV.2.

Table IV.2- New p and q coefficients for reaction IV.9 [114].

Mechanism	p	q
Superoxide	1	-2
Peroxide	1	-2
Peroxicarbonate	1	-1

Taking into account that the concentration of oxygen and carbon dioxide involved species are related to the partial pressure of these gases, we can assume that Henry's law applies for molecular dissolved carbon dioxide, so $C_{CO_2}^0 = H_{CO_2} P_{CO_2}$. Since there are linear dependences on the gas composition from Henry's law, but no dependence between $C_{CO_2}^0$ and P_{O_2} ; the dependences of the electro-active species involved in each mechanism can be defined as the $\log C_{Ox}^0 / \log P_{O_2}$ and $\log C_{Ox}^0 / \log P_{CO_2}$ as per Table IV.3, where C_{Ox}^0 is the concentration of the involved oxide species. These reaction orders can then be related to the inverse of the resistance as per the following expression:

$$\frac{1}{R} = \frac{1}{R_0} P_{O_2}^{\beta_1} P_{CO_2}^{\beta_2} \quad (IV.10)$$

This expression will be useful for us to analyze the data deduced from electrochemical impedance spectroscopy (EIS) in section IV.2.2.

Table IV.3- Theoretical reaction orders for the different mechanisms as a function of gas partial pressure.

Mechanism	$\beta_1 = \log C_{Ox}^0/P_{O_2}$	$\beta_2 = \log C_{Ox}^0/P_{CO_2}$
Superoxide	0.75	-0.5
Peroxide	0.5	-1
Peroxicarbonate	0.5	0

The previously exposed approach to determine the reaction rate equations and reaction orders is useful to determine the dominant species through the analysis of the charge transfer resistance of the reactions taking place at the electrode at different oxygen and carbon dioxide partial pressures. Nevertheless, it does not consider that all the oxygen species of the SOP, POP or POCP could be present simultaneously at the electrode. In this case, we will have to take into consideration the reaction order analysis proposed by Nishina *et al.* [116] to elucidate the dominant mixed oxygen species and their diffusion coefficients by using the EIS as main tool. This approach is discussed below.

IV.1.2. Nishina's reaction order analysis.

For the analysis of impedance spectra Nishina *et al.* [116] related the Warburg coefficient σ to the diffusing species O_2^- , O_2^{2-} , CO_4^{2-} and CO_2 that can be present simultaneously at the surface of the electrode by means of a reaction order analysis of the reactions of each mechanism previously described (eq. IV.1 to IV.7). Thus, species O^{2-} was neglected, considering that: (i) impedance is taken at the rest potential, so the bulk concentration of the reaction products has to be high enough to keep its activity more constant than the bulk concentration of the reactants; (ii) the concentration of O^{2-} is very small compared to the concentration of CO_3^{2-} , since the dissociation constant $K_d = p_{CO_2} \cdot [O^{2-}]/[CO_3^{2-}]$ is very small; (iii) the standard electrode potential of the reduction of O_2^- to O^{2-} and O_2^{2-} to O^{2-} are by far more cathodic than the rest potential of the reference electrode; and (iv) the reaction product is considered to be CO_3^{2-} and reaction IV.4 is very fast and reversible. It was also considered that the relation between the partial pressures of oxygen and carbon dioxide and the oxygen species O_2^- , O_2^{2-} and CO_4^{2-} is given by:

$$[O_2^-] = K_1 P_{O_2}^{0.75} P_{CO_2}^{-0.5} \quad (IV.10)$$

$$[O_2^{2-}] = K_2 P_{O_2}^{0.5} P_{CO_2}^{-1.0} \quad (IV.11)$$

$$[CO_4^{2-}] = K_3 P_{O_2}^{0.5} \quad (IV.12)$$

The Warburg coefficient σ , under conditions of semi-infinite diffusion is defined as:

$$\sigma = \sum \frac{RT}{n_i^2 F^2 \sqrt{2}} \left(\frac{1}{c_i \sqrt{D_i}} \right) \quad (IV.13)$$

As in this case the measured coefficient σ is a function of the simultaneous reactions taking place in parallel at the electrode, it should be regarded as an apparent Warburg coefficient σ_{app} . In this case, it will be a function of the concentrations of the reactants present at the electrode. Hence, it could be expressed as:

$$\sigma_{app} = f([O_2^-], [O_2^{2-}], [CO_4^{2-}], [CO_2]) \quad (IV.14)$$

Where [] means the bulk concentration of a species in the melt. Using Eqs IV.10, IV.11 and IV.12 for $[O_2^-]$, $[O_2^{2-}]$ and $[CO_4^{2-}]$, respectively, and Henry's law ($[CO_2] = K_h P_{CO_2}$), where K_h is the Henry constant for CO_2 at 650 °C for $[CO_2]$, we can express eq. IV.14 as a complicated function of P_{O_2} and P_{CO_2} . This complex relation can be simplified, if the following six mixed diffusion cases can apply:

1. $[O_2^-] > [O_2^{2-}], [CO_4^{2-}]$; O_2^-/CO_2 mixed diffusion case, where σ_{app} is given by:

$$\sigma_{app} P_{CO_2} = a P_{O_2}^{-0.75} P_{CO_2}^{1.5} + b \quad (IV.15)$$

or

$$\sigma_{app} P_{O_2}^{0.75} P_{CO_2}^{-0.5} = a + b P_{O_2}^{0.75} P_{CO_2}^{-1.5} \quad (IV.16)$$

2. $[O_2^{2-}] > [O_2^-], [CO_4^{2-}]$; O_2^{2-}/CO_2 mixed diffusion case:

$$\sigma_{app} P_{CO_2} = a P_{O_2}^{-0.5} P_{CO_2}^2 + b \quad (IV.17)$$

or

$$\sigma_{app} P_{O_2}^{0.5} P_{CO_2}^{-1} = a + b P_{O_2}^{0.5} P_{CO_2}^{-2} \quad (IV.18)$$

3. $[CO_2] > [O_2^-], [O_2^{2-}] > [CO_4^{2-}]; O_2^-/O_2^{2-}$ mixed diffusion case:

$$\sigma_{app}^{-1} P_{O_2}^{-0.5} P_{CO_2} = a P_{O_2}^{0.25} P_{CO_2}^{0.5} + b \quad (IV.19)$$

4. $[CO_4^{2-}] > [O_2^-], [O_2^{2-}]; CO_4^{2-}/CO_2$ mixed diffusion case:

$$\sigma_{app} P_{O_2}^{0.5} P_{CO_2}^{-1} = a P_{O_2}^{-0.5} P_{CO_2} + b \quad (IV.20)$$

5. $[CO_2] > [O_2^-], [CO_4^{2-}] > [O_2^{2-}]; O_2^-/CO_4^{2-}$ mixed diffusion case:

$$\sigma_{app}^{-1} P_{O_2}^{-0.75} P_{CO_2}^{0.5} = a P_{O_2}^{-0.25} P_{CO_2}^{0.5} + b \quad (IV.21)$$

or

$$\sigma_{app}^{-1} P_{O_2}^{-0.5} = a + b P_{O_2}^{0.25} P_{CO_2}^{-0.5} \quad (IV.22)$$

6. $[CO_2] > [O_2^{2-}], [CO_4^{2-}] > [O_2^-]; O_2^{2-}/CO_4^{2-}$ mixed diffusion case:

$$\sigma_{app}^{-1} P_{O_2}^{0.5} P_{CO_2} = a P_{CO_2} + b \quad (IV.23)$$

or

$$\sigma_{app}^{-1} P_{O_2}^{-0.5} = a + b P_{CO_2}^{-1} \quad (IV.24)$$

By substituting equations IV.10, IV.11 or IV.12 and Henry's law for $[CO_2]$ in eq. IV.13, we can obtain an equation relating P_{O_2} and P_{CO_2} to σ_{app} . For example, the form of eq. IV.13 for the first mixed diffusion case O_2^-/CO_2 can be expressed as follows:

$$\sigma_{app} = \frac{RT}{3^2 F^2 \sqrt{2} K_1 P_{O_2}^{0.75} P_{CO_2}^{-0.5} \sqrt{D_{O_2^-}}} + \frac{RT}{1.5^2 F^2 \sqrt{2} K_h P_{CO_2} \sqrt{D_{CO_2}}} \quad (IV.25)$$

By using this equation, constants a and b of equations IV.15 and IV.16 can be deduced:

$$a = \frac{RT}{3^2 F^2 \sqrt{2} K_1 \sqrt{D_{O_2^-}}} \quad (IV.26)$$

$$b = \frac{RT}{1.5^2 F^2 \sqrt{2} K_h \sqrt{D_{CO_2}}} \quad (IV.27)$$

When graphing eqs. IV.15 to IV.24, a straight line should be obtained for the mixed diffusion case that dominates the reaction; in such case, the slopes and intercepts of the linear regression of the points will represent respectively the constants a and b for that specific diffusion case. Hence, if K_x and/or K_h are known one could deduce the respective diffusion coefficient. This is important, since the diffusion coefficient is directly related to the speed at which the oxygen reduction reaction and the neutralization reaction can take place. Thus, it can be a direct indicator of the performance of a given system. Higher values of the diffusion coefficients mean a faster reaction rate, and a better cell performance in MCFC conditions.

The approaches described in sections IV.1.1. and IV.1.2. will now be developed for the practical evaluation of the influence of additives such as Cs and Rb in the molten carbonate electrolyte. EIS will be used as tool to deduce the Warburg coefficient with a golden flag electrode completely immersed in the molten carbonates. The additive will be incorporated gradually into the electrolyte and the EIS will be taken at different P_{O_2} and P_{CO_2} .

IV.2. Oxygen and CO₂ kinetics in Cs modified electrolyte

Cs₂CO₃ was added to the standard Li-K (62-38 mol %) eutectic mixture, first at 3 mol% and after at 5 mol%, the electrochemical behavior was investigated by EIS on a gold flag electrode. The analysis of the impedance data was carried out with two circuit models. The first one was proposed by Nishina *et al.* [116] takes into account a Randles-Elsher type circuit with a Warburg element, as shown in Figure IV.1a). Considering that the Warburg semi-infinite diffusion does not describe the data in a proper way, in a second model, depicted in Figure IV.1b), we selected a Gerischer element for processing EIS data, as shown in

Figure IV.2. Gerischer element was developed by Heinz Gerischer in early 50's [117–119] to model an electroactive species that undergoes an heterogeneous chemical reaction in the bulk.

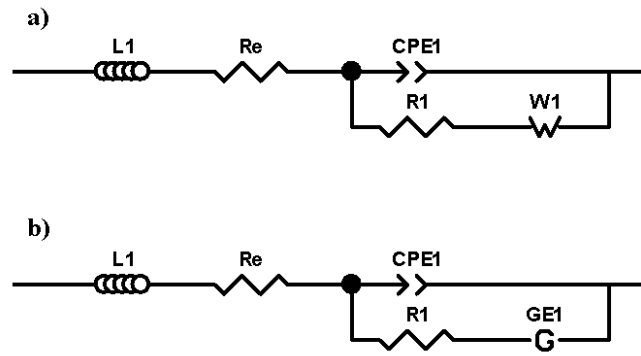


Figure IV.1- Equivalent circuits used for the analysis of the EIS data, a) considering a Warburg diffusion element, b) considering a Gerischer type element.

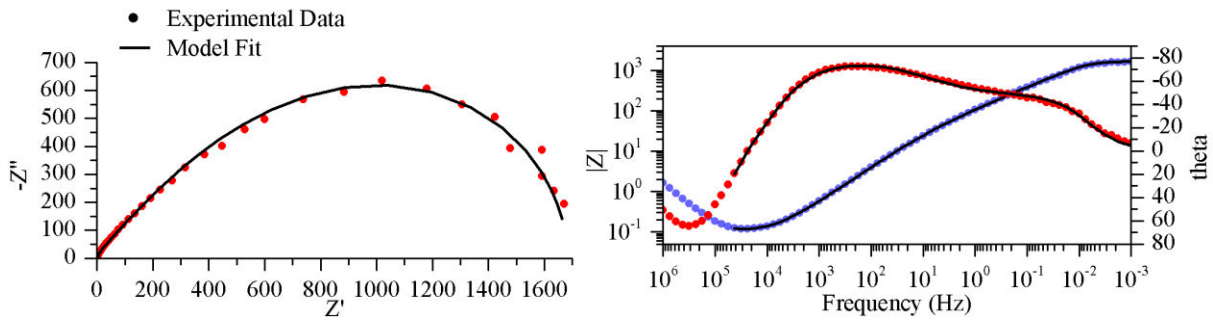


Figure IV.2- Example of the EIS data acquired in our experiments fitted with circuit b) of Figure IV.1.

The Gerischer function is the same as the finite-length Warburg impedance at the high frequency limit and yields pure resistive behavior in the low frequency limit, but differs from it since it could present an arc closer to the real axis in the Z plane. The equation describing the Gerischer element is as follows:

$$Z(\omega) = \frac{1}{Y_0 \sqrt{k + j\omega}} \quad (IV.28)$$

Where k is a rate constant parameter in s^{-1} and Y_0 is an admittance in $S \cdot s^{1/2}$ equivalent to the Warburg coefficient σ by applying the equation:

$$\sigma = \frac{1}{\sqrt{2} \cdot Y_0} \quad (IV.29)$$

This coefficient allows calculating the diffusion coefficients of the oxidized or reduced species as per the method described by Nishina.

IV.2.1. Data analysis by Nishina's diffusion cases

For analysing the six mixed diffusion cases, we compared the Warburg fit of the high frequency data with the Gerischer fit like (as in

Figure IV.2), the Gerischer coefficient Y_0 obtained from the fit was then used to plot the six mixed diffusion cases after being transformed into the equivalent Warburg coefficient σ by using equation IV.29. The diagrams, corresponding to the six mixed diffusion cases, were plotted for each of the three different Cs contents (0, 3 and 5 mol %). The plots for 3 mol % of Cs are shown in

Figure IV.3 (1 to 6), with a linear tendency for cases 1 and 4 (R^2 of 0.99 and 0.98, respectively), although more pronounced for the superoxide mechanism (case 1). The results obtained for the samples with 0 and 5 mol % of Cs (not shown here), show a linear tendency only in the case 1, which tends to confirm the hypothesis of a predominant superoxide reduction mechanism; therefore, this mechanism was adopted for all the tested electrolytes. Figure IV.4 shows the mixed diffusion case $[O_2^-] > [O_2^{2-}], [CO_4^{2-}]; O_2^-/CO_2$ plot for all the electrolytes studied. The slopes and intercepts of the linear regression for case 1, considering each Cs content, were used to deduce the values of a and b . A comparison between their values obtained by the Warburg fitting and the Gerischer fitting is shown in Table IV.4. **Erreur ! Source du renvoi introuvable.** These values were then substituted in equations IV.26 and IV.27 to calculate the values of $K_{1\sqrt{D_{O_2^-}}}$ and $K_{h\sqrt{D_{CO_2}}}$. The values obtained with the Warburg and Gerischer fits are shown in Table IV.5

Table IV.4- Values of a and b obtained from the slope and intercepts of the mixed diffusion case $[O_2^-] > [O_2^{2-}], [CO_4^{2-}]; O_2^-/CO_2$ by Warburg and Gerischer fitting for 0, 3 and 5 mol-% of Cs in Li-K at 650 °C.

Added Cs mol %	Gerischer Fit		Warburg Fit	
	a	b	a	b
0	88.44	33.73	78.13	33.22
3	96.8	30.47	91.66	29.42
5	82.23	23.99	75.72	23.77

Table IV.5- Values obtained with a and b of linear regression of plot for the mixed diffusion case $[O_2^-] > [O_2^{2-}], [CO_4^{2-}]; O_2^-/CO_2$ by Warburg and Gerischer fitting for 0, 3 and 5 mol-% of Cs in Li-K at 650 °C.

added Cs (mol%)	From Gerischer Fit		From Warburg Fit	
	$K_h\sqrt{D_{CO_2}}$	$K_1\sqrt{D_{O_2^-}}$	$K_h\sqrt{D_{CO_2}}$	$K_1\sqrt{D_{O_2^-}}$
0	7.67981E-9	7.32398E-10	7.80E-09	8.29E-10
3	8.50138E-9	6.69135E-10	8.81E-09	7.07E-10
5	1.08005E-8	7.8768E-10	1.09E-08	8.55E-10

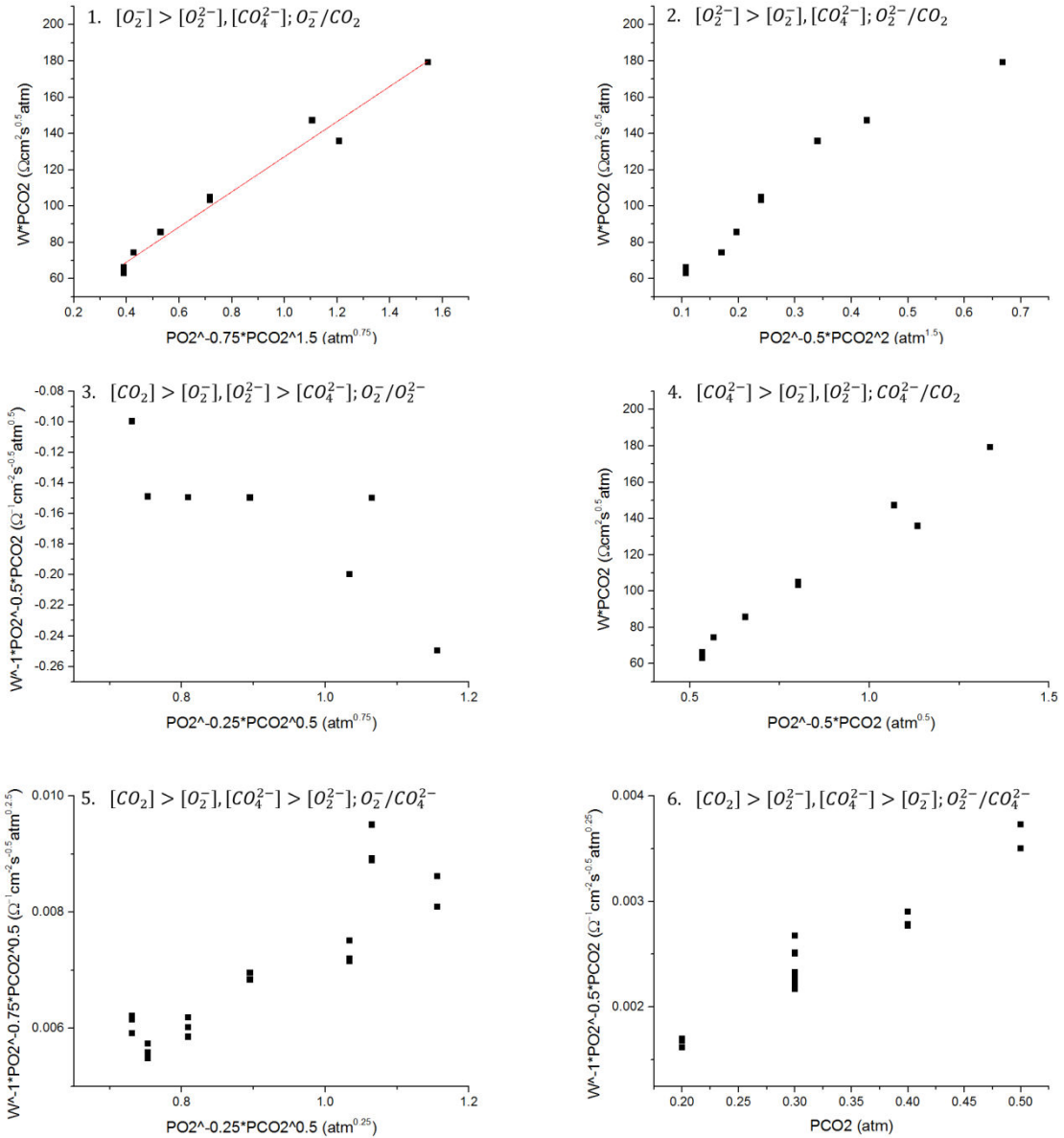


Figure IV.3- Six mixed diffusion cases analysis taken the Gerischer coefficient of fitted EIS data, from case 1 to 6 as described in section 4.1.2 only for 3 mol% added Cs in Li-K Eutectic at 650 °C.

Diffusion coefficients $D_{O_2^-}$ and D_{CO_2} can be calculated if constants K_h and K_1 are known. T. Nishina *et al.* have calculated the values of these constants from the literature, being $K_1 = 1.708 \cdot 10^{-7}$ and $K_h = 7.174 \cdot 10^{-6}$ for Li-K (62–38 mol. %) at 650 °C [23]. Of course, the values of the constants should vary also with the added Cs, but in this case the amount of added Cs is very small and we can suppose that constants K_h and K_1 should not change significantly. The diffusion coefficient variation with added Cs is shown in Figure IV.5, where also a comparison between the Warburg and Gerischer calculated coefficients as denoted.

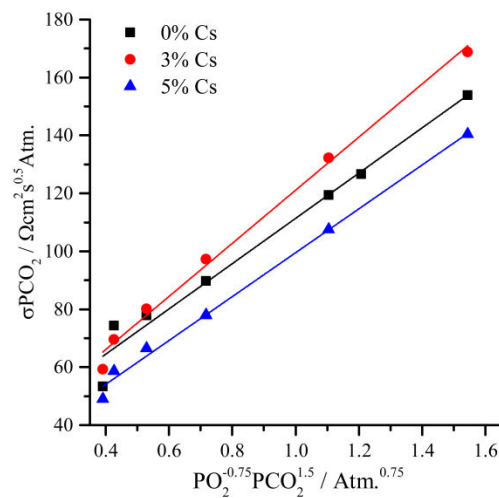


Figure IV.4- Mixed diffusion case $[O_2^-] > [O_2^{2-}]$, $[CO_4^{2-}]$; O_2^-/CO_2 plot for 0, 3 and 5 mol% added Cs on Li-K eutectic at 650 °C, the slopes and intercepts were taken to calculate the diffusion coefficients of the involved species.

As observed in Figure IV.5, Warburg and Gerischer diffusion coefficients change significantly for $D_{O_2^-}$, the highest value being obtained with the Warburg fitting. Nevertheless, the tendency is the same in both Warburg and Gerischer fittings, where the 3 mol% added Cs decreases almost by half for Warburg series and one third for Gerischer series, then it increases for 5 mol% of Cs up to a value of $2.1 \cdot 10^{-5} \text{ cm}^2 \cdot \text{s}^{-1}$ for Gerischer fitting and $2.5 \cdot 10^{-5} \text{ cm}^2 \cdot \text{s}^{-1}$ for Warburg fitting. These values are in both cases higher than the initial ones of $1.8 \cdot 10^{-5} \text{ cm}^2 \cdot \text{s}^{-1}$ and $2.3 \cdot 10^{-5} \text{ cm}^2 \cdot \text{s}^{-1}$ for Gerischer and Warburg fittings, respectively.

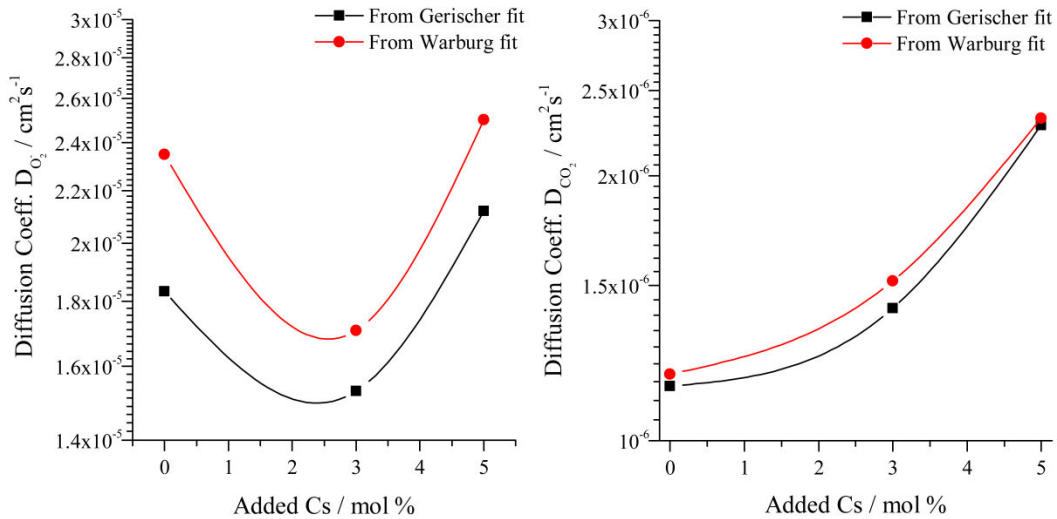


Figure IV.5- Comparison of the diffusion coefficients $D_{O_2^-}$ and D_{CO_2} obtained from Warburg and Gerischer fitting at 0, 3 and 5 mol% added Cs on Li-K eutectic at 650 °C.

In the case of D_{CO_2} , the difference between Warburg and Gerischer fittings is not significant, the tendency is the same in both cases and increases with increasing Cs contents up to a value of $2.2 \cdot 10^{-6} \text{ cm}^2 \cdot \text{s}^{-1}$. This increase in both $D_{O_2^-}$ and D_{CO_2} is important since it demonstrates the influence of an additive on the behaviour of a commonly used electrolyte in MCFC. This increase in mass transport could be due to an increase in the solubility of CO_2 or a more stable oxygen intermediate species at the surface of the electrode slowing the recombination with CO_2 . In both cases, the overall performance of MCFC cell increases when using Cs additive. However, the small increase of the oxoacidity of the molten LI-K carbonates when adding Cs will slightly favour NiO dissolution. In order to control this cathode dissolution, the use of ultra-thin protective layers, fully developed in chapter 0, is compulsory.

IV.2.2. The charge transfer resistance dependency on P_{O_2} and P_{CO_2}

As explained in section IV.1.1. , the charge transfer resistance can be used to estimate the reaction order from equation IV.10 by plotting the logarithm of the inverse of charge transfer resistance *vs.* the logarithm of P_{O_2} and P_{CO_2} where the slope will be the value of β_1 and β_2 respectively.

$$\frac{1}{R} = \frac{1}{R_0} P_{O_2}^{\beta_1} P_{CO_2}^{\beta_2} \quad (\text{IV.10})$$

Figure IV.6 shows the plots of $1/R$ with respect to P_{O_2} and P_{CO_2} for 0, 3 and 5 mol% of Cs respectively, where it can be observed that Cs content changes the slopes. The values of β_1 and β_2 taken from the slopes are shown in Table IV.6. If we compare them with the theoretical values, calculated from the oxygen reduction pathways from Table IV.3, we can note that at 0 mol % Cs the tendency is clearly that of superoxide path, with a value close to 1 for β_1 instead of 0.75 and a very close value of β_2 to -0.5. Addition of 3 and 5 mol% of Cs does not change this tendency since the value of β_1 is always high and the value of β_2 gets lower with increasing Cs content favoring superoxide mechanism due to an increased oxoacidity, as predicted by thermodynamic studies [120,121].

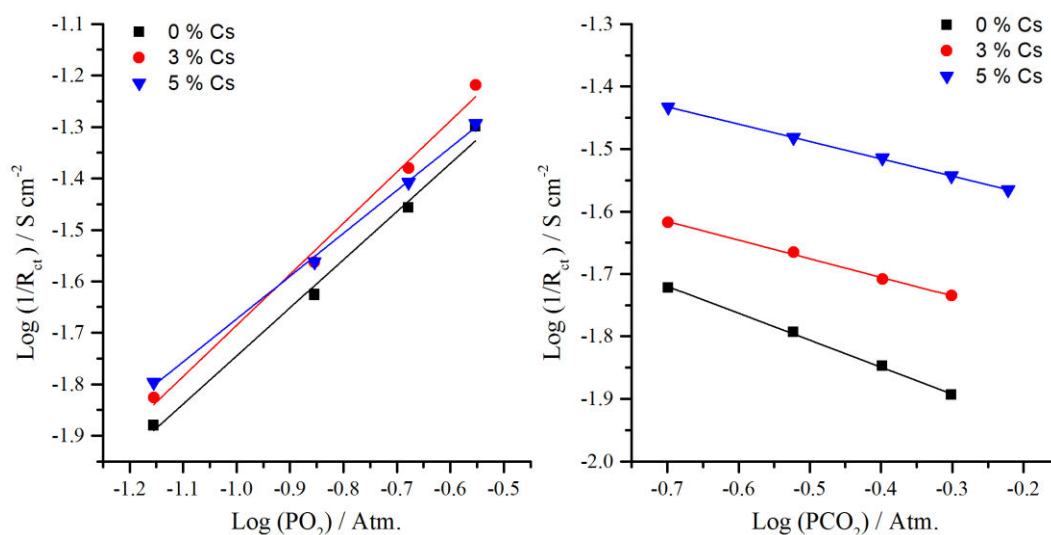


Figure IV.6- P_{O_2} and P_{CO_2} partial pressure dependency of $1/R_{ct}$ plot for 0, 3 and 5 mol% added Cs on Li-K carbonate mixture at 650 °C.

Furthermore, analyzing the charge transfer resistance dependency on partial pressure, we can note that in the case of P_{O_2} variation, 0, 3 and 5 mol % have the same tendency: a decrease in charge transfer resistance by increasing P_{O_2} , which is understandable since increasing oxygen partial pressure favors the oxygen reaction whatever the mechanism followed (SOP, POP or POCP). For P_{CO_2} , we observe that increasing Cs content reduces the charge transfer resistance; the lowest values of charge transfer resistance for the whole P_{CO_2} range are reached with 5 mol % of added Cs. In the case of P_{CO_2} , the tendency is to increase the charge transfer resistance with

increasing P_{CO_2} . Nevertheless, Cs addition is favorable for the charge transfer resistance, influencing specially the behavior under different P_{CO_2} .

Table IV.6- Values of β_1 and β_2 taken from the slopes of Figure IV.6.

Added Cs Mol. %	β_1	β_2
0	0.93	-0.43
3	0.99	-0.29
5	0.83	-0.27

As shown in the previous sections, Cs addition improves the overall performance of the molten Li-K eutectic; however, the previous sections studied this performance by means of a gold flag electrode completely immersed in the molten carbonates. In order to evaluate the improvement of additives in real MCFC conditions, it is important to substitute the gold electrode by the state of the art porous NiO cathode.

IV.3. Porous NiO behavior in Cs and Rb modified electrolytes

Rubidium addition to molten Li-K and electrolyte could be also beneficial for the overall MCFC performance; Rb and Cs additives have been previously studied by Kojima *et al.* [122] and Lair *et al.* [123], showing that they increase electrolyte conductivity. However, the behavior of NiO electrode has been scarcely analyzed with such additives. In this section, we will evaluate the MCFC cathode electrode with both Cs and Rb additions to molten Li-K eutectic and Cs addition to Li-Na electrolyte to elucidate if they could improve the cathode performance on MCFC working conditions. The behavior of the porous Ni cathode in either Li-K or Li-Na eutectics modified by the addition of 5 mol. % of Cs or Rb is analyzed by the OCP evolution over time, which is a key parameter since it reflects the equilibration behavior of Ni in the molten carbonate media as it has been already explained in section III.1.4. The additives should modify this equilibration time since they modify the oxoacidity of the carbonates. OCP of the Ni cathode immersed in Li-K carbonate eutectic modified with 5 mol. % added Cs or Rb and the non-modified one is shown in Figure IV.7. As it can be observed, OCP evolution is very similar for both Cs and Rb additives, both reach the equilibrium about 90 h faster than pristine Li-K electrolyte. However, the potential reached is not the same, Ni porous cathode

immersed in Cs-enriched Li-K reaches an equilibrium potential of $-0.01\text{ V vs Ag/Ag}^+$, the same as pristine Li-K, while the cathode in Li-K modified with Rb reaches an equilibrium potential of $-0.16\text{ V vs Ag/Ag}^+$. However, the potential reached on the Rb modified electrolyte is not far from the expected cathode equilibrium potential of 0 V vs Ag/Ag^+ and is acceptable for MCFC operation.

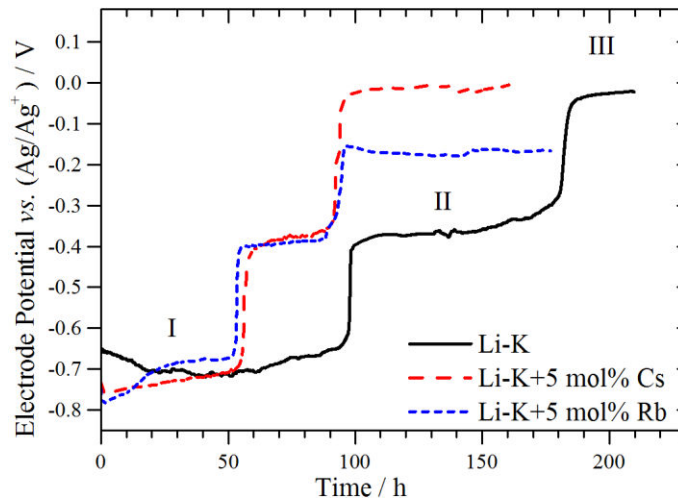


Figure IV.7- OCP evolution of porous Ni cathode immersed in Li-K eutectic (black line), Li-K + 5 mol % of Cs (red line) and Li-K + 5 mol% of Rb (blue line) at 650 °C under 70/30 % air/CO₂ atmosphere at ambient pressure.

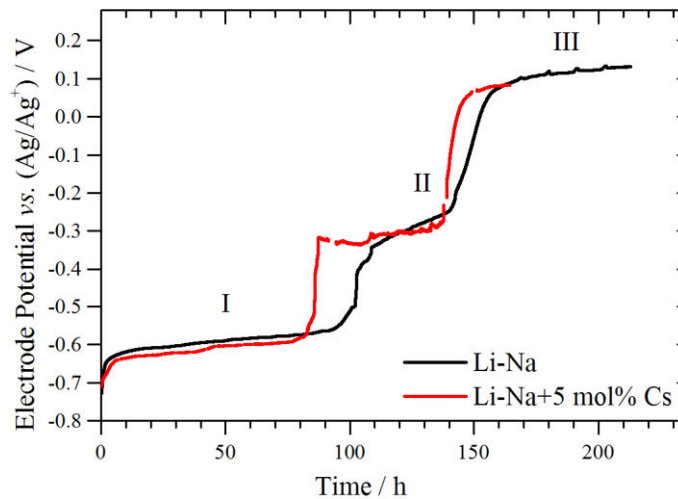


Figure IV.8- OCP evolution of porous Ni cathode immersed in Li-Na eutectic (black line) and Li-Na + 5 mol % of Cs (red line) at 650 °C under 70/30 % air/CO₂ atmosphere at ambient pressure.

OCP evolution of porous Ni cathode immersed in Li-Na electrolyte modified with 5 mol. % of Cs is shown in Figure IV.8. The cathode behavior is close to that of pristine

Li-Na electrolyte, showing a slightly faster equilibration by reaching a potential of -0.08 V *vs* Ag/Ag⁺, not so far from the cathode potential reached with pristine Li-Na eutectic (0.12 V *vs* Ag/Ag⁺). The fact that porous Ni electrode, immersed in Cs modified Li-Na electrolyte, did not present a faster evolution is probably related to the lower oxoacidity of Li-Na with respect to Li-K.

For evaluating the performance of the cathode immersed in modified electrolytes, EIS data were collected each 10 h during the duration of the OCP experiment, and analyzed by fitting to an equivalent circuit. Figure IV.9 shows the equivalent circuit used and an example of data fitting. From this fitting, the charge transfer resistance (R_{ct}), mass transfer resistance (R_{mt}) and total resistance ($R_{tot} = R_e + R_{ct} + R_{mt}$) were deduced.

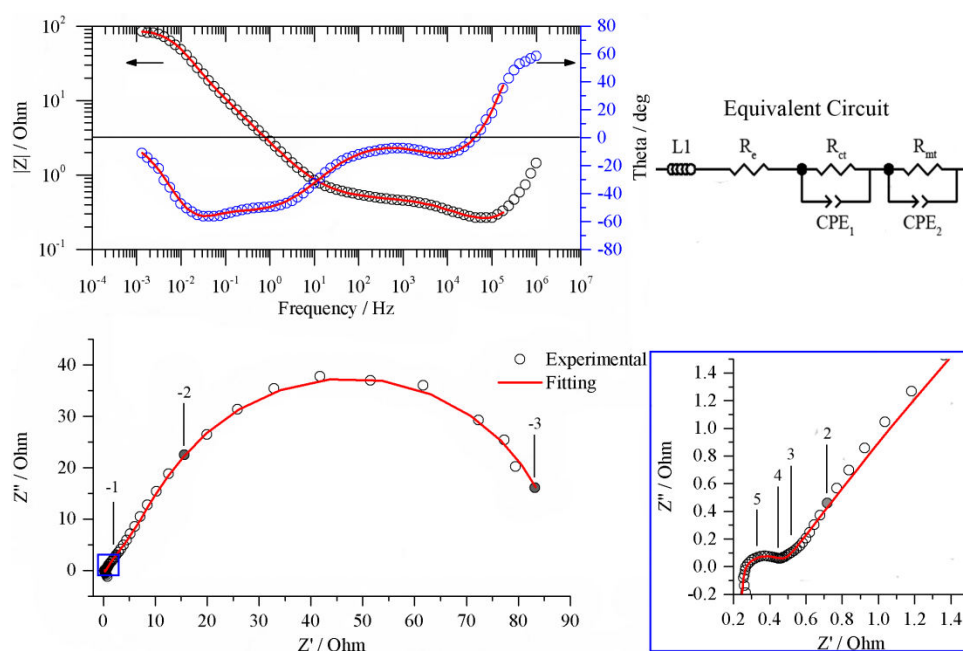


Figure IV.9- EIS data fitting with equivalent circuit shown in upper right corner. Data corresponds to 110 h porous Ni cathode immersion in Li-K eutectic carbonate melt with no additive at 650 °C. Numbers over data points indicate the logarithm of the frequency of the marked point.

Figure IV.10 shows the charge transfer resistance and total resistance evolution of Ni porous electrode immersed in Li-K electrolyte modified with Cs, Rb and the non-modified one *versus* immersion time (OCP duration). As can be appreciated in the graph, charge transfer resistance and total resistance present a similar behavior, resistance increases when the porous Ni oxidizes to form NiO and then decreases again when the

NiO is lithiated *in situ* to become $\text{Li}_x\text{Ni}_{1-x}\text{O}$. However, Cs and Rb modified electrolytes influence the behavior of the porous Ni cathode accelerating the oxidation-lithiation process, which is in accordance with the OCP behavior previously discussed. Nevertheless, resistance behaves differently between Cs and Rb modified electrolytes; the first one has an abrupt R_{ct} increase up to 90 ohms at 65 h of immersion time while the second one reaches only a 5 ohms peak at 91 h of immersion. At the mentioned times, OCP curves do not show any special feature. At 65 h, a R_{ct} resistance peak can be noted in the case of Cs-modified electrolyte, corresponding to the beginning of plateau II. While in the case of Rb-modified eutectic, the peak at 91 h corresponds to the end of plateau II, similarly to the behavior of Ni in pristine Li-K eutectic. Hence, Rb and Cs additions affect the evolution of porous Ni in a positive way, since they favor Ni oxidation. Regarding R_{ct} diminution due to NiO lithiation, in Cs-modified electrolyte, R_{ct} reaches a final value of 5 ohms, while with the Rb-modified electrolyte, R_{ct} reaches a value of only 0.3 ohms.

Compared to the cathode immersed in pristine Li-K eutectic, where R_{ct} peak is around 4.5 ohms at 178 h and the lowest value afterwards is 3 ohms at 225 h, Cs and Rb-modified electrolytes perform positively, being Rb the one with the least R_{ct} value. As can be noted in the right side graph of Figure IV.10, total resistance presents the same behavior as charge transfer resistance; in effect, resistance peaks appear at 70 h and 91 h for Cs and Rb-modified electrolytes, with values of 392 and 283 ohms, respectively. These values are lower than for pristine Li-K peak at 190 h (422 ohms). Then, as NiO is lithiated, the values decrease to a minimum of 40, 111 and 358 ohms for added Cs, Rb and pristine Li-K electrolytes, respectively. In this case, the electrode immersed in Cs-modified Li-K eutectic reaches the lowest R_{tot} value of 40 ohms, in contrast with R_{ct} value, which is the highest. This is due to a major contribution to total resistance of R_{mt} , which is lower in the case of Cs-modified eutectic, in good agreement with previous results in section IV.2. where diffusion coefficients are favored by the presence of Cs. However, R_{mt} values in Rb-modified electrolyte show that this electrolyte also performs better than pristine Li-K, reaching a lower total resistance of 111 ohms, favorable for MCFC operation.

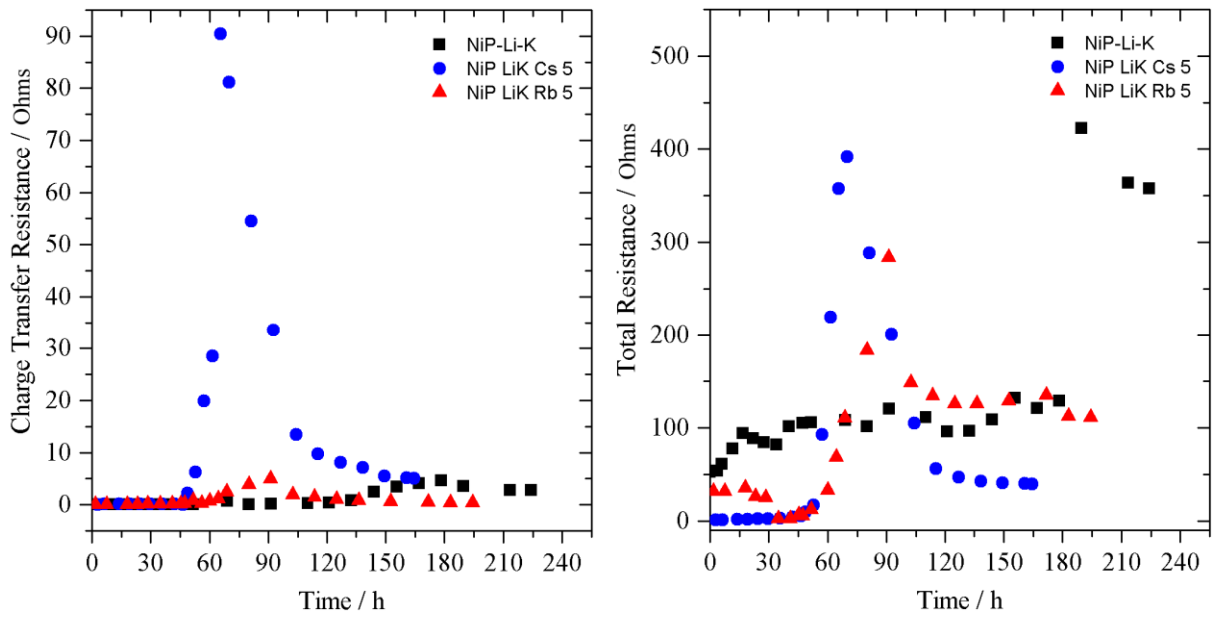


Figure IV.10- Porous Ni electrode charge transfer and total resistance evolution over OCP duration for pristine Li-K electrolyte (squares), 5 mol % added Cs (circles) and 5 mol % added Rb (triangles) at 650 °C under 70/30 % air/CO₂ atmosphere at ambient pressure.

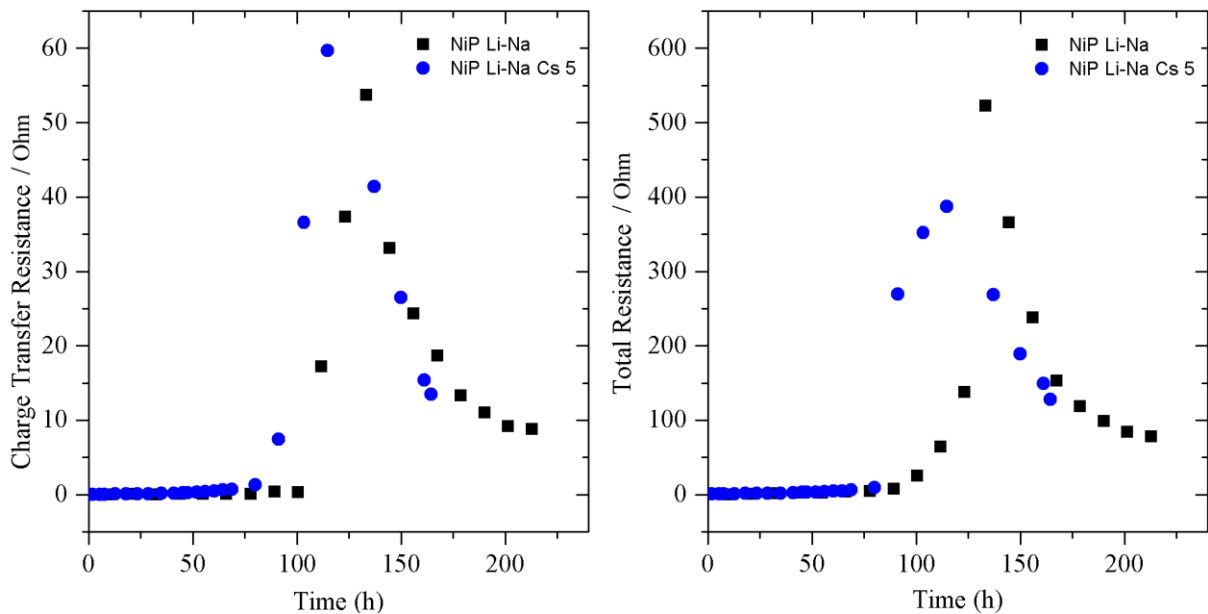


Figure IV.11- Porous Ni electrode charge transfer and total resistance evolution over OCP duration for pristine Li-Na electrolyte (squares) and 5 mol % added Cs (circles) at 650 °C under 70/30 % air/CO₂ atmosphere at ambient pressure.

In the case of Li-Na eutectic modified with 5 mol % of Cs, R_{ct} and R_{tot} , evolutions over time are not so different from pristine Li-Na. As shown in Figure IV.11, in the case of Cs modified electrolyte, cathode presents a R_{ct} peak of 60 ohms at 115 h, while for pristine Li-Na this peak appears at 134 h with a value of 54 ohms. Then, the resistance decreases to a minimum of 13 ohms for Li-Na + 5 mol % of Cs and 9 ohms for pristine Li-Na eutectic. Total resistance evolution follows the same pattern, increasing to a maximum of 388 ohms at 115 h and 522 ohms at 134 h for Cs modified Li-Na and pristine Li-Na electrolytes, respectively. In both cases, Cs modified electrolyte present a higher R_{ct} and R_{tot} values than pristine Li-Na electrolyte, which is less interesting for MCFC application.

IV.4. Conclusions

In this chapter, we have successfully tested modified electrolytes by the addition of Cs and Rb ions, proving that electrolyte modification is an important route for improving the cathode behavior (OCP stabilization, resistance evolution,...), in particular the kinetics of oxygen reduction and, therefore, MCFC performance. First, oxygen reduction reaction kinetics was investigated at an inert gold electrode by EIS fitted with two different circuits, one proposed by Nishina *et al.* containing a Warburg element and another proposed by us, containing instead a Gerischer element. The diffusion coefficients $D_{O_2^-}$ and D_{CO_2} calculated by using our fitting were $1.8 \cdot 10^{-5} \text{ cm}^2 \cdot \text{s}^{-1}$ and $1.15 \cdot 10^{-6} \text{ cm}^2 \cdot \text{s}^{-1}$, respectively, for the non-modified Li-K electrolyte and $2.1 \cdot 10^{-5} \text{ cm}^2 \cdot \text{s}^{-1}$ and $2.2 \cdot 10^{-6} \text{ cm}^2 \cdot \text{s}^{-1}$ for Li-K electrolyte with 5 mol % added Cs. The increase in diffusion rates evidenced that Cs additive improves the oxygen reduction rate. In second instance, we analyzed the inverse of charge transfer resistance dependence to P_{O_2} and P_{CO_2} and found a clear tendency towards the superoxide mechanism, which was evidenced by the reaction orders obtained from the $\log R_{ct}$ vs \log of P_{O_2} and P_{CO_2} plots. Additionally, Cs additions under higher P_{CO_2} tends to decrease charge transfer resistance which is in agreement with a higher diffusion coefficient. Tests were also carried out to investigate the influence of Cs and Rb modified electrolytes on the state-of-the-art porous Ni cathode. From OCP evolution over time, it was found that for Li-K electrolyte Cs and Rb additions favor a faster equilibration of the cathode and lower the total resistance of the

electrode after reaching equilibrium. Thus, better performance from the modified electrolytes is expected in MCFCs.

From these results, we can conclude also that oxoacidity of the molten carbonates plays a very important role in the charge and mass transfer properties; nevertheless, increasing the oxoacidity of the molten carbonates increases Ni dissolution, but as it has been pointed out in Chapter III, cathode protection with ultra-thin layers can be implemented to effectively reduce cathode dissolution. However, it is important to remember that results presented herein were obtained by using a half-cell configuration in bulk molten electrolytes, where the environment is much more aggressive due to bulk convection and nickel dissolution and modification occurs in a more rapid way. Further tests in a single cell composed with the commercial Ni cathode, Ni-Al anode and porous LiAlO_2 matrix supporting the modified Li-K electrolyte, should be performed to have a better insight on the behavior of anode and cathode and overall cell performance.

IV.5. Scientific papers

From the work carried out for evaluating electrolyte modification with Cs and Rb additives, two scientific papers were published in recognized peer reviewed journals. These publications are included in the next pages.



A kinetic approach on the effect of Cs addition on oxygen reduction for MCFC application



A. Meléndez-Ceballos*, V. Albin, V. Lair, A. Ringuedé, M. Cassir**

Institut de Recherche de Chimie Paris, CNRS–Chimie ParisTech, 11 rue Pierre et Marie Curie, 75005 Paris, France

ARTICLE INFO

Article history:

Received 23 June 2015

Received in revised form 21 September 2015

Accepted 13 October 2015

Available online 17 October 2015

Keywords:

Molten Carbonate Fuel Cells

Kinetics

Oxygen reduction

Cesium additive

Gerischer model

ABSTRACT

Optimization of the molten carbonate electrolyte is the most challenging topic in order to increase the lifetime and performance of the molten carbonate fuel cell (MCFC). Besides controlling electrolyte properties such as stability, conductivity, volatility, surface tension, molar volumes etc., it is mandatory to reduce the dissolution of the $\text{Li}_x\text{Ni}_{1-x}\text{O}$ state-of-the-art cathode. Furthermore, the nature of the eutectic also may influence the electrode kinetics and, in particular, at the cathode side where the reduction reaction is known to be slow. The conventional molten salt used in MCFC devices is composed by $\text{Li}_2\text{CO}_3\text{--K}_2\text{CO}_3$ (62/38 mol%), which has a better performance at temperatures below 600 °C than $\text{Li}_2\text{CO}_3\text{/Na}_2\text{CO}_3$ (52/48 mol%) electrolyte but presents a higher Ni solubility than the Li–Na electrolyte. To improve the properties of the Li–K eutectics towards the ORR (oxygen reduction reaction), heavy alkali cations such as Cs or Rb can be used as additives in the electrolyte. The present work is dedicated to a thorough analysis of the oxygen reduction kinetics in $\text{Li}_2\text{CO}_3\text{--K}_2\text{CO}_3$ (62/38 mol%) eutectic containing small amounts of Cs_2CO_3 by means of impedance spectroscopy and fitting performed using Warburg and Gerischer models, showing the favourable effect of this additive and convenience between the two model approaches.

© 2015 Elsevier Ltd. All rights reserved.

1. Introduction

Optimization of the molten carbonate electrolyte is the most challenging topic in order to increase the lifetime and performance of the molten carbonate fuel cell (MCFC). Apart of controlling the properties of such electrolytes, such as stability, conductivity, volatility, surface tension and molar volumes, it is compulsory to reduce the dissolution of the $\text{Li}_x\text{Ni}_{1-x}\text{O}$ state-of-the-art cathode and avoid, in general, the corrosion of electrode and interconnect materials. Furthermore, the nature of the eutectic and its oxobasic properties also may influence favourably the electrode kinetics and, in particular, at the cathode side where the reduction reaction is known to be slow. Even though the conventional molten salt used in MCFC devices is composed by $\text{Li}_2\text{CO}_3\text{--K}_2\text{CO}_3$ (62/38 mol%), $\text{Li}_2\text{CO}_3\text{/Na}_2\text{CO}_3$ (52/48 mol%) electrolyte has interesting properties, such as higher ionic conductivity, better cell performances in certain conditions [1–5] and lower effective volatility [3,6]. The solubility of nickel cathode is significantly lower in the Li–Na eutectic than in Li–K [5,7]; nevertheless, Li–Na eutectic presents

some drawbacks. Below 600 °C, Li–Na cells have lower performances than Li–K cells. This is probably caused by an increase on cathode polarisation due to complex reaction mechanisms, involving peroxide and superoxide ions and/or ion migration [8,9]. Other factors affecting the electrode kinetics are the lower solubility of oxygen in this eutectic and a higher surface tension; the first mentioned parameter seems to be the major cause of low performances at low temperatures [10].

Both mentioned eutectics are therefore interesting to investigate, knowing that they need to be optimised by adding some species improving their properties. It is not our purpose here to gather the literature dedicated to additives, this has been done in several papers, among which an earlier one on their influence on conductivity [11]. According to some authors, heavy alkali cations such as Cs or Rb additives have a favourable influence on MCFC performance. Experiments have been reported in single cells with $\text{Li}_{0.75}\text{Cs}_{0.25}$ carbonate electrolytes showing higher cell potentials, lower cathode and anode overpotentials than $\text{Li}_{0.68}\text{K}_{0.32}$ or $\text{Li}_{0.52}\text{Na}_{0.48}$, usual carbonate eutectics [12]. Cs_2CO_3 is thermally stable up to 700 °C and some $\text{Li}_2\text{CO}_3\text{--Cs}_2\text{CO}_3$ mixtures have melting points below 550 °C [13]. These mixtures have also lower surface tension [14] and greater oxygen solubility as well as increased electrode kinetics, especially at low temperature. But they also have a disadvantage because of their relative acidity which promotes NiO dissolution; however, this drawback may be

* Corresponding author. Tel.: +33155421237.

** Corresponding author.

E-mail addresses: arturo.melendez@chimie-paristech.fr (A. Meléndez-Ceballos), michel.cassir@chimie-paristech.fr, arturo.melendez@chimie-paristech.fr (M. Cassir).

compensated by using Li-rich $\text{Li}_2\text{CO}_3\text{--K}_2\text{CO}_3\text{--Cs}_2\text{CO}_3$ mixtures (NiO solubility being inversely proportional to Li content in the melt) and operating at slightly reduced temperatures. Interesting patent reports the improvement of a MCFC with a Li–K or Li–Na electrolyte modified by the addition of different proportions of Cs or Rb (from 0.05 % to 25 %) [15,16]. This solution is extremely attractive because the favourable role of Cs (or Rb) can be combined to the usual properties of Li–Na or Li–K classical melts.

Apart from a recent paper on the effect of Cs and Rb additives on the conductivity of $\text{Li}_2\text{CO}_3\text{--K}_2\text{CO}_3$ [11], no systematic analysis on the influence of these alkali species on the electrochemical behaviour of the Ni cathode has ever been published. This led us to dedicate this first of a series paper to a thorough analysis of the oxygen reduction kinetics in Li–K carbonate eutectic containing small amounts of Cs_2CO_3 additive by means of impedance spectroscopy and by fitting two different models: a Warburg model and a Gerischer model. The first one proposed by Nishina et al. [17] and the second one proposed by Makkus et al. [18]. Both analysis approaches are combined to extract valuable information as the diffusion coefficients D_{CO_2} and D_{O_2} . In previous studies, we have analysed by DC techniques, such as cyclic voltammetry at gold flag electrodes, the behaviour of reduced oxygen species responsible of the oxygen reduction kinetics; however, these techniques are not easy to handle in the case of molten carbonates because of passivation phenomena at the gold working electrode and perturbations of the natural diffusion regime caused by thermal convection in such high temperature molten media [19–22]. AC techniques such as Electrochemical Impedance Spectroscopy (EIS) have shown usefulness in studying complex electrochemical systems such as the MCFC; the technique operating around the open circuit potential (OCP) has the advantage of being less aggressive than cyclic voltammetry [17,23–27].

2. Experimental

Lithium and potassium carbonates, of high grade purity >98 % (Sigma–Aldrich[®]), were mixed in a proportion of 62:38 mol%. Cs_2CO_3 was mixed to the carbonate eutectic calculating the weight of the dried carbonate powder in order to add 1, 3 and 5 mol% of the additive. The high-temperature electrochemical cell was a single-compartment crucible of dimensions $70 \times 50 \text{ mm}^2$ contained in an alumina Al_2O_3 reactor of dimensions $250 \times 60 \text{ mm}^2$ hermetically sealed by a stainless steel cover with a Viton O-ring. The whole electrochemical set-up has been fully described in previous papers [22,23]. Temperature was maintained constant at 650°C by means of a calibrated chromel/alumel thermocouple protected by an alumina tube and a temperature controller. The standard cathode atmosphere was a mixture of $\text{O}_2/\text{CO}_2/\text{Ar}$ (14:30:56 Atm.%) with a total flow of 50 mL min^{-1} , of high grade purity gas (Air Liquide[®]) at a pressure of 1 atmosphere. For kinetic studies the partial pressure of O_2 and CO_2 was varied as indicated in Table 1. After stabilizing the molten carbonate eutectic under the selected cathode atmosphere for at least 8 h, the working electrode was immersed in the melt and electrochemical measurements were performed.

Table 1
Gas compositions tested.

Gas Composition $\text{O}_2/\text{CO}_2/\text{Ar}$ Atm. %	Gas Composition $\text{O}_2/\text{CO}_2/\text{Ar}$ Atm. %
7/30/63	14/20/66
14/30/56	14/30/56
21/30/49	14/40/46
28/30/42	14/50/36

The electrochemical experimental data was collected using a potentiostat/galvanostat (AutoLab[®] PGSTAT-302N with FRA module). A three-electrode system was used, the working electrode being a gold flag ($10 \times 10 \times 0.5 \text{ mm}$) polished between each atmosphere change with SiC sand paper up to grain 4000, the counter electrode was a gold wire and the reference electrode a silver wire dipped into an Ag_2SO_4 ($10^{-1} \text{ mol kg}^{-1}$) saturated $\text{Li}_2\text{CO}_3\text{--K}_2\text{CO}_3$ eutectic contained in an alumina tube sealed by a porous alumina membrane. The parameters used for impedance measurements were the following: scanning frequencies set from 10^6 to 10^{-3} Hz , with 11 points per decade, and signal amplitude of 5 mV respecting the system linearity. The fitting of the equivalent circuit was carried out with the software Z-View[®] V3.3e. It is worth noting that R_{ct} obtained from data fittings is normalised considering the geometric surface area of the electrode.

3. Results and discussion

3.1. EIS data fitting

We processed our EIS data according to two different fitting approaches. The first one is that proposed by Nishina et al. assuming a Randles–Ershler circuit (Fig. 1a) in a limited frequency range between 1 MHz and 100 mHz (Fig. 2a) and semi-infinite diffusion through a Warburg element, W [17]. Even though our results are roughly congruent with those of Nishina *et al.*, as shown in Fig. 1b, EIS data obtained do not follow the Warburg semi-infinite diffusion, but a stationary diffusion regime as shown in Fig. 1b. Hence, to improve data treatment, a second approach consisting of a Randles–Ershler circuit shown in Fig. 2b, was adopted [18,28]. In such model, a Gerischer element, G , representing homogenous-reaction impedance, replaces the Warburg element. A good fitting was obtained with χ^2 error of around 10^{-5} . An illustration of this fitting is given in the Nyquist and Bode plots of Fig. 3. Gerischer and Warburg coefficients, respectively Y_0 (in $\text{S s}^{1/2}$) and σ (in $\Omega \text{ s}^{-1/2}$), are related as follows [29]:

$$\sigma = \frac{1}{\sqrt{2} \cdot Y_0} \quad (10)$$

In our study, the Gerischer coefficient will be transformed into its Warburg equivalent through Eq. (10) and will be denoted: σ_{GE} (in $\Omega \text{ s}^{-1/2}$). This procedure will allow us to follow in a more accurate way the reaction order analysis proposed by Nishina *et al.*, where the Warburg coefficient is related to the partial pressures of O_2 and CO_2 [17]. Since we are using Nishina's approach to evaluate the influence of Cs addition, it will be briefly described in Section 3.3.

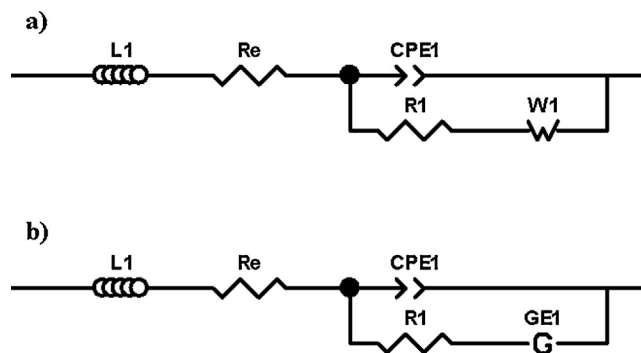


Fig. 1. Randles–Ershler equivalent circuit for: a) Warburg fitting and b) Gerischer fitting models. Electrolyte resistance (R_e), Constant Phase Element ascribed to double layer capacitance (CPE1), charge transfer resistance (R_1) and Warburg (W) or Gerischer (G) elements taken into account.

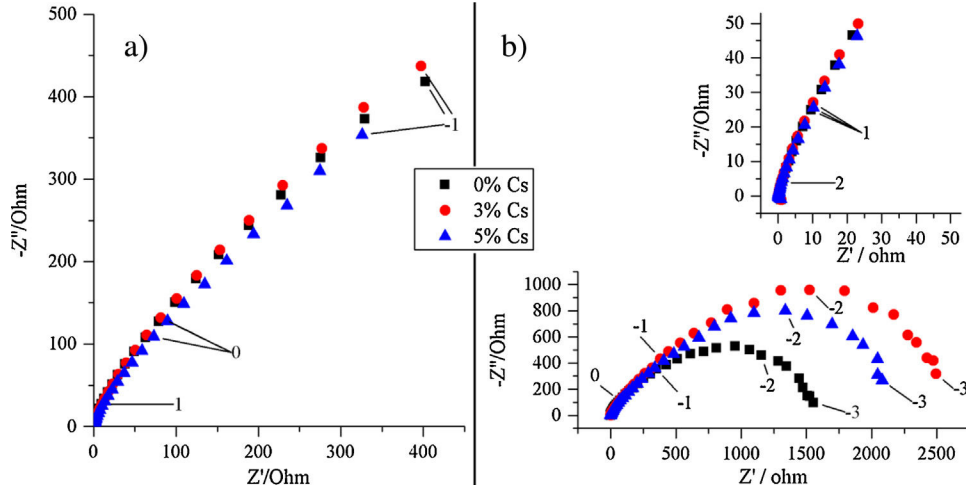


Fig. 2. EIS Nyquist diagrams: a) for Warburg fitting and b) for Gerischer fitting and detail of the same. Additions of 0, 3 and 5 mol.% of Cs in Li–K carbonates eutectic, at 650 °C. Gas composition 14/50/36 O₂/CO₂/Ar Atm.%.

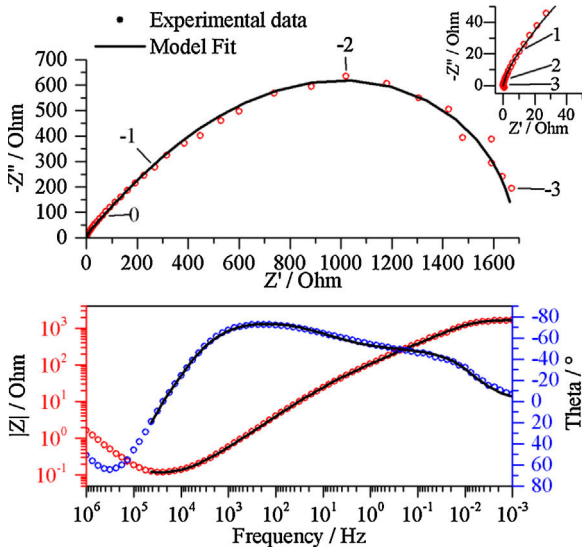


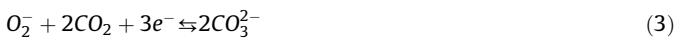
Fig. 3. Nyquist and Bode diagrams representing Gerischer model fitting, with addition of 5 mol.% of Cs in LiK carbonates eutectic at 650 °C and gas composition 14/50/36 O₂/CO₂/Ar Atm.%.

3.2. Assumed possible mechanisms for oxygen reaction

As proposed by different authors, there are three main possible mechanisms for the oxygen reaction under molten carbonate. Appleby and Nicholson [30–33] have described both superoxide and peroxide mechanisms. In a simplified scheme expressed as:



$$[O_2^-] = K_1 P_{O_2}^{0.75} P_{CO_2}^{-0.5} \quad (2)$$



$$[O_2^{2-}] = K_2 P_{O_2}^{0.5} P_{CO_2}^{-1.0} \quad (5)$$



The presence of superoxide and peroxide ion has been confirmed by Electron Spin Resonance and Raman Spectroscopy in Na₂CO₃, K₂CO₃, Li₂CO₃ and Li–K eutectics [34–37].

The existence of CO₄²⁻ has been suggested from electrochemical measurements [38], even though this species has never been detected by other techniques. Thus, a third possible mechanism involving this species has been proposed by Selman et al. [38]:

Peroxy monocarbonate Path (POMCP)



$$[CO_4^{2-}] = K_3 P_{O_2}^{0.5} \quad (8)$$



Eqs. (3),(6) and (9) can be described in a series of steps, e.g. Eq. (3) can be given as:



In this work, we will adopt the hypothesis of Nishina et al. stating that the oxygen reduction process is limited by the neutralization reaction between oxide ions and CO₂ (Eq. (3c)) [17]. Then, by identifying the species controlling the mixed diffusion process (CO₂ and oxygen species), we can elucidate the reaction mechanism and from the data obtained, evidence the influence of Cs addition.

3.3. $D_{O_2^-}$ and D_{CO_2} coefficients calculation form Warburg and Gerischer fittings

Warburg coefficient, σ , under semi-infinite diffusion is given as follows:

$$\sigma = \sum \frac{RT}{n_i^2 F^2 \sqrt{2}} \left(\frac{1}{C_i \sqrt{D_i}} \right) \quad (11)$$

Where i is the diffusing species, n_i the electron number per molecule of species i , C and D are the concentration and the diffusion coefficient respectively, while R and F keep their usual meanings and T is the temperature (in K).

As proposed by Nishina *et al.*, the following hypothesis are assumed:

1. $1/c_{CO_3^{2-}} \sqrt{D_{CO_3^{2-}}}$ is negligible compared to the other $1/\sqrt{iD_i}$ terms, because CO_3^{2-} concentration is that of the molten carbonate;
2. When SOP, POP or POMCP mechanisms take place simultaneously, diffusing species: O_2^- , O_2^{2-} , CO_4^{2-} and CO_2 have to be considered;
3. O_2^- concentration is neglected due to the oxoacidic conditions inherent to oxygen reduction in the presence of CO_2

In the case of multiple parallel reaction paths, σ and σ_{GE} do not reflect the reaction order of a specific reaction path but a mixture of them; thus, an apparent Warburg diffusion coefficient can be expressed as:

$$\sigma_{app} = f([O_2^-], [O_2^{2-}], [CO_4^{2-}], [CO_2]) \quad (12)$$

Where $[]$ means the bulk concentration of a species in the melt. Using Eqs. (2), (5) and (8) for $[O_2^-]$, $[O_2^{2-}]$ and $[CO_4^{2-}]$ respectively, and Henry's law for $[CO_2]$, we can deduce the following relation:

$$[CO_2] = K_h P_{CO_2} \quad (13)$$

Where K_h is the Henry constant for CO_2 at 650 °C.

We analyzed six different cases of mixed diffusion as proposed by Nishina *et al.* The one that better corresponds to our data is the case of the superoxide described as follows:

$$[O_2^-] > [O_2^{2-}], [CO_4^{2-}]; O_2^-/CO_2 \text{ mixed diffusion case}$$

$$\sigma_{app} P_{CO_2} = a P_{O_2}^{-0.75} P_{CO_2}^{1.5} + b \quad (14)$$

The graph in Fig. 4 corresponding to the above description has a good linear trend for all the samples. The rest of the cases did not have a linear trend and are not shown in this paper. If we consider Eq. (14) and extend it for both O_2^- and CO_2 species based on Eq. (3), it can be then rewritten as follows:

$$\sigma_{app} = \frac{RT}{3^2 F^2 \sqrt{2} K_1 P_{O_2}^{0.75} P_{CO_2}^{-0.5} \sqrt{D_{O_2^-}}} + \frac{RT}{1.5^2 F^2 \sqrt{2} K_h P_{CO_2} \sqrt{D_{CO_2}}} \quad (15)$$

Where K_1 is the Henry constant of oxygen gas at 650 °C

By using this equation, constants a and b of Eq. (14) can be deduced:

$$a = \frac{RT}{3^2 F^2 \sqrt{2} K_1 \sqrt{D_{O_2^-}}} \quad (16)$$

$$b = \frac{RT}{1.5^2 F^2 \sqrt{2} K_h \sqrt{D_{CO_2}}} \quad (17)$$

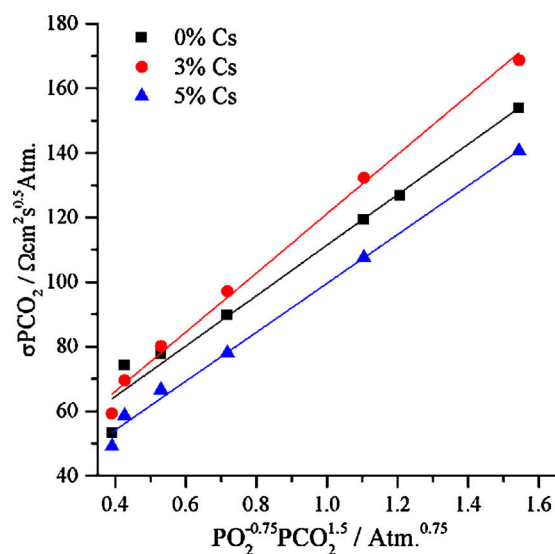


Fig. 4. Reaction order plots of the Warburg coefficient in the case of O_2^-/CO_2 mixed diffusion at 650 °C and different Cs contents in Li-K carbonates eutectic.

The slopes and intercepts of the lines in Fig. 4 are respectively the parameters a and b of Eq. (14) for each sample with different content of Cs. Values of both constants for each Cs content are shown in Table 2. The diffusion coefficient of the involved species can be obtained from Eq. (16) and (17) if the value of K_1 and K_h are known. T. Nishina *et al.* calculated the values of these constants based on the literature, being $K_1 = 1.708 \cdot 10^{-7}$ and $K_h = 7.174 \cdot 10^{-6}$ for $Li_2CO_3-K_2CO_3$ (62–38 mol. %) at 650 °C [17]. Even though addition of Cs_2CO_3 might affect the calculated value of K_1 , we assume that the small amount added in our case will have a negligible impact on this constant.

Figs. 5 and 6 summarize the evolution of the diffusion coefficients $D_{O_2^-}$ and D_{CO_2} with respect to the added % Cs for the coefficients obtained, respectively, from the Warburg and Gerischer fits. Although the tendency is similar in both cases, there are some discrepancies in the data obtained, especially for O_2^- diffusion. Data will be deduced in priority from the Gerischer model, since we consider it as more accurate. Contrarily to what we expected in the case of O_2^- diffusion, no clear trend can be deduced. At 3% of Cs, $D_{O_2^-}$ only drops from a value of $1.8 \cdot 10^{-5} \text{ cm}^2 \text{ s}^{-1}$ to $1.5 \cdot 10^{-5} \text{ cm}^2 \text{ s}^{-1}$. At 5% addition of Cs, $D_{O_2^-}$ value increases to $2.1 \cdot 10^{-5} \text{ cm}^2 \text{ s}^{-1}$. At this stage, it is difficult to conclude on the behaviour of $D_{O_2^-}$ and further investigation is required. In the case of CO_2 , a clear trend is observed, D_{CO_2} increases with the addition of Cs reactant from the initial value of $1.1 \cdot 10^{-6} \text{ cm}^2 \text{ s}^{-1}$ to $2.3 \cdot 10^{-6} \text{ cm}^2 \text{ s}^{-1}$, which favours the reduction process involving this species.

3.4. Analysis of charge transfer resistance

As part of the Randles–Ershler equivalent circuit fitting, the charge transfer resistance contribution R_1 was obtained and its dependence with the partial pressure variations analysed.

Table 2
Values of a and b parameters obtained from the linear fittings in Fig. 4.

Added Cs mol %	Gerischer fit		Warburg fit	
	a	b	a	b
0	88.44	33.73	78.13	33.22
3	96.8	30.47	91.66	29.42
5	82.23	23.99	75.72	23.77

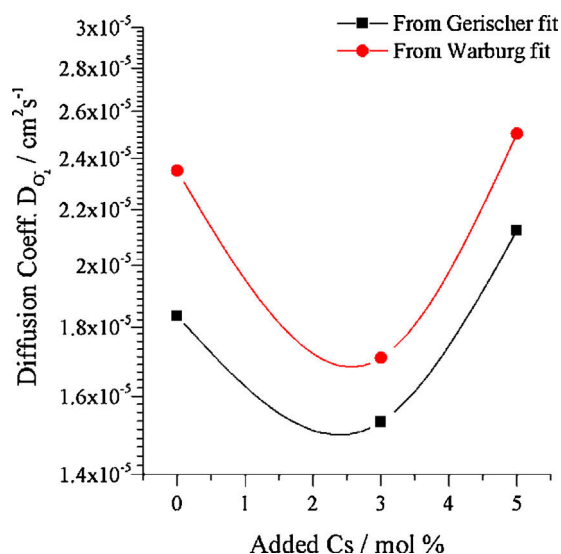


Fig. 5. Values of diffusion coefficient D_{O_2} vs.% Cs at 650°C deduced from Warburg and Gerischer models applying Nishina's reaction order analysis.

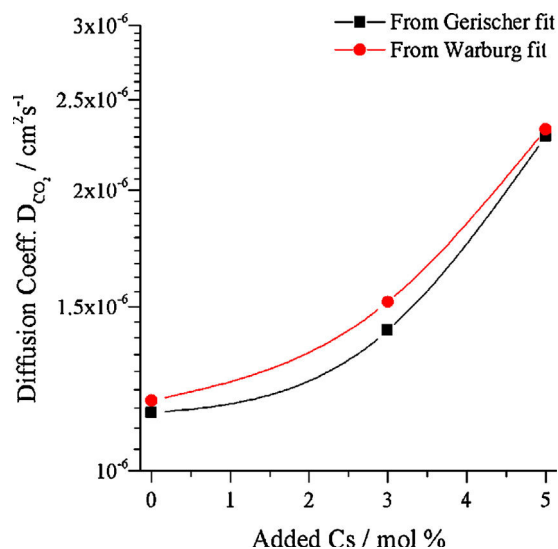


Fig. 6. Values of diffusion coefficient D_{CO_2} vs.% Cs at 650°C deduced from Warburg and Gerischer models applying Nishina's reaction order analysis.

Figs. 7 and 8 show the variation of the inverse of charge transfer resistance ($R_2 = R_{ct}$) with respect to the partial pressures of O_2 and CO_2 , respectively. From these graphs, we can observe in the case of oxygen partial pressure that the general trend when increasing PO_2 is the same for all Cs additions. Charge transfer resistance decreases when increasing PO_2 , which is in agreement with the fact that higher PO_2 is favourable to the reaction mechanism, whatever the pathway: SOP, POP or POMCP. Both 3 and 5% of Cs content seem slightly better than for the 0% sample. In the case of CO_2 , the resistance decreases by adding Cs in all the PCO_2 range and increases when increasing PCO_2 for all Cs additions. The most favourable is 5% Cs sample, with a smaller resistance than that observed for the 0% one, over the entire PCO_2 range. In general, both 3 and 5% showed a better behaviour than Li-K eutectic with respect to charge transfer resistance. If we consider the relation: $1/R = 1/R_0 P_{CO_2}^\alpha P_{O_2}^\beta$, the reaction orders α and β can be obtained from the slopes of Figs. 7 and 8. In Table 3, α and β values obtained for all the different Cs contents are shown. From these

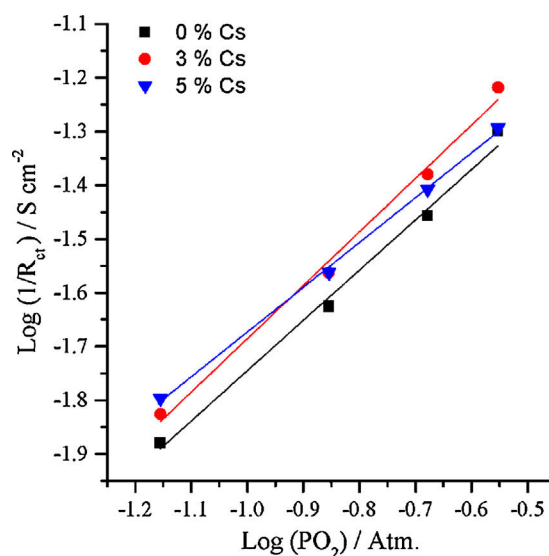


Fig. 7. Variation of surface area normalized $1/R_{ct}$ vs. partial pressure of O_2 at 650°C deduced from R1 in Gerischer model and values in Table 1.

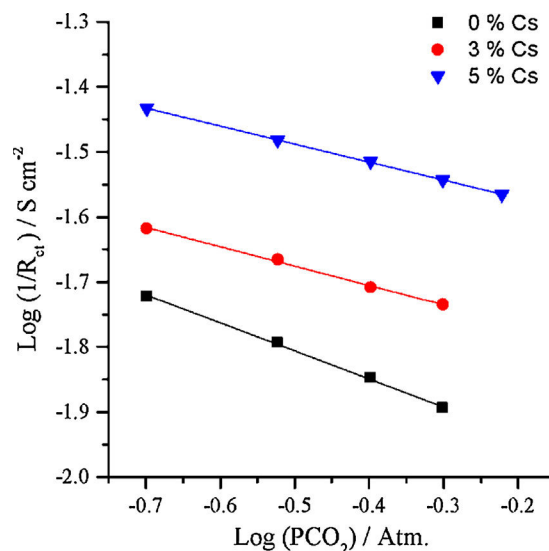


Fig. 8. Variation of $1/R_{ct}$ vs. partial pressure of CO_2 at 650°C deduced from R1 in Gerischer model and values in Table 1.

Table 3
Reaction order values α and β obtained from the slopes on Figs. 7 and 8.

Added Cs mol%	α	β
0	0.93553	-0.43167
3	0.99371	-0.29814
5	0.83336	-0.27724

values, we can deduce that the addition of Cs does not affect the predominance of superoxide mechanism. This is in good agreement with the reaction order analysis in Section 3.3 and thermodynamic predictions where Cs addition acidifies the electrolyte and favours the stability of superoxide ions [20,23].

4. Conclusions

Oxygen reduction mechanism at the cathode of the molten carbonate fuel cell was investigated by electrochemical impedance

spectroscopy. EIS data were fitted to a Randles–Ershler type equivalent circuit obtaining the Warburg or Gerischer coefficients. After performing a reaction order analysis, we deduced that the superoxide mechanism dominates the overall reaction at the electrode for all the samples with different Cs contents. Evidence was given that Cs improves oxygen reduction by doubling the value of D_{CO_2} from $1.1 \times 10^{-6} \text{ cm}^2 \text{ s}^{-1}$ to $2.3 \times 10^{-6} \text{ cm}^2 \text{ s}^{-1}$, thus facilitating the reduction process. The benefit of adding Cs to the Li–K eutectics with respect to charge transfer resistance is clear since, in all the partial pressure range of CO_2 , all the Cs-containing electrolytes show a lower charge transfer resistance than the pure Li–K eutectic mixture. A thorough understanding of the evolution of D_{O_2} with Cs additions requires further investigation.

Acknowledgments

This work was supported by the French program PLANEX ANR-11-EQPX-0-01 and benefited of a Mexican CONACYT Ph.D. scholarship 314518 and the project number 252003.

References

- [1] M. Cassir, C. Belhomme, Technological applications of molten salts: the case of the molten carbonate fuel cell, *Plasma Ionics* 2 (1999) 3–15, doi:http://dx.doi.org/10.1016/S1288-3255(99) 80006-9.
- [2] H. Morita, M. Komoda, Y. Mugikura, Y. Izaki, T. Watanabe, Y. Masuda, et al., Performance analysis of molten carbonate fuel cell using a Li/Na electrolyte, *J. Power Sources* 112 (2002) 509–518, doi:http://dx.doi.org/10.1016/S0378-7753(02) 00468-8.
- [3] M. Yoshikawa, Y. Mugikura, T. Watanabe, T. Ota, A. Suzuki, The Behavior of MCFCs Using Li/K and Li/Na Carbonates as the Electrolyte at High Pressure, *J. Electrochem. Soc.* 146 (1999) 2834–2840, doi:http://dx.doi.org/10.1149/1.1392016.
- [4] Y. Mugikura, F. Yoshida, Y. Izaki, T. Watanabe, K. Takahashi, S. Takashima, et al., Performance and life of 10-kW molten-carbonate fuel cell stack using Li/K and Li/Na carbonates as the electrolyte, *J. Power Sources* 75 (1998) 108–115, doi: http://dx.doi.org/10.1016/S0378-7753(98) 00103-7.
- [5] S. Scaccia, Investigation on NiO solubility in binary and ternary molten alkali metal carbonates containing additives, *J. Mol. Liq.* 116 (2005) 67–71, doi:http://dx.doi.org/10.1016/j.molliq.2004.07.078.
- [6] H. Mohn, H. Wendt, Molecular Thermodynamics of Molten Salt Evaporation*, *Z. Für Phys. Chem.* 192 (1995) 101–119.
- [7] M. Cassir, M. Olivry, V. Albin, B. Malinowska, J. Devynck, Thermodynamic and electrochemical behavior of nickel in molten Li_2CO_3 – Na_2CO_3 modified by addition of calcium carbonate, *J. Electroanal. Chem.* 452 (1998) 127–137, doi: http://dx.doi.org/10.1016/S0022-0728(98)00118-1.
- [8] C. Sishla, R. Donado, E.T. Ong, R. Remick, Temperature Sensitivity of MCFCs Using Lithium/Sodium Electrolytes, in: J.R. Selman (Ed.), *Electrochem. Soc. Proc.*, Montreal, Canada, 1997, pp. 315.
- [9] S.H. Lu, Ph.D. Dissertation, Electrode kinetics of fuel oxidation and oxygen reduction in molten carbonate, Illinois Inst. of Tech., Chicago (USA), 1985.
- [10] S.-G. Kim, J. Jun, J. Jun, Predictions of the optimum ternary alkali-carbonate electrolyte composition for MCFC by computational calculation, *J. Power Sources* 160 (2006) 805–810, doi:http://dx.doi.org/10.1016/j.jpowsour.2006.04.067.
- [11] V. Lair, V. Albin, A. Ringuedé, M. Cassir, Theoretical predictions vs. experimental measurements of the electrical conductivity of molten Li_2CO_3 – K_2CO_3 modified by additives, *Int. J. Hydrog. Energy* 37 (2012) 19357–19364, doi:http://dx.doi.org/10.1016/j.ijhydene.2011.09.153.
- [12] D.S. Smith, J. Winnick, Cesium-Containing Electrolyte for the Molten Carbonate Fuel Cell, *Electrochem. Solid-State Lett.* 2 (1999) 207–209, doi: http://dx.doi.org/10.1149/1.1390785.
- [13] T. Kojima, Y. Miyazaki, K. Nomura, K. Tanimoto, Physical Properties of Molten Li_2CO_3 – Na_2CO_3 (52:48 mol%) and Li_2CO_3 – K_2CO_3 (62:38 mol%) Containing Additives, *J. Electrochem. Soc.* 160 (2013) H733–H741, doi:http://dx.doi.org/10.1149/2.073410jes.
- [14] G.J. Janz, Thermodynamic and transport properties for molten salts; correlated equations for critically evaluated density, surface tension electrical conductance, and viscosity data, *J. Phys. Chem. Ref. Data* 17 (1988) 320.
- [15] J. Hoffmann, Schmelzkarbonatbrennstoffzelle und Elektrolytmischung für eine solche, DE10136156 A1, 2002.
- [16] A. Hilmi, C.-Y. Yuh, M. Farooque, United States Patent: 8557468 - High performance electrolyte for molten carbonate fuel cells comprising carbonate electrolyte doped with additive material(s) and lithium precursor(s), 8557468, 2013.
- [17] T. Nishina, I. Uchida, J.R. Selman, Gas Electrode Reactions in Molten Carbonate Media Part V. Electrochemical Analysis of the Oxygen Reduction Mechanism at a Fully Immersed Gold Electrode, *J. Electrochem. Soc.* 141 (1994) 1191–1198, doi:http://dx.doi.org/10.1149/1.2054895.
- [18] R.C. Makkus, Ph.D. Dissertation Electrochemical studies on the oxygen reduction and NiO(Li) dissolution in molten carbonate fuel cells, Delft, 1991.
- [19] G. Moutiers, M. Cassir, C. Piolet, J. Devynck, Thermodynamic and voltammetric study of oxygen systems in molten Na_2CO_3 – K_2CO_3 (56–44 mol. %) eutectic at 750°C, *Electrochimica Acta* 36 (1991) 1063–1071, doi:http://dx.doi.org/10.1016/0013-4686(91)85316-Y.
- [20] G. Moutiers, M. Cassir, J. Devynck, Oxygen reduced species in molten Li_2CO_3 + K_2CO_3 (42.7 + 57.3 mol%) at 650°C: A thermodynamic, voltammetric and convolution potential sweep characterization, *J. Electroanal. Chem.* 324 (1992) 175–189, doi:http://dx.doi.org/10.1016/0022-0728(92)80044-5.
- [21] M. Cassir, G. Moutiers, J. Devynck, Stability and Characterization of Oxygen Species in Alkali Molten Carbonate: A Thermodynamic and Electrochemical Approach, *J. Electrochem. Soc.* 140 (1993) 3114–3123, doi:http://dx.doi.org/10.1149/1.2220995.
- [22] M. Cassir, B. Malinowska, C. Canevet, L. Sportouch, J. Devynck, Molten carbonate fuel cells: contribution to the study of cathode behaviour and oxygen reduction in molten Li_2CO_3 – K_2CO_3 at 650°C, *J. Power Sources* 61 (1996) 149–153, doi:http://dx.doi.org/10.1016/S0378-7753(96)02365-8.
- [23] M. Cassir, B. Malinowska, W. Peelen, K. Hemmes, J.H.W. de Wit, Identification and electrochemical characterization of in situ produced and added reduced oxygen species in molten Li_2CO_3 + K_2CO_3 , *J. Electroanal. Chem.* 433 (1997) 195–205, doi:http://dx.doi.org/10.1016/S0022-0728(97)00292-1.
- [24] B.B. Dave, R.E. White, S. Srinivasan, A.J. Appleby, Impedance Analysis for Oxygen Reduction in a Lithium Carbonate Melt: Effects of Partial Pressure of Carbon Dioxide and Temperature, *J. Electrochem. Soc.* 140 (1993) 2139–2145, doi:http://dx.doi.org/10.1149/1.2220786.
- [25] P. Tomczyk, M. Mosiałek, Investigation of the oxygen electrode reaction in basic molten carbonates using electrochemical impedance spectroscopy, *Electrochimica Acta* 46 (2001) 3023–3032, doi:http://dx.doi.org/10.1016/S0013-4686(01)00522-9.
- [26] J.A. Prins-Jansen, G.A.J.M. Plevier, K. Hemmes, J.H.W. de Wit, An ac-impedance study of dense and porous electrodes in molten-carbonate fuel cells, *Electrochimica Acta* 41 (1996) 1323–1329, doi:http://dx.doi.org/10.1016/0013-4686(95)00453-X.
- [27] C.L. Zeng, W. Wang, W.T. Wu, Electrochemical impedance models for molten salt corrosion, *Corros. Sci.* 43 (2001) 787–801, doi:http://dx.doi.org/10.1016/S0010-938X(00)00108-6.
- [28] R.C. Makkus, K. Hemmes, J.H.W. De Witt, Impedance Measurements on Oxygen Reduction Reaction in Molten Carbonate, *Für Phys. Chem.* 94 (1990) 960–967, doi:http://dx.doi.org/10.1002/bbpc.19900940916.
- [29] A.J. Bard, L.R. Faulkner, *Electrochemical methods: fundamentals and applications*, 2nd ed, Wiley, New York, 2001.
- [30] A.J. Appleby, S.B. Nicholson, Reduction of oxygen in lithium-potassium carbonate melt, *J. Electroanal. Chem. Interfacial Electrochem.* 112 (1980) 71–76, doi:http://dx.doi.org/10.1016/S0022-0728(80) 80008-8.
- [31] A.J. Appleby, S.B. Nicholson, Reduction of oxygen in alkali carbonate melts, *J. Electroanal. Chem. Interfacial Electrochem.* 83 (1977) 309–328, doi:http://dx.doi.org/10.1016/S0022-0728(77) 80176-9.
- [32] A.J. Appleby, S. Nicholson, The reduction of oxygen in molten lithium carbonate, *J. Electroanal. Chem. Interfacial Electrochem.* 53 (1974) 105–119, doi:http://dx.doi.org/10.1016/0022-0728(74) 80007-0.
- [33] A.J. Appleby, S. Nicholson, Oxygen reduction in carbonate melts: Significance of the peroxide and superoxide ions, *J. Electroanal. Chem. Interfacial Electrochem.* 38 (1972) A13–A18, doi:http://dx.doi.org/10.1016/S0022-0728(72) 80369-3.
- [34] I. Uchida, Y. Mugikura, T. Nishina, K. Itaya, Gas electrode reactions in molten carbonate media Part II. Oxygen reduction kinetics on conductive oxide electrodes in (Li + K) $2CO_3$ eutectic at 650°C, *J. Electroanal. Chem. Interfacial Electrochem.* 206 (1986) 241, doi:http://dx.doi.org/10.1016/0022-0728(86) 90272-X.
- [35] T. Itoh, K. Abe, K. Dokko, M. Mohamedi, I. Uchida, A. Kasuya, In Situ Raman Spectroelectrochemistry of Oxygen Species on Gold Electrodes in High Temperature Molten Carbonate Melts, *J. Electrochem. Soc.* 151 (2004) A2042–A2046, doi:http://dx.doi.org/10.1149/1.1812735.
- [36] T. Itoh, T. Maeda, A. Kasuya, In situ surface-enhanced Raman scattering spectroelectrochemistry of oxygen species, *Faraday Discuss* 132 (2006) 95–109, doi:http://dx.doi.org/10.1039/b506197k.
- [37] D.A. Tryk, E.D. Yeager, The 2nd symposium on Molten Carbonate Fuel Cell Technology, in: J.R. Selman, D.A. Shores, H.C. Maru, I. Uchida (Eds.), *Electrochem. Soc. Proceeding Ser. PV-90-16*, Pennington, NJ, 1990, pp. 395.
- [38] G.B. Dunks, D. Stelman, Electrochemical studies of molten sodium carbonate, *Inorg. Chem.* 22 (1983) 2168–2177, doi:http://dx.doi.org/10.1021/ci00157a015.



ELSEVIER

Available online at www.sciencedirect.com

ScienceDirect

journal homepage: www.elsevier.com/locate/hydro

Influence of Cs and Rb additions in Li–K and Li–Na molten carbonates on the behaviour of MCFC commercial porous Ni cathode

A. Meléndez-Ceballos, V. Albin, C. Crapart, V. Lair, A. Ringuedé, M. Cassir*

Chimie ParisTech, PSL Research University, CNRS, Institut de Recherche de Chimie Paris (IRCP), F-75005 Paris, France

ARTICLE INFO

Article history:

Received 19 April 2016
 Received in revised form
 13 September 2016
 Accepted 17 September 2016
 Available online 7 October 2016

Keywords:

Molten carbonate fuel cell
 Electrolyte performance
 Caesium and rubidium additives
 OCP
 Impedance measurements

ABSTRACT

Improvement of the molten carbonate fuel cell electrolyte is a key parameter to increase the performance of such electrochemical generator. One of the main challenges is to enhance the global oxygen reduction at the state-of-the-art porous nickel cathode. In this study, the effect of adding 5 mol% of caesium in Li–K and Li–Na molten carbonate eutectics or 5 mol% of rubidium in Li–K melt was analysed with respect to the behaviour of nickel cathode towards oxygen reduction. Evolution of the open-circuit potential and electrochemical impedance spectroscopy measurements were carried out over time. In Li–K melt, both Cs and Rb additives induced an improved cathode behaviour: more rapid equilibration reaching more rapidly the equilibrium potential, and significantly lower total resistance (9 times less with Cs and 3 times less with Rb), in particular mass transport, with respect to the pristine electrolyte. Moreover, charge transfer resistance was significantly lower with Rb and nearly the same with Cs versus pristine Li–K. Both additions are significantly positive for enhancing oxygen reduction at the porous electrode, which seems to be particularly the case for Cs addition. However, addition of Cs to Li–Na did not show an important effect. Changing the composition of Li–K with the mentioned additives could be an important step towards a more performing MCFC, but more insight on oxygen reduction kinetics with Rb addition and single cell tests with both cases are compulsory.

© 2016 Hydrogen Energy Publications LLC. Published by Elsevier Ltd. All rights reserved.

Introduction

The molten carbonate fuel cell (MCFC) has been developed over the last decades up to the point of being the most important fuel cell technology worldwide in terms of total installed power worldwide in the last three years (about 300 MW) [1]. Nevertheless, there are some drawbacks of the technology that require further improvement as are cathode

endurance and electrolyte performance among the most important. The standard MCFC cathode is constituted by porous Ni which is oxidised and lithiated *in situ* to form a $\text{Li}_x\text{Ni}_{1-x}\text{O}$ phase at the electrode surface. Along operation time, Ni solubilises in the carbonate melt and, after an eventual reaction with hydrogen proceeding from the anode side, can be reduced into metallic Ni in the electrolyte matrix, causing in a long term a short circuit between anode and cathode, which reduces the performance and stack endurance. Several

* Corresponding author.

E-mail address: michel.cassir@chimie-paristech.fr (M. Cassir).
<http://dx.doi.org/10.1016/j.ijhydene.2016.09.118>

0360-3199/© 2016 Hydrogen Energy Publications LLC. Published by Elsevier Ltd. All rights reserved.

efforts have been made to increase cathode lifetime, among the most significant are cathode protection by different coatings and new cathode materials [2–9], recently, CeO_2 , TiO_2 , Co_3O_4 and Nb_2O_5 cathode coatings prepared by novel methods as atomic layer deposition (ALD) have been tested with good results [10–12]. The conventional molten salt used as electrolyte is composed by Li_2CO_3 – K_2CO_3 (62/38 mol%), which has a better performance at temperatures below 600 °C than Li_2CO_3 – Na_2CO_3 (52/48 mol%), but presents a higher Ni solubility [13]. In order to improve these electrolytes, some studies have been made on the addition of CaCO_3 , BaCO_3 , La_2CO_3 , Y_2O_3 , Gd_2O_3 , CeO_2 and La_2O_3 to the molten carbonates, with the aim of reducing cathode dissolution and/or improving electrolyte ionic conductivity [13,14]. Less mentioned additives are heavy cations such as caesium and rubidium, even though few papers and patents mentioned their positive role on the decrease of cathode and anode overpotentials and, thus, on MCFC performance [15–18]. Moreover, these additives allow obtaining mixtures thermally stable up to 700 °C, with lower surface tension at the nickel cathode and higher oxygen reduction [19,20]. Nevertheless, these melts have a drawback which is their slight oxoacidity promoting a higher cathode dissolution with respect to Li–Na and Li–K carbonate eutectics; this negative aspect can be easily solved by adding a small excess of lithium ions known to decrease NiO solubility.

In a recent paper, we have analysed oxygen reduction kinetics at a gold flag electrode in Li_2CO_3 – K_2CO_3 (62/38 mol%) with the addition of 5 mol% Cs_2CO_3 [21] and proven the benefits of using such additive. It is evident that porous nickel has to be tested to confirm the potential of Cs additive for MCFC application. Hence, in the present study we further investigate the benefits of Cs or Rb additions when using a commercial porous Ni cathode by testing it in both Li–K and Li–Na eutectics with and without 5 mol% of Cs or Rb additives and we compare their performance. The general evolution of Ni cathode in the different melts is analysed through its open-circuit potential (OCP) over the time, which is a key parameter to understand how this cathode material is progressively transformed in the carbonate melt and is a manner to qualify equilibration of the media, an essential step to initiate the concrete operation as a fuel cell. This equilibration is correlated to the electrical/electrochemical parameters deduced from electrochemical impedance spectroscopy. This study is compulsory to decide whether or not Cs or Rb additives will be part of the next generation MCFC electrolytes.

Materials and methods

Lithium, sodium and potassium carbonates, of high grade purity >98% (Sigma–Aldrich®), were used. Li–K and Li–Na eutectics were prepared by mixing the respective carbonates in a proportion of 62:38 mol. % and 52:48 mol. %, respectively. Cs_2CO_3 or Rb_2CO_3 were added to a carbonate eutectic calculating the weight of the dried carbonate powder in order to add 5 mol % of the additive. The high-temperature electrochemical cell was a single-compartment crucible of dimensions $70 \times 50 \text{ mm}^2$ contained in an alumina Al_2O_3 reactor of dimensions $250 \times 60 \text{ mm}^2$ hermetically sealed by a stainless steel cover with a Viton O-ring. The whole electrochemical

set-up has been fully described in previous papers [22,23]. Temperature was maintained constant at 650 °C by means of a calibrated chromel/alumel thermocouple protected by an alumina tube and a temperature controller. The standard cathode atmosphere was a mixture of $\text{O}_2/\text{CO}_2/\text{Ar}$ (14:30:56 Atm. %) with a total flow of 50 mL min^{-1} of high grade purity gas (Air Liquide®) at a pressure of 1 atm. The electrochemical experimental data was collected using a potentiostat/galvanostat (AutoLab® PGSTAT-302N with FRA module). A three-electrode system was used, the working electrode being a porous nickel plate (DOOSAN Korea) ($10 \times 10 \times 0.8 \text{ mm}$), the counter electrode was a gold wire and the reference electrode a silver wire dipped into an Ag_2SO_4 ($10^{-1} \text{ mol kg}^{-1}$) saturated Li–K or Li–Na eutectic contained in an alumina tube sealed by a porous alumina membrane. The parameters used for impedance measurements were the following: scanning frequencies set from 10^6 to 10^{-3} Hz , with 11 points per decade, and signal amplitude of 5 mV respecting the system linearity. The fitting of the equivalent circuit was carried out with the software Z-View® V3.3e. Open circuit potential (OCP) measurements were carried out from the moment the electrode was immersed in the molten carbonate eutectic until the potential was stable around 0 V. OCP measurements were interrupted periodically to run electrochemical impedance spectroscopy tests from which charge transfer resistance (R_{ct}), mass transport resistance (R_{mt}) and total resistance (R_{tot}) were deduced.

Results and discussion

Open circuit potential (OCP) evolution over time

OCP evolution over the time is depicted in Fig. 1 for Li–K molten carbonate eutectic, without or with addition of 5 mol. % of Cs or Rb. As has been discussed in previous papers [10–12,16], porous Ni follows a 2 step potential evolution where the plateaus are denoted as I ($\approx -0.68 \text{ V}/(\text{Ag}/\text{Ag}^+)$), II (\approx

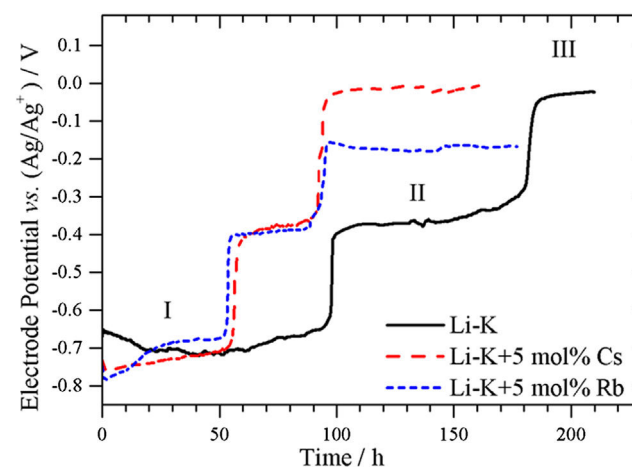


Fig. 1 – Open circuit potential (OCP) evolution over time of porous Ni immersed into Li–K carbonate eutectic and modified Li–K with added 5 mol % Cs_2CO_3 and Li–K with added 5 mol % Rb_2CO_3 . All the measures were taken at 650 °C.

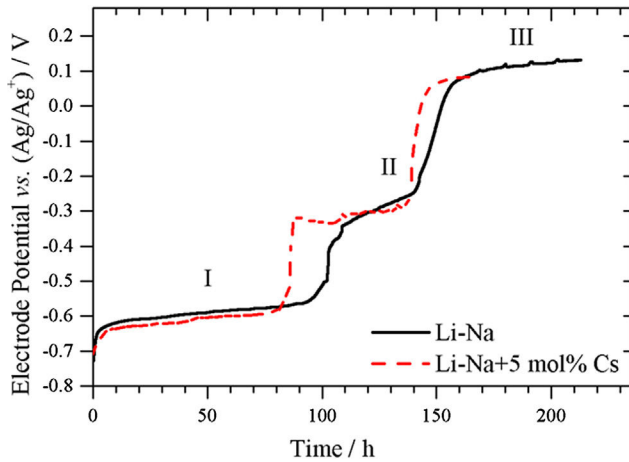


Fig. 2 – Open circuit potential (OCP) evolution over time of porous Ni immersed in Li–Na eutectic and modified Li–Na eutectic with added 5 mol % Cs_2CO_3 both tests performed at 650°C .

$-0.37\text{ V}/(\text{Ag}/\text{Ag}^+)$) and III ($\approx 0\text{ V}/(\text{Ag}/\text{Ag}^+)$). The three plateaus corresponding to porous nickel in a non-modified electrolyte are related to the modification of the porous Ni electrode into $\text{Li}_x\text{Ni}_{1-x}\text{O}$, in a progressive way. The first plateau (I) from 0 to 98 h is ascribed to the *in situ* oxidation of metallic nickel, after the first potential jump at 98 h, a second plateau (II) is reached at a potential around $-0.4\text{ V}/(\text{Ag}/\text{Ag}^+)$. This plateau corresponds to the *in situ* lithiation of NiO, [24–26]. At equilibrium, lithium content in NiO cathode was estimated by nuclear microprobe to be roughly of 0.2 at% [27]. After 182 h, the lithiation process is completed and the third plateau (III) at $-0.03\text{ V}/(\text{Ag}/\text{Ag}^+)$ corresponds to an equilibrium potential

between O_2 , CO_2 and carbonates. At this stage, the electrode works as a stable cathode for oxygen reduction.

This behaviour is the same for a porous nickel cathode in a non-modified Li–Na eutectic as shown in Fig. 2, the slight difference is related to the time of each stage of the cathode evolution. In the case of Li–Na, the first potential jump occurs nearly at the same time as in case of Li–K, the second plateau has a shorter duration of 35 h, and the second potential jumps takes place at 138 h, that is 44 h before Li–K eutectic, and reaches a plateau at 0.13 V at 209 h, 0.11 V higher than Li–K at the duration. Roughly, at the conditions of the experiment, Li–Na allows a more rapid equilibration better than Li–K. Due to its oxoacidity, caesium addition modifies the oxidation/lithiation process of the porous Ni cathode. Cs influence in the case of Li–K electrolyte is evidenced in Fig. 1, where it can be observed that the first potential jump occurs at 56 h, reaching a plateau around $-0.37\text{ V}/(\text{Ag}/\text{Ag}^+)$ similar to that of non-modified Li–K. The second jump takes place at 93 h and reaches a potential of $-0.01\text{ V}/(\text{Ag}/\text{Ag}^+)$, similar to pristine Li–K but 89 h earlier. Rb addition also influences the OCP behaviour of porous Ni in Li–K eutectics, the first plateau starts at a lower potential of $-0.78\text{ V}/(\text{Ag}/\text{Ag}^+)$ and rapidly reaches a stable plateau potential around $-0.68\text{ V}/(\text{Ag}/\text{Ag}^+)$, at 53 h the first potential jump appears and reaches a plateau around $-0.39\text{ V}/(\text{Ag}/\text{Ag}^+)$ that lasts for 36 h until the second potential jump appears and reaches a potential of $-0.15\text{ V}/(\text{Ag}/\text{Ag}^+)$ that later decreases a little to a potential of $-0.16\text{ V}/(\text{Ag}/\text{Ag}^+)$ this behaviour is comparable to that of the added Cs, even though the final potential is not as high as in pristine Li–K or Cs modified Li–K, it can still perform as MCFC cathode without problem. In the case of Cs added in Li–Na electrolyte, the first potential jump occurs at 86 h, 16 h earlier than pure Li–Na and reaches a potential of $-0.32\text{ V}/(\text{Ag}/\text{Ag}^+)$ that increases slightly until the second potential jump occurs at 139 h, almost at the same time as non-modified Li–Na, reaching

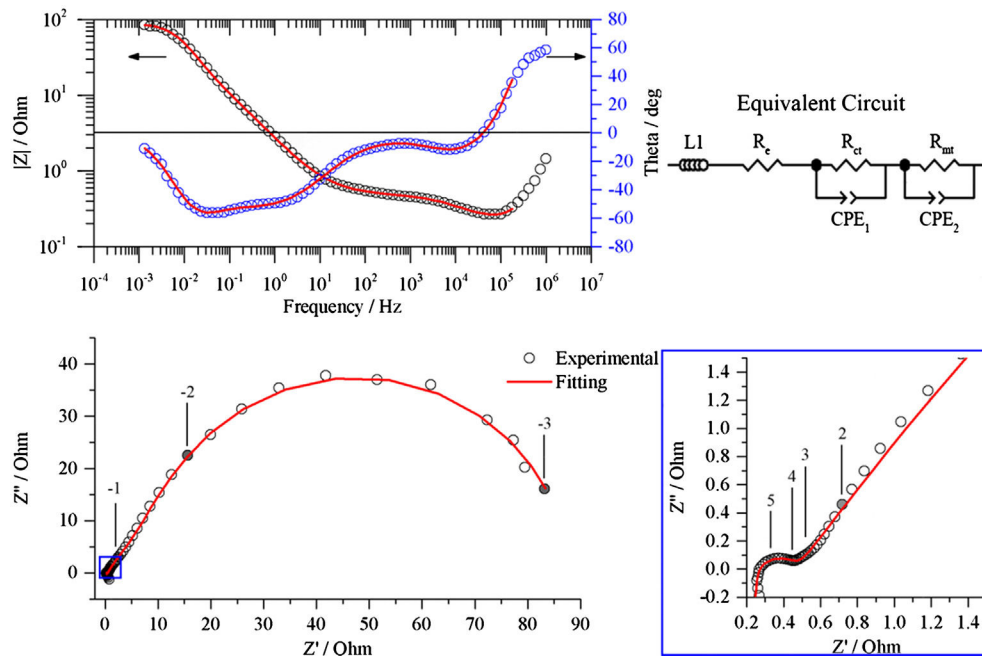


Fig. 3 – Electrochemical impedance spectroscopy data of porous Ni after being immersed in Li–K eutectic at 650°C for 121 h. Bode (upper left), Nyquist (down left) and Nyquist high frequency zoom (down right) plots show experimental data (dots) and fitted data (line) using the equivalent circuit shown (upper right). Numbers indicate the Log of the frequency.

a final plateau at 0.08 V/(Ag/Ag⁺) that is comparable to bare Li–Na eutectic. It is clear that Cs addition has a positive influence in the OCP evolution of porous Ni whatever the eutectic used; nevertheless, a more significant effect is observed when added to Li–K eutectic, reducing the time necessary to reach potential equilibration.

Electrochemical impedance spectroscopy data (EIS)

As shown in Fig. 3, impedance spectra were fitted by using an equivalent circuit composed by an inductance (L1) in series with a resistance (R_e) accounting for the inductance of the physical wiring from the potentiostat to the electrochemical cell and the electrolyte resistance, respectively. Following, two circuits in series each one composed by a resistance in parallel with a constant phase element (CPE), the first component accounts for the charge transfer resistance (R_{ct}) and the double layer capacitance (CPE_1), the last element represents the mass transfer resistance contribution (R_{mt}) and a capacitance associated with a finite diffusion regime (CPE_2). The described circuit was chosen since it is the simplest way to represent closely the impedance diagrams of the porous Ni immersed in the carbonate melts. Contrarily to our previous study [21],

where Warburg and Gerischer elements were used for fitting the impedance data obtained with a gold flag electrode; in this case, porous Ni is well fitted by a simpler circuit. From the fitting of impedance spectra taken over the duration of each experiment, as shown in Fig. 3, for all the studied electrolytes we have deduced the values of charge transfer resistance (R_{ct}) and total resistance ($R_{tot} = R_e + R_{ct} + R_{mt}$). Evolution of R_{ct} and R_{tot} over time is depicted in Figs. 4 and 5 for Li–K and Li–Na electrolytes, respectively. As shown in Fig. 4, pristine Li–K presents a maximum resistance around 180 h of 5 Ω and 422 Ω for R_{ct} and R_{tot} , respectively, then at 224 h a value of 3 Ω and 358 Ω is reached. In the case of the modified Li–K molten salts, Cs addition shows a different behaviour than pristine Li–K eutectic: a significant increase in R_{ct} and R_{tot} is evidenced at 70 h where the resistances are 90 Ω and 392 Ω , respectively, then they decrease to reach a final value of 5 Ω and 40 Ω at 164 h. Rubidium addition to Li–K eutectic shows a R_{ct} and R_{tot} with maximum values at 91 h of 5 Ω and 284 Ω , respectively, that later decrease to 0.4 Ω and 111 Ω after 195 h of immersion. In the overall scheme, it is clear that Cs and Rb reduce the total resistance of the electrode, being Cs the best in terms of R_{tot} due to the low contribution of the R_{mt} , which indicates that Cs addition favours mass transport at the electrode. This effect is

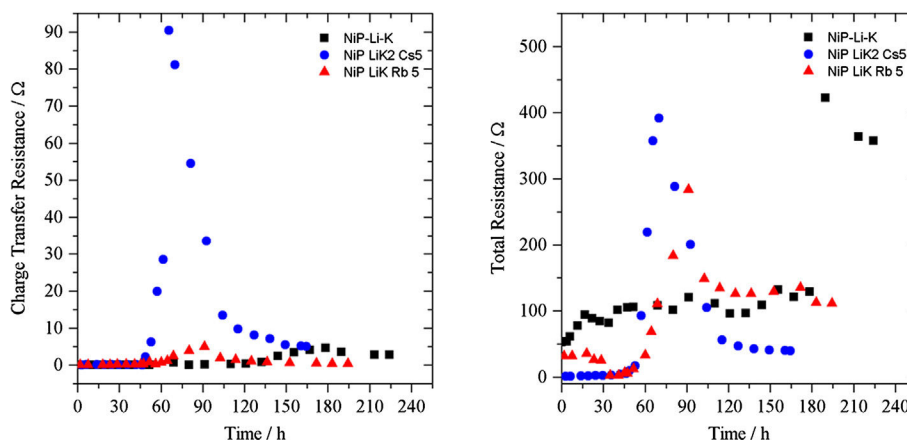


Fig. 4 – Charge transfer resistance and total resistance evolution over time of the porous Ni electrode immersed in Li–K molten eutectic with and without Cs or Rb addition.

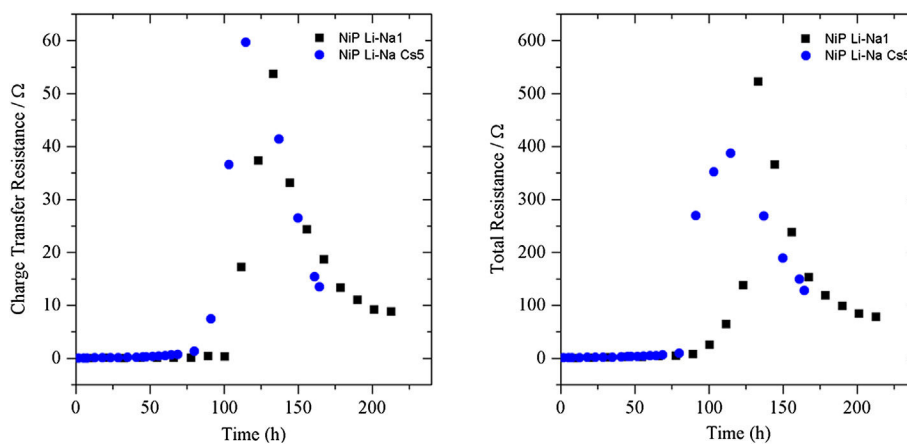


Fig. 5 – Charge transfer resistance and total resistance evolution over time of the porous Ni electrode immersed in Li–Na molten eutectic with and without Cs addition.

consistent with the results obtained in a study on oxygen kinetics where the addition of Cs allowed increasing the diffusion coefficients D_{CO_2} and D_{O_2} [21]; nevertheless, Cs modified Li–K shows a value of R_{ct} 2 Ω higher than pristine Li–K, which can be considered acceptable in terms of MCFC electrode. Li–K electrolyte with addition of Rb shows a low R_{ct} and a favourable R_{tot} and can be used as MCFC electrolyte; however, a deeper kinetic study concerning addition of Rb is still necessary. As shown in Fig. 5, Cs addition does not influence significantly the behaviour of Li–Na electrolyte in terms of R_{ct} and R_{tot} , both electrolytes have a maximum resistance around 123 h. Therefore, we can conclude that Cs addition to Li–Na eutectic does not influence the behaviour of such eutectic and appears not relevant as additive in this case.

Conclusions

The influence of 5 mol % Cs_2CO_3 and Rb_2CO_3 additives in Li–K molten carbonate eutectic (and Li–Na for caesium only) on the nickel cathode electrochemical behaviour was analysed. We concluded that Li–K electrolyte with both additives present a better performance than the non-modified one, which is evidenced by a faster OCP evolution, reaching the equilibrium 88 h before pristine Li–K and by a reduced total resistance 3 times lower in the case of Rb addition and almost 9 times for Cs. Rb modified electrolyte shows a very good response that requires further investigation. Contrarily, Cs addition to Li–Na carbonate eutectic did not improve the electrochemical performance, what makes it unlikely to be used as additive in Li–Na electrolyte. In conclusion, Cs and Rb additions to the Li–K eutectic have a positive influence on the electrochemical behaviour of porous Ni electrode and are promising additives. With respect to the application, the use of such additives should lead to a better stack performance by increasing the output power; however, tests in a single cell are compulsory for determining the improvement of performance before these additives could be used commercially.

Acknowledgements

This work was supported by the French program PLANEX ANR-11-EQPX-0-01 and benefited of a Mexican CONACYT Ph.D. scholarship 314518.

REFERENCES

- [1] McPhail S, Leto L, Della Pietra M, Cigolotti V, Moreno A. International status of molten carbonate fuel cells technology - 2015. ENEA; 2015. <http://www.enea.it/en/publications/abstract/Molten-Carbonate-Fuel-Cells-2015> [Accessed 17 March 2015].
- [2] Antolini E. The stability of molten carbonate fuel cell electrodes: a review of recent improvements. *Appl Energy* 2011;88:4274–93. <http://dx.doi.org/10.1016/j.apenergy.2011.07.009>.
- [3] Chauvaut V, Cassir M, Denos Y. Behavior of titanium species in molten $\text{Li}_2\text{CO}_3\text{--Na}_2\text{CO}_3$ and $\text{Li}_2\text{CO}_3\text{--K}_2\text{CO}_3$ under anodic and cathodic conditions. I – thermodynamic predictions at 550–750°C. *Electrochimica Acta* 1998;43:1991–2003. [http://dx.doi.org/10.1016/S0013-4686\(97\)10139-6](http://dx.doi.org/10.1016/S0013-4686(97)10139-6).
- [4] Chauvaut V, Cassir M. Behaviour of titanium species in molten $\text{Li}_2\text{CO}_3\text{+Na}_2\text{CO}_3$ and $\text{Li}_2\text{CO}_3\text{+K}_2\text{CO}_3$ in the anodic conditions used in molten carbonate fuel cells: II. Electrochemical intercalation of Li^+ in Li_2TiO_3 at 600 and 650°C. *J Electroanal Chem* 1999;474:9–15. [http://dx.doi.org/10.1016/S0022-0728\(99\)00298-3](http://dx.doi.org/10.1016/S0022-0728(99)00298-3).
- [5] Chauvaut V, Albin V, Schneider H, Cassir M, Ardéléan H, Galtayries A. Study of cerium species in molten $\text{Li}_2\text{CO}_3\text{--Na}_2\text{CO}_3$ in the conditions used in molten carbonate fuel cells. Part I: thermodynamic, chemical and surface properties. *J Appl Electrochem* 2000;30:1405–13. <http://dx.doi.org/10.1023/A:1026595117970>.
- [6] Belhomme C, Gourba E, Cassir M, Tessier C. Chemical and electrochemical behaviour of Ni–Ti in the cathodic conditions used in molten carbonate fuel cells. *J Electroanal Chem* 2001;503:69–77. [http://dx.doi.org/10.1016/S0022-0728\(01\)00375-8](http://dx.doi.org/10.1016/S0022-0728(01)00375-8).
- [7] Mendoza L, Albin V, Cassir M, Galtayries A. Electrochemical deposition of Co_3O_4 thin layers in order to protect the nickel-based molten carbonate fuel cell cathode. *J Electroanal Chem* 2003;548:95–107. [http://dx.doi.org/10.1016/S0022-0728\(03\)00228-6](http://dx.doi.org/10.1016/S0022-0728(03)00228-6).
- [8] Albin V, Mendoza L, Goux A, Ringuedé A, Billard A, Briois P, et al. Morphological, structural and electrochemical analysis of sputter-deposited ceria and titania coatings for MCFC application. *J Power Sources* 2006;160:821–6. <http://dx.doi.org/10.1016/j.jpowsour.2006.04.066>.
- [9] Escudero MJ, Ringuedé A, Cassir M, González-Ayuso T, Daza L. Porous nickel MCFC cathode coated by potentiostatically deposited cobalt oxide: III. Electrochemical behaviour in molten carbonate. *J Power Sources* 2007;171:261–7. <http://dx.doi.org/10.1016/j.jpowsour.2007.06.013>.
- [10] Meléndez-Ceballos A, Albin V, Ringuedé A, Fernández-Valverde SM, Cassir M. Electrochemical behavior of M_{x-1}O_x ($\text{M} = \text{Ti}, \text{Ce}$ and Co) ultra-thin protective layers for MCFC cathode. *Int J Hydrog Energy* 2014;39:12233–41. <http://dx.doi.org/10.1016/j.ijhydene.2014.03.213>.
- [11] Meléndez-Ceballos A, Albin V, Fernández-Valverde SM, Ringuedé A, Cassir M. Electrochemical properties of atomic layer deposition processed CeO_2 as a protective layer for the molten carbonate fuel cell cathode. *Electrochimica Acta* 2014;140:174–81. <http://dx.doi.org/10.1016/j.electacta.2014.05.025>.
- [12] Meléndez-Ceballos A, Fernández-Valverde SM, Barrera-Díaz C, Albin V, Lair V, Ringuedé A, et al. TiO_2 protective coating processed by Atomic Layer Deposition for the improvement of MCFC cathode. *Int J Hydrog Energy* 2013;38:13443–52. <http://dx.doi.org/10.1016/j.ijhydene.2013.07.083>.
- [13] Cassir M, Olivry M, Albin V, Malinowska B, Devynck J. Thermodynamic and electrochemical behavior of nickel in molten $\text{Li}_2\text{CO}_3\text{--Na}_2\text{CO}_3$ modified by addition of calcium carbonate. *J Electroanal Chem* 1998;452:127–37. [http://dx.doi.org/10.1016/S0022-0728\(98\)00118-1](http://dx.doi.org/10.1016/S0022-0728(98)00118-1).
- [14] Kulkarni A, Giddey S. Materials issues and recent developments in molten carbonate fuel cells. *J Solid State Electrochem* 2012;16:3123–46. <http://dx.doi.org/10.1007/s10008-012-1771-y>.
- [15] Smith DS, Winnick J. Cesium-Containing electrolyte for the molten carbonate fuel cell. *Electrochem Solid-State Lett* 1999;2:207–9. <http://dx.doi.org/10.1149/1.1390785>.
- [16] Hoffmann J. Schmelzkarbonatbrennstoffzelle und Elektrolytmischung für eine solche. DE10136156 A1. 2002.

- [17] Hilmi A, Yuh C-Y, Farooque M. United States Patent: 8557468-High performance electrolyte for molten carbonate fuel cells comprising carbonate electrolyte doped with additive material(s) and lithium precursor(s), 8557468, 2013.
- [18] Lair V, Albin V, Ringuedé A, Cassir M. Theoretical predictions vs. experimental measurements of the electrical conductivity of molten Li_2CO_3 - K_2CO_3 modified by additives. *Int J Hydrog Energy* 2012;37:19357–64. <http://dx.doi.org/10.1016/j.ijhydene.2011.09.153>.
- [19] Kojima T, Miyazaki Y, Nomura K, Tanimoto K. Physical properties of molten Li_2CO_3 - Na_2CO_3 (52:48 mol%) and Li_2CO_3 - K_2CO_3 (62:38 mol%) containing additives. *J Electrochem Soc* 2013;160:H733–41. <http://dx.doi.org/10.1149/2.073410jes>.
- [20] Janz GJ. Thermodynamic and transport properties for molten salts; correlated equations for critically evaluated density, surface tension electrical conductance, and viscosity data. *J Phys Chem Ref Data* 1988;17:320.
- [21] Meléndez-Ceballos A, Albin V, Lair V, Ringuedé A, Cassir M. A kinetic approach on the effect of Cs addition on oxygen reduction for MCFC application. *Electrochimica Acta* 2015;184:295–300. <http://dx.doi.org/10.1016/j.electacta.2015.10.057>.
- [22] Cassir M, Malinowska B, Canevet C, Sportouch L, Devynck J. Molten carbonate fuel cells: contribution to the study of cathode behaviour and oxygen reduction in molten Li_2CO_3 - K_2CO_3 at 650°C. *J Power Sources* 1996;61:149–53. [http://dx.doi.org/10.1016/S0378-7753\(96\)02365-8](http://dx.doi.org/10.1016/S0378-7753(96)02365-8).
- [23] Cassir M, Malinowska B, Peelen W, Hemmes K, de Wit JHW. Identification and electrochemical characterization of in situ produced and added reduced oxygen species in molten Li_2CO_3 + K_2CO_3 . *J Electroanal Chem* 1997;433:195–205. [http://dx.doi.org/10.1016/S0022-0728\(97\)00292-1](http://dx.doi.org/10.1016/S0022-0728(97)00292-1).
- [24] Yazici MS, Selman JR. Dissolution of partially immersed nickel during in situ oxidation in molten carbonate: cyclic, stripping and square wave voltammetry measurements. *J Electroanal Chem* 1998;457:89–97. [http://dx.doi.org/10.1016/S0022-0728\(98\)00126-0](http://dx.doi.org/10.1016/S0022-0728(98)00126-0).
- [25] Antolini E. Behaviour of Ni, NiO and $\text{Li}_x\text{Ni}_{1-x}\text{O}$ in molten alkali carbonates. *J Mater. Sci* 2000;35:1501–5. <http://dx.doi.org/10.1023/A:1004745332382>.
- [26] Nishina T, Takizawa K, Uchida I. Electrochemical characterization of in situ NiO formation in a molten carbonate. *J Electroanal Chem Interfacial Electrochem* 1989;263:87–96. [http://dx.doi.org/10.1016/0022-0728\(89\)80126-3](http://dx.doi.org/10.1016/0022-0728(89)80126-3).
- [27] Belhomme C, Cassir M, Tessier C, Berthoumieux E. Lithium depth profile in NiO molten carbonate fuel cell cathode by nuclear microprobe. *Electrochem Solid-State Lett* 2000;3:216–9. <http://dx.doi.org/10.1149/1.1391006>.

V. CO₂ Reduction: study by chronopotentiometry

“We build science from facts as we build a house from stones; but an accumulation of facts is no science, as a pile of stones is not a house.”

Henri Poincaré

V.1. The importance of CO₂ reduction in molten carbonates

Carbon capture and valorization is a route increasingly discussed to reduce greenhouse gases emissions. The objective of carbon capture is the long term confinement of CO₂, as for example in the case of geological sequestration [124]. In addition, the captured CO₂ can be recycled by selling it to the CO₂ consuming industry. However, the CO₂ industrial demand projected to 2020 is only of 140 Mt per year while the CO₂ produced by industry and available to capture will be of 500 Mt per year, being the oil industry the biggest CO₂ consumer for oil extraction [125]. If industrial CO₂ demand is so limited, then the market for CO₂ as raw material is not big enough to encourage the investment in CO₂ capture aside subsidies or penalizations by governments. Hence, valorization of CO₂ into more valuable products could be a way to impulse CO₂ economy.

One of the paths foreseen for CO₂ valorization is its transformation into fuels, which are value-added products with already a broad market. Reducing electrochemically carbon dioxide is one of the possible ways to produce fuels [126,127]. Today, there are already advanced researches regarding high temperature Solid Oxide Electrolysis Cells. Ceramatec, Utah [128], uses co-electrolysis of water and carbon dioxide to produce syngas, which is further converted into fuels via the Fisher-Tropsch process. In molten carbonates, Licht *et al.* [129] demonstrated the feasibility of the electrolysis thanks to the so-called STEP process (Solar Thermal Electrochemical Production), although there is no pilot plant yet.

Molten carbonates are of particular interest compared to other electrolytes [130]. They are advantageous from technological and economical viewpoints. First, they can be used to capture CO₂ molecule because of its high solubility rate of in molten carbonates and, in a second step, to valorize it by an electrolysis process [131]. Therefore, gaseous effluents from industry could be used without being pretreated to obtain a high degree of purity. Second, increasing the temperature of the melts lowers the electrical power required to perform the electrolysis [132]. Since process heat is easily recycled and is cheaper than electricity, this would decrease the electrolysis cost. Consequently, molten carbonate electrolysis cells could be more competitive than other conversion technologies.

V.2. Synthesis of previous works by cyclic voltammetry

Several studies [133–136] have been carried out on CO₂ reduction but its specific mechanism in molten carbonate is not fully justified yet. It has been suggested that CO₂ can be reduced indirectly through the reduction of carbonates and their regeneration by absorption of CO₂ [137–139]. Other authors studied the direct reduction of CO₂ into CO *via* a radical CO₂⁻ [140]. Peelen *et al.* [141] have studied CO₂ reduction in Li₂CO₃-K₂CO₃ (62:38 mol%), in the temperature range of 575-800°C *via* linear sweep voltammetry and chronoamperometry. Their analysis and the calculation from Cottrell equation suggested a one-electron transfer, diffusion-controlled mechanism:



The overall reaction being:



According to a preliminary study by cyclic voltammetry, by our research team [142], two phenomena occurring at -1.2 V vs Ag/Ag⁺ and at -0.8V vs Ag/Ag⁺, respectively, have been identified. In Li-Na eutectic, two peaks instead of one have been observed below -1 V vs Ag/Ag⁺ (Figure V.1). Analogously, the following two mechanisms were suggested for the overall reduction [142]:



and:



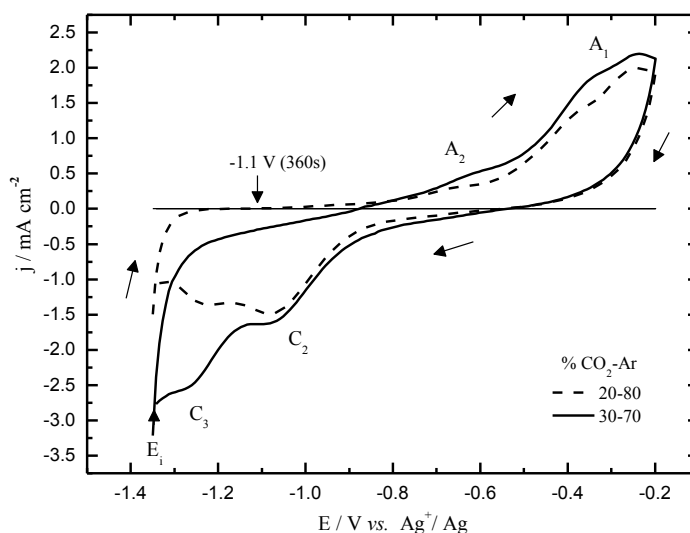


Figure V.1- Cyclic voltammograms at a gold electrode in Li-Na carbonate eutectic at 600 °C, $v=100$ mV/s, after a pre-electrolysis at -1.1 V vs Ag/Ag^+ during 360 s; (dashed line) $P_{\text{CO}_2} = 0.2$ atm.; (solid line) $P_{\text{CO}_2} = 0.3$ atm [142].

Most of the mechanistic studies on CO₂ electroreduction were based on cyclic voltammetry at a gold electrode in the molten carbonate bulk [138, 141, 142]. Knowing that the surface of gold is very sensitive to carbonates and is quite often passivated, it is very difficult to obtain reproducible results; thus, it is important to acquire independently other data by chronopotentiometry and current reversal chronopotentiometry (CRC) that could confirm the mechanism followed by the reaction.

V.3. Chronopotentiometry on Gold and Graphite electrodes

All the common alkali carbonate eutectic mixtures were analyzed mainly by chronopotentiometry and, in some cases, by CRC or chronoamperometry. The influence of CO₂ pressures and temperatures were investigated in Li₂CO₃-Na₂CO₃ (52:48 mol%), Li₂CO₃-K₂CO₃ (62:38 mol%) and Li₂CO₃-Na₂CO₃-K₂CO₃ (43.5:31.5:25.0 mol%), and Na₂CO₃- K₂CO₃ (58:42 mol%) using gold and graphite electrode materials.

V.3.1. Chronopotentiometric measurements

Chronopotentiograms corresponding to CO₂ reduction in four alkali carbonate eutectics, Li-Na, Li-K, Li-Na-K and Na-K are depicted in Figure V.2 (a-c). Even though these curves can roughly be seen as similar, they differ by the potentials of the plateaus and by their shape. In all cases, as expected, the transition time τ , tends to decrease with the absolute value of the imposed current (higher currents consuming more rapidly the

electroactive species). Another general feature is that quarter time potentials $E_{\tau/4}$, in most of the cases (Figure V.2 a,c,d) become slightly more negative as the absolute value of the current increases, which indicates that the corresponding electrochemical reaction is not fully reversible [143]. This phenomenon is quite clear in the case of Li-Na-K at 600 °C (Figure V.2c), but less pronounced at higher temperatures, 650 °C in Li-Na (Figure V.2a) and 750 °C in Na-K (Figure V.2c). In Li-Na (Figure V.2a), a first plateau is observed at around -1.1 to -1.2 V *vs* Ag/Ag⁺, corresponding to the main reduction peak of CO₂ observed at the same potential by cyclic voltammetry (CV) and that has been attributed to the reduction of soluble CO₂ into soluble CO [142].

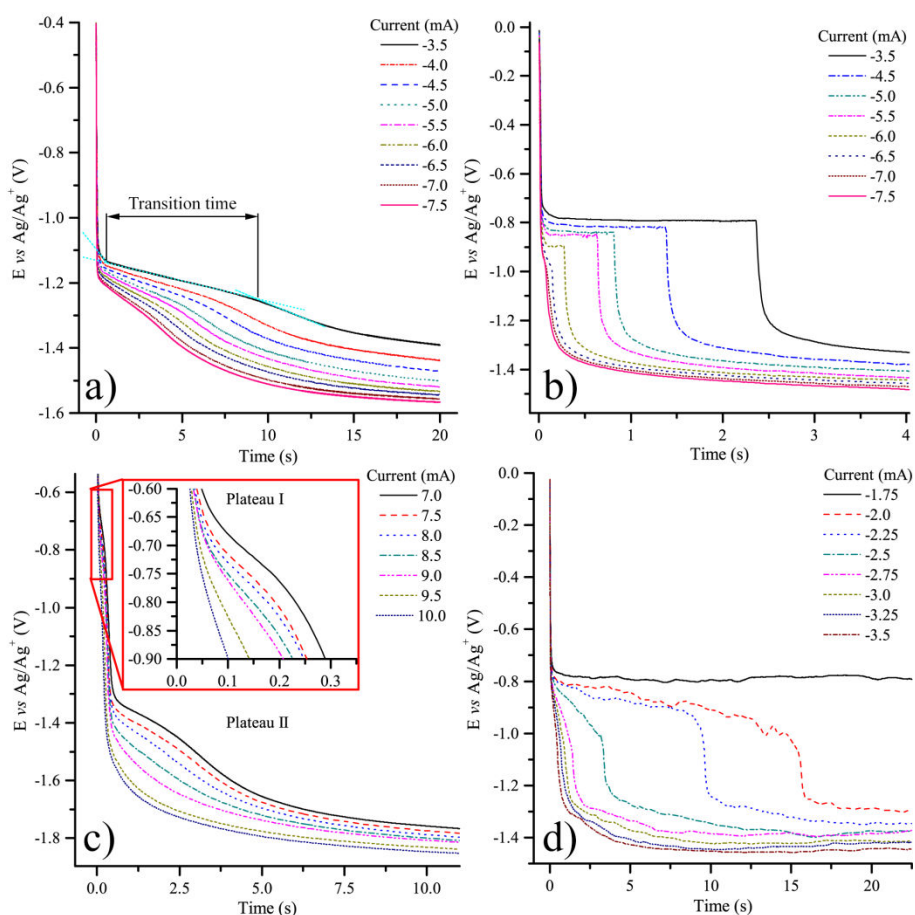


Figure V.2- Chronopotentiometry at a gold electrode in different carbonate eutectics: a) Li-Na at 650 °C and P_{CO_2} 0.5 atm.; b) Li-K at 650 °C and P_{CO_2} 0.05 atm.; c) Li-Na-K 600 °C and P_{CO_2} 0.5 atm. and d) Na-K at 750 °C and P_{CO_2} 0.5 atm.

Another plateau at around -1.4 V *vs* Ag/Ag⁺ is due to the reduction of carbonates from the electrolyte. A similar CO₂ reduction plateau (II) is observed in Li-Na-K (Figure

V.2c) but at slightly lower potentials, which is in accordance with a slower electrochemical reaction ($E_{\tau/4}$ potentials are more affected at higher currents). The second plateau due to the reduction of carbonates, occurring at potentials values more negative than $-1.6 \text{ V vs Ag/Ag}^+$, shows again that systems are less reversible in Li-Na-K ($600 \text{ }^\circ\text{C}$) (Figure V.2c) than in Li-Na ($650 \text{ }^\circ\text{C}$) (Figure V.2a), which is mainly an effect of temperature. However, when zooming into lower currents of Li-Na-K chronopotentiograms, we find small plateaus at around $-0.75 \text{ V vs Ag/Ag}^+$, which are related to the CV peak observed at nearly the same potential in previous work [142]. Li-K (Figure V.2b), under a lower partial pressure of CO₂ (P_{CO_2} of 0.05 atm. instead of 0.5 atm.) shows clearly the same plateau, with a sharp shape probably due to adsorbed species ($E_{\tau/4}$ with a constant value). Another plateau follows at less than $-1.2 \text{ V vs Ag/Ag}^+$ corresponding to the main CO₂ reduction peak observed by CV in previous work [142]. The same tendency is observed for Na-K (Figure V.2d) at higher temperature but with a slight slope for the first plateau. The plateau beginning at $-0.8 \text{ V vs Ag/Ag}^+$ could be due to the reduction of pre-adsorbed CO₂, but without strong evidence.

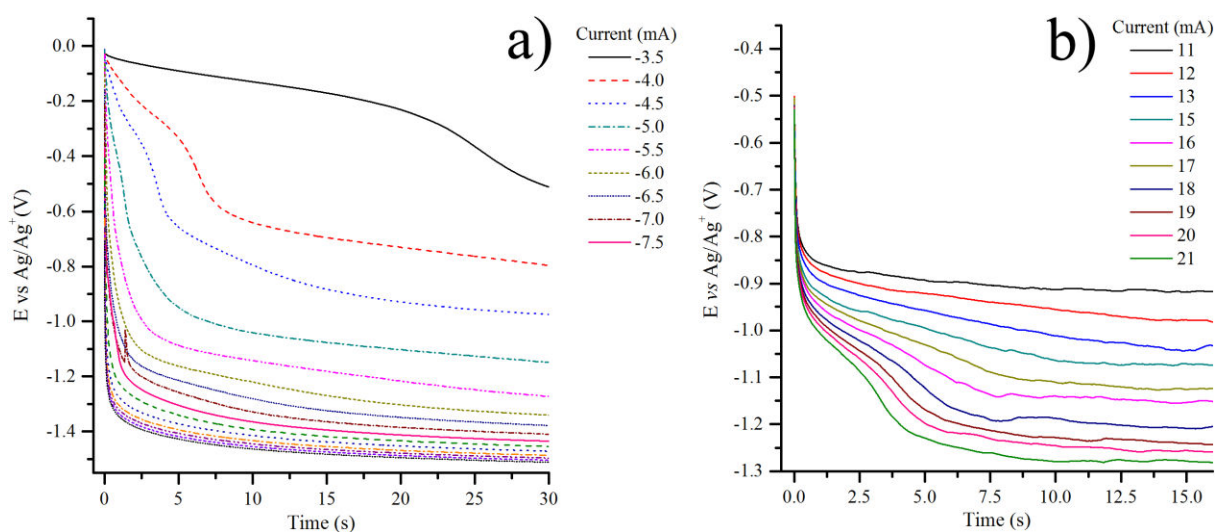


Figure V.3- Chronopotentiometry at P_{CO_2} 0.5 atm of: a) gold electrode immersed in Li-Na eutectic at $700 \text{ }^\circ\text{C}$ and b) graphite electrode immersed in Li-K eutectic at $650 \text{ }^\circ\text{C}$.

In the case of Li-Na carbonate eutectic at $700 \text{ }^\circ\text{C}$, at very low imposed currents, as shown in Figure V.3a, chronopotentiograms display a new reduction plateau at around $-0.35 \text{ V vs Ag/Ag}^+$, which was hypothetically attributed in a previous paper [142] to the

reduction of CO_{2ads} into CO_{ads}. In effect, by CV in Na-K at 750 °C, a reduction peak clearly appeared at a similar potential, associated to the reverse CO_{ads} oxidation peak. The influence of temperature is evident when comparing Figure V.2a and Figure V.3a, the plateau appearing at -1.2 V *vs* Ag/Ag⁺ in Figure V.2a appears only from -6.0 to -7.0 mA in the form of a poorly defined transition, which means the CO₂ at the electrode is depleted faster at 700 °C than at 650 °C. Moreover, an equally poorly defined transition appears between -0.6 and -1.0 V *vs* Ag/Ag⁺ between -4.5 and -5.5 mA that also disappears rapidly at more negative currents. Finally, Figure V.3b shows the chronopotentiogram of Li-K at 650 °C at a graphite electrode, two reduction plateaus can be observed: one at around -0.95 V *vs* Ag/Ag⁺ and the other at around -1.2 V *vs* Ag/Ag⁺ stable in the practical conditions used. Since the reduction of carbonates under these conditions is not observed until a potential between -1.6 and -2.0 V *vs* Ag/Ag⁺ [147]. These two plateaus probably correspond to reactions V.1 (around -0.95 V *vs* Ag/Ag⁺) and V.4 - V.5 (around -1.2 V *vs* Ag/Ag⁺), with two steps of one electron followed by the neutralization of CO₂²⁻.

Figure V.4 (a-c) shows the transition time dependence on applied current as a function of temperature, oxoacidity of the carbonate melt (P_{CO_2}), nature of the electrolyte and working electrode; the legends PI and PII correspond to the so called Plateau I and Plateau II that are not always present under different conditions tested herein. As already mentioned, the quarter potential $E_{\tau/4}$ tends to decrease with the increase in the transition time (related to the decrease of the absolute value of current), which indicates that the electrochemical systems involved are quasi-reversible, as analyzed before by CV [142]. Figure V.4a (Li-Na with $P_{CO_2}=0.5$ atm. at a gold electrode) shows the evolution of $E_{\tau/4}$ with temperature, and is related to different reduction processes, as mentioned before; at around -0.1 V *vs* Ag/Ag⁺ (plateaus I) and at around -1.2 to -1.4 V *vs* Ag/Ag⁺ (plateaus II). For plateau II, when increasing the temperature from 600 to 650 °C, the transition time becomes larger, this is consistent with the fact that both the solubility and the diffusion coefficient of CO₂ increase with the temperature.

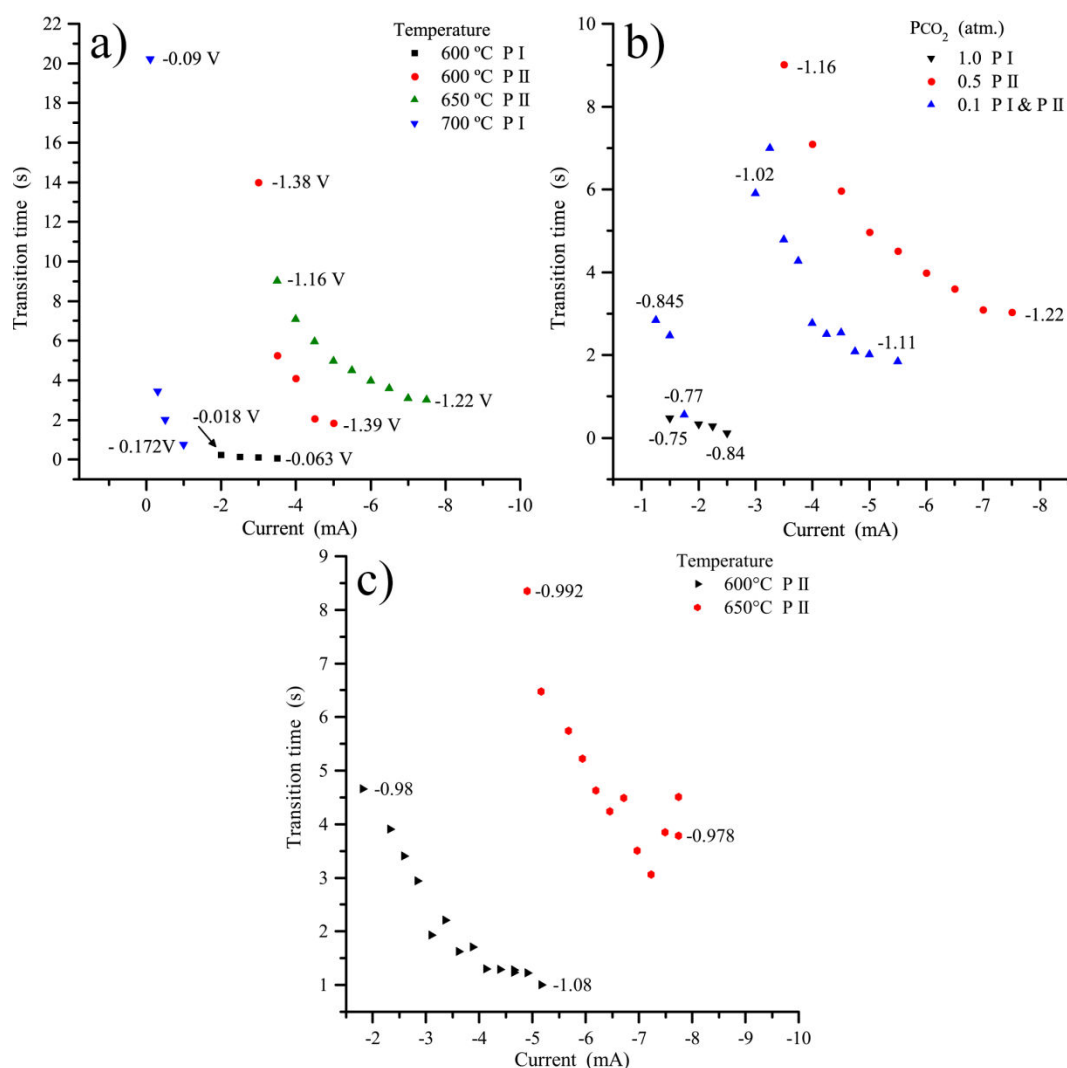


Figure V.4- Transition time dependence on applied current in different conditions: a) gold electrode in Li-Na at $P_{CO_2} = 0.5$ atm. and different temperatures; b) gold electrode in Li-Na eutectic at 650 °C and different P_{CO_2} , and c) graphite electrode in Li-K eutectic at $P_{CO_2} = 0.05$ atm. and different temperatures. The small numbers indicate the value of $E_{\tau/4}$ (quarter potential).

Another observation is that the potentials ($E_{\tau/4}$) are more negative at lower temperatures (Figure V.2c and Figure V.4a,c), which seems to be related to a slightly slower kinetics. For plateaus I (Figure V.4a), the behavior is quite different at the two studied temperatures, with a constant transition time at 600 °C, showing probably an adsorption phenomenon that is not present at 700 °C. Thus, it is more difficult to conclude about plateau I (Figure V.4a), but as we mentioned it could be related to adsorbed species (CO_{2ads} reduced into CO_{ads}) [142]. Figure V.4b shows the influence of P_{CO_2} on the transition times in Li-Na at 650 °C. The four series displayed can be divided in two groups; in the first one, the potentials belong to plateau I (PI) and are between -

0.75 and -0.8 V *vs* Ag/Ag⁺ and, in the second, the potentials corresponds to plateau II (PII) varying between -1 to -1.2 V *vs* Ag/Ag⁺. Transition times tends to increase with the partial pressure of carbon dioxide in the case of plateau II which represents the reduction of soluble CO₂ into soluble CO; this is in agreement with the fact that increasing the amount of CO₂ requires higher currents for being entirely consumed. Situation is more complex in the case of plateau I and we can just note that the transition times are larger at CO₂ 0.1 atm. than at 1 atm., which is difficult to explain. Evolution of the quarter time potentials is in favor of a quasi-reversible system. In the case of a graphite electrode in Li-K eutectic at $P_{CO_2} = 0.05$ atm. (Figure V.4c), the influence of temperature for plateau II ($E_{\tau/4}$ at around -1 V *vs* Ag/Ag⁺) is similar than in Figure V.4a: with potentials lower at 600 °C and systems are quasi-reversible.

V.3.2. Current reversal chronopotentiometry (CRC)

Current reversal chronopotentiometry (CRC) tests were carried out for exploring the reversibility and the characteristics of the reduction product. CRC graphs at a gold electrode in Li-K eutectic at 650°C, $P_{CO_2} = 0.1$ atm., displayed in Figure V.5a, show that two plateaus are successively observed in reduction (P I and P II), as well as in re-oxidation (P III and P IV). However, when a reversal current is applied immediately after P I, no reverse plateau is observed and P I appears to correspond to an irreversible reaction. Since the potential continues to decrease after P II (Figure V.5a), it is possible that P III (Figure V.5a inset) corresponds to the re-oxidation of the last product generated between 0.5 and 1 s and P IV to the re-oxidation of product P II; thus, it seems that P III and P IV are both linked to P II. The observation of two reverse plateaus when P II is re-oxidized may correspond to a quasi-reversible two-step oxidation reaction, or to the oxidation of soluble CO and adsorbed CO as proposed by Chery *et al.* [142]. Another CRC at a gold electrode in Li-Na at 650 °C, $P_{CO_2} = 0.1$ atm., shown in Figure V.5b, displays a well-defined plateau in reduction, corresponding to the potential of P II, and another one in oxidation P III. The transition times ratio is $\frac{\tau_2}{\tau_1} = 0.28 \approx \frac{1}{3}$: the reduction product is soluble, which confirms that P III corresponds to the oxidation of soluble CO.

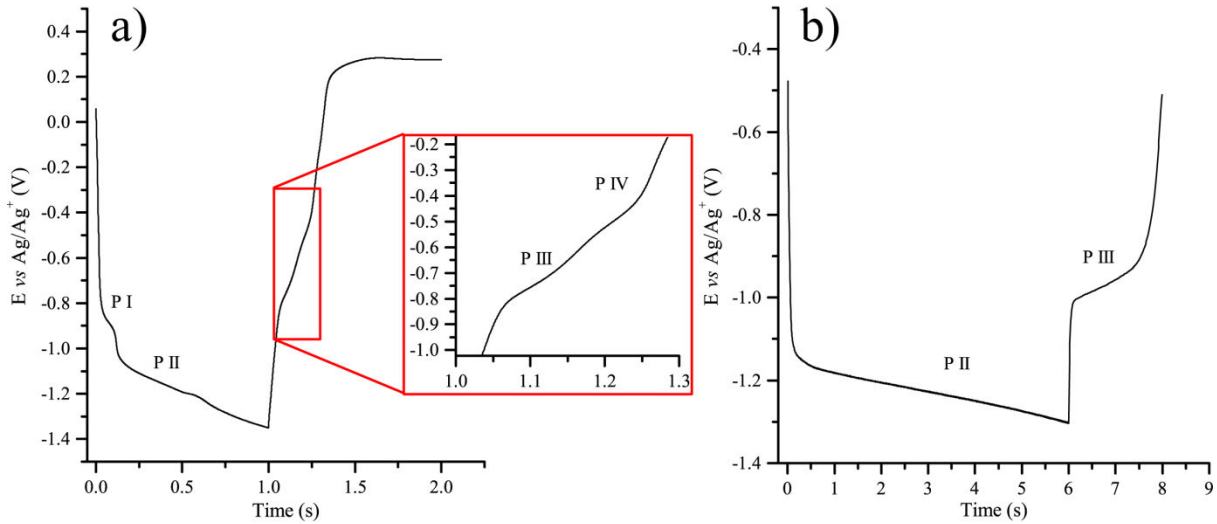


Figure V.5- Current reversal chronopotentiometry performed at a gold electrode: a) Li-K eutectic at 650 °C, $P_{CO_2} = 0.1$ atm., initial current of -8 mA during 1 s, then 8 mA during 1 s; b) in Li-Na eutectic at 650 °C, $P_{CO_2} = 0.5$ atm; initial current of -10 mA during 6 s, then 10 mA during 2 s.

V.3.3. Transition time analysis

Transition time τ , for a reversible electron transfer, is linked to the current by Sand's law [144]:

$$\tau^{1/2} = \frac{\pi^{1/2} n F A C_0 D_0^{1/2}}{2 i} \quad (V.7)$$

If the reaction presents adsorption steps involving more than one electrochemical species, τ expression will extend beyond Sand's law relation. To take into account adsorption phenomena, the relations listed in Table V.1 are considered for elucidating the predominant reaction mechanism and the number of electrons n transferred in each step [143,145].

It is important to keep in mind that in order to determine n , accurate values of $C_0 D_0^{1/2}$ are required as well as careful measurements. For the analysis of τ we have considered the chronopotentiograms taken at a graphite electrode immersed in Li-K eutectic at 650 °C and P_{CO_2} of 1, 0.5 and 0.2; (e.g. Figure V.2b) as well as those taken at a gold electrode immersed in Li-Na-K electrolyte at P_{CO_2} of 0.5 atm. at 550 and 600 °C (e.g. Figure V.2c). These data were the most reliable chronopotentiometric measurements among the experiments performed, in the sense that τ shows a clear linearity with one

or more of the proposed models. Each series of plateaus were analyzed for each of the four proposed mechanisms by plotting different combinations of the data as shown in Table V.1. If any of the plots results in a straight line, the mechanism represented by that plot is dominant.

Table V.1- τ relations for electrochemical reactions including one adsorption step

	Mechanism	Plotting	Equation
SR	Simultaneous reduction of diffusing electroactive species in solution and of adsorbed electroactive species	$i \cdot \tau$ vs $\tau^{1/2}$	$i\tau = nAF\Gamma + \frac{nAFC_0^0(D_0\pi\tau)^{1/2}}{2}$
RA-RD	Reduction of adsorbed species previously to diffusing species	$i \cdot \tau$ vs $1/i$	$i\tau = nAF\Gamma + \frac{(nFC_0^0)^2 D_0 \pi A}{4i}$
RD-RA	Reduction of diffusing species previously to adsorbed species	$(i \cdot \tau)^{1/2}$ vs $1/i^{1/2}$	$(i\tau)^{1/2} = nF\Gamma^{1/2} + \frac{nAFC_0^0(D_0\pi)^{1/2}}{2i^{1/2}}$
FE	Equilibrium mechanism (rapid equilibrium between adsorbed and diffusing species)	$C \cdot \tau^{1/2}$ vs C^2/i	$C_0^0 \tau^{1/2} = \frac{\pi^{1/2} \Gamma}{2D_0^{1/2}} + \frac{nAFC_0^0(D_0\pi)^{1/2}}{2i}$

From the linear regression with the best linearity, we can deduce the possible mechanism and from the slope, the value of n . In the case of Li-K at 650 °C, we took the value of D_{CO_2} from Meléndez-Ceballos *et al.* [146] ($1.1 \times 10^{-6} \text{ cm}^2 \cdot \text{s}^{-1}$) and the concentration C_0^0 was calculated from the solubility obtained in previous research [147]: $13.5 \text{ mol} \cdot \text{L}^{-1} \cdot \text{atm}^{-1}$. We also used other values given by Nishina *et al.* [23], but the results were impossible to interpret, proving the necessity of counting on new sets of experimental data. In the case of Li-Na-K eutectic, as we did not have values from our own, the values of D_{CO_2} and C_0^0 for each temperature were calculated directly from Nishina *et al.* [23]. Table V.2 summarizes the results of the linear regression for the four mechanisms described and the number of electrons n obtained. Based on the linearity of the linear regressions, Li-K seems to change from the mechanism of simultaneous reduction of the species (SR) to the rapid equilibrium mechanism (FE) when decreasing P_{CO_2} . The value of n was found to be 1 electron for high concentrations and around 2 for lower P_{CO_2} . However, at very low concentration, the linearity is not so good and the error in n increases. For Li-Na-K at 550 °C, SR is the dominant mechanism with a number of electrons close to 2 for both reactions. When increasing the temperature and

P_{CO_2} , the phenomena seems to be mixed between the SR and FE mechanisms, and the computed n decreases.

Table V.2- Transition time analysis of the four cases proposed in Table V.1 for Li-K on graphite electrode and Li-Na-K on gold electrode at different temperatures and atmospheres.

Li-K 650 °C	P_{CO_2}					
	1 atm.		0.5 atm.		0.2 atm.	
Mechanism	R ²	n	R ²	n	R ²	n
SR	0.98	1.0	0.93	1.3	0.89	4.0
RA-RD	0.89	2.5	0.79	3.5	0.84	7.6
RD-RA	0.89	0.5	0.79	0.5	0.83	1.0
FE	0.96	1.8	0.95	2.5	0.97	5.6
Li-Na-K 550 °C	0.5 atm.					
	Plateau I			Plateau II		
Mechanism	R ²	n	R ²	n	R ²	n
SR	0.99	1.5	0.98	2.0		
RA-RD	0.94	4.3	0.69	5.0		
RD-RA	0.91	4.7	0.69	4.5		
FE	0.96	3.3	0.87	3.6		
Li-Na-K 600 °C	1 atm.					
	Plateau I			Plateau II		
Mechanism	R ²	n	R ²	n	R ²	n
SR	0.97	1.0	0.93	1.8		
RA-RD	0.82	2.5	0.82	5.0		
RD-RA	0.83	1.7	0.79	2.7		
FE	0.96	1.7	0.96	3.6		

V.4. Chronoamperometry

In order to confirm our hypothesis on CO₂ reduction mechanism, we performed chronoamperometric measurements. Two kinds of curves were obtained with specific shapes according to the imposed potential. In the first one, displayed in Figure V.6a, we can observe at around -0.9 V *vs* Ag/Ag⁺ a distortion of the $\bar{\pi}$ plot with respect to a Cottrell behavior, which most probably indicates an adsorption step and is in agreement with the results obtained by chronopotentiometry. For the second one at around -1.2 V *vs* Ag/Ag⁺ (Figure V.6b), current decreases abruptly and then slowly until reaching the

residual current. Cottrell plots (j vs $1/t^{1/2}$) did not give strictly a straight line, which is supposed to be the case for a diffusion-controlled reaction. However, many parameters may influence the recording of the current (e.g. possible agitation by convection, electrode vibration due to convection, non-perfectly stationary system), so that the hypothesis of a diffusion-controlled mechanism should not be discarded. Therefore, according to chronoamperometry, we conclude that CO₂ undergoes two reduction mechanisms. The first one at the higher potential is irreversible, as no reverse plateau (chronopotentiometry) or peak (by CV [142]) were observed, and is not diffusion-controlled. As this system is not always clearly observed, it might be due to the reduction of adsorbed CO₂, in specific adsorption sites, into CO₂⁻, which is unstable and, therefore, its oxidation cannot be observed. For the second at the lower potential, the reaction is quasi-reversible. The present study does not contradict previous hypothesis of a reaction involving two diffusing species, with a soluble product. This reaction corresponds, as also seen by chronopotentiometry and CV [142], to the reduction of soluble CO₂ into CO, but with different complex steps including adsorption phenomena.

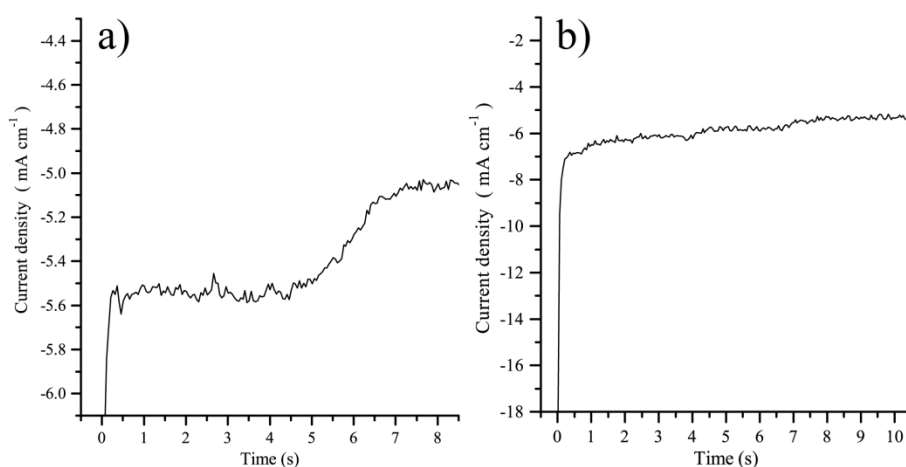


Figure V.6. Chronoamperometry performed at a gold electrode in Li-K eutectic at 650°C; a) $P_{CO_2} = 0.05$ atm., $E = -0.9$ V vs Ag/Ag⁺; b) $P_{CO_2} = 0.1$ atm., $E = -1.2$ V vs Ag/Ag⁺

V.5. Conclusions

Reduction of CO₂ in molten carbonates at gold or graphite electrodes is complex and depends on many factors. As the hypotheses proposed from cyclic voltammetry data

were far from being fully proven, the challenge of the present work was quite important and delicate: using complementary electrochemical tools, such as chronopotentiometry, reversal current chronopotentiometry and chronoamperometry, delicate, not only to confirm but to get a new insight on the mechanisms. According to the experimental conditions, which means nature of electrodes, temperature, partial pressure of CO₂ and electrochemical parameters (potentials or currents imposed, procedure, etc.), significant results were obtained, showing in synthesis the following facts:

- a- There is a main CO₂ reduction phenomenon yielding the formation of CO (reaction V.5) at roughly -1.2 V *vs* Ag/Ag⁺ (value that also depends on the temperature, nature of the eutectic, etc.). This transformation, involving soluble species and most probably adsorbed and instable intermediates, occurs in two one-electron steps or in two-electron unique step. The most probable intermediate species are CO₂⁻ (in all cases one or two steps) and CO₂²⁻, only observed in a second reduction step when sufficiently stable. At high and intermediate P_{CO_2} , a one-electron step is surely the unique step and we only identified a two-electron steps at low P_{CO_2} under specific conditions (e.g. gold electrode in Li-K eutectic at 650 °C, $P_{CO_2} = 0.1$ atm.), meaning that CO₂²⁻ is in general too instable to provoke its own reduction step. The number of electrons according to the most reliable results obtained by transition time analysis seems to evolve from a one-electron to a two-electron step from high to low values of P_{CO_2} , and in the same way from the mechanism of simultaneous reduction of the species (SR) to the rapid equilibrium mechanism between adsorbed and diffusing species (FE). It should be added that measurements at high P_{CO_2} were easier to interpret. The re-oxidation phenomenon due to soluble CO and identified by reversal current chronopotentiometry is harder to be observed due to the low solubility of CO in molten carbonates [147].
- b- A pre-reduction phenomenon also occurs at roughly in some specific conditions (e.g. gold electrode in Li-Na-K at 600 °C and P_{CO_2} 0.5 atm.) and appears to be due to adsorbed CO₂ species on specific adsorption sites of the working electrode. This phenomenon is found around -0.8 V *vs* Ag/Ag⁺, and produces very low intensity peaks by cyclic voltammetry [142].

c- Finally, CO₂ can be reduced to CO at around -0.35 V *vs* Ag/Ag⁺ with both species in an adsorbed form. CO oxidation was identified by reversal current chronopotentiometry. A full analysis of this system is impossible at this stage.

For concluding, we have succeed in proving some previous results and identify some mechanistic approaches, defining whether the systems are diffusion-controlled or not, soluble or insoluble, in one or two steps and according to what kind of mechanism with a mixed diffusion-adsorption phenomenon. Anyhow at high P_{CO_2} , the mechanism of simultaneous reduction of the species (SR) was found to be dominant. To complete our understanding, fine *in situ* analyses of the electrode surfaces would be necessary but delicate to realize.

V.6. Scientific papers

From the results obtained in this section, one scientific paper has been accepted for publication in the Journal of the Electrochemical Society on February 20th, 2017.



Chronopotentiometric Approach of CO₂ Reduction in Molten Carbonates

A. Meléndez-Ceballos,^a A. Brouzgou,^{a,b} C. Crapart,^a V. Albin,^a V. Lair,^a and M. Cassir^{a,z}

^aPSL Research University, Chimie Paristech-CNRS, Institut de Recherche de Chimie de Paris, F-75231 Paris Cedex 05, France

^bUniversity of Thessaly, Thessaly, Greece

Carbon capture and valorization is a new route increasingly discussed to reduce greenhouse gas emissions. One of the paths foreseen for CO₂ valorization is its transformation into fuels by electrochemical reduction of carbon dioxide. In this approach, molten carbonates are of particular interest since they can be used to capture CO₂ molecule because of its high solubility; hence, valorization by electrolysis is possible in molten carbonate media. To better understand CO₂ reduction, chronopotentiometric and chronoamperometric techniques were used at gold and graphite electrodes immersed in four alkali carbonate eutectics, Li-Na, Li-K, Li-Na-K and Na-K. The results complemented a previous work based on cyclic voltammetry and confirmed the existence of a main CO₂ reduction phenomena around -1.2 V vs Ag/Ag⁺ that involves two one-electron steps or a two-electron unique step. Transition time analysis showed that the reduction mechanism is either simultaneous reduction of CO₂ adsorbed and diffusion species or rapid equilibrium between adsorbed and diffusing species. Furthermore, we identified another electrochemical system involving adsorbed CO₂ and CO at higher potentials. In summary, we have succeeded in proving and précising some previous results, as well as identifying reduction mechanisms.

© The Author(s) 2017. Published by ECS. This is an open access article distributed under the terms of the Creative Commons Attribution Non-Commercial No Derivatives 4.0 License (CC BY-NC-ND, <http://creativecommons.org/licenses/by-nc-nd/4.0/>), which permits non-commercial reuse, distribution, and reproduction in any medium, provided the original work is not changed in any way and is properly cited. For permission for commercial reuse, please email: oa@electrochem.org. [DOI: 10.1149/2.0241708jes] All rights reserved.



Manuscript submitted February 20, 2017; revised manuscript received April 3, 2017. Published May 9, 2017. *This paper is part of the JES Focus Issue on Progress in Molten Salts and Ionic Liquids.*

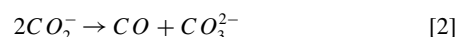
Carbon capture and valorization is a way increasingly discussed to reduce greenhouse gases emissions. The regulatory framework emerging for that purpose will bring large amounts of carbon dioxide to the market, with various degrees of purity and concentrations. One of the paths foreseen for CO₂ valorization is its transformation into fuels, which are value-added products with already broad market. Reducing carbon dioxide electrochemically is one of the possible ways to produce fuels.^{1,2} Today, there are already advanced studies regarding high temperature Solid Oxide Electrolysis Cells. Ceramtec, Utah,³ uses co-electrolysis of water and carbon dioxide to produce syngas, which is further converted into fuels via the Fisher-Tropsch process. In molten carbonates, Licht et al.⁴ demonstrated the feasibility of the electrolysis thanks to the so-called STEP process (Solar Thermal Electrochemical Production), although there is no pilot plant yet.

Molten carbonates are of particular interest compared to other electrolytes.⁵ They are advantageous from technological and economical viewpoints. First, they can be used to capture CO₂ molecule thanks to its high solubility rate in molten carbonates and, second, it could be valorized by an electrolysis process.⁶ Therefore, gaseous effluents from industry could be used without being pretreated to obtain a high degree of purity. Second, increasing the temperature of the melts lowers the electrical power required to perform the electrolysis.⁷ Since process heat is easily recycled and is cheaper than electricity, this would decrease the electrolysis cost. Consequently, molten carbonate electrolysis cells could be more competitive than other conversion technologies such as hydrogenation and electrochemical reduction in chlorides or ionic liquids.⁸

Several studies⁹⁻¹² have been carried out on CO₂ reduction but its specific mechanism in molten carbonate is not fully justified yet. It has been suggested that CO₂ can be reduced indirectly through the reduction of carbonates and their regeneration by absorption of CO₂.¹³⁻¹⁵ Other authors studied the direct reduction of CO₂ into CO via a radical CO²⁻.¹⁶

Peelen et al.¹⁷ have studied CO₂ reduction in Li₂CO₃-K₂CO₃ (62:38 mol%), in the temperature range of 575–800°C via linear sweep voltammetry and chronoamperometry. Their analysis and the

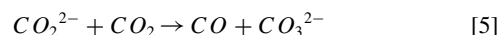
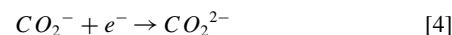
calculation from Cottrell equation suggested a one-electron transfer, diffusion-controlled mechanism:



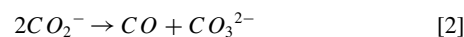
The overall reaction being:



According to a preliminary study by cyclic voltammetry, by our research team,¹⁸ two phenomena occurring at -1.2 V vs Ag/Ag⁺ and at -0.8 V vs Ag/Ag⁺, respectively, have been identified. In Li-Na carbonate eutectic, two peaks instead of one have been observed below -1 V vs Ag/Ag⁺ (Figure 1). Analogously, the following two mechanisms were suggested for the overall reduction:¹⁸



and:



The few mechanistic studies on CO₂ electroreduction were based on cyclic voltammetry at a gold electrode in the molten carbonate bulk.^{14,17,18} Knowing that the surface of gold is very sensitive to carbonates and is quite often passivated, it is very difficult to obtain reproducible results,¹⁸ thus, it is important to perform other measurements, e.g. by normal and current reversal chronopotentiometry (CRC), enabling the observation of successive potential steps

^zE-mail: michel-cassir@ens.chimie-paristech.fr

VI. Single-cell tests in fuel cell mode

“Concentrate all your thoughts upon the work at hand. The sun's rays do not burn until brought to a focus.”

Alexander Graham Bell

VI.1. General concepts

Molten carbonate fuel cells as any other fuel cells are governed by the electrochemistry occurring at the triple phase boundary. Thus, in this section, a description of the reactions taking place at the electrodes, as well as some useful formulations used in MCFC characterization are presented.

VI.1.1. MCFC operated with hydrogen and CO

According to reactions I.4, I.5 and I.16, emf (electromotive force) of the cell can be defined by the equation:

$$emf = emf^0 + \frac{RT}{2F} \ln \left(\frac{P_{H_2} \cdot P_{O_2}^{1/2}}{P_{H_2O}} \right) + \frac{RT}{2F} \ln \left(\frac{P_{CO_2(CAT)}}{P_{CO_2(AN)}} \right) \quad (VI.1)$$

It can be seen that the partial pressures of CO₂ at the cathode and anode have an influence on the total potential. If CO₂ partial pressures are equal, then the potential will depend only on the partial pressure of hydrogen, oxygen and water.

Contrarily to low temperature fuel cells, in which CO is a poisoning agent, this species can be used as fuel in MCFC, the reaction being as follows:



This is the case when reformed methane is used as the fuel. The methane reforming reaction is:



However, Ni is a good catalyst for the water gas shift reaction and most of the CO reacts with water at the anode to form more hydrogen:



Operating with CO and H₂ produces almost the same power. In both cases, the same amount of electrons are transferred in reactions I.4 and VI.2 and the free Gibbs enthalpy ΔG_f of H₂ and CO at 650 °C are very close (-197 and -201 kJ·mol⁻¹,

respectively), thus, the value of $emf^0 = \frac{-\Delta G_f}{2F}$ will be of 1.02 for H₂ and 1.04 V for CO [148].

For a MCFC operating with H₂, fuel and oxygen utilization, as well as outlet flow and water production have to be considered.

Oxygen utilization will be given by the number of transferred electrons per mole of oxygen according to reaction I.4, thus we can define this term as:

$$U(O_2) = \frac{I}{4F} \text{ moles} \cdot \text{s}^{-1} \quad (\text{VI.5})$$

For having a more practical formula for fuel cell parameter adjustment, this ratio can be converted from moles·s⁻¹ to volume flow in standard cubic centimeters per minute (sccm). For that, we can use the volume occupied by one mole of ideal gas (22.4139 L·mole⁻¹) at standard temperature and pressure (STP = 273.15 K at 1 atm.) and changing time base time from seconds to minutes as follows:

$$U(O_2) = \frac{I \text{ moles}}{4F \text{ s}} \times 22.413996 \frac{\text{L}}{\text{mole}} \times 10^3 \frac{\text{cm}^3}{\text{L}} \times 60 \frac{\text{s}}{\text{min}}$$

Leading to:

$$U(O_2) = 3.48457 \cdot I \text{ sccm} \quad (\text{VI.6})$$

If air is used to supply oxygen, we have to consider the amount of oxygen contained in air, which is 21 %; then, the airflow necessary to supply the strict minimum amount of oxygen for the reaction is $U(O_2) = 16.6 \cdot I$ sccm. However, by supplying this amount of air will lead to a completely depleted oxygen stream at the cathode outlet, which is impractical for MCFC operation; typically, airflow should be at least two times the stoichiometric coefficient, so we should consider the “more-than-stoichiometry” factor in the infeed gas calculation as a variable δ , thus, the infeed flow rate will be:

$$Fd(O_2) = 3.48457 \cdot \delta \cdot I \text{ sccm} \quad (\text{VI.7})$$

$$Fd(\text{Air}) = 16.6 \cdot \delta \cdot I \text{ sccm} \quad (\text{VI.8})$$

The outlet gas flow of the oxygen-poor stream will be given by:

$$\text{Outlet flow} = \text{inlet flow} - U(O_2)$$

Where the *inlet flow* is $Fd(O_2)$ or $Fd(\text{Air})$ of eq. VI.7 or VI.8.

For calculating hydrogen utilization rate, we follow the same approach, except that the number of electrons transferred is two in this case. Thus, equations VI.5 and VI.6 become:

$$U(H_2) = \frac{I}{2F} \text{ moles} \cdot \text{s}^{-1} \quad (\text{VI.9})$$

$$U(H_2) = 6.96914 \cdot I \text{ sccm} \quad (\text{VI.10})$$

This fuel utilization rate only applies for hydrogen fuelled MCFC.

Now, for calculating the CO_2 utilization factor, we have to consider that for every mole of H_2 used at the anode, a mole of CO_2 is needed at the cathode, hence:

$$U(H_2) = U(\text{CO}_2) = 6.96914 \cdot I \text{ sccm} \quad (\text{VI.11})$$

Finally, water production at the anode, as per equation I.4, will be of one mole of water for every two electrons; similarly to hydrogen, the flow of water produced within the cell will be given by:

$$\text{Pr}(H_2O) = \frac{I}{2F} \text{ moles} \cdot \text{s}^{-1} \quad (\text{VI.12})$$

Considering that a mole of water is $18.02 \text{ Kg} \cdot \text{mole}^{-1}$, we can obtain a rate of water production in terms of mass. This is more pertinent here since the volumetric flow of water vapor is not constant since it depends on the temperature at the measuring point, hence:

$$\text{Pr}(H_2O) = 5.6 \times 10^{-6} \text{ Kg} \cdot \text{min}^{-1} \quad (\text{VI.13})$$

With equations VI.1 to VI.13, an estimation of the flow rates which have to be delivered to the fuel cell were obtained, as well as the estimated outlet flow.

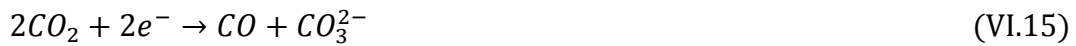
VI.1.2. MCEC for CO₂ reduction

If molten carbonate electrolyzer can be used to perform CO₂ electrolysis then, the overall reaction and the reactions occurring at the electrodes will be as follows:

Overall reaction:



Cathode reaction:



Anode reaction:



The voltage that should be supplied to the electrolyser with respect to the partial pressure of the reactants and products will be given by the Nernst equation as follows:

$$E = E_{CO_2/CO}^0 + \frac{RT}{2F} \ln \left(\frac{P_{O_2}^{1/2}}{P_{CO}} \right) + \frac{RT}{2F} \ln \left(\frac{P_{CO_2(CAT)}}{P_{CO_2(AN)}} \right) \quad (VI.17)$$

Gas utilization rates for these reactions can be calculated following the scheme proposed for the fuel cell working on hydrogen and based on equations VI.14 to VI.16, so they will not be listed herein.

VI.2. Cell assembly and operation

The fuel cell test bench by Fiaxell Sarl, originally designed for SOFCs, was modified by adding some components that allowed us operating as a MCFC. In this section, a brief description of the modifications will be shown as well as the procedure followed to fabricate the electrolyte layers along with the carbonate to matrix ratio. The materials used for the MCFC cell, supplied by ENEA, are listed in Table VI.1.

Table VI.1. Characteristics of fuel cell components employed.

Anode	
Thickness (mm)	0.69
Porosity	55-60%
Material	Ni + 5%wt Al
Cathode	
Thickness (mm)	0.7
Porosity	60-65%
Material	Lithiated NiO
Electrolyte	
Material	Li-K (62-38 mole %)
Fabrication	Tape cast
Matrix	
Material	γ -LiAlO ₂
Thickness (mm)	2 x 0.3

VI.2.1. The gas recovery flange concept and design modification

Originally, the “Fiaxell SOFC flange concept” capable of recovering the outlet gas, consists of two parallel metal plates that hold the cell in between by means of applied pressure. The sealing between the plates and the fuel cell ceramics is achieved by utilizing a non-conductive soft vermiculite mica gasket. The current collectors at each side of the cell are mounted at the end of a ceramic tube that compresses the cell and feeds the reactant gases. This tube is inserted into a bigger metallic tube welded to the flange; the sealing between the two tubes is achieved using Swagelok® type fittings. After passing through the cell, the remaining stream exits the assembly through the space between the ceramic and metallic tube where it can be recovered.

This system was modified to be adapted to MCFC testing by adding two “cell holder cups” that hold the cell within them. Sealing between the MCFC electrolyte and the cell holder cups is achieved thanks to the wet sealing action of molten carbonates, while the sealing between the cups and the metal plates is achieved by using the same soft vermiculite mica gasket. In this way, the contact between the mica sealing and the carbonates is avoided, the pressure on the cell is maintained regularly over the entire surface and proper contact is achieved thanks to gold mesh current collectors. An

illustration of the modified cell assembly is shown in Figure VI.1 where the flow of gases enters the cell through the blue area, passes by the electrodes through the orange area and leaves the cell through the red areas.

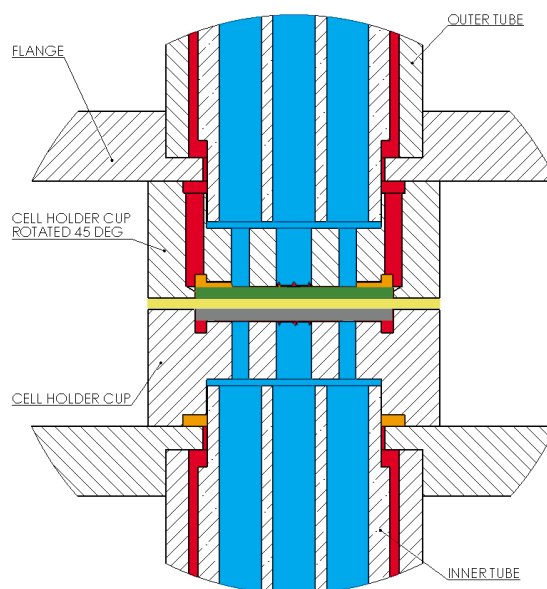


Figure VI.1. Detail of the fuel cell assembly with two identical cell holder cups, electrolyte is in light yellow, anode is in dark green and cathode is in gray.

The electrode compartment of the cell holder is 16 mm diameter and 0.8 mm deep, the contact surface between the electrolyte impregnated matrix and the cell holder cup is 5 mm around the cup, which ensures proper sealing between the cell holder and the electrolyte.

VI.2.2. Tape-cast of carbonate eutectic

Tape cast slurry was prepared following the recipe in Table VI.2 and the mixing procedure shown in Figure VI.2. The resulting slurry is then tape casted in a homemade doctor-blade tape cast table with a blade gap of 1mm and a speed of $5 \text{ mm}\cdot\text{s}^{-1}$. After drying, the flexible laminate is 0.33 mm thick. It should be noted that the carbonates are hydrophilic and the resulting tape should be kept in a dry environment upon utilization.

Table VI.2. Slurry composition for tape casting of eutectic carbonate mixture of Li-K (62-38 mol%).

Slurry Component	Weight (g)
Total mass	50
Carbonates	18.3
Ethanol	23.6
PVB	4.55
DBP	2.9
Zetaspere 2300	0.55
Surfinol DF-75	0.25

Ball milling is performed in a glass jar with 5 mm alumina grinding media in 1:1 slurry to grinding media relation. The jar is rotated to a speed of 10 rpm for the indicated time in the diagram of Figure VI.2. Degasification by vacuum directly made in the jar is necessary until all the ethanol is evaporated and the slurry acquires the high viscosity required for tape cast. After tape cast is finished the tape is left to dry at ambient temperature for 30 min., then it is removed from the tape cast Teflon® bed.

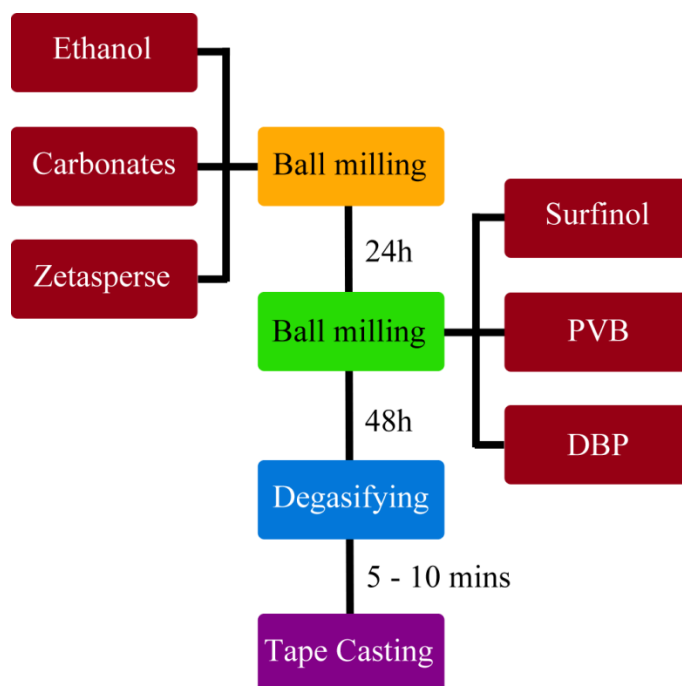


Figure VI.2. Slurry preparation for tape cast forming of Li-K laminates.

The TGA-DSC analysis of the produced tape shown in Figure VI.3 was performed to verify the fusion temperature of the carbonates (488 °C), the deviation of this parameter is an indication that the eutectic relation was changed during the tape cast process. This should be checked in case the solvent is substituted due to possible potassium migration [149,150] causing the eutectic proportion to be lost.

The onset temperature of 480 °C is the fusion point of the carbonates contained in the slurry. According to the calculations, the total mass loss of the slurry if ethanol is completely evaporated will be 31%; however, the mass loss of the slurry is around 34 %, which is not far from the expected value.

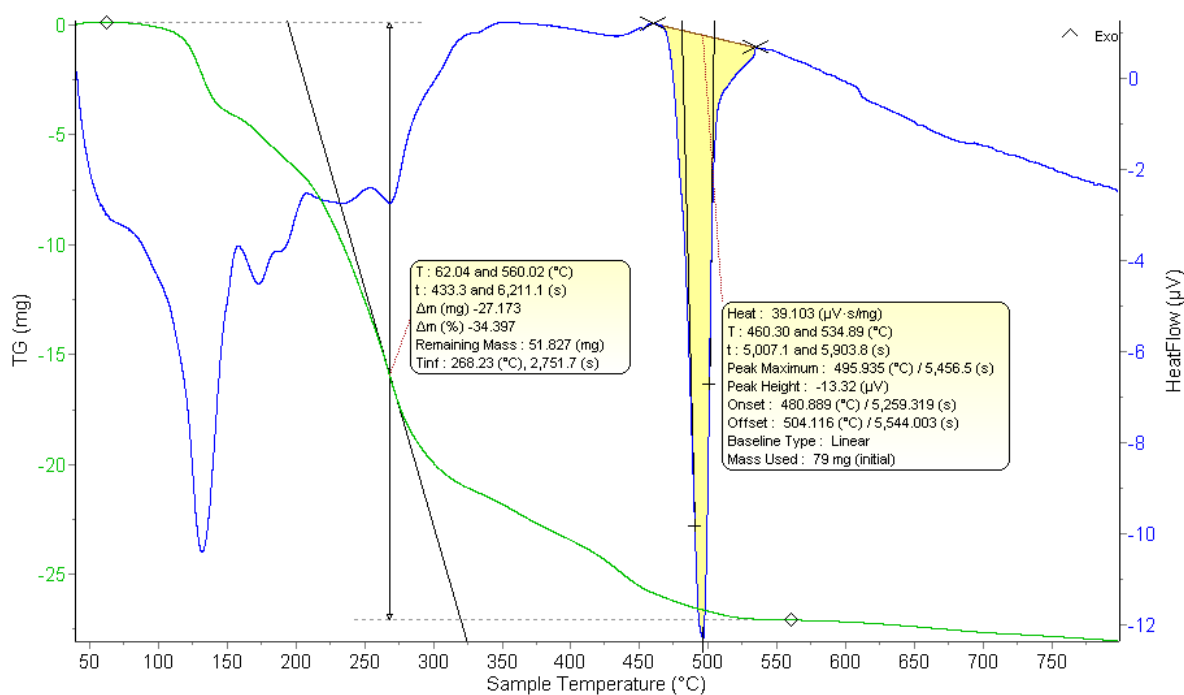


Figure VI.3. TGA-DSC analysis of tape casted laminate of Li-K eutectic mixture.

VI.2.3. Calculating the carbonate/matrix ratio

The weight content of carbonates in the cell should be properly calculated to ensure adequate filling of the matrix and electrodes. For this purpose, BET analysis or mercury intrusion porosimetry should be performed on matrix prior to calculations. In our case, our collaborators at ENEA supplied cathode, anode and matrix materials and

the porosimetry of the matrix is known. In any case, whatever the porosimetry of cathode and anode, the MCFC requirements demand an anode flooding of 20 %, cathode flooding of 40 % and matrix flooding of 100 %.

To achieve this, the void volume to be filled by carbonates in each component must be calculated as follows: the area, thickness and weight of the components to be used in the cell are measured. From this information, we can obtain first the volume V and the apparent density by the formula $\rho_{app} = \frac{M}{V}$, then the porosity of the material is determined by $P_{or} = 1 - \frac{\rho_{app}}{\delta}$, where δ is the bulk density of the material. Now, the void volume has to be calculated using the following expression: $V_{void} = V_{(x)} \times P_{or}$. To know the amount of carbonates to be added, knowing the flooding ratio $f_{r(x)}$, we can calculate $V_{carb(x)} = V_{void(x)} \times f_{r(x)}$, where (x) represent the anode (a), cathode (c) and matrix (m). The amount of carbonates in the matrix will be given by $V_{carb(m)} = V_{matrix} \times 0.628$. Since the porosity of the matrix is known. The total amount of carbonates that should be added in the cell will be given by $V_{carb\ tot} = V_{carb(a)} + V_{carb(c)} + V_{carb(m)}$.

The carbonate to matrix ratio is obtained by dividing the weight of the carbonates to be added by the weight of the matrix and it should always be more than 100 %, a typical value of this ratio is 120 % in our type of cell.

VI.3. Electrochemical measurements on reference cell

Herein, we will present the electrochemical measurements on the first MCFC single cell test performed in our team. The setup has still to be improved to ensure that the measurements can be comparable with literature, specially the reference electrodes. The geometrical area of the electrodes used is 2.01 cm² each; the gas composition was H₂/CO₂/H₂O (64/16/20 %) at the anode side and O₂/CO₂/N₂ (15/30/55 %) at the cathode side. Flowrate at both sides was of 150 sccm, fuel cell temperature was of 650 °C.

VI.3.1. OCP

Figure VI.4 shows the OCP recorded during the initial 6 hours after changing to the working atmosphere. Stabilization of the cell reaches a potential value of 980 mV, corresponding to the emf.

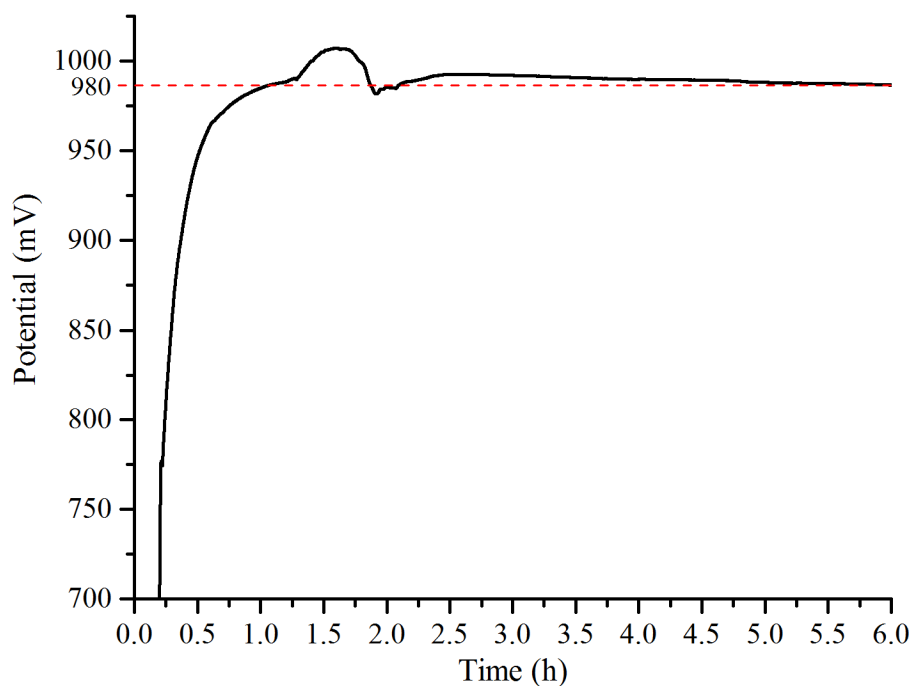


Figure VI.4. OCP of a MCFC single cell over 6 hours after changing to the working atmosphere of $\text{H}_2/\text{CO}_2/\text{H}_2\text{O}$ (64/16/20 %) at the anode and of $\text{O}_2/\text{CO}_2/\text{N}_2$ (15/30/55 %) at the cathode.

The small bump in the graph was caused by the introduction of water in the anode stream, it stabilized after 2 h.

VI.3.2. I-E curves and fuel cell output power

After cell stabilization, current-potential curves were obtained in Figure VI.5. The output current density of the cell was of $142 \text{ mA}\cdot\text{cm}^{-2}$ at 700 mV and a power density of $99.4 \text{ mW}\cdot\text{cm}^{-2}$. The maximum power density output of $127 \text{ mW}\cdot\text{cm}^{-2}$ is reached at 504 mV, a current density of $252 \text{ mA}\cdot\text{cm}^{-2}$. Small perturbations in the curves is probably due to non-homogenous reactant flow over the electrodes surface. This problem might be corrected by changing the dimensions of the flow channels in the cell holder cups.

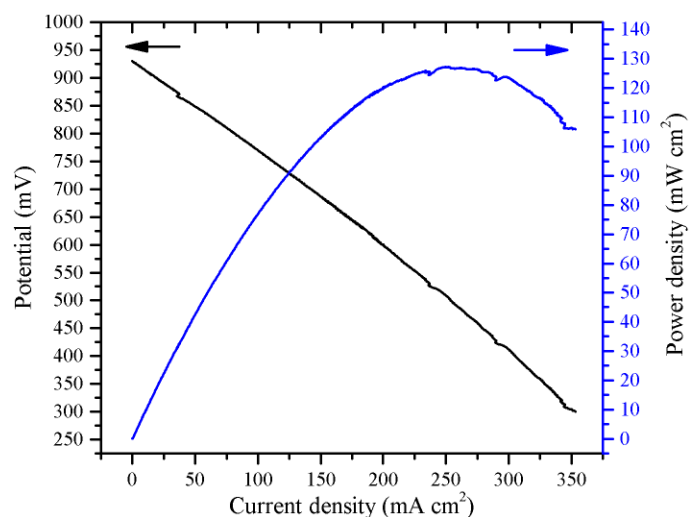


Figure VI.5. I-E and Power curve taken after cell stabilization at $10 \text{ mV}\cdot\text{s}^{-1}$ from 980mV to 400 mV, at $650 \text{ }^\circ\text{C}$, and atmospheres of $\text{H}_2/\text{CO}_2/\text{H}_2\text{O}$ (64/16/20 %) at the anode and of $\text{O}_2/\text{CO}_2/\text{N}_2$ (15/30/55 %) at the cathode.

VI.3.3. EIS

EIS data were obtained at $650 \text{ }^\circ\text{C}$ under $\text{H}_2/\text{CO}_2/\text{H}_2\text{O}$ (of 64/16/20 %) at the anode side and of $\text{O}_2/\text{CO}_2/\text{N}_2$ (15/30/55 %) at the cathode side, in a frequency range between 100 kHz and 0.5 Hz (Figure VI.6).

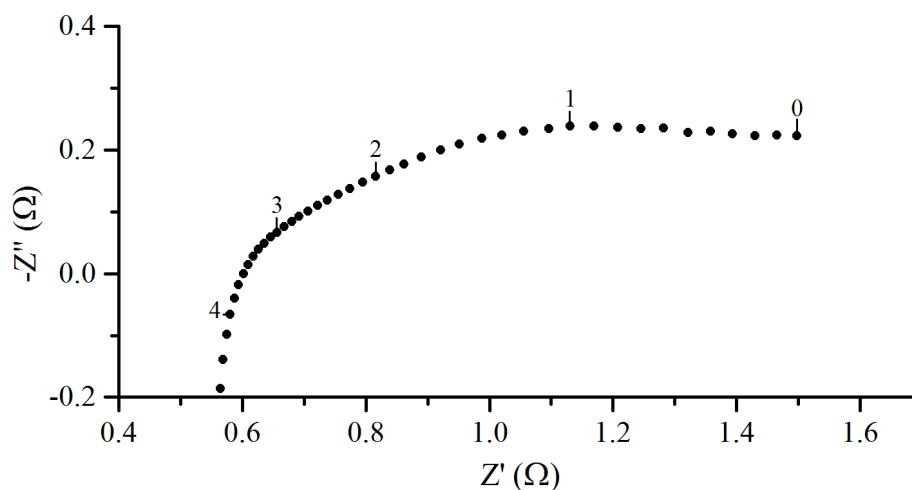


Figure VI.6. Nyquist diagram of MCFC cell at $650 \text{ }^\circ\text{C}$ and working atmosphere $\text{H}_2/\text{CO}_2/\text{H}_2\text{O}$ (64/16/20 %) at the anode side and $\text{O}_2/\text{CO}_2/\text{N}_2$ (15/30/55 %) at the cathode, numbers indicate Log of frequency.

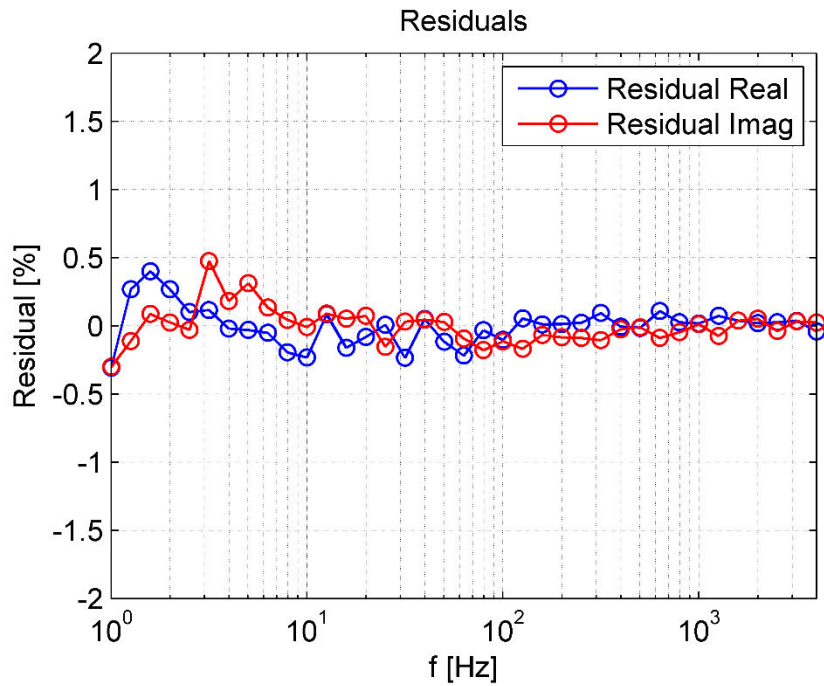


Figure VI.7. Kramers-Kronig test of data set shown in Figure VI.6.

Figure VI.7 shows the Kramers-Kronig test performed on the EIS data shown in Figure VI.6. As can be noted, the error % of the acquired data is under ± 0.5 % which means that the system was stable and EIS data is valid. Controversial interpretation of EIS data concerning MCFC devices are found in the literature; nevertheless, according to some authors EIS data can be divided in three major features: the internal resistance contribution (intersection point of data with Z' axis), a high frequency arc between 10 kHz and 5 Hz and a low frequency arc between 5 Hz and 10 mHz. The first arc is composed of the resistances corresponding to both polarization of the oxygen reduction at the cathode and hydrogen oxidation at the anode. The second arc is related to gas-liquid interphase and varies with the flow rate and composition of the fuel stream [151–155]. DRT curves deduced from EIS data (Figure VI.8) were obtained in order to clarify the number of phenomena present. As shown in the graph, four peaks appear with different relaxation times. However, we cannot assign from this brief analysis the phenomena corresponding to each peak and a more detailed study have to be performed by changing the anode and cathode atmospheres to elucidate their influence on the DRT.

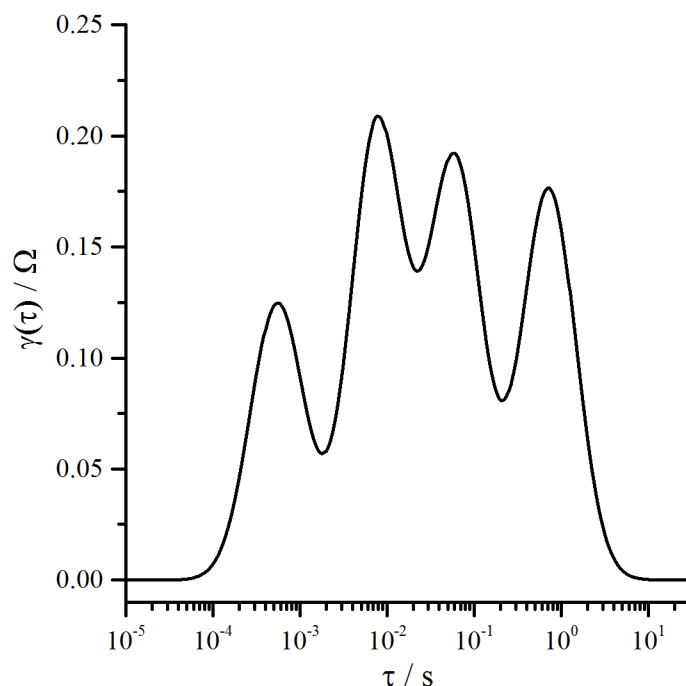


Figure VI.8. DRT of EIS data collected by using DRTTools [82], parameters were: regularization 1E-4, fitted w/o inductance, 1st order regularization derivative and shape factor 1.

VI.4. Conclusions

In this part of the research carried out during this Ph.D., the parameters for tape casting the electrolyte of the MCFC were optimized and, for the first time in our laboratory, a MCFC test was possible. Changes on the original concept of the testing system were necessary and conducted to an acceptable performance of the first cell tested. OCP showed that the emf was around the expected value of 1 V after stabilization for some hours. I-E curves confirmed that the cell was able to output a decent power density of about $100 \text{ mW}\cdot\text{cm}^2$ at 700 mV and a current density of $142 \text{ mA}\cdot\text{cm}^2$ which is not so far from the $160 \text{ mA}\cdot\text{cm}^2$ reported in the literature for this types of button cells. EIS first analysis showed that the measurements performed on the system in a symmetric cell configuration have a small error of $\pm 5 \%$ and can be assumed as valid. Further analysis by DRT suggests the existence of four contributions that could not be attributed in this study due to the lack of experimental data.

DRT is arising as a powerful tool to analyze electrode kinetics and difficult overlapped EIS spectra. Up to now, there is still a discrepancy in the literature

Chapter VI. Single-cell tests in fuel cell mode

concerning the attributions of the phenomena reflected by EIS and, as far as we know, there are no DRT studies carried out for MCFCs. Hence, a deeper analysis by DRT of the contributions found in EIS data should be carried out.

General conclusions and prospects

In the last ten years, a revival of molten carbonate science and technology has been observed through a significant number of new applications, such as metal extraction and recycling, DCFC (direct carbon fuel cell), hybrid fuel cells combining carbonates and oxides and carbon capture and storage. It is not our aim here to develop again this open and promising field related to such molten salt electrolytes, but to emphasize on the results obtained through this thesis in two major directions. The first part, which was developed in chapters III and IV, concerned the optimization of the well-known MCFC application with two main objectives: (i) cathode modification to extend MCFC lifetime without affecting the electrochemical performance and (ii) modification of the electrolyte to enhance the performance of the MCFC. The second part in view of CCS application (chapter V) was focused on the study of the CO₂ reduction reaction by means of chronopotentiometry and chronoamperometry, which complemented and clarified a previous PhD. study in our research group. Finally, the last part (chapter VI), was dedicated to single-cell set-up optimization intended to test the findings of the previous chapters.

The results obtained in Chapter III conduced to a better understanding of the role played by ultra-thin ALD-processed layers, being TiO₂ and CeO₂ the most promising materials for cathode modification since both oxides deposited in thicknesses of 50 and 27 nm, respectively, behaved electrochemically in a very close way to the state-of-the-art Ni cathode. Ni solubility was reduced almost in half by employing such fine layers which is very advantageous considering that the actual technology has a lifetime of 4-5 years in optimal conditions; thus, reducing the dissolution rate by half could represents at least a few years lifetime increase. Even though ALD remains expensive compared to other deposition techniques such as electrodeposition or sol-gel, the advantage of depositing a nanometer scale highly dense layer with a homogenous covering of the electrode surface has an important role in reducing cathode solubility while keeping high the electrochemical performances. This increase in lifetime will represent a considerable reduction in costs per kW of MCFC that could justify the ALD expenses. However, ALD technology has been advancing and improving in the last years which led

to a reduction in costs and increase in the size of substrates that can be employed reaching now up to square meter sizes as in spatial ALD. Nevertheless, work has still to be done to reach the maximum potential of ALD-processed layers since in this work only single oxides were used to modify the cathode and ALD allows very precise control on thicknesses of multilayered structures and dopant compositions of up to three different type of oxides. This will open the variety and properties of the materials that can be deposited allowing not only to protect the cathode from corrosion but also to improve the oxygen reduction kinetics by depositing materials such as yttria-doped ceria or niobium-doped cobalt.

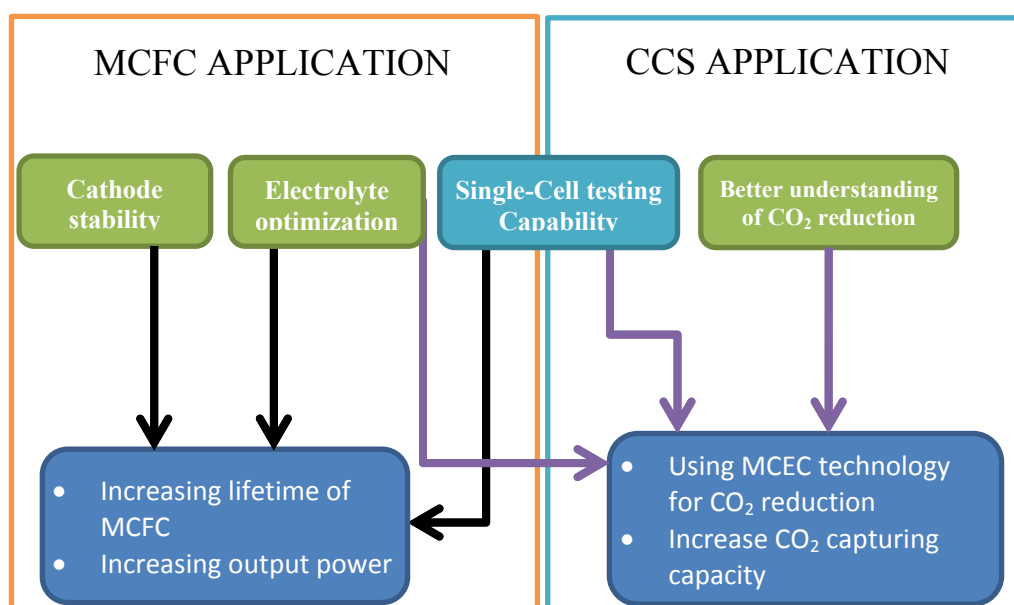
In our research for an improved electrolyte, we explored in chapter IV the influence of Cs in the kinetics of oxygen reduction by developing a testing method based on Nishina's reaction order analysis that served to compare the modified and non-modified electrolyte kinetic behavior and allowed us to deduce the CO₂ diffusion coefficient. By using this approach, we showed that adding 5 mol. % of Cs doubled the value of CO₂ diffusion coefficient compared to the non-modified electrolyte, favoring the oxygen reduction reaction and a higher power output, since it is the oxygen reduction which limits the MCFC overall reaction. We also proved that the state-of-the-art Ni cathode behaved well after Cs and Rb additions shortening the cathode stabilization time, reducing the charge transfer resistance and overall resistance. From these outcomes, we can assert that Cs is the most interesting additive to be used in Li-K carbonate melts. Even though adding Cs or Rb increases slightly the oxoacidity of the molten carbonates which will lead to a small increase in the Ni dissolution rate; thus, cathode protection by ALD as shown in chapter III could be one of the solutions to avoid reducing the MCFC lifetime. Nevertheless, this approach has still to be proven by testing Ni dissolution of a modified cathode in molten carbonate eutectics containing Cs or Rb.

As has already been mentioned, CCS is gaining a great interest as a route for reducing carbon emissions from industry; in this field, molten carbonates may have an interesting upcoming role in CO₂ valorization by its electrochemical reduction into CO. In chapter V, CO₂ reduction was analyzed by chronopotentiometry and chronoamperometry to obtain complementary information on such reaction, confirming that it involves adsorbed and instable species and occurs according to a mechanism of simultaneous reduction of adsorbed and soluble species (SR) in a two one-electron step

or two-electron unique step depending on the partial pressure of CO₂, which confirms some of the hypotheses formulated in previous studies of our research group. We also showed that obtaining more information from chronopotentiometry, such as the number of electrons transferred is possible, but has to be considered carefully, since the electrochemical measurements are very complicated in molten salts. To further investigate the CO₂ reduction mechanism, experiments could be conducted in a single-cell with gold or Ni electrodes in a symmetrical configuration where probably more reliable data could be obtained by EIS or chronopotentiometry.

Finally, chapter VI presents the first MCFC single cell test carried out in our laboratory. Although time was not enough to fulfill the objective of testing a modified cell, a procedure to fabricate the electrolyte by tape casting and assembling the cell was successfully developed, along with the control and parameters necessary to operate the MCFC. We also analyzed the electrochemical performance of this first cell obtaining acceptable results that could be further improved by making small adjustments in the cell holder cups, which will allow establishing rigorous electrochemical measurements to be used as a reference for future tests with modified MCFC components.

The results exposed in this work could lead to the following improvements in MCFC and CCS applications.



General conclusions and prospects

Chapters III and IV evidenced the route for increasing MCFC lifetime and output power by protecting the cathode from corrosion and by optimizing the composition of the carbonate electrolyte. Chapter V complemented our knowledge on the feasibility of CO₂ reduction in molten carbonates, showing some mechanistic hypotheses. However, the possibility of using MCEC for water and CO₂ co-electrolysis to produce H₂ and CO to form syngas, appears as less evident. This seems especially difficult since water and CO will be produced at the Ni cathode of the MCEC, and the water shift reaction between CO and H₂O forming H₂ and CO₂ may occur, even though in a moderate rate at 650°C. One possibility to obtain both H₂ and CO in the same cell avoiding the water shift reaction problem would be operating in a divided-cathode electrolyzer stack. In this concept, a section of stack cathodes will be fed only with CO₂ to produce CO, while another section will be fed by H₂O to produce H₂. Both outlet streams could then be combined for delivering syngas.

In brief, we have made some progress in two significant areas, MCFC optimization and better understanding of CO₂ reduction reaction. Both areas have very interesting applications that could conduce to cost reduction for clean energy production (MCFC) and contribute to reduce CO₂ emissions through CO₂ capture and valorization into fuels (MCEC).

Bibliography

- [1] © OECD/IEA 2015 World Energy Outlook, IEA Publishing. Licence: www.iea.org/t&c. n.d.
- [2] Shao M, Chang Q, Dodelet J-P, Chenitz R. Recent Advances in Electrocatalysts for Oxygen Reduction Reaction. *Chem Rev* 2016;116:3594–657.
- [3] Carter D, Wing J. The Fuel Cell Industry Review 2013. *Fuel Cell Today*; 2013.
- [4] Remick R, Wheeler D. Molten carbonate and phosphoric acid stationary fuel cells: overview and gap analysis. National Renewable Energy Laboratory; 2010.
- [5] Broers GHJ. High Temperature Galvanic Fuel Cells. Universteit van Amsterdam, 1959.
- [6] Di Giulio N, Bosio B, Han J, McPhail SJ. Experimental analysis of SO₂ effects on Molten Carbonate Fuel Cells. *Int J Hydrog Energy* 2014;39:12300–8.
- [7] Bocci E, Di Carlo A, McPhail SJ, Gallucci K, Foscolo PU, Moneti M, et al. Biomass to fuel cells state of the art: A review of the most innovative technology solutions. *Int J Hydrog Energy* 2014;39:21876–95.
- [8] Ghezal-Ayagh H, Farooque M, Maru HC. Carbonate Fuel Cell: Principles and Applications. In: Basu S, editor. *Recent Trends Fuel Cell Sci. Technol.*, Springer New York; 2007, p. 217–47.
- [9] Sangster M, Pelton AD. Special Report to the Phase Equilibria Program. Westerville, Ohio.: American Ceramic Society; 1987.
- [10] Kojima T. Physical and Chemical Properties of Molten Carbonates. Dissertation. Kobe University Graduate School of Natural Science and Technology, 2009.
- [11] Cassir M, Ringuedé A, Lair V. 17 - Molten Carbonates from Fuel Cells to New Energy Devices A2 - Lantelme, Frédéric. In: Groult H, editor. *Molten Salts Chem.*, Oxford: Elsevier; 2013, p. 355–71.
- [12] Flood H, Förland T, Sillén LG, Linnasalmi A, Laukkanen P. The Acidic and Basic Properties of Oxides. *Acta Chem Scand* 1947;1:592–604.
- [13] Flood H, Muan A, Sillén LG, Rottenberg M. The Influence of the Cation Composition on Anion-Equilibria in Molten Salt Mixtures. *Acta Chem Scand* 1950;4:359–63.
- [14] Cassir M, Moutiers G, Devynck J. Stability and Characterization of Oxygen Species in Alkali Molten Carbonate: A Thermodynamic and Electrochemical Approach. *J Electrochem Soc* 1993;140:3114–23.
- [15] Appleby AJ, Nicholson S. Oxygen reduction in carbonate melts: Significance of the peroxide and superoxide ions. *J Electroanal Chem Interfacial Electrochem* 1972;38:A13–8.
- [16] Appleby AJ, Nicholson S. The reduction of oxygen in molten lithium carbonate. *J Electroanal Chem Interfacial Electrochem* 1974;53:105–19.
- [17] Appleby AJ, Nicholson SB. Reduction of oxygen in alkali carbonate melts. *J Electroanal Chem Interfacial Electrochem* 1977;83:309–28.

Bibliography

- [18] Appleby AJ, Nicholson SB. Reduction of oxygen in lithium-potassium carbonate melt. *J Electroanal Chem Interfacial Electrochem* 1980;112:71–6.
- [19] Itoh T, Abe K, Dokko K, Mohamedi M, Uchida I, Kasuya A. In Situ Raman Spectroelectrochemistry of Oxygen Species on Gold Electrodes in High Temperature Molten Carbonate Melts. *J Electrochem Soc* 2004;151:A2042–6.
- [20] Itoh T, Maeda T, Kasuya A. In situ surface-enhanced Raman scattering spectroelectrochemistry of oxygen species. *Faraday Discuss* 2006;132:95–109.
- [21] Tryk DA, Yeager ED. The 2nd symposium on Molten Carbonate Fuel Cell Technology. In: Selman JR, Shores DA, Maru HC, Uchida I, editors. *Electrochem. Soc. Proceeding Ser. PV-90-16*, NJ: Pennington; 1990, p. 395.
- [22] Dunks GB, Stelman D. Electrochemical studies of molten sodium carbonate. *Inorg Chem* 1983;22:2168–77.
- [23] Nishina T, Uchida I, Selman JR. Gas Electrode Reactions in Molten Carbonate Media Part V . Electrochemical Analysis of the Oxygen Reduction Mechanism at a Fully Immersed Gold Electrode. *J Electrochem Soc* 1994;141:1191–8.
- [24] Ang PGP, Sammells AF. Influence of Electrolyte Composition on Electrode Kinetics in the Molten Carbonate Fuel Cell. *J Electrochem Soc* 1980;127:1287–94.
- [25] Broers GHJ, Ketelaar JAA. High Temperature Fuel Cells. *Ind Eng Chem* 1960;52:303–6.
- [26] Belhomme C, Cassir M, Tessier C, Berthoumieux E. Lithium Depth Profile in NiO Molten Carbonate Fuel Cell Cathode by Nuclear Microprobe. *Electrochem Solid-State Lett* 2000;3:216–9.
- [27] Freni S, Barone F, Puglisi M. The dissolution process of the NiO cathodes for molten carbonate fuel cells: state-of-the-art. *Int J Energy Res* 1998;22:17–31.
- [28] Giorgi L, Carewska M, Patriarca M, Scaccia S, Simonetti E, Di Bartolomeo A. Proceedings of the Third Grove Fuel Cell Symposium The Science, Engineering and Practice of Fuel Cells: Development and characterization of novel cathode materials for molten carbonate fuel cell. *J Power Sources* 1994;49:227–43.
- [29] Bloom I, Lanagan MT, Krumpelt M, Smith JL. The Development of LiFeO₂ - LiCoO₂ - NiO Cathodes for Molten Carbonate Fuel Cells. *J Electrochem Soc* 1999;146:1336–40.
- [30] Wijayasinghe A, Kungl. Tekniska högskolan, Institutionen för materialvetenskap. Development and characterisation of cathode materials for the molten carbonate fuel cell. 2004.
- [31] Plomp L, Sitters EF, Vessies C, Eckes FC. Polarization Characteristics of Novel Molten Carbonate Fuel Cell Cathodes. *J Electrochem Soc* 1991;138:629–30.
- [32] Plomp L, Veldhuis JBJ, Sitters EF, van der Molen SB. Improvement of molten-carbonate fuel cell (MCFC) lifetime. *J Power Sources* 1992;39:369–73.
- [33] Yamada K, Uchida I. In Situ Formation Process of LiCoO₂ in the Molten Lithium-Potassium Carbonate Eutectic at 923 K. *Chem Lett* 1994;23:299–302.
- [34] Makkus RC, Hemmes K, Wit JHW de. A Comparative Study of NiO (Li) , LiFeO₂, and LiCoO₂ Porous Cathodes for Molten Carbonate Fuel Cells. *J Electrochem Soc* 1994;141:3429–38.

- [35] Antolini E. LiCoO₂: formation, structure, lithium and oxygen nonstoichiometry, electrochemical behaviour and transport properties. *Solid State Ion* 2004;170:159–71.
- [36] Lundblad A, Schwartz S, Bergman B. Effect of sintering procedures in development of LiCoO₂-cathodes for the molten carbonate fuel cell. *J Power Sources* 2000;90:224–30.
- [37] Zhecheva E, Stoyanova R. Stabilization of the layered crystal structure of LiNiO₂ by Co-substitution. *Solid State Ion* 1993;66:143–9.
- [38] Delmas C, Saadoune I. Electrochemical and physical properties of the Li_xNi_{1-y}Co_yO₂ phases. *Solid State Ion* 1992;53:370–5.
- [39] Ganesan P, Colon H, Haran B, White R, Popov BN. Study of cobalt-doped lithium–nickel oxides as cathodes for MCFC. *J Power Sources* 2002;111:109–20.
- [40] Kim S-G, Yoon SP, Han J, Nam SW, Lim TH, Oh I-H, et al. A study on the chemical stability and electrode performance of modified NiO cathodes for molten carbonate fuel cells. *Electrochimica Acta* 2004;49:3081–9.
- [41] Bloom I. Mcfc Component Development at Anl. Argonne National Lab., IL (US); 1998.
- [42] Wijayasinghe A, Bergman B, Lagergren C. LiFeO₂–LiCoO₂–NiO materials for Molten Carbonate Fuel Cell cathodes. Part I: Powder synthesis and material characterization. *Solid State Ion* 2006;177:165–73.
- [43] Wijayasinghe A, Bergman B, Lagergren C. LiFeO₂–LiCoO₂–NiO materials for Molten Carbonate Fuel Cell cathodes. Part II. Fabrication and characterization of porous gas diffusion cathodes. *Solid State Ion* 2006;177:175–84.
- [44] Simonetti E, Presti RL. Characterization of Ni porous electrode covered by a thin film of LiMg_{0.05}Co_{0.95}O₂. *J Power Sources* 2006;160:816–20.
- [45] Kim MH, Hong MZ, Kim Y-S, Park E, Lee H, Ha H-W, et al. Cobalt and cerium coated Ni powder as a new candidate cathode material for MCFC. *Electrochimica Acta* 2006;51:6145–51.
- [46] Ganesan P, Colon H, Haran B, Popov BN. Performance of La_{0.8}Sr_{0.2}CoO₃ coated NiO as cathodes for molten carbonate fuel cells. *J Power Sources* 2003;115:12–8.
- [47] Escudero MJ, Nóvoa XR, Rodrigo T, Daza L. Influence of lanthanum oxide as quality promoter on cathodes for MCFC. *J Power Sources* 2002;106:196–205.
- [48] Huang B, Ye X, Wang S, Yu Q, Nie H, Hu Q, et al. Electrochemical performance of Y₂O₃/NiO cathode in the molten Li_{0.62}/K_{0.38} carbonates eutectics. *Mater Res Bull* 2006;41:1935–48.
- [49] Paoletti C, Carewska M, Presti RL, Phail SM, Simonetti E, Zaza F. Performance analysis of new cathode materials for molten carbonate fuel cells. *J Power Sources* 2009;193:292–7.
- [50] Durairajan A, Colon-Mercado H, Haran B, White R, Popov B. Electrochemical characterization of cobalt-encapsulated nickel as cathodes for MCFC. *J Power Sources* 2002;104:157–68.
- [51] Chen L j., Zuo J, Lin C-J. A Novel MCFC Cathode Material Modified by the EPD Technique. *Fuel Cells* 2003;3:220–3.
- [52] Kuk ST, Song YS, Suh S, Kim JY, Kim K. The formation of LiCoO₂ on a NiO cathode for a molten carbonate fuel cell using electroplating. *J Mater Chem* 2001;11:630–5.

Bibliography

- [53] Mendoza L, Albin V, Cassir M, Galtayries A. Electrochemical deposition of Co_3O_4 thin layers in order to protect the nickel-based molten carbonate fuel cell cathode. *J Electroanal Chem* 2003;548:95–107.
- [54] Mendoza L, Baddour-Hadjean R, Cassir M, Pereira-Ramos JP. Raman evidence of the formation of LT- LiCoO_2 thin layers on NiO in molten carbonate at 650°C. *Appl Surf Sci* 2004;225:356–61.
- [55] Pauporté T, Mendoza L, Cassir M, Bernard MC, Chivot J. Direct Low-Temperature Deposition of Crystallized CoOOH Films by Potentiostatic Electrolysis. *J Electrochem Soc* 2005;152:C49–53.
- [56] Mendoza L, Ringuedé A, Cassir M, Galtayries A. II. Structural, morphological, chemical and electrochemical analysis of nickel covered by electrochemically deposited Co_3O_4 in molten Li_2CO_3 – Na_2CO_3 at 650 °C. *J Electroanal Chem* 2005;576:147–60.
- [57] Escudero MJ, Rodrigo T, Mendoza L, Cassir M, Daza L. Porous nickel MCFC cathode coated by potentiostatically deposited cobalt oxide: I. A structural and morphological study. *J Power Sources* 2005;140:81–7.
- [58] Mansour C, Pauporté T, Ringuedé A, Albin V, Cassir M. Protective coating for MCFC cathode: Low temperature potentiostatic deposition of CoOOH on nickel in aqueous media containing glycine. *J Power Sources* 2006;156:23–7.
- [59] Albin V, Mendoza L, Goux A, Ringuedé A, Billard A, Briois P, et al. Morphological, structural and electrochemical analysis of sputter-deposited ceria and titania coatings for MCFC application. *J Power Sources* 2006;160:821–6.
- [60] Cassir M, Belhomme C. Technological applications of molten salts: the case of the molten carbonate fuel cell. *Plasmas Ions* 1999;2:3–15.
- [61] Morita H, Komoda M, Mugikura Y, Izaki Y, Watanabe T, Masuda Y, et al. Performance analysis of molten carbonate fuel cell using a Li/Na electrolyte. *J Power Sources* 2002;112:509–18.
- [62] Yoshikawa M, Mugikura Y, Watanabe T, Ota T, Suzuki A. The Behavior of MCFCs Using Li/K and Li/Na Carbonates as the Electrolyte at High Pressure. *J Electrochem Soc* 1999;146:2834–40.
- [63] Mugikura Y, Yoshiba F, Izaki Y, Watanabe T, Takahashi K, Takashima S, et al. Performance and life of 10-kW molten-carbonate fuel cell stack using Li/K and Li/Na carbonates as the electrolyte. *J Power Sources* 1998;75:108–15.
- [64] Scaccia S. Investigation on NiO solubility in binary and ternary molten alkali metal carbonates containing additives. *J Mol Liq* 2005;116:67–71.
- [65] Mohn H, Wendt H. Molecular Thermodynamics of Molten Salt Evaporation*. *Z Für Phys Chem* 1995;192:101–19.
- [66] Cassir M, Olivry M, Albin V, Malinowska B, Devynck J. Thermodynamic and electrochemical behavior of nickel in molten Li_2CO_3 – Na_2CO_3 modified by addition of calcium carbonate. *J Electroanal Chem* 1998;452:127–37.
- [67] Kim S-G, Jun J, Jun J. Predictions of the optimum ternary alkali-carbonate electrolyte composition for MCFC by computational calculation. *J Power Sources* 2006;160:805–10.

- [68] Ota K, Mitsushima S, Kato S, Asano S, Yoshitake H, Kamiya N. Solubilities of Nickel Oxide in Molten Carbonate. *J Electrochem Soc* 1992;139:667–71. doi:10.1149/1.2069282.
- [69] Kojima T. Physical and Chemical Properties of Molten Carbonates. Dissertation. Kobe University Graduate School of Science and Technology, 2009.
- [70] Smith DS, Winnick J. Cesium-Containing Electrolyte for the Molten Carbonate Fuel Cell. *Electrochem Solid-State Lett* 1999;2:207–9.
- [71] Kojima T, Miyazaki Y, Nomura K, Tanimoto K. Physical Properties of Molten $\text{Li}_2\text{CO}_3\text{-Na}_2\text{CO}_3$ (52:48 mol%) and $\text{Li}_2\text{CO}_3\text{-K}_2\text{CO}_3$ (62:38 mol%) Containing Additives. *J Electrochem Soc* 2013;160:H733–41.
- [72] Janz GJ. Thermodynamic and transport properties for molten salts; correlated equations for critically evaluated density, surface tension electrical conductance, and viscosity data. *J Phys Chem Ref Data* 1988;17:320 pages.
- [73] Hoffmann J. Schmelzkarbonatbrennstoffzelle und Elektrolytmischung für eine solche. DE10136156 A1, 2002.
- [74] Hilmi A, Yuh C-Y, Farooque M. United States Patent: 8557468 - High performance electrolyte for molten carbonate fuel cells comprising carbonate electrolyte doped with additive material(s) and lithium precursor(s). 8557468, 2013.
- [75] Suntola T, Antson J. Method for producing compound thin films. US4058430 A, 1977.
- [76] Päiväsääri J, Niinistö J, Myllymäki P, Iv CD, Winter CH, Putkonen M, et al. Atomic Layer Deposition of Rare Earth Oxides. In: Fanciulli M, Scarel G, editors. *Rare Earth Oxide Thin Films*, Springer Berlin Heidelberg; 2007, p. 15–32.
- [77] Macdonald JR. Some new directions in impedance spectroscopy data analysis. *Electrochimica Acta* 1993;38:1883–90.
- [78] Barsoukov E, Macdonald JR, editors. *Impedance spectroscopy: theory, experiment, and applications*. 2nd ed. Hoboken, N.J: Wiley-Interscience; 2005.
- [79] Conway BE, Bockris JO, White RE, editors. *Modern Aspects of Electrochemistry*. vol. 32. Boston: Kluwer Academic Publishers; 2002.
- [80] Boukamp BA. A Linear Kronig-Kramers Transform Test for Immittance Data Validation. *J Electrochem Soc* 1995;142:1885–94.
- [81] Schichlein H, Müller AC, Voigts M, Krügel A, Ivers-Tiffée E. Deconvolution of electrochemical impedance spectra for the identification of electrode reaction mechanisms in solid oxide fuel cells. *J Appl Electrochem* 2002;32:875–82.
- [82] Wan TH, Saccoccio M, Chen C, Ciucci F. Influence of the Discretization Methods on the Distribution of Relaxation Times Deconvolution: Implementing Radial Basis Functions with DRTtools. *Electrochimica Acta* 2015;184:483–99.
- [83] Lvovich VF. *Impedance Spectroscopy: Applications to Electrochemical and Dielectric Phenomena*. Hoboken, NJ, USA: John Wiley & Sons, Inc.; 2012.
- [84] Leonide A, Sonn V, Weber A, Ivers-Tiffée E. Evaluation and Modeling of the Cell Resistance in Anode-Supported Solid Oxide Fuel Cells. *J Electrochem Soc* 2008;155:B36.

Bibliography

- [85] Leonide A, Hansmann S, Weber A, Ivers-Tiffée E. Performance simulation of current/voltage-characteristics for SOFC single cell by means of detailed impedance analysis. *J Power Sources* 2011;196:7343–6.
- [86] Hörlin T. Maximum entropy in impedance spectroscopy of non-inductive systems. *Solid State Ion* 1993;67:85–96.
- [87] Hörlin T. Deconvolution and maximum entropy in impedance spectroscopy of noninductive systems. *Solid State Ion* 1998;107:241–53.
- [88] Kazlauskas S, Kežionis A, Šalkus T, Orliukas AF. Electrical properties of YSZ and CaSZ single crystals. *Solid State Ion* 2013;231:37–42.
- [89] Saccoccio M, Wan TH, Chen C, Ciucci F. Optimal Regularization in Distribution of Relaxation Times applied to Electrochemical Impedance Spectroscopy: Ridge and Lasso Regression Methods - A Theoretical and Experimental Study. *Electrochimica Acta* 2014;147:470–82.
- [90] Boukamp BA, Rolle A. Analysis and Application of Distribution of Relaxation Times in Solid State Ionics. *Solid State Ion* 2016.
- [91] Francesco Ciucci research group. DRTTOOLS. 2016.
- [92] Malinowska B. Etude électrochimique du nickel en milieu carbonate fondu en vue de son application à la réalisation de cathodes de piles à combustibles. Paris: Paris 6; 1996.
- [93] Cassir M, Olivry M, Albin V, Malinowska B, Devynck J. Thermodynamic and electrochemical behavior of nickel in molten $\text{Li}_2\text{CO}_3\text{--Na}_2\text{CO}_3$ modified by addition of calcium carbonate. *J Electroanal Chem* 1998;452:127–37.
- [94] Meléndez-Ceballos A, Fernández-Valverde SM, Barrera-Díaz C, Albin V, Lair V, Ringuedé A, et al. TiO_2 protective coating processed by Atomic Layer Deposition for the improvement of MCFC cathode. *Int J Hydrog Energy* 2013;38:13443–52.
- [95] Chauvaut V, Cassir M, Denos Y. Behavior of titanium species in molten $\text{Li}_2\text{CO}_3\text{--Na}_2\text{CO}_3$ and $\text{Li}_2\text{CO}_3\text{--K}_2\text{CO}_3$ under anodic and cathodic conditions. I – Thermodynamic predictions at 550–750°C. *Electrochimica Acta* 1998;43:1991–2003.
- [96] Belhomme C, Gourba E, Cassir M, Tessier C. Chemical and electrochemical behaviour of Ni–Ti in the cathodic conditions used in molten carbonate fuel cells. *J Electroanal Chem* 2001;503:69–77.
- [97] Albin V, Mendoza L, Goux A, Ringuedé A, Billard A, Briois P, et al. Morphological, structural and electrochemical analysis of sputter-deposited ceria and titania coatings for MCFC application. *J Power Sources* 2006;160:821–6.
- [98] Meléndez-Ceballos A, Albin V, Fernández-Valverde SM, Ringuedé A, Cassir M. Electrochemical properties of Atomic layer deposition processed CeO_2 as a protective layer for the molten carbonate fuel cell cathode. *Electrochimica Acta* 2014;140:174–81.
- [99] Cassir M, Chauvaut V, Alfarrá A, Albin V. Study of cerium species in molten $\text{Li}_2\text{CO}_3\text{--Na}_2\text{CO}_3$ in the conditions used in molten carbonate fuel cells. Part II: Potentiometric and voltammetric behaviour. *J Appl Electrochem* 2000;30:1415–20.
- [100] Chauvaut V, Albin V, Schneider H, Cassir M, Ardéléan H, Galtayries A. Study of cerium species in molten $\text{Li}_2\text{CO}_3\text{--Na}_2\text{CO}_3$ in the conditions used in molten carbonate fuel cells. Part I: Thermodynamic, chemical and surface properties. *J Appl Electrochem* 2000;30:1405–13.

- [101] Escudero MJ, Ringuedé A, Cassir M, González-Ayuso T, Daza L. Porous nickel MCFC cathode coated by potentiostatically deposited cobalt oxide: III. Electrochemical behaviour in molten carbonate. *J Power Sources* 2007;171:261–7.
- [102] Escudero MJ, Mendoza L, Cassir M, Gonzalez T, Daza L. Porous nickel MCFC cathode coated by potentiostatically deposited cobalt oxide: II. Structural and morphological behavior in molten carbonate. *J Power Sources* 2006;160:775–81.
- [103] Meléndez-Ceballos A, Fernández-Valverde SM, Albin V, Lair V, Chávez-Carvayar JÁ, Ringuedé A, et al. Investigation on niobium oxide coatings for protecting and enhancing the performance of Ni cathode in the MCFC. *Int J Hydrog Energy* 2016.
- [104] Antolini E. Behaviour of Ni, NiO and $\text{Li}_x\text{Ni}_{1-x}\text{O}$ in molten alkali carbonates. *J Mater Sci* 2000;35:1501–5.
- [105] Meléndez-Ceballos A, Albin V, Ringuedé A, Fernández-Valverde SM, Cassir M. Electrochemical behavior of M_{x-1}O_x (M = Ti, Ce and Co) ultra-thin protective layers for MCFC cathode. *Int J Hydrog Energy* 2014;39:12233–41.
- [106] Prins-Jansen JA, Plevier GAJM, Hemmes K, de Wit JHW. An ac-impedance study of dense and porous electrodes in molten-carbonate fuel cells. *Electrochimica Acta* 1996;41:1323–9.
- [107] Tomczyk P, Mosiałek M. Investigation of the oxygen electrode reaction in basic molten carbonates using electrochemical impedance spectroscopy. *Electrochimica Acta* 2001;46:3023–32.
- [108] Uchida I, Mugikura Y, Nishina T, Itaya K. Gas electrode reactions in molten carbonate media Part II. Oxygen reduction kinetics on conductive oxide electrodes in $(\text{Li} + \text{K})_2\text{CO}_3$ eutectic at 650°C. *J Electroanal Chem Interfacial Electrochem* 1986;206:241–52.
- [109] Weewer R, Hemmes K, Wit JHW de. The Mechanism of Hydrogen Oxidation at Gold and Nickel Flag Electrodes in Molten Li/K Carbonate. *J Electrochem Soc* 1995;142:389–97.
- [110] Zeng CL, Wang W, Wu WT. Electrochemical impedance models for molten salt corrosion. *Corros Sci* 2001;43:787–801.
- [111] Makkus RC, Hemmes K, De Witt JHW. Impedance Measurements on Oxygen Reduction Reaction in Molten Carbonate. *Berichte Bunsenges Für Phys Chem* 1990;94:960–7.
- [112] Dave BB, White RE, Srinivasan S, Appleby AJ. Impedance Analysis for Oxygen Reduction in a Lithium Carbonate Melt: Effects of Partial Pressure of Carbon Dioxide and Temperature. *J Electrochem Soc* 1993;140:2139–45.
- [113] Bockris JOM, Srinivasan S. *Fuel cells: their electrochemistry*. McGraw-Hill; 1969.
- [114] Jansen JA. *Cathodes in molten-carbonate fuel cells: mathematical modeling and experimental characterization*. 1996.
- [115] Makkus RC. *Electrochemical studies on the oxygen reduction and NiO(Li) dissolution in molten carbonate fuel cells*. Delft: 1991.
- [116] Nishina T, Uchida I, Selman JR. Gas Electrode Reactions in Molten Carbonate Media Part V . Electrochemical Analysis of the Oxygen Reduction Mechanism at a Fully Immersed Gold Electrode. *J Electrochem Soc* 1994;141:1191–8.

Bibliography

- [117] Gerischer H. Alternating current polarization of electrodes with a potential-defined step at the equilibrium potential. I. *Z Phys Chem* 1951;198:286–313.
- [118] Gerischer H. Alternating current polarization of electrodes with a potential-defined step at the equilibrium potential. II. *Z Phys Chem* 1952;201:56–7.
- [119] Gerischer KJ H.Vetter. Concentration polarization in electrolytes after previous chemical reaction and its part in the stationary polarization resistance at equilibrium potential. *Z Phys Chem* 1951;197:92–104.
- [120] Moutiers G, Cassir M, Devynck J. Oxygen reduced species in molten $\text{Li}_2\text{CO}_3 + \text{K}_2\text{CO}_3$ (42.7 + 57.3 mol%) at 650°C: A thermodynamic, voltammetric and convolution potential sweep characterization. *J Electroanal Chem* 1992;324:175–89.
- [121] Cassir M, Malinowska B, Peelen W, Hemmes K, de Wit JHW. Identification and electrochemical characterization of in situ produced and added reduced oxygen species in molten $\text{Li}_2\text{CO}_3 + \text{K}_2\text{CO}_3$. *J Electroanal Chem* 1997;433:195–205.
- [122] Kojima T, Miyazaki Y, Nomura K, Tanimoto K. Electrical Conductivity of Molten $\text{Li}_2\text{CO}_3 - \text{X}_2\text{CO}_3$ (X: Na, K, Rb, and Cs) and $\text{Na}_2\text{CO}_3 - \text{Z}_2\text{CO}_3$ (Z: K, Rb, and Cs). *J Electrochem Soc* 2007;154:F222–30.
- [123] Lair V, Albin V, Ringuedé A, Cassir M. Theoretical predictions vs. experimental measurements of the electrical conductivity of molten $\text{Li}_2\text{CO}_3 - \text{K}_2\text{CO}_3$ modified by additives. *Int J Hydrog Energy* 2012;37:19357–64.
- [124] Akhurst MC, Callaghan EA, Hannis SD, Kirk KL, Monaghan AA, Pearce JM, et al. Optimising CO_2 storage in geological formations. SCCS; 2015.
- [125] Parson Brinckerhoff. Accelerating the uptake of CCS: industrial use of captured carbon dioxide. Global Carbon Institute; 2011.
- [126] Chery D, Lair V, Cassir M. CO_2 electrochemical reduction into CO or C in molten carbonates: a thermodynamic point of view. *Electrochimica Acta* 2015;160:74–81.
- [127] Chery D, Albin V, Lair V, Cassir M. Thermodynamic and experimental approach of electrochemical reduction of CO_2 in molten carbonates. *Int J Hydrog Energy* 2014;39:12330–9.
- [128] Solid Oxide Co-Electrolysis Cells :: Ceramtec n.d. <http://www.ceramtec.com/technology/ceramic-solid-state-ionic-technologies/co2-benefication/solid-electrolysis-cells.php> (accessed April 1, 2016).
- [129] Licht S. STEP (Solar Thermal Electrochemical Photo) Generation of Energetic Molecules: A Solar Chemical Process to End Anthropogenic Global Warming. *J Phys Chem C* 2009;113:16283–92.
- [130] Cassir M, McPhail SJ, Moreno A. Strategies and new developments in the field of molten carbonates and high-temperature fuel cells in the carbon cycle. *Int J Hydrog Energy* 2012;37:19345–50.
- [131] Discepoli G, Cinti G, Desideri U, Penchini D, Proietti S. Carbon capture with molten carbonate fuel cells: Experimental tests and fuel cell performance assessment. *Int J Greenh Gas Control* 2012;9:372–84.
- [132] Ren J, Lau J, Lefler M, Licht S. The Minimum Electrolytic Energy Needed To Convert Carbon Dioxide to Carbon by Electrolysis in Carbonate Melts. *J Phys Chem C* 2015;119:23342–9.

- [133] Ijije HV, Sun C, Chen GZ. Indirect electrochemical reduction of carbon dioxide to carbon nanopowders in molten alkali carbonates: Process variables and product properties. *Carbon* 2014;73:163–74.
- [134] Deng B, Tang J, Mao X, Song Y, Zhu H, Xiao W, et al. Kinetic and Thermodynamic Characterization of Enhanced Carbon Dioxide Absorption Process with Lithium Oxide-Containing Ternary Molten Carbonate. *Environ Sci Technol* 2016;50:10588–95.
- [135] Deng B, Chen Z, Gao M, Song Y, Zheng K, Tang J, et al. Molten salt CO₂ capture and electrotransformation (MSCC-ET) into capacitive carbon at medium temperature: effect of the electrolyte composition. *Faraday Discuss* 2016;190:241–58.
- [136] Wu H, Li Z, Ji D, Liu Y, Li L, Yuan D, et al. One-pot synthesis of nanostructured carbon materials from carbon dioxide via electrolysis in molten carbonate salts. *Carbon* 2016;106:208–17.
- [137] Ijije HV, Lawrence RC, Chen GZ. Carbon electrodeposition in molten salts: electrode reactions and applications. *RSC Adv* 2014;4:35808–17.
- [138] Kaplan V, Wachtel E, Gartsman K, Feldman Y, Lubomirsky I. Conversion of CO₂ to CO by Electrolysis of Molten Lithium Carbonate. *J Electrochem Soc* 2010;157:B552–6.
- [139] Yin H, Mao X, Tang D, Xiao W, Xing L, Zhu H, et al. Capture and electrochemical conversion of CO₂ to value-added carbon and oxygen by molten salt electrolysis. *Energy Environ Sci* 2013;6:1538.
- [140] Halmann MM, Steinberg M. Greenhouse gas carbon dioxide mitigation: science and technology. Boca Raton (Florida): Lewis; 1999.
- [141] Peelen WHA, Hemmes K, de Wit JHW. CO₂ reduction in molten 62/38 mole% Li/K carbonate mixture. *Electrochimica Acta* 1998;43:763–9.
- [142] Chery D, Albin V, Meléndez-Ceballos A, Lair V, Cassir M. Mechanistic approach of the electrochemical reduction of CO₂ into CO at a gold electrode in molten carbonates by cyclic voltammetry. *Int J Hydrog Energy* 2016.
- [143] Jain RK, Gaur HC, Welch BJ. Chronopotentiometry: A review of theoretical principles. *J Electroanal Chem Interfacial Electrochem* 1977;79:211–36.
- [144] Bockris JOM, Reddy AKN, Gamboa-Aldeco ME. *Modern Electrochemistry 2A - Fundamentals of Electrodeics*. vol. 2A. Springer New York; 2001.
- [145] Jain RK, Gaur HC, Frazer EJ, Welch BJ. Chronopotentiometry: A review of applications in molten salts. *J Electroanal Chem Interfacial Electrochem* 1977;78:1–30.
- [146] Meléndez-Ceballos A, Albin V, Lair V, Ringuedé A, Cassir M. A kinetic approach on the effect of Cs addition on oxygen reduction for MCFC application. *Electrochimica Acta* 2015;184:295–300.
- [147] Chery D. Approche prévisionnelle de la valorisation électrochimique du CO₂ dans les carbonates fondus. Ph.D. Dissertation. Université Pierre et Marie Curie -Paris VI, 2015.
- [148] Larminie J, Dicks A. *Fuel cell systems explained*. 2nd ed. Chichester, West Sussex: J. Wiley; 2003.

Bibliography

- [149] Allen J, Schoonmaker D. Aqueous based electrolyte slurry for MCFC and method of use. US20030162082 A1, 2003.
- [150] Allen JP, Schoonmaker DA. Aqueous based electrolyte slurry for MCFC and method of use. US6844102 B2, 2005.
- [151] Morita H, Nakano H, Mugikura Y, Izaki Y, Watanabe T, Uchida I. EIS as a Tool to Determine Fuel Flow Distribution in Molten Carbonate Fuel Cells. *J Electrochem Soc* 2003;150:A1693–8.
- [152] Yuh CY, Selman JR. The Polarization of Molten Carbonate Fuel Cell Electrodes I . Analysis of Steady-State Polarization Data. *J Electrochem Soc* 1991;138:3642–8.
- [153] Yuh CY, Selman JR. The Polarization of Molten Carbonate Fuel Cell Electrodes II . Characterization by AC Impedance and Response to Current Interruption. *J Electrochem Soc* 1991;138:3649–56.
- [154] Yuh CY, Selman JR. Characterization of fuel cell electrode processes by AC impedance. *AIChE J* 1988;34:1949–58.
- [155] Kreuer K-D. Fuel cells selected entries from the Encyclopedia of Sustainability Science and Technology. New York, NY: Springer; 2013.

Index of figures

Figure I.1- Fuel cell classification by temperature, working principle and main components.	10
Figure I.2- Total MW of power generated by fuel cell type.	11
Figure I.3- General scheme of a MCFC installation.	12
Figure I.4- Scheme of three different concepts of fuel cell reforming of infeed stream.	13
Figure I.5- Scheme of a MCFC single cell components.	14
Figure I.6- Potential-oxoacidity diagram for Li-K (62-38 mol%) at 650 °C that allows the study of each redox system as function of P_{CO_2} .	16
Figure II.1- Schema of the purge and pulse sequence in ALD.	27
Figure II.2- Vertical gas flow reactor scheme.	28
Figure II.3- Equivalent circuit for a simple faradaic electron transfer with semi-infinite diffusion a) with ZF component, b) with decomposition of ZF.	30
Figure II.4- Nyquist plot of the impedance data for an electrochemical reaction with semi-infinite diffusion and the parameters that can be found in it.	31
Figure II.5- Example of data validation by Kramers-Kronig transforms by using the program developed by Boukamp K-K test V1.01.	32
Figure II.6. Chronopotentiogram at a graphite electrode in Li-Na, 650 °C, P_{CO_2} =0.5 atm, with a current of -1.5 mA	35
Figure II.7- Half-cell set up for cathode material and modified electrolyte testing.	36
Figure II.8- Schema of GC configuration for fuel cell gas stream composition measurements.	39
Figure II.9- Electrical wiring of complete fuel cell electronic components.	40
Figure II.10- Gas and water supply schema of complete cell testing system.	40
Figure III.1- SEM micrographs of the as-deposited layers onto porous nickel substrates: TiO ₂ 50 and 300 nm (a, b), CeO ₂ 27 and 127 nm (c, d), Nb ₂ O ₅ 5, 50 and 300 (e, f, g) and Co ₃ O ₄ 50 nm (h).	47
Figure III.2- SEM images of t some samples after immersion in molten Li-K carbonate eutectic for 230 h at 650 °C: TiO ₂ 50 and 300 nm (a, b), CeO ₂ 27 and 127 nm (c, d), Co ₃ O ₄ 50 nm (e) and Nb ₂ O ₅ 50 (f).	49
Figure III.3- XRD diffractograms for all samples after 230 h immersion in molten Li-K carbonates at 650 °C.	50
Figure III.4- OCP evolution over 230h immersion time for the most relevant samples :TiO ₂ 50 nm, Co ₃ O ₄ 50 nm, CeO ₂ 27 nm and Nb ₂ O ₅ 50 nm.	51

Figure III.5- EIS Nyquist representation of CeO ₂ coated sample and the equivalent circuit used to fit the data. The fitting is shown in red.	52
Figure III.6- Total resistance evolution over immersion time.	53
Figure IV.1- Equivalent circuits used for the analysis of the EIS data, a) considering a Warburg diffusion element, b) considering a Gerischer type element.	67
Figure IV.2- Example of the EIS data acquired in our experiments fitted with circuit b) of Figure IV.1.	67
Figure IV.3- Six mixed diffusion cases analysis taken the Gerischer coefficient of fitted EIS data, from case 1 to 6 as described in section 4.1.2 only for 3 mol% added Cs in Li-K Eutectic at 650 °C.	69
Figure IV.4- Mixed diffusion case $[O_2^-] > [O_2^{2-}], [CO_4^{2-}]$; O_2^-/CO_2 plot for 0, 3 and 5 mol% added Cs on Li-K eutectic at 650 °C, the slopes and intercepts were taken to calculate the diffusion coefficients of the involved species.	70
Figure IV.5- Comparison of the diffusion coefficients $D_{O_2^-}$ and D_{CO_2} obtained from Warburg and Gerischer fitting at 0, 3 and 5 mol% added Cs on Li-K eutectic at 650 °C.	71
Figure IV.6- P_{O_2} and P_{CO_2} partial pressure dependency of 1/Rct plot for 0, 3 and 5 mol% added Cs on Li-K carbonate mixture at 650 °C.	72
Figure IV.7- OCP evolution of porous Ni cathode immersed in Li-K eutectic (black line), Li-K + 5 mol % of Cs (red line) and Li-K + 5 mol% of Rb (blue line) at 650 °C under 70/30 % air/CO ₂ atmosphere at ambient pressure.	74
Figure IV.8- OCP evolution of porous Ni cathode immersed in Li-Na eutectic (black line) and Li-Na + 5 mol % of Cs (red line) at 650 °C under 70/30 % air/CO ₂ atmosphere at ambient pressure.	74
Figure IV.9- EIS data fitting with equivalent circuit shown in upper right corner. Data corresponds to 110 h porous Ni cathode immersion in Li-K eutectic carbonate melt with no additive at 650 °C. Numbers over data points indicate the logarithm of the frequency of the marked point.	75
Figure IV.10- Porous Ni electrode charge transfer and total resistance evolution over OCP duration for pristine Li-K electrolyte (squares), 5 mol % added Cs (circles) and 5 mol % added Rb (triangles) at 650 °C under 70/30 % air/CO ₂ atmosphere at ambient pressure.	77
Figure IV.11- Porous Ni electrode charge transfer and total resistance evolution over OCP duration for pristine Li-Na electrolyte (squares) and 5 mol % added Cs (circles) at 650 °C under 70/30 % air/CO ₂ atmosphere at ambient pressure.	77
Figure V.1- Cyclic voltammograms at a gold electrode in Li-Na carbonate eutectic at 600 °C, $v=100$ mV/s, after a pre-electrolysis at -1,1 V vs Ag/Ag ⁺ during 360 s; (dashed line) $P_{CO_2}=0.2$ atm.; (solid line) $P_{CO_2}=0.3$ atm [142].	85
Figure V.2- Chronopotentiometry at a gold electrode in different carbonate eutectics: a) Li-Na at 650 °C and P_{CO_2} 0.5 atm.; b) Li-K at 650 °C and P_{CO_2} 0.05 atm.; c) Li-Na-K 600 °C and P_{CO_2} 0.5 atm. and d) Na-K at 750 °C and P_{CO_2} 0.5 atm.	86

Figure V.3- Chronopotentiometry at P_{CO_2} 0.5 atm of: a) gold electrode immersed in Li-Na eutectic at 700 °C and b) graphite electrode immersed in Li-K eutectic at 650 °C.	87
Figure V.4- Transition time dependence on applied current in different conditions: a) gold electrode in Li-Na at P_{CO_2} = 0.5 atm. and different temperatures; b) gold electrode in Li-Na eutectic at 650 °C and different P_{CO_2} , and c) graphite electrode in Li-K eutectic at P_{CO_2} = 0.05 atm. and different temperatures. The small numbers indicate the value of $E\tau/4$ (quarter potential).	89
Figure V.5- Current reversal chronopotentiometry performed at a gold electrode: a) Li-K eutectic at 650 °C, P_{CO_2} = 0.1 atm., initial current of -8 mA during 1 s, then 8 mA during 1 s; b) in Li-Na eutectic at 650 °C, P_{CO_2} = 0.5 atm.; initial current of -10 mA during 6 s, then 10 mA during 2 s.	91
Figure V.6. Chronoamperometry performed at a gold electrode in Li-K eutectic at 650°C; a) P_{CO_2} = 0.05 atm., E = -0.9 V vs Ag/Ag+; b) P_{CO_2} = 0.1 atm., E = -1.2 V vs Ag/Ag+	94
Figure VI.1. Detail of the fuel cell assembly with two identical cell holder cups, electrolyte is in light yellow, anode is in dark green and cathode is in gray.	104
Figure VI.2. Slurry preparation for tape cast forming of Li-K laminates.	105
Figure VI.3. TGA-DSC analysis of tape casted laminate of Li-K eutectic mixture.	106
Figure VI.4. OCP of a MCFC single cell over 6 hours after changing to the working atmosphere of H ₂ /CO ₂ /H ₂ O (64/16/20 %) at the anode and of O ₂ /CO ₂ /N ₂ (15/30/55 %) at the cathode.	108
Figure VI.5. I-E and Power curve taken after cell stabilization at 10 mV·s ⁻¹ from 980mV to 400 mV, at 650 °C, and atmospheres of H ₂ /CO ₂ /H ₂ O (64/16/20 %) at the anode and of O ₂ /CO ₂ /N ₂ (15/30/55 %) at the cathode.	109
Figure VI.6. Nyquist diagram of MCFC cell at 650 °C and working atmosphere H ₂ /CO ₂ /H ₂ O (64/16/20 %) at the anode side and O ₂ /CO ₂ /N ₂ (15/30/55 %) at the cathode, numbers indicate Log of frequency.	109
Figure VI.7. Kramers-Kronig test of data set shown in Figure VI.6.	110
Figure VI.8. DRT of EIS data collected by using DRTTools [82], parameters were: regularization 1E-4, fitted w/o inductance, 1st order regularization derivative and shape factor 1.	111

Index of tables

Table I.1- MCFC improvement objectives and proposed strategies	19
Table II.1- Gas compositions tested.	37
Table II.2- Preconditioning sequence for MCFC operation.	41
Table III.1- ALD deposited materials for cathode protection.	45
Table III.2- ALD deposition parameters for all the deposited materials.	46
Table III.3- Different phases found in the tested samples after immersion in molten carbonates for 230 h by various techniques and their reference articles.	48
Table III.4- Solubility values of Ni for the cathodes coated by different metal oxides after 230 h immersion in molten Li-K carbonates at 650 °C.	54
Table IV.1- Coefficients for reaction IV.12 for the three mechanisms described (eq. IV.1 to IV.7) [114].	61
Table IV.2- New p and q coefficients for reaction IV.9 [114].	62
Table IV.3- Theoretical reaction orders for the different mechanisms as a function of gas partial pressure.	63
Table IV.4- Values of a and b obtained from the slope and intercepts of the mixed diffusion case $[O_2^-] > [O_2^{2-}], [CO_4^{2-}]$; O_2^-/CO_2 by Warburg and Gerischer fitting for 0, 3 and 5 mol-% of Cs in Li-K at 650 °C.	68
Table IV.5- Values obtained with a and b of linear regression of plot for the mixed diffusion case $[O_2^-] > [O_2^{2-}], [CO_4^{2-}]$; O_2^-/CO_2 by Warburg and Gerischer fitting for 0, 3 and 5 mol-% of Cs in Li-K at 650 °C.	69
Table IV.6- Values of β_1 and β_2 taken from the slopes of Figure IV.6.	73
Table V.1- τ relations for electrochemical reactions including one adsorption step	92
Table V.2- Transition time analysis of the four cases proposed in Table V.1 for Li-K on graphite electrode and Li-Na-K on gold electrode at different temperatures and atmospheres.	93
Table VI.1. Characteristics of fuel cell components employed.	103
Table VI.2. Slurry composition for tape casting of eutectic carbonate mixture of Li-K (62-38 mol%).	105

Publications

Scientific papers

1. Meléndez-Ceballos A, Fernández-Valverde SM, Barrera-Díaz C, Albin V, Lair V, Ringuedé A, et Cassir M*. TiO₂ protective coating processed by Atomic Layer Deposition for the improvement of MCFC cathode. *International Journal of Hydrogen Energy* 2013; 38:13443–52.
2. Meléndez-Ceballos A, Albin V, Fernández-Valverde SM*, Ringuedé A, Cassir M*. Electrochemical properties of Atomic layer deposition processed CeO₂ as a protective layer for the molten carbonate fuel cell cathode. *Electrochimica Acta* 2014;140:174–81.
3. Meléndez-Ceballos A, Albin V, Ringuedé A, Fernández-Valverde SM*, Cassir M. Electrochemical behavior of M_{x-1}O_x (M = Ti, Ce and Co) ultra-thin protective layers for MCFC cathode. *International Journal of Hydrogen Energy* 2014;39:12233–41.
4. Meléndez-Ceballos A, Fernández-Valverde SM, Albin V, Lair V, Chávez-Carvayar JÁ, Ringuedé A, et al. Investigation on niobium oxide coatings for protecting and enhancing the performance of Ni cathode in the MCFC. *International Journal of Hydrogen Energy* 2016;41:18721–31.
5. Meléndez-Ceballos A*, Albin V, Lair V, Ringuedé A, Cassir M. A kinetic approach on the effect of Cs addition on oxygen reduction for MCFC application. *Electrochimica Acta* 2015;184:295–300.
6. Meléndez-Ceballos A, Albin V, Crapart C, Lair V, Ringuedé A, Cassir M*. Influence of Cs and Rb additions in LiK and LiNa molten carbonates on the behaviour of MCFC commercial porous Ni cathode. *International Journal of Hydrogen Energy* 2016.
7. Chery D, Albin V, Meléndez-Ceballos A, Lair V, Cassir M*. Mechanistic approach of the electrochemical reduction of CO₂ into CO at a gold electrode in molten carbonates by cyclic voltammetry. *International Journal of Hydrogen Energy* 2016.
8. J. Swiatowska*, L. Santos, V. Lair, S. Zanna, A. Seyeux, A. Meléndez-Ceballos, P. Tran-Van, M. Cassir, P. Marcus. Mechanisms of enhanced lithium intercalation into ALD-processed V₂O₅ in Ionic Liquids (Pyr13FSI and Pyr14TFSI) investigated by XPS and ToF-SIMS. Submitted to *Journal of Power Sources* February 2017.
9. Meléndez-Ceballos, A. Brouzgou, C. Crapart, V. Albin, V. Lair, M. Cassir*. Chronopotentiometric approach of CO₂ reduction in molten carbonates. *Journal of the Electrochemical Society*, Accepted April 2017.

Book Chapters

1. Cassir M*, Meléndez-Ceballos A, Ringuedé A, Lair V. 3 - Molten carbonate fuel cells. In: *Compendium of Hydrogen Energy*. Veziroğlu FBBN, editor. Oxford: Woodhead Publishing; 2016, p. 71–87.
2. Cassir M*, Meléndez-Ceballos A. 15- Fuel cells: a general overview, applications and future trends. In: *Membrane Reactor Engineering: Applications for a Green Process Industry*, First Edition, Angelo Basile, Marcello De Falco, Gabriele Centi and Gaetano Iaquaniello, editors. John Wiley & Sons, Ltd; 2016.
3. Cassir M*, Meléndez-Ceballos A, Chavanne M-H, Dallel D, Ringuedé A. 7- ALD-processed oxides for high temperature fuel cells. In: *Atomic layer deposition in energy conversion applications*. Julien Bachmann, editor. John Wiley & Sons, Ltd; 2016. p. 219-234.
4. Cassir M*, Meléndez-Ceballos A, Chavanne M-H, Dallel D, Ringuedé A. L'ALD dans le domaine de piles à combustible à haute température. In: *Techniques de l'ingénieur*, Paris, France. 2016 pp RE256-1 – RE256-12.

Adequacy of new electrolyte compositions and nanostructured protective layers for the cathode of molten carbonate fuel cells

Abstract:

In this work, we develop two major research routes related to molten carbonates. The first one is the molten carbonate fuel cell optimization, with two approaches: (i) cathode lifetime improvement through ultra-thin layers of metal oxides deposited by atomic layer deposition; (ii) Li-K and Li-Na electrolyte modification by Cs or Rb additions. The second one is dedicated to CO₂ valorization through its electrochemical reduction in molten carbonate electrolytes, where we analyze CO₂ reduction by means of chronopotentiometry and chronoamperometry. Finally, in order to test some of the component modifications described in the two first parts, we installed and adapted a single-cell setup coupled to gas chromatography. We obtained some significant results in all the approaches; concerning point (i), we found that TiO₂ and CeO₂ are suitable for cathode corrosion protection without affecting the electrochemical properties of the electrode and reducing almost by half the dissolution of Ni. The results obtained from point (ii) are also fruitful, since we established a method for comparing two different electrolytes and obtained the diffusion coefficients of the superoxides and carbon dioxide. We also compared the performance of the state-of-the-art NiO cathode in Cs and Rb modified electrolytes. From these studies, we found that Cs addition improves significantly the CO₂ diffusion coefficient and reduces the charge transfer and total resistance at the electrode, being a promising additive. Regarding CO₂ reduction, after all the tests performed, we found that the reaction involves adsorbed and instable species and occurs in two one-electron steps or in two-electron unique step; thus, it follows most probably a mechanism of simultaneous reduction of the adsorbed and dissolved species. Finally, we performed the first MCFC single-cell tests in our laboratory obtaining an acceptable cell performance and output power. However, small improvements are still necessary to be able to test MCFC modified components.

Adéquation de nouvelles compositions d'électrolytes et de revêtements protecteurs nanostructurés de la cathode pour les piles à combustible à carbonates fondus

Abstract:

Dans ce travail, nous développons deux grands axes de recherche liés aux carbonates fondus. Le premier est l'optimisation des piles à combustible à base de carbonates fondus, avec deux approches : (i) l'amélioration de la durée de vie de la cathode grâce à des couches ultra-minces d'oxydes métalliques élaborés par la technique de dépôt de couches atomiques; (ii) la modification des électrolytes Li-K et Li-Na par addition de Cs ou de Rb. Le second est consacré à la valorisation du CO₂ par sa réduction électrochimique dans les électrolytes à carbonates fondus, où nous analysons la réduction du CO₂ par chronopotentiométrie et chronoamperométrie. Finalement, afin de tester les modifications subies par certains des composants analysés dans les deux premières parties, nous avons installé et adapté une configuration de cellule complète couplée à la chromatographie en phase gazeuse. Nous avons obtenu quelques résultats significatifs dans l'ensemble des approches abordées ; en ce qui concerne le point (i), nous avons constaté que TiO₂ et CeO₂ sont appropriés pour protéger la cathode contre la corrosion sans affecter ses propriétés électrochimiques en réduisant presque de moitié la dissolution du Ni. Les résultats obtenus pour le point (ii) sont également fructueux, car nous avons établi une méthode pour comparer deux électrolytes différents en déterminant les coefficients de diffusion des ions superoxyde et du dioxyde de carbone. Nous avons également comparé les performances de la cathode de NiO dans les électrolytes modifiés avec Cs et Rb. De ces études, nous avons constaté que l'addition de Cs améliore significativement le coefficient de diffusion de CO₂ en réduisant la résistance de transfert de charge et la résistance totale à l'électrode, étant l'additif le plus prometteur testé ici. En ce qui concerne la réduction du CO₂, nous avons constaté que la réaction implique des espèces adsorbées et instables et se produit en deux étapes à un électron ou une étape à deux électrons ; ainsi, il s'agit très probablement d'un mécanisme de réduction simultanée d'espèces adsorbées et dissoutes. Finalement, nous avons effectué les premiers tests sur cellule complète MCFC dans notre laboratoire, obtenant une performance et une puissance acceptables. Cependant, de petites améliorations sont encore nécessaires pour pouvoir tester les composants modifiés de cellule MCFC.

Keywords : [MCFC, MCEC, molten carbonates, impedance, chronoamperometry, cathode dissolution, cathode protection, electrolyte improvement, carbon capture, CO₂ reduction, CO₂ valorization]